

TECHNISCHE UNIVERSITÄT MÜNCHEN

Fakultät für Physik
Lehrstuhl für Funktionelle Materialien

Thermoelectric thin films based on conducting polymers

Nitin Saxena, M. Sc.

Vollständiger Abdruck der von der Fakultät für Physik der Technischen Universität München zur Erlangung des akademischen Grades eines

Doktors der Naturwissenschaften (Dr. rer. nat.)

genehmigten Dissertation.

Vorsitzender: Prof. Dr. Andreas Weiler
Prüfer der Dissertation: 1. Prof. Dr. Peter Müller-Buschbaum
2. Prof. Dr. Martin Brandt

Die Dissertation wurde am 20.02.2019 bei der Technischen Universität München eingereicht und durch die Fakultät für Physik am 05.04.2019 angenommen.

Abstract

In this thesis, conducting polymer films are investigated regarding their potential application in thermoelectric thin films. Key parameters for the conversion efficiency of heat into electricity are addressed and correlated with structural and optical properties. PEDOT:PSS thin films are nanostructured with inorganic nanoparticles in order to reduce the thermal conductivity of the thin films. This is proven using infrared thermography and explained with the help of resonant x-ray scattering. The intrinsically high charge carrier concentration in PEDOT:PSS is systematically reduced with the help of inorganic salts with acido-basic and redox properties in order to increase the Seebeck coefficient. The impact on electronic, compositional and conformational properties is observed with various spectroscopic techniques. Ionic liquids are used for post-treatment of PEDOT:PSS thin films, in order to simultaneously increase Seebeck coefficients and electrical conductivities. The combined effect on electronic and structural properties is proven with the help of spectroscopy and x-ray scattering. P(NDI2OD-T2) is a popular representative among n-type polymers, and is doped with N-DPBI. The effect of doping on optical, structural and thermoelectric properties is assessed, and the obtained knowledge is used for the fabrication of a thermoelectric generator based on conducting polymers.

Zusammenfassung

In dieser Arbeit werden leitfähige Polymerfilme hinsichtlich ihrer potenziellen Anwendung in thermoelektrischen Dünnschichten untersucht. Für die Umwandlung von Wärme in Elektrizität wichtige Parameter werden adressiert, und mit strukturellen und optischen Eigenschaften korreliert. Dünne PEDOT:PSS-Filme werden mithilfe von Silizium-Nanopartikeln nanostrukturiert, um die thermische Leitfähigkeit in Ersteren zu reduzieren. Dies wird mithilfe von Infrarot-Thermographie und resonanter Röntgenstreuung bewiesen. Die intrinsisch hohe Ladungsträgerkonzentration in PEDOT:PSS wird mit anorganischen Salzen, welche Säure-Base- und Redox-Eigenschaften besitzen, gezielt reduziert um den Seebeck-Koeffizienten in diesen Filmen zu erhöhen. Der Einfluss auf elektronische Eigenschaften, Zusammensetzung und Konformation wird mit verschiedenen spektroskopischen Methoden untersucht. Ionische Flüssigkeiten werden für die Nachbehandlung von PEDOT:PSS-Filmen eingesetzt, um simultan Seebeck-Koeffizienten und elektrische Leitfähigkeiten zu erhöhen. Der kombinierte Effekt auf elektronische und strukturelle Eigenschaften wird mithilfe von optischer Spektroskopie und Röntgenstreuung bewiesen. P(NDI2OD-T2) ist ein klassischer Vertreter der n-Typ-Polymere und wird mit N-DPBI dotiert. Das Dotieren wirkt sich auf optische, strukturelle und thermoelektrische

Eigenschaften der Filme aus. Das erlangte Wissen wird dann benutzt um einen thermoelektrischen Generator herzustellen, welcher auf leitfähigen Polymeren basiert.

Contents

Contents	iii
List of abbreviations	vii
1 Introduction	1
2 Theoretical background	7
2.1 Thermoelectric principles	7
2.1.1 Thermoelectric effects	7
2.1.2 Thermoelectric figure of merit ZT	10
2.2 Conducting polymers	12
2.2.1 Doping of conjugated polymers	14
2.2.2 PEDOT:PSS	17
2.2.3 P(NDI2OD-T2)	19
2.3 Scattering basics	20
2.3.1 Grazing-incidence scattering	22
2.3.2 Grazing-incidence resonant tender x-ray scattering (GIR-TeXS) . .	24
3 Characterization methods	27
3.1 Thermoelectric characterization	27
3.1.1 Gradient chamber	27
3.1.2 XAVER: X-ray analysis voltage-emulation rig	29
3.1.3 4-point probe measurement	35
3.1.4 Surface profilometry	36
3.1.5 Infrared thermography (IRT)	36
3.2 Spectroscopic characterization	39
3.2.1 UV-Vis spectroscopy	39
3.2.2 Raman spectroscopy	40
3.2.3 X-ray photoelectron spectroscopy (XPS)	41
3.2.4 Near-edge x-ray absorption fine structure spectroscopy (NEXAFS) .	43
3.3 Morphological characterization	44
3.3.1 Optical microscopy (OM)	44
	iii

3.3.2	Scanning electron microscopy (SEM)	44
3.3.3	Scattering methods	45
4	Sample preparation	53
4.1	Materials	53
4.1.1	Polymers	53
4.1.2	Polymer additives	55
4.1.3	Substrate materials	58
4.2	Thin film preparation	59
4.2.1	Substrate cleaning	59
4.2.2	PEDOT:PSS thin films	60
4.2.3	Free-standing PEDOT:PSS films	65
4.2.4	P(NDI2OD-T2) thin films	67
4.3	Thermoelectric generator based on conducting polymers as active materials	69
5	Nanostructuring of PEDOT:PSS thin films with silicon nanoparticles for enhancement of thermoelectric properties	73
5.1	Selection of a fabrication route	74
5.2	Thermoelectric properties of composite PEDOT:PSS/Si-NPs thin films	81
5.2.1	Influence of Si-NPs on power factor	81
5.2.2	Measurement of thermal conductivity: Infrared thermography	83
5.2.3	Calculation of full figure of merit ZT	84
5.3	Morphological properties of composite PEDOT:PSS/Si-NPs thin films	86
5.3.1	Real-space morphology: scanning electron microscopy	86
5.3.2	Grazing-incidence resonant tender x-ray scattering	88
5.4	Summary	98
6	Dedoping of PEDOT:PSS with inorganic salts for optimization of thermoelectric power factors	101
6.1	Thermoelectric characterization of dedoped PEDOT:PSS thin films	103
6.1.1	Acido-basic dedoping with sodium hydrogencarbonate	103
6.1.2	Redox dedoping with sodium sulfite and sodium borohydride	105
6.2	Spectroscopic characterization	109
6.2.1	Analysis of electronic structure with UV-Vis spectroscopy	109
6.2.2	Compositional analysis with x-ray photoelectron spectroscopy	111
6.2.3	Conformational analysis with Raman spectroscopy	116
6.3	Summary	120

7	Simultaneous enhancement of Seebeck coefficient and electrical conductivity in PEDOT:PSS through post-treatment with ionic liquids	123
7.1	Thermoelectric characterization	125
7.2	Spectroscopic characterization	131
7.3	Structural characterization	133
7.3.1	Analysis of π - π -stacking distances	136
7.3.2	Analysis of changes in the PEDOT-to-PSS ratio	138
7.3.3	Analysis of preferred orientation	140
7.4	Structure-conductivity correlation	141
7.5	Summary	143
8	P(NDI2OD-T2) as n-type polymer for thermoelectric applications	145
8.1	Spectroscopic characterization using UV-Vis spectroscopy	146
8.1.1	Influence of dopant concentration	146
8.1.2	Influence of temperature	148
8.2	Structure characterization using grazing-incidence wide-angle x-ray scattering	151
8.2.1	P(NDI2OD-T2) films on glass substrates for in-plane measurements	153
8.2.2	P(NDI2OD-T2) films on FTO substrates for cross- and pseudo-in-plane measurements	159
8.2.3	Structural model	166
8.3	Thermoelectric characterization	167
8.3.1	In-plane geometry	168
8.3.2	Cross-plane geometry	170
8.3.3	Pseudo-in-plane geometry	172
8.4	Performance of a thermoelectric generator	174
8.5	Summary	178
9	Conclusion and outlook	181
	Bibliography	185
	List of publications	193
	Acknowledgements	199

List of abbreviations

DA	decoupling approximation
DCB	1,2-dichlorobenzene
DESY	Deutsches Elektronen-Synchrotron
DMSO	dimethyl sulfoxide
DOS	density of states
DWBA	distorted-wave Born approximation
EG	ethylene glycol
EMIM BF ₄	1-ethyl-3-methylimidazolium tetrafluoroborate
EMIM DCA	1-ethyl-3-methylimidazolium dicyanamide
EMIM TCB	1-ethyl-3-methylimidazolium tetracyanoborate
FTO	fluorine-doped tin oxide
GISAXS	grazing-incidence small-angle x-ray scattering
GIWAXS	grazing-incidence wide-angle x-ray scattering
GIR-TeXS	grazing-incidence resonant tender x-ray scattering
HOMO	highest occupied molecular orbital
IL	ionic liquid
IRT	infrared thermography
LMA	local monodisperse approximation
LUMO	lowest unoccupied molecular orbital
N-DPBI	4-(1,3-dimethyl-2,3-dihydro-1H-benzoimidazol-2-yl)-N,N-diphenylaniline
NaBH ₄	sodium borohydride
NaHCO ₃	sodium hydrogencarbonate
Na ₂ SO ₃	sodium sulfite
NEXAFS	near-edge x-ray absorption fine structure
P(NDI2OD-T2)	poly[N,N'-bis(2-octyldodecyl)naphthalene-1,4,5,8-bis(dicarboximide)-2,6-diyl]-alt-5,5'-(2,2'-bithiophene)
PA	polyacetylene
PDMS	poly(dimethyl siloxane)
PEDOT:PSS	poly(3,4-ethylene dioxythiophene):poly(styrene sulfonate)
PTFE	poly(tetrafluoroethylene)
PVA	poly(vinyl alcohol)
RPSD	radial power spectral density
RSoXS	resonant soft x-ray scattering
SDD	sample-to-detector distance

SEM	scanning electron microscopy
Si-NPs	silicon nanoparticles
TDAE	tetrakis(dimethylamino)ethylene
SLD	scattering length density
TDTR	time-domain thermoreflectance
TE	thermoelectric
THF	tetrahydrofuran
TOF-GISANS	time-of-flight grazing incidence small-angle neutron scattering
XAVER	x-ray analysis voltage-emulation rig
XPS	x-ray photoelectron spectroscopy
XRD	x-ray diffraction

1 Introduction

In recent centuries, humanity made several significant leaps in its evolution in terms of society, economy and technology. While this evolution enabled many inventions that improved the livelihood for a large part of earth's population, it also left a significant negative impact on the earth over time. Unsustainable usage of natural resources, especially of oil, in concordance with an increased standard of living and steady urbanization took their toll on the environment. With the beginning of the new millenium, more and more evidence for a man-made climate change as result of strongly increased emissions of so-called greenhouse gases was found, slowly ushering a change in paradigm regarding a more sustainable approach in resource usage and consumption of goods.

This process, however, relies greatly on technological innovation driven by research on new 'green' energy conversion methods, which make use of renewable sources of energy such as solar radiation and wind. While these exemplary technologies have been developed to a great degree and already make a significant part of the corresponding renewable energy sources available, one major contribution is not being made use of. All kinds of physical, chemical and biological processes involve in one way or another the exchange of energy in the form of heat. Typically, excess energy in the form of heat is dispersed into the environment and becomes unusable. This way, a large part of the energy which is contained e.g. in combustion fuels, the human body, etc. cannot be efficiently transformed into electrical power through e.g. an electric generator.

Thomas Johann Seebeck's discovery of the change of electrical and magnetic properties of a material as a result of a temperature gradient in 1822 lead to in the understanding of the so-called thermoelectric effects. These effects describe the relationship between temperature gradients acting on a thermoelectric material and the corresponding induced electrical power, or vice versa. In principle, the thermoelectric effects or thermoelectricity in general can be used in order to harvest the energy and reuse what would otherwise be lost to the environment.

While in theory this approach appears to be very promising, in practice one faces several challenges which have prevented wide-spread application of thermoelectric materials for sustainable energy conversion. These factors include limitations regarding suitable materials with respect to their abundance, processability and environmental and health

aspects. Many thermoelectric materials with high conversion efficiencies comprise heavy and/or toxic elements such as bismuth, tellurium, lead, sulfur, etc. and often also require harsh conditions for processing, additionally increasing the energy payback time of such devices.

Organic, carbon-based compounds have been looked at favorably by the research community in recent years. Especially conducting polymers unite properties which render them promising candidates as thermoelectric materials. Among those properties are the light weight, tunable optical and electrical properties and their mechanical flexibility, inherent to organic compounds. These factors in principle enable a more decentralized approach in the re-usage of energy in the form of heat and its subsequent conversion into electrical power.

All of the above-mentioned factors incentivize investigations on conducting polymers as promising thermoelectric materials. Therefore, conducting polymers are chosen as the primary subjects of investigation in the presented work. The main challenge to be overcome in the framework of this thesis is to apply concepts known from the rich knowledge base of inorganic thermoelectrics and apply them to conducting polymers. Even though the latter have been studied extensively, being most appreciated for their optoelectronic properties and potential usage in organic solar cells as transparent electrodes, the focus herein is placed differently. In the following a brief prospect on the topics discussed in this work shall be given, graphically represented by Figure 1.1.

After a long period of stagnating research on inorganic thermoelectrics, Hicks and Dresselhaus ushered in a new era in the field with their theoretical work on the influence of nanostructuring in these materials. [1] One of their main findings was the possibility of improving the properties of thermoelectric materials through the reduction of their dimensionality. Specifically, nanostructuring in inorganic thermoelectric materials can be used to reduce the thermal conductivity which is detrimental to the overall conversion capabilities. Similarly, herein we investigate nanostructuring of polymer thin films with inorganic nanoparticles with respect to their thermoelectric, as well as structural properties. This also includes the implementation of a measurement for the thermal conductivity of thin films.

Another way to optimize thermoelectric materials is to modify the number of charge carriers present. Researchers were able to show that each of the relevant thermoelectric parameters, namely Seebeck coefficient, electrical and thermal conductivity, is dependent on this number. As such, the degree of doping in a thermoelectric material provides tunability and allows for optimization of the thermoelectric properties, due to varying correlations of the parameters to the number of charge carriers. In this case, the question is, if it is at all possible to tune the degree of doping, but also the influence on spectro-

scopic, compositional and conformational properties of the polymer. These questions are based on the fact that chemically speaking, doping in organic semiconductors proceeds in a very different way, as compared to inorganic semiconductors.

The last point also provokes the question, whether it is possible to circumvent the counteracting dependencies of the different thermoelectric quantities. In inorganic materials, this is achieved to a certain degree through doping and the aforementioned nanostructuring approach. Consequently, the question is whether in polymeric systems a combination of modification of electronic doping and structural re-arrangement in thin films can be exploited in order to improve the latters' thermoelectric capabilities.

In a setup of an inorganic thermoelectric generator, one finds in most cases an alternation of p-type semiconductors and n-type semiconductors connected electrically in series. This allows for either power generation using a temperature-gradient or the formation of a temperature gradient when applying an electrical current. When reviewing the literature on organic thermoelectrics, and specifically on organic thermoelectric generators, one finds that most organic thermoelectric generators employ a p-type conducting polymer, but not a n-type one. The n-type leg is typically represented by small molecules or simply replaced with metal electrodes. This reflects also the comparatively lower amount of publications dealing with n-type conducting polymers, as opposed to p-type ones. A question arises as to why that is the case, in addition to if and how n-type polymers differ from their p-type counterparts. The conceptualization of a thermoelectric generator which is made of both, p-type and n-type, polymers offers challenges with respect to the fabrication and potential power conversion efficiencies.

This introduction is followed by theoretical basics, as discussed in Chapter 2 and a description of the employed characterization methods in Chapter 3. After description of the sample preparation procedures in Chapter 4, the main part of this thesis follows, comprising the research results and conclusions.

The projects in this thesis all evolve around the thermoelectric figure of merit ZT , shown in the center of Figure 1.1. Each individual project aims at the directed modification of certain parameters which affect the thermoelectric capabilities of conducting polymers, in order to shed light on the underlying concepts and improve the understanding of the link between thermoelectric properties and the morphology of conducting polymer thin films. The main question to be answered in Chapter 5 is, whether nanostructuring of polymer thin films leads to a favorable decrease of the thermal conductivity or not, and whether there is a link between the structure and thermoelectric properties. It is largely based on the publication entitled " 'Morphology-Function Relationship of Thermoelectric Nanocomposite Films from PEDOT:PSS with Silicon Nanoparticles' ", which was written in collaboration with Mihael Coric, Anton Greppmair and Mika Pflüger. [2] Chapter 6

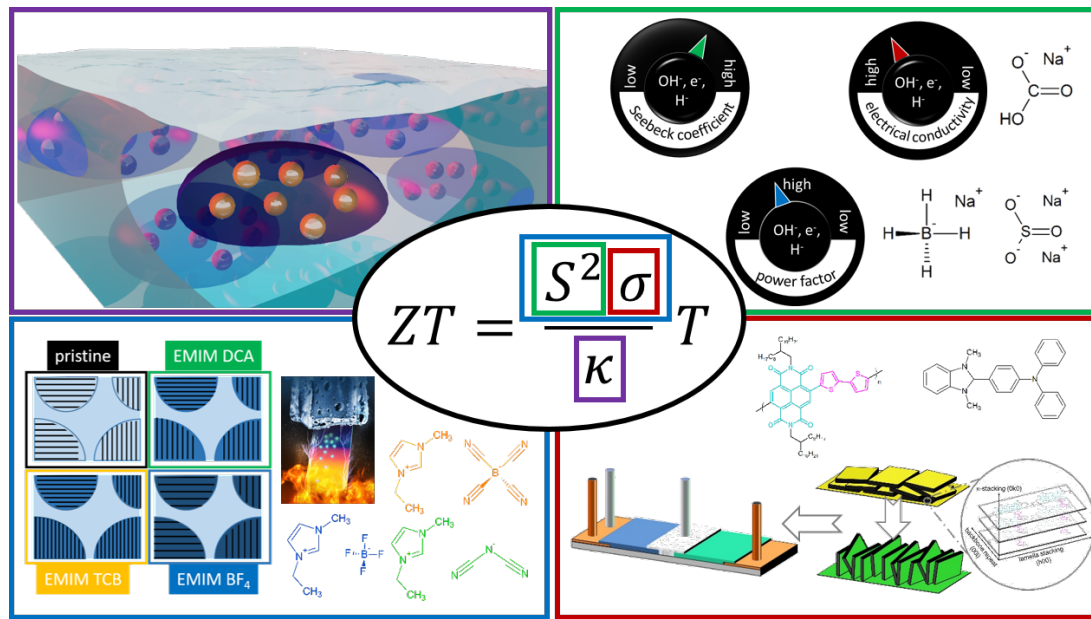


Figure 1.1: Graphical abstract of the current thesis, focusing on the different contributions to the thermoelectric figure of merit ZT at the center of the image. Top left: nanostructuring of poly(3,4-ethylene dioxythiophene):poly(styrene sulfonate) (PEDOT:PSS) thin films with silicon nanoparticles (Si-NPs). Top right: dedoping of PEDOT:PSS with inorganic salts. Bottom left: simultaneous enhancement of S and σ after post-treatment of PEDOT:PSS with ionic liquids (ILs). Bottom right: Doping of poly[N,N'-bis(2-octyldodecyl)naphthalene-1,4,5,8-bis(dicarboximide)-2,6-diyl]-alt-5,5'-(2,2'-bithiophene) (P(NDI2OD-T2)) thin films with 4-(1,3-dimethyl-2,3-dihydro-1H-benzoimidazol-2-yl)-N,N-diphenylaniline (N-DPBI) and subsequent fabrication of a thermoelectric generator based on conducting polymers as active materials.

explores methods for modifying charge carrier concentration in polymer thin films using inorganic salts, being based on the publication entitled 'Facile Optimization of Thermoelectric Properties in PEDOT:PSS thin films through Acido- base and Redox Dedoping Using Readily Available Salts', in collaboration with Giuseppino Fortunato and Jan Overbeck. [3] The data is partially taken from the bachelor's thesis of Josef Keilhofer, with the basic concepts having been initially studied by Anjani Kumar Maurya in the framework of his master's thesis. Chapter 7 deals with the post-treatment of polymer thin films with so-called ionic liquids (ILs) and the analysis of the treated films regarding their thermoelectric properties, degree of doping and structure. This chapter is largely based on the publication 'Ionic liquids as post-treatment agents for simultaneous improvement of Seebeck coefficient and electrical conductivity in PEDOT:PSS films'. [4] Initial investigations on the IL post-treatment were performed by Xaver Lamprecht and Benjamin Pretzl in their respective bachelors' theses. In Chapter 8, a n-type polymer is investigated

regarding the influence of electronic doping on spectroscopic, structural and thermoelectric properties. With the obtained knowledge from this work, a thermoelectric generator based on conducting polymers as active materials is fabricated. The results were obtained with Regina Kluge in the framework of her master's thesis.

Finally, a brief conclusion is given in order to give answers to the questions posed thus far. An outlook into possible interesting topics shall provide stimulation for future research endeavors in the field of organic thermoelectrics.

2 Theoretical background

This chapter aims at deepening the understanding of the underlying concepts for the discussion of the results obtained in the framework of this thesis. Therefore, it is divided into three parts. Firstly, principles of thermoelectricity will be discussed, since they are the foundation for understanding the obtained results in terms of power conversion capabilities. Secondly, a theoretical foundation for conducting polymers will be layed out, since they are the primary subjects of investigation. Lastly, a section on the basics of scattering techniques will be included. For the most part, scattering techniques aid in the elucidation of the morphology and allow for a link to the measured thermoelectric properties of the investigated thin films.

2.1 Thermoelectric principles

This section deals with some of the concepts involved in the description of thermoelectricity in general. After discussing thermoelectricity conceptually, the three main thermoelectric effects, namely the Seebeck effect, Peltier effect and Thomson effect will be briefly outlined. This is followed by the discussion of the thermoelectric figure of merit ZT and how it can be optimized for more efficient energy conversion.

2.1.1 Thermoelectric effects

When describing thermoelectric processes, it is necessary to keep in mind that equilibrium thermodynamics cannot be used. Upon application of a temperature gradient, the system is forced out of thermal equilibrium. To this end, the Onsager reciprocity relations can be used to understand forces (which represent gradients of state variables herein) and resulting fluxes in a non-equilibrium state. In thermoelectric processes, the forces comprise gradients in the temperature ∇T and the chemical potential $\nabla \mu$, which cause a flux of particles and heat. Correspondingly, the particle flux density J and the heat flux density Q can be written as seen in Equations 2.1 and 2.2, respectively, in which L_{ij} are elements of the Onsager matrix. For further details, the reader is referred to [5].

$$-J = L_{11} \frac{1}{T} \nabla \mu + L_{12} \nabla \frac{1}{T} \quad (2.1)$$

$$Q = L_{22} \nabla \frac{1}{T} + L_{21} \frac{1}{T} \nabla \mu \quad (2.2)$$

In simple terms, these equations describe on the one hand the direct correlation of the particle flux density to the gradient in chemical potential $\nabla \mu$ and the heat flux density to the inverse temperature gradient $\nabla \frac{1}{T}$, indicated by the diagonal terms L_{ii} of the Onsager matrix. On the other hand, the respective terms with the off-diagonal elements L_{ij} in both equations describe the cross-correlation. This means that e.g. the particle flux is not only induced by the gradient in chemical potential, but also by the temperature gradient. Similarly, the heat flux is also caused by the gradient of the chemical potential.

As mentioned before, within the Onsager matrix, the diagonal matrix elements L_{11} and L_{22} represent the transport coefficients for direct correlation, while the off-diagonal elements L_{12} and L_{21} describe cross-correlations. Using the transport coefficients, important physical quantities of the thermoelectric material can be computed, according to Equations 2.3 and 2.4.

$$\nabla \frac{1}{T} = 0 \quad \Rightarrow \quad \sigma = \frac{e^2 L_{11}}{T} \quad (2.3)$$

$$J = 0 \quad \Rightarrow \quad \kappa = \frac{L_{11} L_{22} - L_{12}^2}{T^2 L_{11}} \quad (2.4)$$

These equations show that transport of charge carriers and heat within a thermoelectric material are inter-dependent and cannot be discussed separately. As will be seen later on in this discussion, this poses several challenges with respect to the enhancement of conversion efficiencies in thermoelectric materials.

Seebeck effect

The effect of the same name was discovered by the german physicist Thomas Johann Seebeck in the year 1821. He observed an open-circuit voltage between two dissimilar materials with conducting properties, when heating their junction. The conjunction of two materials which shows this effect is called a thermocouple. Conversely, when an electric current flows through a junction of a thermocouple, the latter is either heated or cooled. This so-called Peltier effect, named after the french watch maker Jean Peltier, was discovered in 1834. These effects are, however, related as was seen by William Thomson in 1855, also known as Lord Kelvin. The Thomson effect states that a conductor through

which an electrical current is running and which is subjected to a temperature gradient, additionally exhibits changes in the heat flux.

However, since in the framework of this thesis, thermoelectric materials are used for the sole purpose of conversion of heat into electricity, the Seebeck effect is the most relevant for the discussion.

When subjecting a one-dimensional conductor to a temperature gradient, both the electric current density J_e (seen in Equation 2.5) and the heat flux density J_Q (seen in Equation 2.6) are influenced.

$$E = \frac{1}{\sigma} J_e + S \nabla T \quad (2.5)$$

$$Q = \Pi J_Q - \kappa \nabla T \quad (2.6)$$

Herein, σ is the electrical conductivity, S the Seebeck coefficient, Π the Peltier coefficient and κ the thermal conductivity. Under the influence of a temperature gradient, charge carriers within an exemplary one-dimensional solid conductor begin diffusing from the hot to the cold end of the gradient. This yields a surplus of charge carriers at the cold end, while leaving a deficiency of the former at the hot end. The imbalance in charge distribution leads to an electrical potential, irrespective of the type of majority charge carrier in the material. The magnitude of the electrical potential is proportional to the magnitude of the temperature difference and is therefore often called thermovoltage. Additionally, the thermovoltage yields a drift current, which drives charge carriers against the temperature gradient and is larger as more charge carriers are present. In steady-state condition, while not canceling out, the two currents lead to a net potential which can be measured.

With the previous discussion, general principles for the efficiency for different types of materials can be derived. Insulators possess theoretically high Seebeck coefficients, but very low electrical conductivities due to their inability to transport charge carriers. Metals are good electrical conductors, but typically possess low Seebeck coefficients, since the abundance of charge carriers leads to large drift currents. In terms of the Seebeck coefficient, semiconductors are the material type of choice, due to their favorable combination of decent electrical conductivity and intermediate charge carrier concentration. For further reading on the Seebeck coefficient and thermoelectricity in general, the reader is referred to [6].

2.1.2 Thermoelectric figure of merit ZT

The thermoelectric figure of merit ZT allows for gauging the energy conversion efficiency of a thermoelectric device, and is given in Equation 2.7.

$$ZT = \frac{S^2 \sigma}{\kappa} T \quad (2.7)$$

In this equation, S represents the Seebeck coefficient, σ the electrical conductivity, κ the thermal conductivity and T the absolute temperature. ZT is a dimensionless, temperature-dependent quantity and is directly related to the conversion efficiency η via Equation 2.8. [7] It should be noted that in different instances, ZT can either refer to the figure of merit of a single material or to that of a full generator. For the remainder of this thesis, only the former is valid.

$$\eta = \frac{T_h - T_c}{T_h} \frac{\sqrt{1 + Z\bar{T}} - 1}{\sqrt{1 + Z\bar{T} + \frac{T_c}{T_h}}} \quad (2.8)$$

The first part of the equation represents the Carnot efficiency and thus places an upper limit to the electrical power which can be obtained from a certain temperature gradient, as both the hot temperature T_h and the cold temperature T_c are included, as well as the average temperature \bar{T} . The second term takes the properties of the employed thermoelectric material into account. It can be seen that the material properties, through the inclusion of ZT , pose an additional limitation to the energy conversion capabilities. Still, Equation 2.8 is proof that in order to efficiently convert temperature differences into electrical power, larger values of ZT are required. In order to achieve this, both the electrical conductivity and the Seebeck coefficient have to be increased, while the thermal conductivity must be kept at a minimum, as seen in Equation 2.7.

Most importantly out of all the contributions to ZT , the Seebeck coefficient refers to the ability of a thermoelectric material to convert temperature differences into an electrical voltage. In a simplified approach, in which charge carriers can be considered as free, the Seebeck coefficient can be written as shown in Equation 2.9.

$$S = -\frac{\pi^2 k_B}{6 e} \frac{T}{T_F} \quad (2.9)$$

In this equation, k_B is the Boltzmann constant, e the elementary charge and T_F represents the Fermi temperature. The ratio T/T_F describes the fraction of charge carriers which actually contribute to the charge transport, as the Pauli exclusion principle prevents charge carriers far from the Fermi level to be transported. T_F can be computed as shown in Equation 2.10.

$$T_F = \frac{\hbar}{2mk_B}(3\pi^2n)^{2/3} \quad (2.10)$$

The Fermi temperature depends on the reduced Planck constant \hbar , the effective mass of the charge carriers m and the number of charge carriers n . From this, it can be concluded, that a smaller m is favorable.

In very simple terms, the electrical conductivity can be described in terms of the number of charge carriers n , the elementary charge e and the mobility of charge carriers μ within the material. Their relation to the total electrical conductivity σ is shown in Equation 2.11.

$$\sigma = ne\mu \quad (2.11)$$

While a proportionality of σ to the number of charge carriers n is apparent, one also has to take into account the latters' respective ability to be transported within the material. This is described by the mobility μ , which in inorganic materials is calculated from the curvature of the band structure. As is discussed below in Section 2.2.1, for polymers the concepts are very similar. The spatial and energetic distribution of states largely determine the macroscopically measurable conductivity properties of a material, whereby the former can be easily influenced in conducting polymers by enhancing the polymer structure through secondary doping. The latter concept will be discussed in more detail in Section 2.2.1.

The thermal conductivity is a factor which negatively affects the energy conversion efficiency, as can be seen in Equation 2.7. A low thermal conductivity is favorable, as it prevents the equilibration of the temperature gradient across the material, which would cease all thermoelectric processes. Within a typical thermoelectric material, κ is mediated by contributions from both charge carriers (κ_{ch}) and phonons (κ_{ph}), as is shown in Equation 2.12.

$$\kappa = \kappa_{ch} + \kappa_{ph} = \frac{1}{3}C_{el}\nu_F l_{el} \quad (2.12)$$

In a solid material, heat can be transported by phonons, i.e. vibrational modes of the lattice. However, additionally, heat is transported by the charge carriers. The charge carrier contribution to the thermal conductivity κ_{ch} can be described using the specific heat of charges C_{el} , their Fermi velocity ν_F and their mean free path l_{el} . This contribution becomes more prominent, as more charge carriers are present within the material. In inorganic thermoelectric materials, this effect leads to comparatively large thermal conductivities, which are detrimental to the conversion efficiency. On the other hand,

polymers are a suitable material class regarding the thermal conductivity due to their comparatively low structural order. One of the problems one is faced with when attempting to either increase the electrical or decrease the thermal conductivity, is their intercorrelation. As mentioned earlier, the charge carriers do not only carry electrical charges, but also a part of the heat. Therefore, it can be concluded that the electrical and thermal conductivity cannot be fully decoupled, as is seen in the Wiedemann-Franz law shown in Equation 2.13.

$$\frac{\kappa_{ch}}{\sigma} = LT \quad (2.13)$$

The Wiedemann-Franz law states a proportionality between the electrical conductivity and the charge-mediated contribution to the thermal conductivity with temperature. Therein, L is the Sommerfeld-value of the Lorenz number, with a typical value being $L = 2.44 \cdot 10^{-8} \text{ W}\Omega\text{K}^{-2}$.

2.2 Conducting polymers

The nobel prize for chemistry in the year 2000 was awarded to Hideki Shirakawa, Alan Heeger and Alan MacDiarmid for the discovery of electrical properties in doped polyacetylene (PA). They found that treatment of PA through oxidation with agents such as iodine, bromine or chlorine leads to unprecedented electrical conductivities, approaching values typically found for metals. While PA has issues regarding its practicability due to its instability in ambient atmosphere, it has sparked great interest in further development of organic, conjugated polymers. Conjugated polymers are defined as possessing an alternation of single and double bounds between carbon atoms, leading to sp^2 -hybridization. Apart from a strictly defined geometry around the carbon atoms, the sp^2 -hybridization leads to the formation of π -orbitals perpendicular to the polymer backbone with one electron per carbon atom. Within this delocalized electron cloud charges are allowed to move freely. This is dependent on the dimensional extent of the delocalization, the conformation of the monomers within the polymer backbone, etc.

Still, similarly to metals or semiconductors, the formation of π -orbitals results in a band structure of the conjugated polymer. Therefore in the following, a model will be described which allows for the understanding of the semiconducting properties of conjugated polymers and the description of band structures therein.

The Peierl's instability theorem, which is schematically depicted in Figure 2.1 assumes a one-dimensional chain composed of metal atoms. In first instance, these lattice points are located at a constant distance a from each other. If each of these lattice points

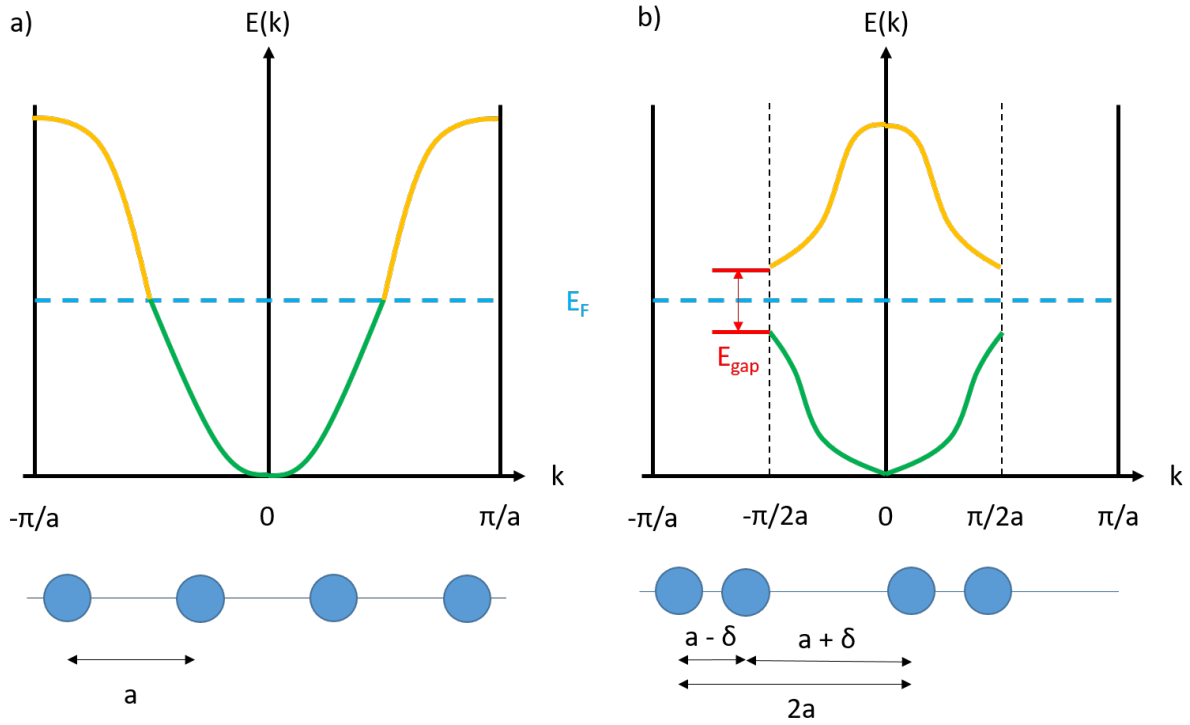


Figure 2.1: Scheme of the Peierl's instability theorem. a) One-dimensional chain of metal atoms with constant spacing a . The bands are half-filled up to the Fermi level E_f . b) Stabilization of system through distortion of lattice spacing by δ , and subsequent formation of a band-gap E_g . The unit cell of the chain doubles in size, while the corresponding Brillouin zone is halved.

contributes a single electron, this leads to a half-filled band, with the Fermi level E_f found at the maximum energy where states are occupied. This changes, however, when considering a conjugated polymer such as e.g. PA. Even though each atom contributes one additional electron to the system, in this more realistic case, the alternation between single and double bonds leads to changes in the lattice spacing. This is depicted in Figure 2.1b. Single and double bonds exhibit different distances between neighboring atoms, represented by δ in the scheme. This effectively doubles the size of the unit cell. Additionally, it leads to stronger interaction for the atoms with smaller nearest-neighbor distances, while the interaction becomes weaker for larger nearest-neighbor distances. The degenerate energy levels found in the first case, are therefore no longer present and in total lower the energy of the system by $E_f - E_{gap}/2$. This can also be seen from the Brillouin zone which halves in size, and now shows the borders at $k = \pm\pi/2a$. Effectively, the system reduces its total energy through the change in unit cell size and introduction of the band gap. In summary, the presence of alternating single and double bonds leads to the formation of a band gap, with a highest-occupied molecular orbital (HOMO) and a lowest-unoccupied molecular orbital (LUMO). The magnitude of this band-gap largely

depends on parameters such as the degree of polymerization, the structure e.g. within a thin film, the degree of doping, all of which will be discussed in the following, and is typically found to be larger than for inorganic compounds.

2.2.1 Doping of conjugated polymers

This section deals with the concept of doping of conjugated polymers, strongly influencing the obtainable electrical properties. A clear distinction will be made between the concepts of primary doping and secondary doping, respectively.

Primary doping in conjugated polymers

Primary doping refers to the introduction or removal of charge carriers in a conjugated polymer through chemical oxidation or reduction processes. Depending on the polymer, either positive or negative charge carriers can then be transported. This largely depends on the energy landscape of the system in question. P-type doping is favored in systems, in which the polymer can easily transfer electrons to the dopant, i.e. a high highest occupied molecular orbital (HOMO) level, while for n-type doping a low lowest unoccupied molecular orbital (LUMO) level of the polymer is required, in order to accept electrons from the dopant. It turns out that a favorable energy landscape is linked to the molecular structure of the polymer, as e.g. polythiophene derivatives show mostly p-type behavior, while naphthalene-diimide-based polymers show mostly n-type behavior. [8]

In the following three distinct types of charge carriers will be discussed, namely solitons, polarons and bipolarons. It shall be noted here that charge carriers in conjugated polymers cannot be described as free electrons or holes, but have to be described as quasiparticles.

Three types of the latter are shown in Figure 2.2. The formation of a neutral soliton (denoted as S^0) is easily understood when inspecting the structure of the exemplary trans-PA more closely. In trans-PA the single and double bonds can be arranged in two different ways, rendering both ground states degenerate. This means that no additional energy is required for the transformation of one into the other. Since both structures can coexist on a single chain, a defect is created at the site at which they meet. This defect, which is shown as an unpaired electron in the scheme, is commonly known as a neutral soliton. [9] This originates from the fact that the unpaired electron interacts with the chain and entails a distortion in the latter's bond geometry. The unpaired electron and the distortion cannot diffuse independently, which is why the soliton has to be deemed a quasiparticle. It should also be noted that the soliton itself has a spatial extent, and is thus to a certain extent delocalized over the conjugated π -system. [10] The net charge of the chain is still zero. The latter can, however, be transformed into a positive soliton

(S^+) through chemical oxidation or a negative soliton (S^-) through chemical reduction. While the neutral soliton does not carry a charge but a spin, the opposite is true for both the positive and negative cases. Notably, the soliton only exists in polymers in which there are two degenerate ground states. This is only fulfilled for trans-PA, due to its high symmetry. Therefore, in more complex conjugated polymers solitons are typically not found.

Depending on the number of solitons on a single PA chain, it is possible for the former to interact with each other. If a neutral soliton interacts with a charged one, a polaron is created. Depending on the sign of the charged soliton, the polaron can either be positive (P^+) or negative (P^-). As opposed to the soliton, a polaron carries both a charge and a spin.

The third class of charge carriers is represented by the bipolarons. These can either be created through the interaction of two solitons of the same charge, or through the interaction of a polaron with a soliton of the same charge. The positive (B^+) and negative (B^-) bipolarons, carry double the respective charge but no spin.

Since the charge carrier concentration has a strong impact on the Seebeck coefficient, it is necessary to correlate this quantity with the preceding discussion. A high density of charge carriers is equivalent to an increased probability for interaction among them. Thus,

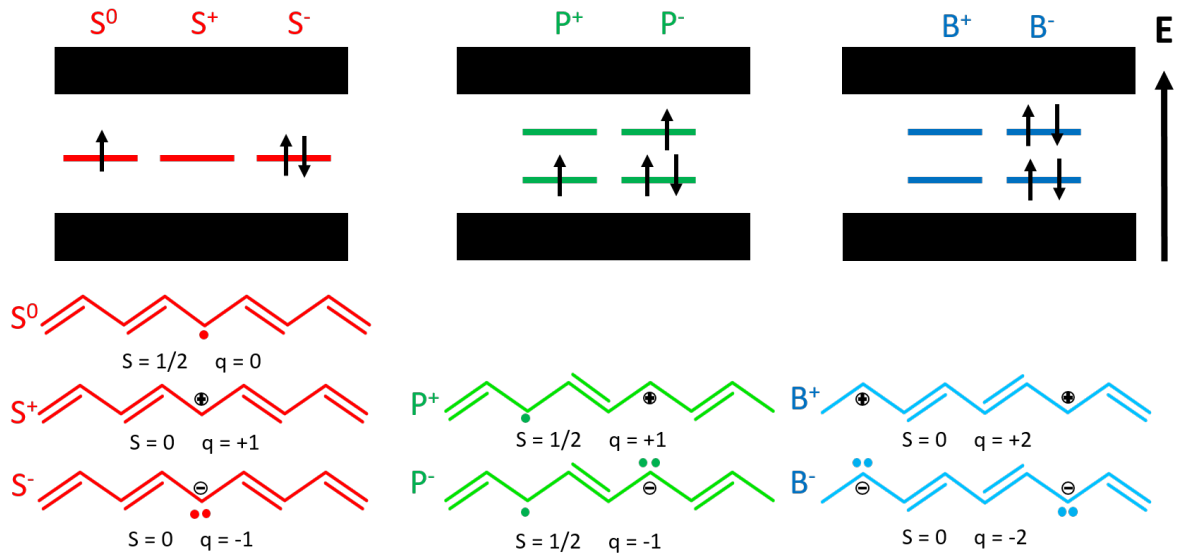


Figure 2.2: Schematic representation of three different types of charge carriers, exemplarily shown for PA. Solitons are shown in red, polarons in green and bipolarons in blue. While a soliton can exist in a neutral, positive or negative state, polarons and bipolarons are always either positively or negatively charged. The band diagrams for the different charge carrier types are shown at the top, with filled states being indicated by black arrows.

a high charge carrier concentration is typically associated with an increased amount of bipolarons. The more the charge carrier concentration is reduced, the more the bipolaron concentration decreases and the polaron concentration increases. [11] This knowledge will be used later on for the discussion of the spectroscopic characterization and the corresponding Seebeck coefficients in Chapters 6, 7 and 8.

Secondary doping

Secondary doping refers to changes in the charge transport capabilities of a film depending on its structure. Charges are not only transported along single polymer chains, but also among multiple polymer chains. Theoretically, charge transport is best described by the Su-Schrieffer-Heeger model (SSH), shown in Equation 2.14. [10]

$$\mathcal{H}_{SSH} = \mathcal{H}_0 + \mathcal{H}_{trans} + \mathcal{H}_{e-ph} + \mathcal{H}_{stat} + \mathcal{H}_{dyn} \quad (2.14)$$

The model includes a Hamiltonian \mathcal{H}_{SSH} comprised of several contributions. A one-dimensional chain comprised of carbon atoms is assumed, in which the electrons are treated in a tight-binding approximation. Structural relaxation can be calculated between the polymer and the electrons contained in the p-orbitals, while no electron-electron interactions are present.

\mathcal{H}_0 represents the total energy of the system, including electronic and phononic excitations. The transfer hamiltonian \mathcal{H}_{trans} describes the transfer of charges due to orbital overlap. With \mathcal{H}_{e-ph} , electron-phonon scattering is implemented, which has implications for band-like and hopping charge transport. \mathcal{H}_{stat} and \mathcal{H}_{dyn} represent static and dynamic disorder within the polymer, respectively. Disorder influences charge transport through phonon-assisted hopping.

For all intents and purposes, charge transport can be divided into two categories. Firstly, hopping transport is mostly found in systems of low structural order, i.e. with a large fraction of amorphous regions. It is characterized by a proportionality to temperature. This can be easily understood when considering a broad energy distribution of sites which can be accessed by charges. The comparatively large energy differences require thermal activation for hopping transport to occur. Hopping transport is assisted by phonons, whose contribution increases with temperature. If an insufficient amount of energy is present, charges become trapped in low-energy states, which presents itself as low charge mobility.

On the other hand, band-like charge transport is characterized by comparatively small energetic differences between sites, and therefore a higher mobility of charges. This is found in polymers in which the overlap of π -orbitals between different chains is large. In these cases, one typically finds an increase of the resistance with temperature due to increased scattering with phonons.

In general, the ability of a polymeric system to transport charges can conceptually be written combining the influence of primary and secondary doping, as seen in Equation 2.15.

$$\vec{j} = \sigma \vec{E} = ne\mu \vec{E} \quad (2.15)$$

Herein, the current density \vec{j} is described by an electric field \vec{E} and the proportionality constant σ , also termed electrical conductivity. The latter, in turn, can be described in terms of the number of charge carriers, and therefore by the degree of primary doping, the number of charges on a single charge carrier e , and the mobility μ which depends on the degree of structural order/disorder and thus on the secondary doping.

2.2.2 PEDOT:PSS

PEDOT:PSS is a water-soluble, conductive polymer blend shown in Figure 2.3. Therein, PEDOT as polythiophene allows for the transport of charges due to its conjugated backbone. PSS stabilizes the positive charges on the PEDOT chains and renders the blend as a whole soluble in water. PEDOT is electrochemically synthesized in presence of PSS, yielding core-shell-like nanoparticles in the dispersion. These are characterized by a PSS-rich shell and a core in which short fragments are grafted onto PSS chains via coordinative bonds. [12]

PEDOT:PSS is commercially available in aqueous dispersions, which mostly differ in their PEDOT-to-PSS ratio. This impacts properties such as the work function, transparency properties, viscosity, electrical properties, etc. While the different properties render PEDOT:PSS suitable as transparent electrode, e.g. in organic solar cells or light-emitting diodes due to its favorable transparency properties and work function, the focus in the framework of this thesis lies on the electrical conductivity which can be achieved in thin films. Park *et al.* performed a systematic study, in which they varied the PEDOT-to-PSS ratio during synthesis. [13] They characterized the thin films regarding their electrical conductivities and Seebeck coefficients. A ratio of 1 : 2.5 between PEDOT-to-PSS was found to show the highest electrical conductivities, whereby a drastic drop was seen for higher relative amounts of PSS. This can be easily understood when considering the inability of PSS to transport charge carriers, due to its lack of a conjugated π -system. The

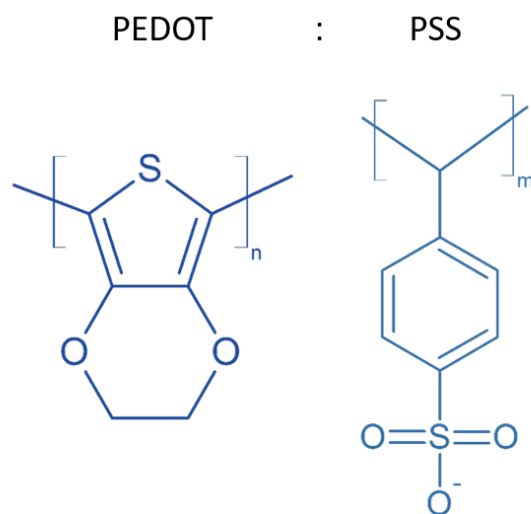


Figure 2.3: Chemical structures of the conductive polymer blend PEDOT:PSS. The conjugated thiophene PEDOT is shown on the left (dark blue), while the water-soluble polyanion PSS can be seen on the right.

ratio of PEDOT-to-PSS of 1 : 2.5 in this case is such that a very high number of positive charges on the PEDOT chains, which are introduced during the electrochemical synthesis, can be electrostatically stabilized by the PSS. This leads to a high concentration of bipolarons. While the high bipolaron concentration is favorable for achieving high electrical conductivities, the presence of electrically insulating PSS is detrimental. [13]

When fabricating the PEDOT:PSS solution into a thin film, phase separation between PEDOT and PSS is known to occur. [14,15] This leads to PEDOT-rich domains, which are embedded in a matrix of excess PSS. Charge transport within the PEDOT-rich domains is possible, while the excess PSS prevents charges to be efficiently transported between domains. This manifests itself as low electrical conductivity in as-prepared films. Different chemical treatments can be used to alter the composition of the film with respect to its PEDOT-to-PSS ratio, as well as inducing a denser packing PEDOT stacks in addition to a more favorable orientation thereof. An increase in the electrical conductivity can typically be observed upon treatment of PEDOT:PSS with different chemical agents.

As will especially be seen in Chapters 6 and 7, the coordinative bond (i.e. the stabilization of charges on PEDOT chains by PSS) can be altered with various treatments, of either the solution prior to thin film fabrication or post-treatment of prepared thin films.

2.2.3 P(NDI2OD-T2)

P(NDI2OD-T2) is a donor-acceptor alternating copolymer. This means that charges within a single repeating unit of the polymer can be redistributed by irradiation with visible light, rendering P(NDI2OD-T2) photo-active. The bithiophene sub-units primarily transport positive charge carriers, while the naphthalene-diimide sub-units are responsible for the transport of negative ones. Similarly to PEDOT chains in PEDOT:PSS thin films, the polymer chains can stack on top of each other, allowing for charge transport through naphthalene-diimide units of adjacent chains. Modification of the latter with long alkyl moieties prevents aggregation of the chains, and renders the polymer soluble in organic solvents. The morphology of P(NDI2OD-T2) thin films, and the impact of doping will be discussed in more detail in Chapter 8.

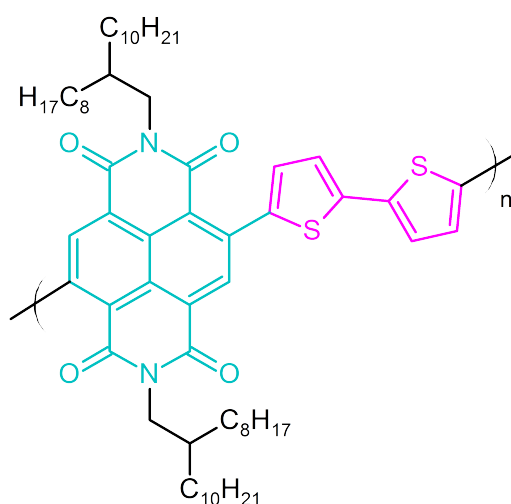


Figure 2.4: Chemical structure of the n-type alternating copolymer P(NDI2OD-T2), with the n-type naphthalene-diimide unit colored turquoise and the p-type bithiophene unit in magenta.

P(NDI2OD-T2) is most appreciated for its high mobility for negative charge carriers, making it suitable for usage in transistors, among others, in addition to its chemical stability in air. However, it should be noted that as opposed to PEDOT:PSS, P(NDI2OD-T2) is not intrinsically doped, which means that thin films are electrically insulating in their pristine state. Still, charges can be introduced through addition of a dopant, which is able to transfer negative charge carriers onto the polymer chains. Among the most popular agents are metallocenes, salts such as caesium fluoride, strong reducing agents such as tetrakis(dimethylamino)ethylene (TDAE), or benzimidazoline derivatives, out of which N-DPBI will be the dopant used for the investigation in Chapter 8.

2.3 Scattering basics

Scattering techniques are powerful tools for structure analysis of polymeric materials. As opposed to many real-space scanning probe techniques, they allow for structural analysis in reciprocal space. This yields statistically relevant information not only of surfaces, as is the case for many real-space techniques, but also of buried objects and interfaces. Especially for thin film samples the so-called grazing-incidence geometry offers the advantage of a large illuminated sample volume, which in the case of a x-ray beam impinging perpendicularly would be much smaller. For our purposes, the grazing-incidence geometry is used in order to elucidate the structure of organic thermoelectric thin films on different length scales. In the following, scattering basics shall be discussed for x-rays, whereas it should be noted that these concepts also apply for neutrons.

The interaction of a material with x-rays can be discussed in terms of the energy(E)-dependent refractive index n , shown in Equation 2.16.

$$n(E) = 1 - \delta(E) + i\beta(E) \quad (2.16)$$

Herein, the real contribution δ represents the dispersion properties, while the imaginary contribution β represents the absorption properties of a material. Notably, the refractive index n and its components are energy-dependent, which is of importance for the discussion below. Within the hard x-ray regime with typical photon energies larger than 5 keV, dispersion values lie in the range of 10^{-5} to 10^{-6} , while absorption values lie in the range of 10^{-7} to 10^{-8} . As a consequence, the refractive index for most organic materials is smaller than one in the hard x-ray regime. Thus, when traversing from an optically dense medium (e.g. air) into a polymer thin film, total reflection occurs with the x-ray beam impinging under a sufficiently shallow angle. The angle above which the beam penetrates the film is called the critical angle α_c and can be approximated using the dispersion, as seen in Equation 2.17.

$$\alpha_c = \sqrt{2\delta} \quad (2.17)$$

This approximation especially holds in the hard x-ray regime and far from resonance energies of atomic species contained in the sample, where absorption can be neglected. For the case of resonant x-ray scattering, which will be discussed below, the absorption contribution is non-negligible and the critical angle can be calculated according to Equation 2.18.

$$\alpha_c = 90^\circ - \text{Re}(\arcsin(n)) \quad (2.18)$$

Nevertheless, the critical angle is an important quantity regarding the grazing-incidence scattering experiments, performed throughout this thesis. In scattering patterns collected in the grazing-incidence geometry, as is done in the frame of this thesis, a maximum in the diffuse scattering is found at the critical angle of the illuminated material. [16] At this position, a material-sensitivity of the scattering signal is achieved, as the critical angle itself is a material-dependent property. Due to the plethora of materials with varying compositions and constitutions, no database with measured values for δ and β for all possible materials as function of energy exists. Thus, it is of high importance to be able to theoretically predict the optical properties of materials. Henke *et al.* tabulated values for atomic scattering form factors f as function of energy for all chemical elements, which determine the response towards x-ray radiation. [17] Alternatively, the *HEPHAESTUS* software package can be used for simple predictions of the atomic scattering form factors. Equation 2.19 shows the energy-dependence of the atomic scattering form factors f_i , as well as the imaginary contribution.

$$f = f_i^0 + f_i'(E) + i f_i''(E) \quad (2.19)$$

With the knowledge of the chemical composition of the investigated sample, the so-called scattering length density (SLD) can be calculated according to Equation 2.20. Each type of element is included by taking into account its stoichiometric fraction c_i , together with the respective total atomic scattering form factor f_i . The electron density is represented by ρ_e , while $r_0 = e^2/(4\pi\epsilon_0 m_e c^2)$ is the classical Thomson scattering radius and Z_i the total number of electrons within the investigated species. The former can also be written in terms of the mass density ρ , the Avogadro constant N_A , and the molar mass M_i .

$$SLD = r_0 \rho_e \frac{\sum_{i=1}^N c_i f_i}{\sum_{i=1}^N Z_i} = r_0 \rho N_A \frac{\sum_{i=1}^N c_i f_i}{\sum_{i=1}^N M_i} \quad (2.20)$$

The SLD of a material is calculated from f , which contains both real and imaginary contributions. Therefore, the SLD can be deconstructed similarly, with the real part being used for the calculation of the dispersion, and the imaginary for the calculation of the absorption, as can be seen in Equations 2.21 and 2.22, respectively.

$$\delta(E) = \frac{\lambda^2}{2\pi} \text{Re}(SLD) \quad (2.21)$$

$$\beta(E) = \frac{\lambda^2}{2\pi} \text{Im}(SLD) \quad (2.22)$$

2.3.1 Grazing-incidence scattering

Grazing-incidence scattering is a suitable method for the structure determination in thin films. While the path length of an incident beam in the thin film would be very small when measuring in a transmission geometry in which the beam impinges the sample perpendicularly, the grazing-incidence geometry leads to a large illuminated area. This is due to a combination of a shallow incident angle, which typically below 1° , and small but finite spatial dimensions of the beam itself. As a result, one obtains enhanced statistics due to a macroscopically probed sample volume. Additionally, through careful variation of the incident angle below or above the critical angle of the investigated material, the scattering signal predominantly originates from only the surface or the surface and bulk of the film, respectively.

The electric field of the incident beam is modified through the interaction with the illuminated material, and thus scattered. Equation 2.23 shows the general definitions and contributions to the scattering vector \vec{q} . Herein, α denotes angles in the scattering plane, while ψ represents out-of-plane angles. The subscripts i and f denote incident and exit angles, respectively. Equation 2.23 therefore links the reciprocal q -vectors to the real-space exit angles. Generally, elastic scattering occurs when plane electromagnetic waves interact with a single object with a characteristic shape and the magnitude of the vector is unchanged.

$$q = \frac{2\pi}{\lambda} \begin{pmatrix} q_x \\ q_y \\ q_z \end{pmatrix} = \frac{2\pi}{\lambda} \begin{pmatrix} \cos(\psi_f)\cos(\alpha_f) - \cos(\alpha_i) \\ \sin(\psi_f)\cos(\alpha_f) \\ \sin(\alpha_i) + \sin(\alpha_f) \end{pmatrix} \quad (2.23)$$

Grazing-incidence small-angle scattering (GISAS)

As the name implies, in grazing-incidence small-angle scattering, only scattering in small exit angles is captured on the detector, which can be ensured by having large sample-to-detector distances (SDDs). This has several implications, and allows for the simplification of the scattering vector q , as seen in Equation 2.24.

$$q = \frac{2\pi}{\lambda} \begin{pmatrix} 0 \\ 2\psi_f \\ \alpha_i + \alpha_f \end{pmatrix} \quad (2.24)$$

The components q_x , q_y and q_z represent the scattering contribution in direction of the beam, perpendicular to the beam but parallel to the substrate and perpendicular to both beam and substrate, respectively. The former contribution can be neglected, while it becomes additionally possible to decouple scattering in horizontal and vertical direction, and therefore q_y and q_z .

A factor which has to be taken into account is the possibility of a single photon being scattered multiple times. This originates from the large footprint of the beam on the sample. Due to the drastically increased path length of the beam in the sample, the probability for multiple scattering events is greatly enhanced. The Born approximation assumes scattering of photons as consequence of the interaction with a homogeneous scatterer. In the grazing-incidence geometry this assumption does not hold any more, which is why the former has to be modified. The so-called distorted-wave Born approximation (DWBA) is a perturbation-theoretical treatment of the Born approximation and accounts for the presence of a substrate layer and various combinations of reflection and refraction events. More specifically, it differentiates between (1) simple refraction off a scatterer, (2) reflection from the substrate layer prior to refraction off a scatterer, (3) reflection from the substrate layer after refraction off a scatterer and (4) reflection from the substrate before and after refraction off a scatterer. The DWBA treats the scattered intensity as result of the superposition of photons scattered according to the four afore-mentioned processes. [18]

In the framework of the DWBA, the scattering cross-section can be described according to Equation 2.25.

$$\frac{d\sigma}{d\Omega}|_{diff} = \frac{C\pi^2}{\lambda^4} \Delta n^2(E) |t_i^F|^2 |t_f^F|^2 P_{diff}(\vec{q}) \quad (2.25)$$

Herein, C represents the illuminated surface area, while t_i and t_f are the Fresnel transmission coefficients for the incident and exiting beam, respectively. $\Delta n(E)^2$ describes the energy-dependent scattering contrast between e.g. a scatterer and its surrounding medium. In the discussion of resonant x-ray scattering below in Section 2.3.2, this will be of importance. Lastly, the diffuse scattering factor P_{diff} takes into account the structure of the sample on the mesoscale. [19] The form factor $F(\vec{q})$ refers to the average shape of scattering objects, while the spatial distribution of the latter can be parametrized in the structure factor $S(\vec{q})$. Since there is often no significant order on the mesoscale in polymeric thin films, $S(\vec{q})$ typically represents a paracrystalline lattice, in which the scatterers are placed. Additionally, P_{diff} is proportional to the number N of scatterers present in the illuminated area.

$$P_{diff}(\vec{q}) \propto NF(\vec{q})S(\vec{q}) \quad (2.26)$$

For the analysis, several simplifications are being made which will be listed in the following. As the simulation of a full 2D grazing-incidence small-angle x-ray scattering (GISAXS) pattern is computationally expensive, an alternative route for the structure analysis is taken. Instead, line profiles from the pattern are extracted vertically or horizontally. While the former contain information on correlation perpendicular to the substrate and the chemical composition, the latter are used for modelling and elucidation of lateral structure shapes, sizes and spatial arrangements. It is allowed to treat both components as decoupled. The vertical line cuts can be used to determine the position of the Yoneda peak of a material in question, at which point the corresponding scattering contribution is maximal. [16] On the other hand, in the horizontal line cuts spatial correlation of structures is only considered in lateral, not in vertical direction. In other words, the q_z -component is considered constant in the horizontal line profiles. [20] Since, however, in polymer systems one not only finds objects with a monodisperse size distribution, but rather a polydisperse one, the variation in sizes has to be taken into account. The relation seen in Equation 2.26 has to be modified by adding the average form factor $\langle F(\vec{q}) \rangle$, as seen in Equation 2.27.

$$P_{diff}(\vec{q}) \propto N \langle F(\vec{q}) \rangle S(\vec{q}) \quad (2.27)$$

Most often, modeling is done in the framework of the decoupling approximation (DA) or the local monodisperse approximation (LMA). [21] In the DA, all objects interact with each other and collectively contribute to the scattering signal. It holds better in systems with small polydispersities, as position and type of scatterers are uncorrelated. On the other hand, in the LMA different 'families' of objects are regarded as spatially separated, thus leading to selective interaction of domains within one structural family. Scattering between objects of different families is not included in the LMA model. For the modelling, form factors representing spherical objects are used. As mentioned above, these are arranged in a one-dimensional para-crystalline lattice, in which the distances between objects are also subject to a certain statistical variation.

It should be noted that all aforementioned concepts hold true for both x-ray and neutron scattering.

2.3.2 Grazing-incidence resonant tender x-ray scattering (GIR-TeXS)

Resonant x-ray scattering is a modified version of scattering with hard x-rays. One reason for that is the strongly enhanced chemical sensitivity, due to measurements being carried out with x-ray wavelengths adjusted to core-electronic transitions of constituent chemical species. Due to the effect of chemical shift on the fine structure in atomic

absorption spectra close to absorption edges, the components of the refractive index shown in Equation 2.16 change drastically and non-linearly.

Equations 2.21 and 2.22 have important implications for the elucidation of optical properties of the investigated materials, as $\beta(E)$ can be determined from absorption measurements in the x-ray range according to Equation 2.28.

$$\beta(E) = \frac{\mu\rho}{2k} = \frac{\mu\rho hc}{4\pi E} \quad (2.28)$$

In this equation, h is the Planck constant, c the speed of light and ρ the density of the material. Since the real part of the refractive index δ cannot be measured directly, it has to be determined as function of energy from β using the Kramers-Kronig relations, shown in Equations 2.29 and 2.30. [22] For this purpose, the freely available software package *KKcalc* is used. The calculation of integrals with infinity as boundaries which would be necessary for the determination of δ from the Kramers-Kronig relation is circumvented with the help of the so-called Henke-database. [17] It lists photoabsorption cross-sections and atomic scattering factors, which relate to β and δ , respectively, for each single element in a range from 50 eV to 30 000 eV. For the energies outside the range of the near-edge x-ray absorption fine structure (NEXAFS) spectra, the *KKcalc* software plugs in the database values, thus allowing for the calculation of the quasi-infinite integral.

$$\delta(E) = \frac{2}{\pi} \wp \int_0^\infty \frac{E' \beta(E')}{E'^2 - E^2} dE' \quad (2.29)$$

$$\beta(E) = -\frac{2E'}{\pi} \wp \int_0^\infty \frac{\delta(E')}{E'^2 - E^2} dE' \quad (2.30)$$

Using the Kramers-Kronig relations it becomes possible to determine the dispersion properties in the vicinity of absorption edges with the knowledge of their corresponding absorption properties. This allows for the calculation of the energy-dependent scattering contrast $\Delta n^2(E)$, which is shown in Equation 2.31.

$$\Delta n^2(E) = \Delta \delta^2(E) + \Delta \beta^2(E) = (\delta_1(E) - \delta_2(E))^2 + (\beta_1(E) - \beta_2(E))^2 \quad (2.31)$$

$\Delta n^2(E)$ can only be calculated for a pair of two materials, for one of which the optical properties are denoted with index 1, while for the other the index 2 is used. Referring back to the scattering cross-section in a GISAXS experiment shown in Equation 2.25, its dependency on the diffuse scattering factor P_{diff} , the Fresnel transmission coefficients and the scattering contrast Δn^2 is apparent. This has implications for the analysis of the 2D grazing-incidence resonant tender x-ray scattering (GIR-TeXS) data, as will be discussed in Section 3.3.3.

Grazing-incidence wide-angle scattering (GIWAXS)

As opposed to GISAXS, in a grazing-incidence wide-angle x-ray scattering (GIWAXS) experiment scattering under large angles is captured on a 2D detector. Translating from large q -values in reciprocal space, one obtains information on possible structural order on short length scales in the investigated material. As opposed to a x-ray diffraction (XRD) measurement, additionally possible preferred orientation of structural elements within the material can be discerned.

Ewald's construction aids in the understanding of the processes which lead to distinct scattering peaks in the final image. In contrast to the theoretical description of the scattering vector \vec{q} in GISAXS, the small-angle approximation does not hold anymore, as the curvature of the Ewald's sphere is no longer negligible. This leads to the description of the scattering vector according to Equation 2.23.

Generally speaking, the occurrence of a scattering signal relies on the intersection of the surface of the Ewald's sphere with the reciprocal lattice of the material. The size of the former directly correlates to the employed wavelength of the x-ray beam. This necessitates the fulfillment of the so-called Laue condition, which states that the scattering vector $\vec{q} = \vec{G}$. Geometrically speaking, the scattering vector \vec{G} represents any reciprocal lattice point that intersects with the Ewald's sphere, and thus yields a signal on the detector. In turn, this leads to the condition of elastic scattering, such that the magnitude of the incident wave vector \vec{k}_i is equal to that of the exiting wave vector \vec{k}_f .

Collection of large scattering angles in a GIWAXS experiment has ramifications on the correct representation of data and the information which can be obtained. Most importantly, when converting the data into reciprocal space, the information on vertical correlation within the film, thus in q_z -direction, is not accessible in a GIWAXS measurement. This so-called 'missing wedge' appears due to the significant curvature of the Ewald's sphere, and a strong requirement for contributions of the other reciprocal lattice vectors \vec{q}_x and \vec{q}_y . In reciprocal space a scattering vector \vec{q} with a certain magnitude which can be oriented in all possible directions, spans a so-called orientation sphere. The intersection of the latter with the Ewald's sphere will determine if a scattering peak will appear on the detector or not. In other words, a diffraction peak with a certain magnitude of its q -vector in z -direction has to be tilted in either q_x - or q_y -direction, in order to be projectable on the Ewald's sphere and ultimately show the scattering signal. Accordingly, at larger q_z -values the missing wedge becomes larger with respect to the polar angle χ . [23] This so-called χ -correction, among others, is discussed in more detail in Section 3.3.3.

3 Characterization methods

Different methods used for the characterization of thermoelectric thin films are discussed in this chapter. The first section deals with the thermoelectric characterization, including measurement methods for the Seebeck coefficient, the electrical and thermal conductivity. Afterwards, spectroscopic techniques are discussed which are used for deeper understanding of the electronic structure, composition and conformational states in polymer films. Lastly, characterization techniques for the analysis of thin film structures using electron microscopy and scattering techniques with a special focus on GIWAXS and GIR-TeXS are described.

3.1 Thermoelectric characterization

The measurement of thermoelectric properties in conducting polymer thin films represents the main focus of this thesis, as it allows for gauging of the feasibility of certain treatments regarding power conversion efficiency and for linking the observations to properties of the thin films, such as the composition, structure, etc. This section deals with the experimental setups used for measurement of the Seebeck coefficient, the electrical conductivity, the film thickness and the thermal conductivity of conducting polymer films.

3.1.1 Gradient chamber

The gradient chamber, a custom-made setup built by Tobias Titz in 2003 at the Chair for Functional Materials E13, Technical University Munich, is used for the measurement of the Seebeck coefficients discussed in Chapter 5, and shown in Figure 3.1. While originally designed for the fabrication of polymer thin films on a temperature gradient, in order to achieve different effective annealing temperatures at different locations of the substrate, it serves for the measurement of the Seebeck coefficient. The main components are two copper blocks, one of which can be heated using a positive temperature coefficient (PTC) heating element. It is connected to a power source through a *Lakeshore* 330 temperature controller (Lake Shore Cryotronics Inc., Westerville, USA). On the one hand, this allows for setting a target temperature of the hot side, on the other hand the Lakeshore controls

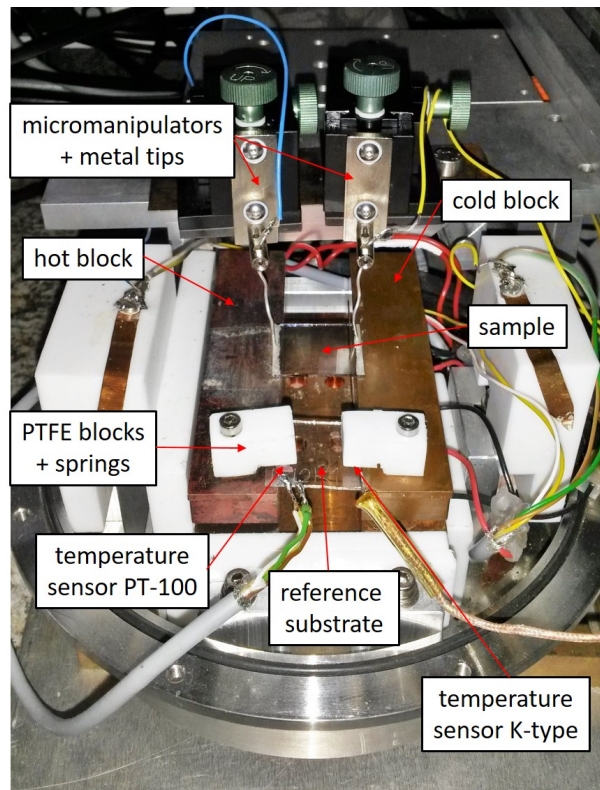


Figure 3.1: Photograph of the gradient chamber used for the measurement of the Seebeck coefficient in Chapter 5. The sample is placed between two copper blocks, out of which one is heated with a PTC element, while the other is cooled using a Peltier element. The established temperature gradient along the sample, which is monitored using a *Lakeshore 330* temperature controller (Lake Shore Cryotronics Inc., Westerville, USA), leads to a thermovoltage which is measured using a *Keithley 2000* multimeter.

the current flow to the heating element and thus keeps the actual temperature close to the designated one with the help of a PID-controller. Underneath the other copper block, three Peltier elements are mounted, which themselves are connected to a power source directly. Upon application of an electrical current, the Peltier element generates a temperature gradient, which cools the top side while the bottom side is heated. Both temperatures are monitored using a PT-100 thermoelement on the hot side and a K-type thermocouple on the cold side, which both are fixed on a reference substrate with the small poly(tetrafluoroethylene) (PTFE) blocks and springs and feed the temperature values directly into the Lakeshore 330. When placing a polymer thin film across the gap between the hot and cold block, a temperature gradient is established on the sample itself, therefore generating a thermovoltage. After application of conducting silver paste (article number 530042, Ferro GmbH, Frankfurt a. Main) on the edges of the thin films, the latter can be contacted by two metal tips connected to a *Keithley 2000* Multimeter. The

thermovoltage measured on the multimeter is then divided by the temperature gradient from the hot to the cold side in order to obtain the Seebeck coefficient, using Equation 3.1.

$$S = \frac{\Delta V}{(T_h - T_c)} \quad (3.1)$$

Here, ΔV is the measured thermovoltage, while T_h and T_c represent the temperatures on the hot and cold side in Kelvin, respectively. The temperature of the hot side was set to 100 °C, while the cold side equilibrated at 15 °C. A stable temperature gradient of 85 K was established. An average value for the Seebeck coefficient is obtained by repeating the measurement multiple times.

It should be noted that the gradient chamber turned out to show severe problems. These include a lack of reproducible contact pressure of the metal tips for the thermovoltage measurement and measurement of the temperatures on a reference substrate instead of the sample itself. In addition, the setup cannot be operated under vacuum by sealing the chamber with the corresponding lid, since the heat generation from both the PTC and Peltier element cannot be dissipated into the environment, but is instead stored in the metal encasing, which is thermally in contact. This may lead to overheating of the components, and their subsequent failure. The gradient chamber also lacks a reliable way of mounting it at beamlines in synchrotrons for performing in-situ/in-operando x-ray scattering measurements. All of these issues are tackled with the conceptualization and implementation of the x-ray analysis voltage-emulation rig (XAVER), discussed in the following section.

3.1.2 XAVER: X-ray analysis voltage-emulation rig

XAVER was built by Xaver Lamprecht (bachelor's thesis 2016, Chair for Functional Materials E13, Technical University Munich) in the frame of this thesis, and aims at solving some of the issues which one faces during operation of the gradient chamber. It is used for measuring Seebeck coefficients in Chapters 6, 7 and 8, and also temperature-dependent resistances for the latter.

In general, it can be said that the XAVER is designed for the measurement of thermoelectric properties of thin films, especially the Seebeck coefficient and temperature-dependent resistance. To this end, XAVER can be used in two different configurations, namely the Seebeck configuration, shown in Figure 3.2 and the two-point configuration in Figure 3.3.

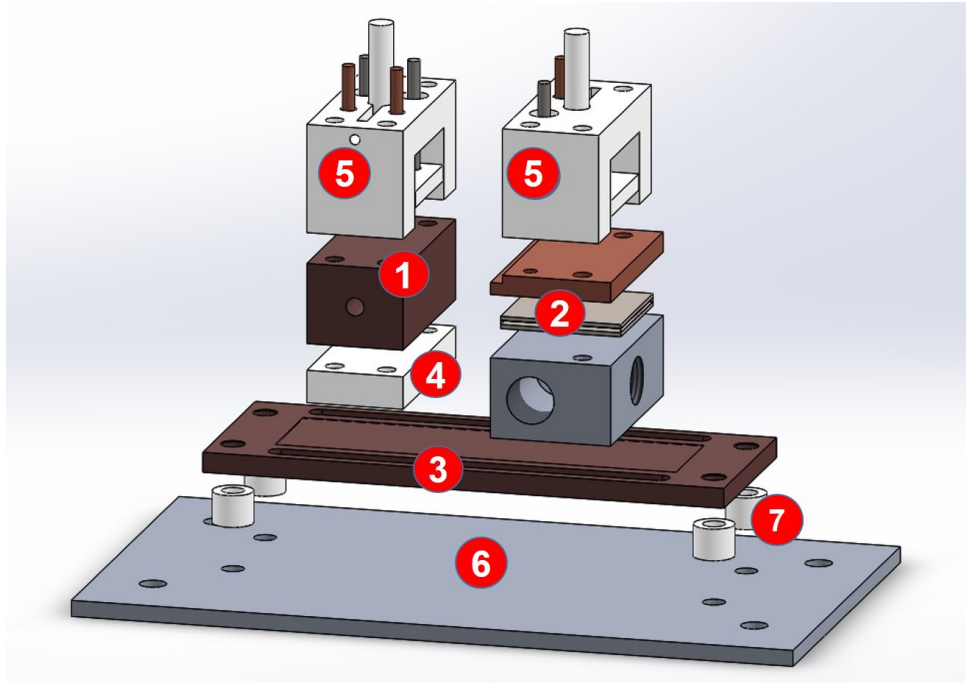


Figure 3.2: Exploded view of the Seebeck configuration of XAVER. Numbered elements correspond to: 1) 'Hot' copper block with heating cartridge, 2) Peltier element with copper block for the attachment of an external cooling circuit (gray) underneath, and thin copper plate for matching the height of the 'hot' copper block, 3) copper plate with extended slots for distance adjustment of the 'hot' and 'cold' block, 4) PTFE spacer for thermal disconnection of the hot copper block from the copper plate, 5) PTFE bridges containing copper tips and Pt-100 temperature sensors for measurement of the thermovoltage and temperature, respectively, 6) aluminum base plate and 7) PTFE feet for fixing the measurement setup on the base plate. [24]

The design of XAVER differs in many aspects from the gradient chamber. The heating cartridge (100 W, 6 mm · 33 mm two-pole version, Friedrich Freek GmbH) inside the copper block (copper alloy W-200, Albromet GmbH) on the hot side (designated as number 1) and the Peltier element (70 W, 42147/UEPT-130-071-120M150S, uwe electronic GmbH, designated as number 2) are responsible for heating and cooling, respectively. Both the 'hot' and 'cold' copper block rest on top of a copper plate (copper alloy W-200, Albromet GmbH, designated as number 3), whose two slots along the length of the plate allow for adjustment of the distance between the hot and cold copper blocks. Thus, even samples with differing sizes or electrode distances can be accommodated and measured. The hot copper block is thermally disconnected from the copper plate using a PTFE spacer (number 4). Dissipation of the heat generated upon operation of the Peltier element is possible through the inclusion of the copper block underneath (shown in grey), which has two attaching points. An external cooling circuit can be plugged into the block, act-

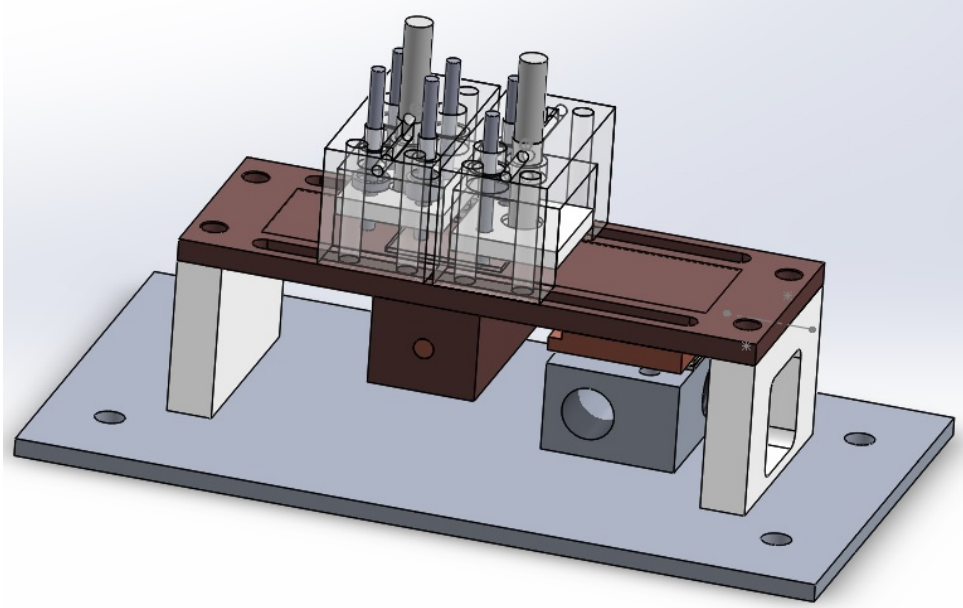


Figure 3.3: Two-point configuration of XAVER. The 'hot' copper block with the heating cartridge is thermally connected to the copper plate, allowing for homogeneous heating of the sample. In order to measure temperature-dependent resistances, a constant electrical bias voltage is applied, while simultaneously measuring the current and the temperature. The PTFE feet on both sides of the copper plates thermally disconnect the setup from the base plate, and bring the sample into the pivot point of the chamber. [24]

ing as heat sink and therefore allowing for transfer of the heat to the cooling medium, thus allowing the Peltier element to run properly even in an evacuated environment. The measurement of both thermovoltage and temperature on both ends of the sample is done using the PTFE bridges (number 5). These contain copper tips for the thermovoltage measurement and rod-like Pt-100 temperature sensors (Pt-100, class A, 4-wire configuration, encased, -50°C to 200°C , Thermo Sensor GmbH). Since the temperature is measured directly on the sample, and both the copper tips and temperature sensors are pressed on the sample with springs (spring constant 1 N), the measurement is more reproducible. The signals of the thermovoltage and temperature measurement are both fed through a 16-pole, vacuum-tight wall conducting plug system (SGJ.1B.316.CLHSV, FGG.1B.316.CLAD76, FGJ.1B.316.CLLD76, Lemo Electronic GmbH) to the *Keithley 2000* multimeter and *Lakeshore 330* temperature controller, respectively. This allows for encasing of the setup in the vacuum chamber discussed below. The whole setup rests on top of a base plate (number 6), but is thermally disconnected from the latter through the PTFE feet (number 7).

The two-point configuration shown in Figure 3.3 allows for the study of charge transport

properties of polymer thin films. For this purpose, the components of the XAVER are re-arranged in a way that the heating cartridge heats the copper plate homogeneously. When placing the sample on the copper plate it is also heated homogeneously. Thus, when applying a bias voltage U using a *Keithley 2400* sourcemeter, and measuring the current I , a dependency of the resistance as function of temperature can be inferred. The resistance is calculated according to Equation 8.1.

$$R = \frac{U}{I} \quad (3.2)$$

This is especially useful for the discussion of the results in Chapter 8, since the resistances of P(NDI2OD-T2) films are typically very high. Therein, electrical conductivities are calculated in in-plane and cross-plane direction, taking into account the resistance values from Equation 8.1 and the film thickness t , the distance d and length l of the electrodes and the overlap area A of the electrodes, as seen in Equations 3.3 and 3.4, respectively.

$$\sigma_{in} = \frac{d}{Rtl} \quad (3.3)$$

$$\sigma_{out} = \frac{t}{RA} \quad (3.4)$$

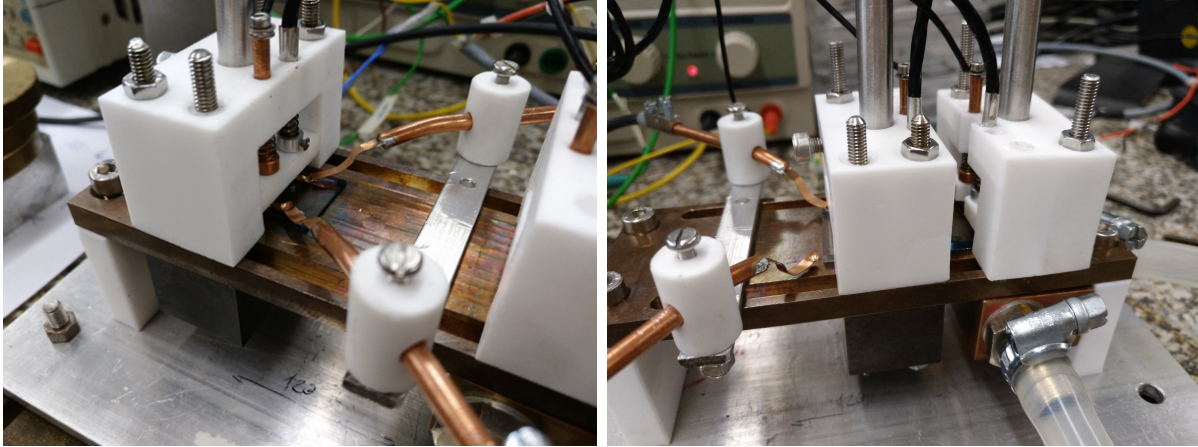


Figure 3.4: Photograph of the addition to XAVER made for easier contactability of samples with irregular geometries/dimensions used for measurement of temperature-dependent resistances of P(NDI2OD-T2) films (left) and for measurement of thermoelectric generators (right) discussed in Chapter 8. [25]

An addition to the XAVER was made, in order to facilitate the measurement of the high-resistance P(NDI2OD-T2) films, discussed in Chapter 8. The additional set of copper-beryllium tips is shown in Figure 3.4. Due to the varying geometries in which P(NDI2OD-T2) thin films are prepared, the ability to accurately position the measurement tips on the electrodes, and having the former also connected to a *Keithley 2400* sourcemeter, allowed for the measurement of temperature-dependent resistances. In general, measurement of the resistance as function of temperature is a facile way of getting insight into the charge-transport properties of polymer thin films. Samples in which hopping transport is prevalent, show a decrease of the resistance with increasing temperature. For samples in which band-like transport is dominant, the opposite is the case.

Measurement of the electric parameters of the thermoelectric generators discussed in Chapter 8 became possible using this device, by using it to contact one of the fluorine-doped tin oxide (FTO) electrodes on the edge of the substrate. The PTFE bridges were used to measure the temperature on top of the center aluminum electrode (the 'cold' end of the generator) and contact the other FTO electrode while measuring its temperature (the 'hot' end of the generator), respectively. Thermovoltages were measured by applying a temperature gradient between 5 °C to 10 °C perpendicular to the substrate, and monitoring the output voltage U by contacting the FTO electrodes on either end of the substrate. The power output P was determined according to Equation 3.5.

$$P = \frac{U^2}{R} \quad (3.5)$$

In order to measure the resistance R of the device, different bias voltages were applied while the induced current was measured over time. According to Ohm's law (Equation 8.1), the resistance can be calculated using the slope obtained from a linear fit in the U - I plot.

Another feature of the XAVER is the vacuum chamber, which makes the implementation at synchrotron beamlines possible. Both the chamber and the adapter plate are shown in Figure 3.5. The chamber is fabricated from a large block of aluminum. It possesses both in- and outlets for the x-ray beam, which are elongated along the width of the chamber, making it possible to arrange the hot and cold copper blocks in a way that different sample geometries can be accommodated. The Kapton windows (300 HN, polyimide derivative, Du Pont de Nemours, Luxembourg) on the in- and outlet for the x-ray beam allow for scattering experiments in the chamber due to their high x-ray transmissivity while also ensuring vacuum-tightness of the chamber. The height of both configurations of the measurement setup inside the chamber is chosen in a way that the sample rests on the pivot point, facilitating x-ray scattering measurements. Additionally, two tubes can be attached to the side of the chamber in order to lead the external cooling circuit out.

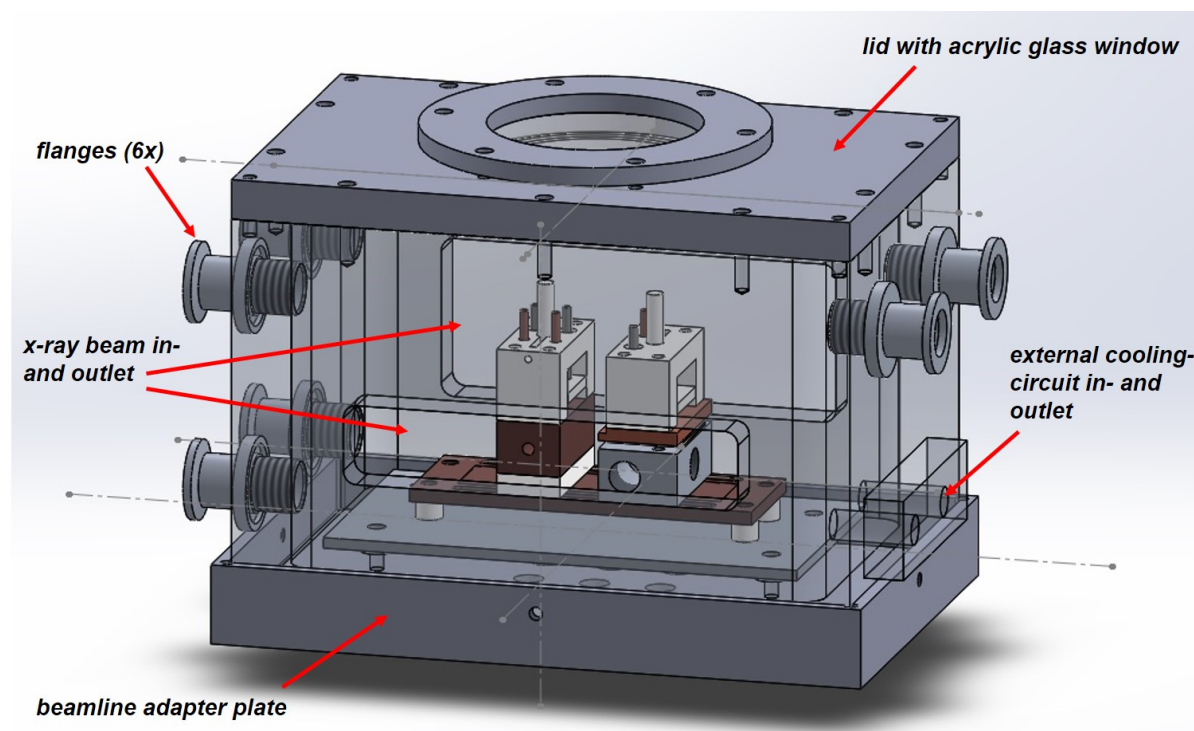


Figure 3.5: Vacuum chamber and beamline adapter plate for XAVER. Features of the chamber include an in- and outlet for x-ray beams covered with Kapton foil (not shown here), an in- and outlet for the external cooling circuit, a lid with an acrylic glass window and six flanges for feed-in of the power cables for the heating cartridge and Peltier element, and for the feed-out of the measured thermovoltage and temperature signals. The adapter plate is specifically designed for implementation at the beamlines P03 at DESY and the Austrian SAXS beamline at Elettra-Sincrotrone Trieste.

Six flanges are attached, out of which two are used for the power inlet for the heating cartridge and Peltier element via a four-pole vacuum-tight wall conducting plug system (SGJ.1B.304.CLLSV, FGG.1B.304.CLAD72, FGJ.1B.304.CLLD72, Lemo Electronic GmbH), and for the lead out of the measured temperature and thermovoltage signals via the 16-pole plug system mentioned above. The other four flanges can be used in various ways, e.g. for inducing gas flow, solvent atmospheres, vacuum, etc. The chamber is topped with a lid with an acrylic glass window, which is vacuum-tight due to the usage of O-rings (NBR70, HUG Industrietechnik und Arbeitssicherheit GmbH). The beamline adapter plate is specifically designed for usage at the beamlines P03 at DESY and the Austrian SAXS beamline at Elettra Sincrotrone Trieste. It possesses four screws on all edges, which can be used to fix the vacuum chamber on the adapter plate, thus allowing for reproducible positioning of the latter on the adapter plate.

3.1.3 4-point probe measurement

Four-point probe measurements for the determination of sheet resistances in PEDOT:PSS thin films are carried out with a Cascade Microtech (C4S-54/5) setup. Therein, four equidistant tungsten carbide tips with a spacing of 1 mm, tip radii of 125 μm are placed on the thin film, as can be seen in Figure 3.6. Since the tips are mounted on a spring, piercing of the films is prevented. A current I is applied on the outer two tips, while the inner two tips measure the induced voltage U .

The four-point probe setup allows for the measurement of sheet resistances, while excluding contact resistances from the tips and wires. The sheet resistance can be calculated using Equation 3.6, and then be used in conjunction with the film thickness d , to calculate the electrical conductivity in S/cm , according to Equation 3.7.

$$R_{sh} = \frac{\pi}{\ln 2} \frac{U}{I} \quad (3.6)$$

$$\sigma = \frac{1}{R_{sh}d} \quad (3.7)$$

It should be noted that above equations especially hold when the film thickness d is much smaller than the characteristic distance of the tips, as is the case throughout this thesis. Values for the sheet resistance are typically given in Ohms per square (Ω/sq), representing the resistance of 1 Ω along the direction of a square sheet of any size.

Four-point probe measurements are carried out on up to seven positions on the sample, with the thicknesses measured at the corresponding positions using surface profilometry, discussed below. The electrical conductivity was calculated for each position, and then averaged over the whole sample.

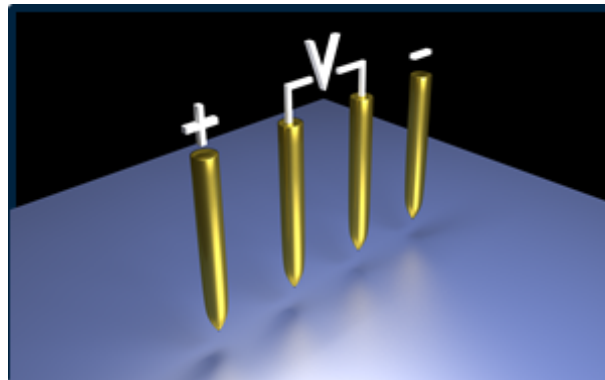


Figure 3.6: Scheme of the four-point probe measurement setup, with the outer two tips used for current application, while the inner two are used for measurement of the resulting voltage.

3.1.4 Surface profilometry

Surface profilometry is a facile way of determining thicknesses of thin polymer thin films. In the framework of this thesis, a *DekTak XT* surface profiler by Bruker Corporation, Billerica, USA is used. The obtained thickness values are primarily used for calculation of the electrical and thermal conductivity and for absorption coefficients in UV-Vis and NEXAFS spectra.

Measurements are carried out by introducing scratches into the films with metal tweezers after performing all other necessary measurements. Scratches were made at multiple positions of the sample, in order to account for potential thickness inhomogeneities which originate from the fabrication. A tip with a radius of 250 μm was pressed on the sample with a force of 1 mg and scanned across the scratch. From the resulting height profile, the film thickness with respect to the substrate surface could be inferred.

3.1.5 Infrared thermography (IRT)

Large parts of this section are adapted from the publication by Greppmair *et al.*, to which the reader is referred. [26] In the frame of this thesis, infrared thermography (IRT) is used to measure changes in the thermal conductivity of PEDOT:PSS/Si-NPs composite thin films compared to pristine PEDOT:PSS and as function of Si-NPs concentration. Firstly, the basic principles of the technique will be layed out, before detailing the measurement procedure.

Figure 3.7 shows a schematic of the principles of IRT. Since a temperature gradient is required for the measurement of the thermal conductivity, a heat flux of known magnitude is necessary. The heat flux is represented by the solid red arrows in the sketch. In our case, a light-emitting diode of known wavelength (632 nm) with variable but well-defined power is used. The calibration of the illumination is carried out with a circular photodiode placed in the plane of the sample. The thin films to be investigated are transferred on the steel substrates shown in Section 4.1.3 using the procedure described in Section 4.2.3. The steel substrates exhibit an opacity towards the used wavelengths of the light-emitting diode, and thus act as shadow mask. In addition, since the suspended polymer film is in thermal contact with the steel substrate at the edges of the circular cavities, the substrate also acts as heat sink. This is especially important, since the measurements are typically carried out under vacuum conditions, because convection effects can be suppressed for pressures below $1 \cdot 10^{-3}$ mbar.

The circular shape of the cavities leads to rotational invariance of the temperature distribution, which holds especially if the size of the cavity is small and homogeneous illumination of the free-standing section of the thin film can be ensured. Thus, the radial

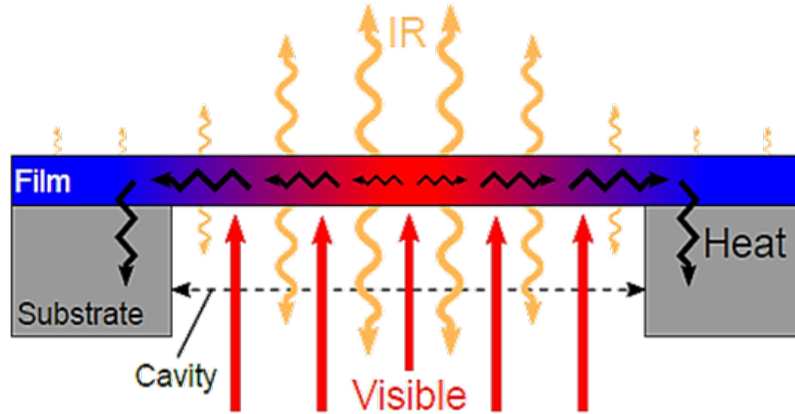


Figure 3.7: Schematic of the IRT measurement. Solid red arrows on the bottom represent thermal excitation with a light-emitting diode through the cavity. The polymer film is free-standing on top of the latter. The resulting temperature gradient is indicated by the color transition from red in the center to blue at the edges. Heat transport is signified with jagged black arrows for conduction to the substrate acting as heat sink and with serpentine yellow arrows for emission of infrared radiation. [26]

component of the heat flux vector Q_r can be written as function of distance r from the center in an analytical solution according to Equation 3.8.

$$Q_r(r) = -\kappa_{||} \frac{\partial T(r)}{\partial r} \quad (3.8)$$

$\kappa_{||}$ is the in-plane thermal conductivity of the thin film, while $T(r)$ represents the temperature distribution at distance r from the center. In case of a homogeneously absorbed areal power density p_{abs} , the heat flux vector vanishes for $r = 0$, thus at the center of the cavity.

A steady-state condition is reached if the absorbed p_{abs} in a circular area is equal to the power flowing through the circumference of that circle. For a steady-state condition to be reached Equation 3.9 must be fulfilled.

$$r^2 \pi p_{abs} = 2r \pi d Q_r(r) \quad (3.9)$$

Herein, r is the radius of the circle while d represents the film thickness. Together with the boundary condition that $T(r = R) = T_{substr}$, where $T(R)$ is the temperature distribution at the edge of the cavity and T_{substr} is the temperature of the substrate, Equations 3.8 and 3.9 can be combined to yield a new expression for the temperature distribution, as shown in Equation 3.10.

$$T(r) = -\frac{p_{abs}}{4\kappa_{||}d}r^2 + \frac{p_{abs}}{4\kappa_{||}d}R^2 + T_{substr} \quad (3.10)$$

The latter two summands in Equation 3.10 relate to the substrate temperature and can therefore be combined to the effective substrate temperature $T_{substr,eff}$, equal to $T_{substr,eff} = \frac{p_{abs}}{4\kappa_{||}d}R^2 + T_{substr}$. Since the effective substrate temperature is a simple offset, Equation 3.10 can be re-written, as seen in Equation 3.11

$$T(r) = -\frac{p_{abs}}{4\kappa_{||}d}r^2 + T_{substr,eff} \quad (3.11)$$

The thermal conductivity can thus be calculated with the knowledge of the absorbed areal power density p_{abs} , the film thickness d and the curvature of the temperature distribution close to the center of the cavity. The film thickness was measured using height profilometry of thin films suspended on glass substrates. p_{abs} is determined using UV-Vis spectroscopy, taking into account the dimension of the cavity and the absorptance A calculated from the transmittance T and reflectance R , such that $A + T + R = 1$ and weighting the obtained spectra with the spectrum of the light-emitting diode to obtain an effective absorptance. Values for the thermal conductivity κ are extracted and averaged for effective temperature increases between 0.6 K to 4 K.

Figure 3.8 shows the exploded view of the chamber used for IRT measurements. The sample is placed on a holder which is thermally disconnected to the vacuum chamber. It can be thermally excited using a red light-emitting diode (wavelength 632 nm) from below with the glass window blocking the infrared radiation emitted from the light-emitting diode due to operation. The emitted infrared light from the sample is able to pass through a sapphire window and is collected by an infrared camera (InSb 640 SM, DCG systems) that is mounted above the sample holder. The distance between two pixels on the detector corresponds to a real-space distance of 14.7 μm , with the total detector size being 640 pixels \cdot 480 pixels. It records the temperature distribution in a contact-free fashion, which can then be converted into an infrared emissivity. In order to ensure a statistically relevant value for the infrared emissivity, the measurement is performed on multiple cavities of different sizes (varying between 0.2 mm to 0.8 mm) and using different powers of the light-emitting diode. This causes varying degrees of thermal excitation. Additionally, since macroscopic sections of the films are transferred, the obtained results are deemed representative of the sample. The whole setup is mounted on a positioning stage in order to allow for precise positioning of the sample underneath the infrared camera and measurement of the illumination power density.

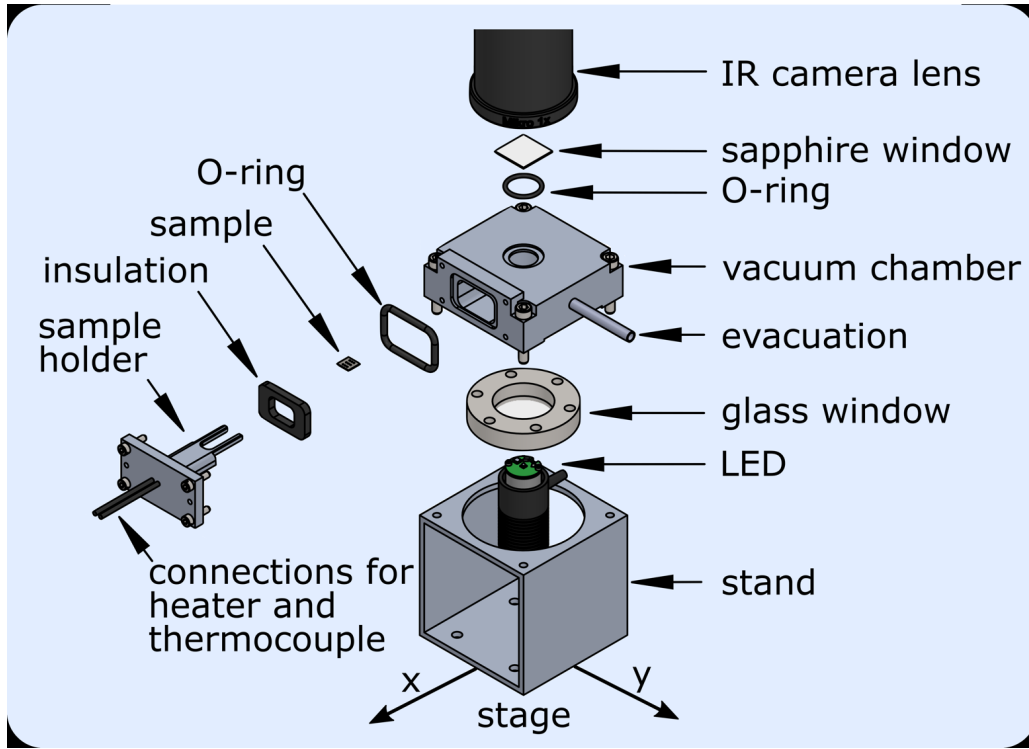


Figure 3.8: Exploded view of the setup used for IRT. It possesses a vacuum chamber in which the sample holder is placed. The sample is illuminated with the light-emitting diode, and the resulting infrared radiation is collected by the infrared camera above. The whole setup is mounted on a movable stage. [26]

3.2 Spectroscopic characterization

3.2.1 UV-Vis spectroscopy

UV-Vis spectroscopy is used in the framework of this thesis to investigate the electronic structure, i.e. degrees of doping in both PEDOT:PSS and doped P(NDI2OD-T2) films. Measurements are carried out on a *Lambda 650 S* UV-Vis spectrometer (Perkin Elmer, Waltham, USA) in a wavelength range from 400 nm to 1100 nm. The spectrometer uses a deuterium and tungsten-halogen lamp as light source. The transmittance T of a thin film is defined as seen in Equation 3.12.

$$T = \frac{I}{I_0} \quad (3.12)$$

Herein, I_0 is the intensity of the incident beam, while I represents the intensity of the beam after passing the sample. The transmittance thus describes the degree to which the sample material can absorb light of different wavelengths. The absorption process leads to electronic excitation according to the Bohr-Einstein relation, seen in Equation 3.13.

$$\Delta E = E_f - E_i = \frac{hc}{\lambda} \quad (3.13)$$

The transmittance T which is obtained from the measurement can be converted into the absorbance A via Equation 3.14.

$$A = -\log_{10}(T) \quad (3.14)$$

However, since the degree of absorption is dependent on the path length of the beam inside the material, the absorbance is divided by the respective sample thickness, in order to obtain a quantity which allows for better comparison of different samples. For the remainder of this work, this quantity will be called absorption coefficient in units of $1/nm$.

UV-Vis spectroscopy allows for the determination of the degree of doping in conducting polymer films. It is used herein, to make statements about changes in the charge carrier density upon different treatments of the samples. As the Seebeck coefficient is strongly dependent on the charge carrier concentration, links are made between the observations in the UV-Vis spectra and the former in Chapters 6, 7 and 8.

3.2.2 Raman spectroscopy

Raman spectroscopy is a type of vibrational spectroscopy which allows to probe the dynamics of vibrations and rotations of molecules in a material. It makes use of a monochromatic laser source for irradiation of the sample, which leads to the excitation into a so-called 'virtual' state, i.e. one that is typically not accessible by the illuminated species. Three different routes can be taken for relaxation from this virtual state. The first and most efficient one is elastic scattering and thus emitting a photon of the same energy, which yields the intense Rayleigh line in the Raman spectrum. The other two processes involve energy transfer either from the photon to the material, yielding a Stokes-shift, or from the material to the photon, resulting in an anti-Stokes shift. The processes are schematically shown in Figure 3.9.

Raman spectroscopy gives characteristic features in the spectra that correspond to vibrations or rotations in molecules which alter the polarizability of the electron cloud through dipole-dipole interactions in a molecule or a specific moiety therein. This is also the case with the electric field of the incident light, which modifies the polarizability tensor and thus enables the above-mentioned processes. Since the polarizability is typically larger if a molecule does not intrinsically carry permanent dipoles, as they are found e.g. in water, Raman spectroscopy allows for better study of vibrations and rotations which are otherwise inaccessible to techniques such as infrared absorption spectroscopy.

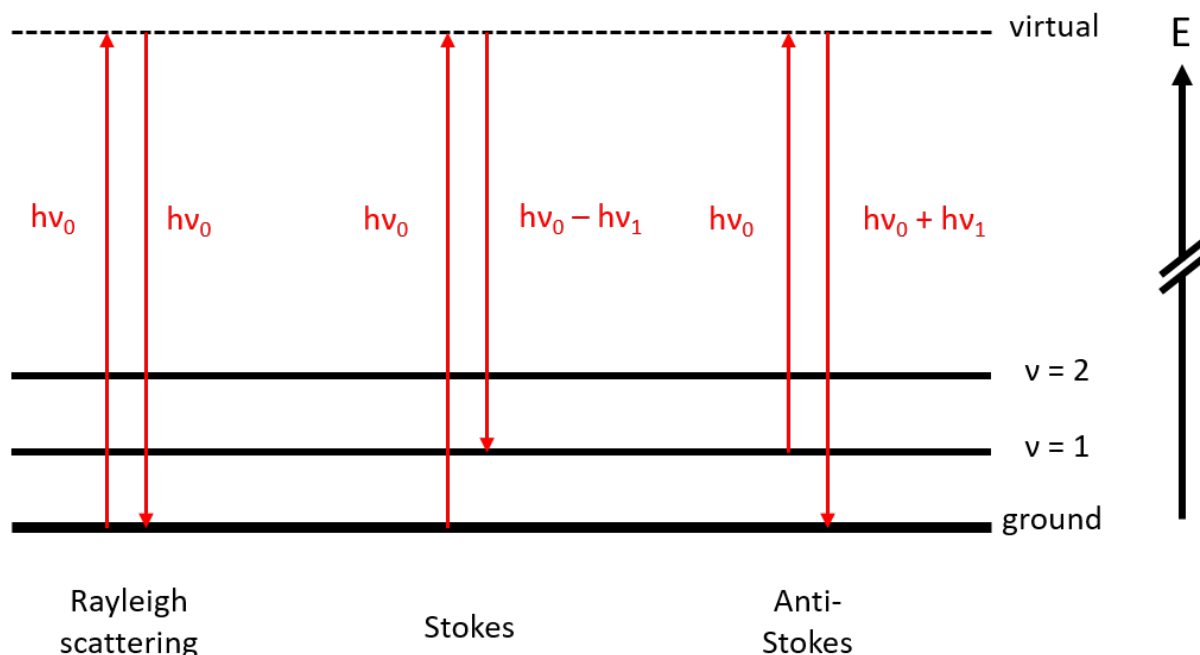


Figure 3.9: Schematic drawing of the Raman processes. The ground state of vibration is represented by the solid thick black line, while excited states are shown with thinner lines. The Raman process involves excitation into a virtual state, shown by the dashed black line. Energies of incident and scattered photons are represented by the length of the red arrows, leading either to Rayleigh scattering (no energy exchange), a Stokes-shift (energy loss of photon) or an anti-Stokes shift (energy gain of photon). The label on the right arrows of each process indicates the magnitude of the Raman shift.

For our purposes, Raman spectroscopy is used specifically in Chapter 6 to study potential changes in the conformational state of PEDOT chains in PEDOT:PSS films on which the dedoping procedure outlined in Section 4.2.2 is applied. As discussed in Section 6.2.3, PEDOT exists in both the benzoid and quinoid state, which can be distinguished using Raman spectroscopy due to their differing vibrational properties.

Measurements are performed on a *WITec alpha 300R* confocal Raman microscope, with an *Andor Newton* CCD-detector. A linearly polarized laser with a wavelength of 532 nm was used for excitation. Details of the measurement will be discussed in Section 6.2.3.

3.2.3 X-ray photoelectron spectroscopy (XPS)

X-ray photoelectron spectroscopy (XPS) is a surface-sensitive spectroscopy technique, in which x-rays impinge on a solid target and cause excitations of core electrons in the atoms contained within the sample. The excited electrons are then detected with respect

to their kinetic energy. Together with the knowledge of the energy of the incident beam, the binding energy E_b of the electrons can be determined according to Equation 3.15.

$$E_b = h\nu - E_{kin} - \Phi_w \quad (3.15)$$

E_{kin} represents the measured kinetic energy of the electrons, which depends on the energy $h\nu$ provided by the photon. Φ_w relates to the work function of a material. In an XPS spectrum the number of detected electrons is shown as function of the binding energy E_b . Each element has a set of distinct peaks which correspond to the energetic states of the core electrons. E_b is thus both a characteristic quantity of an element, but also more specifically of the state of that element. Thus, shifts of peaks assigned to a certain core electron transition of an element give insight into the latter's oxidation state. For positive oxidation states, a shift towards higher binding energies is expected since the same electrostatic force of the nucleus acts on fewer electrons, and thus binds each individual electron more strongly. Spin-orbit coupling of p-, d- and f-orbitals leads to splitting of the peaks, and thus has to be taken into account during fitting. The strength of XPS is its sensitivity towards the chemical environments of atoms. Since the molecular environment of an atom modifies its electron distribution, e.g. through covalent bonding or coordination, the binding energies of core electrons are changed as well. In this case, it becomes possible to distinguish between the sulfur contained in the thiophene ring of PEDOT from the sulfur in the sulfonate group of PSS.

XPS also allows for the quantification of the chemical composition of a sample, through integration of peak areas. However, this is limited to the upper-most layers of the sample (typically a few nm), due to the comparatively low kinetic energy of the electrons and their strong interaction with matter, which therefore leads to a small escape depth.

Other processes which can be triggered through illumination of a sample with x-rays are x-ray fluorescence which is caused by radiative relaxation of a higher energy electron into the vacancy left by the photo-emitted electron, or by non-radiative relaxation through emission of a third electron, which is also then called an Auger electron.

Samples are prepared on $1.5\text{ cm} \cdot 1.5\text{ cm}$ Si substrates. Measurements are carried out on a *PHI 5000 VersaProbe II* instrument with a monochromatic Al- K_α x-ray source. Initial survey scans are performed at a resolution of 0.8 eV/step , and at a resolution of 0.1 eV/step for the high resolution scans, respectively. The carbon 1s peak at 284.5 eV is used to account for charging effects as calibration. Data analysis is performed with the *CasaXP* software (Casa Software Ltd., United Kingdom). Spin-orbit coupling of the S2p-signal is taken into account during fitting of the signal with Gaussian-Lorentzian line shapes.

3.2.4 Near-edge x-ray absorption fine structure spectroscopy (NEXAFS)

As seen in Section 3.2.3, XPS can be used to determine the composition and electronic structure of thin film surfaces. However, when the wavelength of the x-rays becomes tunable, such as is the case for synchrotron radiation, it becomes possible to study the properties of materials regarding their optical response to x-rays. This optical response can be represented by the equation for the refractive index for x-rays shown in Equation 2.16.

Herein, the real component δ represents the dispersion properties of a material, i.e. the scattering power, while the imaginary component β represents the ability of the material to absorb the incident photons at a given energy. Specifically, when performing NEXAFS measurements, β becomes non-negligible since the optical properties change drastically near the absorption edge. The fine structure is dependent on the molecular constitution of the material. Thus, NEXAFS is an x-ray absorption spectroscopy technique which allows for clear distinction of chemical species due to the influence of the chemical shift on the fine structure of absorption bands. Similarly to XPS, core electron transitions are triggered by irradiating a sample with high-energy x-rays, whereby the latter are absorbed by atomic species which possess absorption edges with matching energies. The chemical environment of the atomic species in question largely affects the absorption fine structure, due to changes in the electron distribution caused by neighboring atoms and groups. Therefore, each species exhibits a fingerprint-type absorption close to the absorption edge. Even binary or ternary systems with components of similar electron densities can be distinguished simply through the investigation of the absorption fine structure with NEXAFS.

As will be seen in Chapter 5, NEXAFS is used for the determination of the optical constants of PEDOT, PSS and Si-NPs in the vicinity of the sulfur K-edge. Similarly to UV-Vis spectroscopy, a transmission measurement of the materials to be investigated is performed in an energy range of 2440 eV to 2500 eV. The distinction of PEDOT and PSS is possible, since they both constitute sulfur but in different chemical environments.

Thin films of PEDOT, PSS and Si-NPs are prepared on silicon substrates with a square Si_3N_4 window of 1.5 mm · 1.5 mm size (Silson Ltd., England). This window had a thickness of 200 nm. Due to the low mechanical stability of the window, a special disk-shaped substrate holder was used, which directed the vacuum towards all four edges of the substrate rather than the center. The measurements were performed at the four-crystal monochromator beamline of the PTB laboratory at the BESSYII synchrotron in Berlin. [27] All

curves were corrected using a reference measurement, performed on an empty Si_3N_4 substrate.

3.3 Morphological characterization

3.3.1 Optical microscopy (OM)

Optical microscopy is a reliable way to determine the quality of a thin film quickly. In Chapter 6, it is used to gauge the homogeneity of PEDOT:PSS films subjected to dedoping with inorganic salts.

All measurements are performed on an *Axio Lab* microscope (Carl Zeiss GmbH, Jena, Germany) in ten- and 50-fold magnification. The micrographs are captured digitally using a *PixeLink PL-S621CU* CCD sensor with 1280 pixels · 1024 pixels. Images are processed with the *ImageJ* software package. [28]

3.3.2 Scanning electron microscopy (SEM)

Scanning electron microscopy (SEM) is a scanning probe technique which allows for the morphological analysis of materials in real-space. The samples are irradiated with a focused electron beam, which is scanned across a macroscopic area. The interaction of the electron beam with the sample, which is either intrinsically electrically conducting or rests on a conducting substrate, leads to the generation of secondary electrons. As function of the position on the sample, the number of counts is translated and shown in a two-dimensional array as intensity. The interaction of the electrons is not limited to the focal point but leads to a large bulb-shaped interaction volume from which the secondary electrons escape. SEM is sensitive to the surface topography because the effective shape of the bulb-shaped interaction volume is altered by e.g. roughness effects, allowing more secondary electrons to escape. Thus, sharp edges appear very bright in scanning electron micrographs. On top of that, materials with higher electrical conductivity also appear brighter, which in Chapter 5 serves the distinction of PEDOT and PSS in PEDOT:PSS/Si-NPs composite thin films. Therein, PEDOT-rich domains are expected to appear brighter than PSS-rich domains.

All measurements are performed on a *FESEM Gemini NVision 40* instrument (Carl Zeiss GmbH, Jena, Germany) using the software *SmartSEM*. A field-emission gun with a tungsten filament is used as electron source. The implementation of electrostatic and magnetic 'condensor lenses' ensures focusing of the electron beam. The latter is scanned across the sample using an additional set of coils. Detection of the secondary electrons is

done using an in-lens detector. The system is operated at pressures of $2 \cdot 10^{-6}$ mbar and at an acceleration voltage of 2 keV with working distances between 2.5 mm to 3.5 mm. All images are processed using the *ImageJ* software package. [28] Images are adjusted regarding contrast and brightness for better visibility of features. Additionally, horizontal line artifacts originating from the scanning process are removed through the usage of a Fast-Fourier transform filter. Scale bars are given in all electron micrographs.

3.3.3 Scattering methods

Scattering techniques are powerful methods for the determination of nanoscaled structures in thin films, since the obtained information is typically averaged of macroscopic areas of the sample. This is especially true, when investigating thin films using the grazing-incidence geometry for x-ray scattering experiments, as schematically shown in Figure 3.10. A grazing-incidence experiment is characterized by a shallow incident angle, which is typically smaller than 1° . Due to the finite dimensions of the beam (both in width and height), a large illumination footprint on the thin film sample is achieved.

Since x-ray scattering is a reciprocal-space technique, a change of the SDD leads to changes in the accessible q-range and thus to different length scales which can be probed. As seen in Figure 3.10, with small SDDs large scattering angles are captured on the detector. The large scattering angles correspond to large q-values and thus to atomic length scales. In this case, the technique is called GIWAXS, allowing for the probing of short-range order. Correspondingly, when going to large SDDs, only small scattering angles are captured on the two-dimensional area detector. The small scattering angles are equivalent to small q-values and thus to large structures. In that case, one refers to the technique as GISAXS. With GISAXS, mesoscopic structures on the scale from 2 nm to 300 nm can be observed depending on parameters such as the wavelength of the incident x-rays, SDD, etc.

In the following, experimental procedures for both GIWAXS and a modified version of GISAXS, called GIR-TeXS, will be described in detail, since different instruments at different sites were used.

Grazing-incidence wide-angle scattering (GIWAXS)

Firstly, GIWAXS is used for the investigation of changes in the short-range order of PEDOT:PSS post-treated with ILs in Chapter 7. These measurements were carried out at the Austrian SAXS beamline of the Elettra Sincrotrone Trieste in Italy at an incident beam energy of 8 keV. The *Pilatus 1M* area detector was placed at an SDD of 295.8 mm,

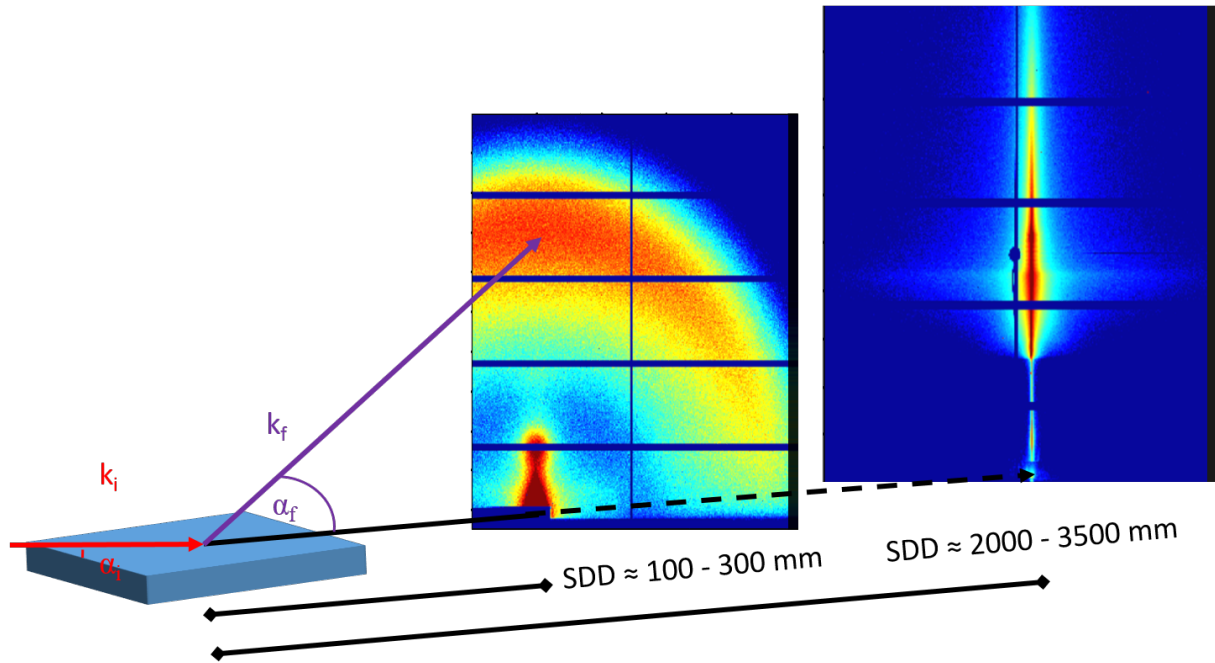


Figure 3.10: Schematic representation of a grazing-incidence x-ray scattering experiment. The thin film sample on the left is irradiated by a x-ray beam under a shallow incident angle α_i . The beam is scattered under the exit angle α_f and captured by a *Pilatus3 1M* detector. In a GIWAXS measurement, large scattering angles are detected, because the SDD is small. In a GISAXS measurement, small scattering angles are detected because the SDD is large.

whereby an incidence angle of 0.4° was used. Scattering patterns were recorded for 10 s each.

In Chapter 8, GIWAXS is used in order to elucidate ramifications of the doping of P(NDI2OD-T2) with N-DPBI. Doped P(NDI2OD-T2) were on the one hand prepared on glass substrates and measured using the in-house *Ganesha 300XL* instrument by Xenox SAS, Sassenage, France (formerly SAXSLAB). For these measurements a $\text{Cu-K}_{\alpha 1}$ source was used. The two-dimensional *Pilatus 300k* area detector was placed at a SDD of 108 mm, with an incidence angle of 0.2° . Samples were illuminated for four hours, while simultaneously recording the scattering patterns. Doped P(NDI2OD-T2) were also prepared on conducting FTO-substrates and were taken to the Deutsches Elektronen-Synchrotron (DESY), Hamburg, and measured at the MiNaXS-beamline P03 of the PETRA III storage ring. Here, the samples were irradiated with x-rays with an energy of 12.955 keV at an incidence angle of 0.2° . The scattering pattern was recorded on a *Pilatus 300k* area detector placed at a SDD of 150 mm. The illumination time was set to 10 s.

In all cases, reduction of the 2D GIWAXS patterns is performed with the *MatLab*-based tool *GIXSGUI*. [29] Firstly, this involves a number of corrections, which have to be applied to the data. The efficiency correction accounts for the fact that larger attenuation

of photons is observed for scattering in larger oblique angles. Depending on the medium and on the path length from the sample to the detector, the intensity is corrected for each pixel by a factor. Additionally, the probability of a photon being absorbed by a single detector pixel at larger oblique angles is increased, which also has to be taken into account. Similarly, the purely geometric solid-angle correction is applied due to differences in the effective pixel area as function of the scattered solid-angle. Also here the scattering intensity is modified for each pixel. Synchrotron radiation is typically linearly polarized in horizontal direction, which is adjusted with a corresponding correction function. Most important, however, is the proper representation of 2D GIWAXS data, the intricacies for which are discussed in more detail in Section 2.3.2.

2D GIWAXS patterns give information on the short-range order of the sample with respect to characteristic stacking distances and the presence or absence of preferred orientations. Sector integration maps the intensity as function of the scattering vector q . Peaks in the scattering curves correspond to the repeating occurrence of structural elements on very short length-scales of up to few nanometers. Sector integration can be confined with respect to the azimuthal angle χ in order to obtain structural information in different principal directions of the sample. In this work, sector integration in vertical direction is represented by χ -values in a range from -15° to 15° , yielding information of characteristic stacking distances perpendicular to the substrate. On the other hand sector integration confined to χ -values in a range from 70° to 80° gives information of stacking in the plane of the substrate. This has ramifications regarding macroscopically measurable properties such as the electrical conductivity, which is expected to depend on structural parameters like characteristic inter-molecule distances and their arrangement on longer length scales. Peak positions, amplitudes and widths are obtained through fitting with Gaussian line shapes. In Chapter 7, for the determination of peak positions and peak areas at high q -values a function comprising two Gaussians and a weighted function accounting for the amorphous glass substrate background signal are used.

Another way to evaluate the 2D GIWAXS images is to perform azimuthal integration. Therein, the intensity is mapped as function of the azimuthal angle χ . For the integration, typically a family of scattering peaks is selected which appear at similar q -values, whereby the latter is the confining parameter. Azimuthal integration gives insight into potential preferred orientation of repeating structural elements, and is mostly used to discuss changes therein upon certain treatments of the investigated samples. For conducting polymers one often observes an anisotropy regarding the charge transport properties, therefore strong implications of preferred orientations on the electrical properties of the thin films can be expected.

Grazing-incidence resonant tender x-ray scattering (GIR-TeXS)

GIR-TeXS is a powerful method for the elucidation of nanostructures in multi-component systems. In the frame of this work, it is used to give insight into the morphology of the ternary PEDOT:PSS/Si-NPs composite system, investigated in Chapter 5. Similarly to resonant soft x-ray scattering (RSoXS), the wavelength of the incident x-ray beam is adjusted to closely match with a core electronic transition of atomic species contained within the sample. As schematically shown in Figure 3.11, the incident photon excites core electrons in the atom with the matching energy transition. This excited state decays under the coherent emission of a photon. In this case, the wavelength of the incident beam was adjusted to the sulfur K-edge, located at 2473 eV. Both PEDOT and PSS comprise sulfur, while the Si-NPs do not. Therefore, it is possible to distinguish these materials by closely investigating the changes in the scattering behavior as function of incident beam energy.

In order to facilitate future experiments of this kind, a possible workflow will be discussed in the following, highlighting crucial steps from the conceptualization of an experiment to a final morphological model.

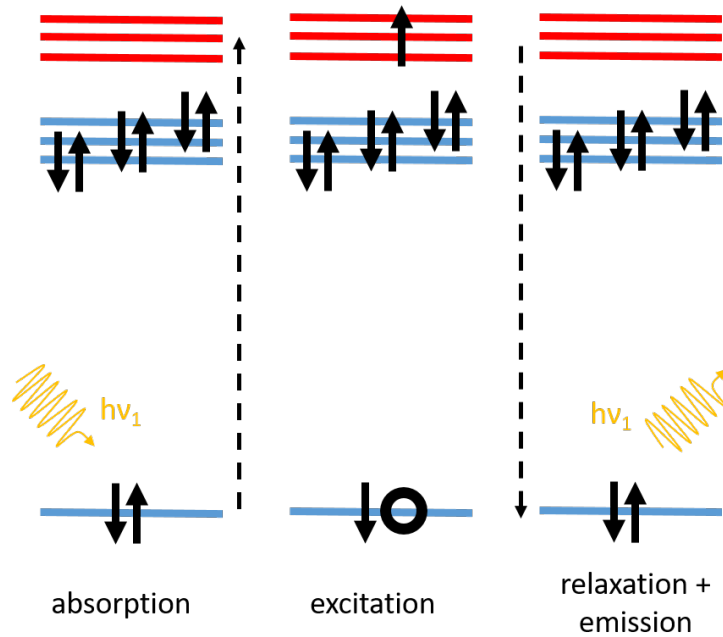


Figure 3.11: Schematic energy diagram, showcasing the process during a GIR-TeXS measurement. A photon with an energy matching that of a resonance excites an electron from a core state (blue line) to an empty state (red line). Radiative relaxation from the excited state leads to the coherent emission of a photon of the same energy. Adapted from [30].

1. Choice of materials and subsequent choice of core electron transition to be exploited.
2. Measurement of NEXAFS spectra for each individual component.
3. Calculation of the energy-dependent absorption coefficient using the NEXAFS spectra and subsequent calculation of the imaginary part of the refractive index.
4. Computation of the energy-dependent real component of the refractive index from the absorption coefficient using the Kramers-Kronig relation.
5. GISAXS measurement with several incident beam energies close to the absorption edge.
6. Horizontal line integration in 2D GISAXS patterns at critical angle of the material in question.
7. Modelling of the curves extracted from all images in an energy-series.
8. Calculation of energy-dependent scattering contrasts $\Delta n^2(E)$ for different possible arrangements of components.
9. Comparison of intensity evolution for the different scattering contributions as function of energy with calculated scattering contrasts $\Delta n^2(E)$.

The choice of materials is crucial for a GIR-TeXs measurement, as the incident energy has to be chosen in accordance with the elemental composition of the materials in question. Only with an energy close to a core electron transition, changes in the optical properties (namely absorption and dispersion) can be discerned as function of energy. As mentioned above, for the composite system investigated in Chapter 5 the sulfur K-edge was chosen. While the Si-NPs do not contain sulfur themselves, PEDOT and PSS can be readily distinguished due to their differing molecular constitution.

A NEXAFS measurement allows for the elucidation of the absorption behavior of each individual component close to the investigated transition energy. The influence of the chemical shift modifies the absorption of materials comprising atomic species which exhibit the core electron transition in question. Even though PEDOT and PSS are very similar in their chemical composition and thus in their electron density, their NEXAFS spectra are different due to changes in the chemical environment of the sulfur atoms.

The energy-dependent mass absorption coefficient $\mu(E)$ of the materials is calculated from the NEXAFS spectra with knowledge of the density ρ and film thickness d from the Beer-Lambert law, seen in Equation 3.16.

$$-\log\left(\frac{I}{I_0}\right) = \mu(E)\rho d \quad (3.16)$$

The mass absorption coefficient can be transformed into the energy-dependent imaginary part β of the refractive index using Equation 2.28.

Subsequently, the GISAXS measurement at energies close to the chosen core electron transition can be performed. In our case, measurements were carried out at the four-crystal monochromator beamline of PTB at the BESSYII synchrotron, Berlin. [27] As mentioned above, the energy interval was chosen to be from 2471 eV to 2475 eV as on-resonance and 2465 eV as off-resonance energy. A feature of the beamline is the custom-built in-vacuum *Pilatus 1M* detector by Dectris Ltd., Switzerland. [31] This is necessary, since the smaller energy of the x-ray beam would lead to strong air scattering, which is why all measurements were carried out in vacuum. At the energies given above the incident angle was set to 0.5° , while the SDD was 3215 mm.

The obtained 2D GISAXS patterns are analyzed by horizontally integrating the intensities at the critical angle of PEDOT. After performing the line integration for one sample at all energies, the obtained scattering curves can be modeled. Modelling in the framework of the DWBA was implemented using form factors of spherical shape, arranged in a one-dimensional para-crystalline lattice. In this work, three distinct families of spherical structures are necessary to model the data. It is of the utmost importance to find values for the structure sizes and average distances together with their respective distributions, which can be used to model all curves within a single energy series. This leaves only the scattering intensity of each structural family as free parameter, which is expected to change as function of energy.

Using the energy-dependent δ - and β -values obtained earlier, it is possible to calculate the scattering contrast $\Delta n^2(E)$ which is expected to change drastically close to the chosen core electron transition energy, as shown in Equation 3.17.

$$\Delta n^2(E) = \Delta \delta^2(E) + \Delta \beta^2(E) \quad (3.17)$$

$\Delta n^2(E)$ is used for comparison with the scattering intensities obtained from the analysis of the 2D GISAXS patterns. The $\Delta n^2(E)$ curves can be compared with the obtained scattering intensities as function of energy for the three structural families used in the modelling of the horizontal line cuts from the 2D GISAXS images. In our case, two possible structural models for the morphology of the ternary PEDOT:PSS/Si-NPs system are proposed, and will be discussed in Chapter 5. Details of the calculation will be given in the corresponding section.

A qualitative match between the evolution of scattering intensities with the $\Delta n^2(E)$ curves suggests the validity of the proposed morphology and can subsequently be used to devise a morphological model.

Time-of-flight grazing-incidence small-angle neutron scattering (TOF-GISANS)

Time-of-flight grazing incidence small-angle neutron scattering (TOF-GISANS) experiments were performed at the REFSANS instrument at the neutron reactor FRMII operated by the Heinz Maier-Leibnitz Zentrum (MLZ) in Garching, Germany. [32] This technique makes use of the fact that neutrons of different wavelength possess different velocities, and thus can be distinguished by their so-called 'time of flight' (TOF). This can be seen in Equation 3.18.

$$\lambda = \frac{h}{p} = \frac{h}{mv} \quad (3.18)$$

Here, the deBroglie wavelength λ is a function of Planck's constant h and the momentum p of the neutron. It should be noted that due to the finite mass of the neutrons, they are subjected to gravity effects which are accounted for in data reduction. Therein, slower neutrons (i.e. at larger wavelengths) are affected more strongly.

In the TOF-mode, a pulsed neutron beam with a wavelength band from 3.3 Å to 12.12 Å is achieved with the help of a chopper system. Here, the average wavelengths are 3.3 Å, 3.65 Å, 4.03 Å, 4.45 Å, 4.92 Å, 5.44 Å, 6.01 Å, 6.65 Å, 7.35 Å, 8.12 Å, 8.97 Å, 9.92 Å, 10.96 Å and 12.12 Å. For each wavelength, a scattering image is obtained. In order to achieve a favorable trade-off between wavelength resolution and intensity, a so-called λ -slicing is performed. Therein, the scattering images are binned according to their wavelength, such that the ratio $\frac{\Delta\lambda}{\lambda}$ of each slice is 10 %. Apart from a reasonably high signal-to-noise ratio, this kind of λ -slicing still allows for distinction of wavelength-dependent scattering features. Due to changes in the average wavelength of the images, the accessible q -range is also modified, leading to enhanced scattering from small structures at lower wavelengths, and larger structures at higher wavelengths.

Neutron scattering differs from x-ray scattering in the interactions of the former with matter. Since neutrons do not carry a charge but only a nuclear spin, they only weakly interact with nuclear spins of the atomic species contained in the sample. Correspondingly, the scattering cross-sections are typically small and vary non-linearly within the periodic table of elements. As opposed to x-rays, the scattering contrast for neutrons does not change with the atomic number, but is isotope-dependent.

A TOF-GISANS measurement offers several advantages. Apart from the overall increased q -range due to the wavelength band, which potentially yields structural information on many different length scales, it also exploits the wavelength-dependence of the SLD which directly affects the critical angle α_c , as seen in Equation 3.19. [33]

$$\alpha_c = \lambda \sqrt{\frac{SLD}{\pi}} \quad (3.19)$$

Equation 3.19 reveals that while the position of the specular peak in a wavelength-series is relatively constant, the material-sensitive Yoneda peak shifts towards larger scattering angles with increasing λ . One can make use of this fact, by tracking the position of the Yoneda peak as function of wavelength and consequently infer the actual SLD of the sample and compare it to theoretical calculations. Additionally, since the incident angle of the beam on the sample is fixed, a bulk-sensitivity is achieved for small wavelengths ($\alpha_i > \alpha_c$), whereas scattering for larger wavelengths is more surface-sensitive ($\alpha_i < \alpha_c$).

In the experiment discussed in Chapter 5, the incident angle was chosen to lie in a range of 0.46° to 0.50° . Scattering patterns are collected on a $500 \text{ mm}^2 \cdot 500 \text{ mm}^2$ ^3He detector. It consists of $340 \text{ pixels} \cdot 340 \text{ pixels}$, with a size of $1.378 \text{ mm}^2 \cdot 1.378 \text{ mm}^2$ each. The SDD was set to 10.52 m.

4 Sample preparation

The aim of this chapter is the comprehensive description of the different materials used in this thesis, and the various ways in which they were processed. Since for part of the discussion later on samples were prepared differently, the different sections in this chapter serve as point of reference for reproduction of the respective experiments.

After listing the various polymers, additives and substrate materials, the sample preparation procedures used for the different investigations will be described in detail, in addition to the procedure for fabrication of a thermoelectric generator based on conducting polymers as active materials.

4.1 Materials

4.1.1 Polymers

This thesis deals with the thermoelectric properties of conducting polymers. As such, two representatives of this material class are primarily investigated in the frame of this work. PEDOT:PSS is a promising candidate for a p-type material, while P(NDI2OD-T2) is interesting regarding its ability to transport negative charge carriers.

PEDOT:PSS

PEDOT:PSS is a conductive polymer blend, which is soluble in water. In solution, dispersed particles can be found in which long chains of PSS carry shorter fragments of PEDOT. PSS is a water-soluble poly-anion, while the conjugated polythiophene PEDOT is responsible for charge transport, and therefore responsible for the observed thermoelectric properties of thin films. Both components of the blend are shown in Figure 2.3. PEDOT:PSS is typically prepared by electrochemical polymerization of PEDOT in the presence of PSS. Thus, the latter not only allows for the dispersion of PEDOT in solution, but also aides in the stabilization of charges on the former.

Many different formulations of PEDOT:PSS can be found, all employed for different purposes. The formulations mostly differ in the ratio of PEDOT to PSS, largely influencing properties such as the band-gap, optical transparency and possibly achievable electrical conductivity, respectively sheet resistance. Out of this library, the formulation commonly referred to as PH1000, is most suited for application in thermoelectric thin films. The PEDOT-to-PSS ratio of 1:2.5 is such that the highest electrical conductivity values can be obtained with appropriate treatments of the polymer either prior or after the fabrication of the thin film.

Heraeus Clevios PH1000 is purchased from *Ossila Ltd.*, Sheffield, UK as aqueous dispersion with a mass content of 1.1 wt% to 1.3 wt%.

P(NDI2OD-T2)

P(NDI2OD-T2) is an alternating copolymer, in which the n-type naphthalene-diimide groups are bridged by bithiophene units. The naphthalene-diimide moieties are able to transport negative charge carriers, as opposed to the bithiophene bridges, while the long alkyl chains attached to the nitrogen centers prevent agglomeration of the monomers, and simultaneously allow for dissolution of the polymer in organic solvents. P(NDI2OD-T2) is investigated in the framework of this thesis as potential n-type thermoelectric thin film, and thus used as n-type leg in the thermoelectric generator.

P(NDI2OD-T2) was purchased as powder from 1-MATERIAL Inc., Quebec, Canada. The structure of a single repeating unit can be seen in Figure 2.4.

Polymers for the preparation of free-standing PEDOT:PSS films

As will be discussed in Section 3.1.5, the measurement of the thermal conductivities of PEDOT:PSS is a crucial part of this work. For this purpose, Section 4.2.3 details the fabrication of free-standing PEDOT:PSS films in order to suspend them on substrates with cavities for measurement of the thermal conductivity of thin films using IRT. The additional polymers required for this procedure are shown in Figure 4.1.

Poly(dimethyl siloxane) (PDMS) is spin-cast as thin film on top of cleaned glass substrates in order to form a low-adhesion layer, due to the intrinsically low interfacial energy of PDMS. PDMS was purchased from *SYLGARD 184*, Dow Corning GmbH, Wiesbaden, Germany. It is delivered as oligomeric precursor, to which a cross-linking agent has to be added.

Figure 4.1 shows poly(vinyl alcohol) (PVA) (Mowiol 4-88), a water-soluble polymer which was purchased as powder from Sigma-Aldrich Chemie GmbH, Steinheim, Germany.

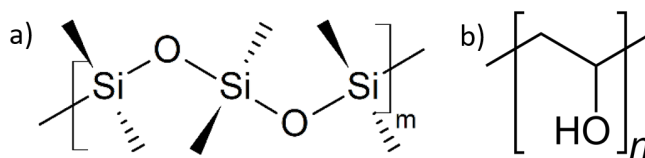


Figure 4.1: Chemical structures of a) PDMS and b) PVA.

4.1.2 Polymer additives

In the framework of this thesis many different treatments were applied to the investigated conducting polymers. This section lists all the used agents, including solvents, surfactants, nanoparticles, dopants and ionic liquids.

Organic solvents

All of the used organic additives are shown in Figure 4.2. The amphiphilic fluorosurfactant Zonyl FS-300 is a registered trademark of the company *E. I. du Pont de Nemours & Co.*, Wilmington, Delaware, USA. It was purchased from Sigma-Aldrich, whose subsidiary *Fluka* produces it. It comes as an aqueous solution with 40 wt% solid content and has a density of 1.10 g/ml at 20 °C and a boiling point of 80 °C. For the remainder of this thesis, it will simply be referred to as Zonyl. Ethylene glycol (EG) (99.8 %, anhydrous) is used as high-boiling point solvent for post-treatment of PEDOT:PSS thin films, since this leads to high electrical conductivities. It was purchased from Sigma Aldrich Chemie GmbH, Steinheim, Germany. Hexane (Carl Roth GmbH & Co. KG) is used for dilution of the high-viscosity PDMS oligomer-cross-linker mixture prior to spin-coating, in order to allow for homogeneous deposition. Tetrahydrofuran (THF) ($\geq 99.9\%$, Sigma Aldrich Chemie GmbH, Steinheim) is used as solvent for ILs, which can enhance the thermoelectric properties of PEDOT:PSS films after post-treatment. 1,2-dichlorobenzene (DCB) (99 %, anhydrous, Sigma Aldrich Chemie GmbH, Steinheim) is used as solvent for both P(NDI2OD-T2) and N-DPBI.

Si-NPs

Boron-doped (p-type) Si-NPs, used to prepare PEDOT:PSS/Si-NPs composite films in Chapter 5, were provided by the group of Prof. Martin S. Brandt from the Walter-Schottky-Institut, Garching, Germany. They were produced in a gas phase synthesis, for which an exemplary high-resolution transmission electron micrograph showing single nanoparticles is shown in Figure 4.3. The Si-NPs used in this thesis had an average diameter of roughly 25 nm, with a logarithmic size distribution. Notably, the particles obtained from the gas phase synthesis are effectively core-shell nanoparticles, since they

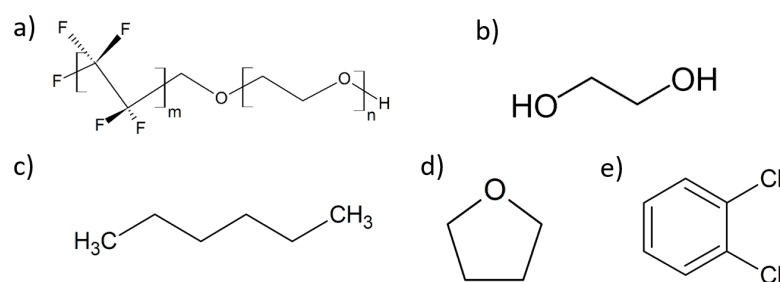


Figure 4.2: Chemical structures of organic additives used in this thesis. a) Zonyl[®] FS-300, b) EG, c) hexane, d) THF, e) DCB.

exhibit a highly ordered, single-crystalline silicon core, while carrying an amorphous, thin oxide shell.

Prior to usage, dispersions of Si-NPs in ethanol were subjected to ultrasound for two hours in a cooled ultrasonic bath, in order to break up potential aggregates. The concentration of the stock solution was 7 wt%. Dilutions were prepared with absolute ethanol (Sigma-Aldrich Chemie GmbH, Steinheim), and also briefly sonicated before application in PEDOT:PSS/Si-NPs composite films.

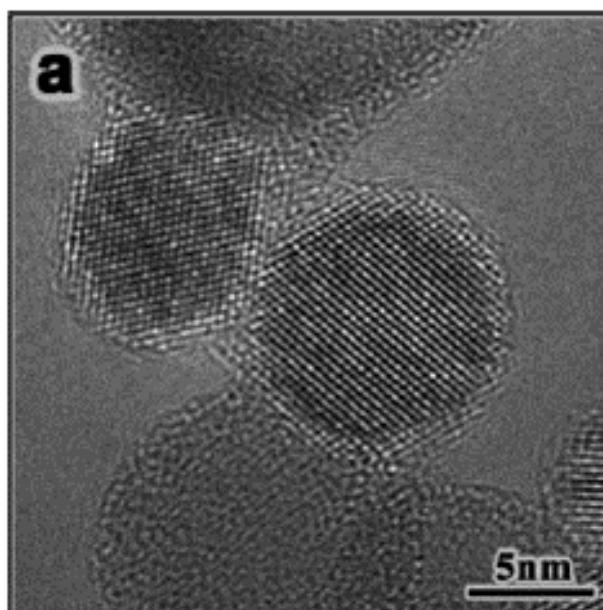


Figure 4.3: High-resolution transmission electron micrograph of exemplary Si-NPs obtained from gas phase synthesis. The nanoparticles exhibit a core-shell structure, with single-crystalline silicon as core, being surrounded by amorphous silicon oxide as shell. Image taken from [34].

Materials for (De)doping

The conductive properties of conjugated polymers rely on the presence of dopants, which induce charge carriers (positive or negative, depending on the oxidative, respectively reductive properties of the agents) on the chains.

The inorganic salts shown in Figure 4.4 are all used in order to tune the electronic properties of PEDOT:PSS, by a procedure outlined in Section 4.2.2. Sodium sulfite (Na_2SO_3) ($\geq 98\%$) and sodium borohydride (NaBH_4) ($\geq 99\%$) were purchased from Sigma Aldrich Chemie GmbH, Steinheim, while sodium hydrogencarbonate (NaHCO_3) was purchased from Merck KGaA EMD Millipore Corporation, Darmstadt, Germany.

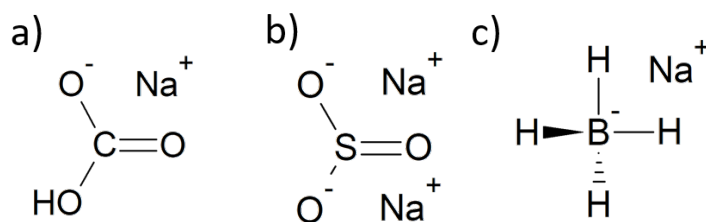


Figure 4.4: Inorganic salts used for dedoping of PEDOT:PSS films. a) NaHCO_3 , b) Na_2SO_3 and c) NaBH_4 .

The conducting polymer P(NDI2OD-T2) is intrinsically insulating, when deposited on a substrate. Therefore, the small molecule N-DPBI, shown in Figure 4.5, is used in order to induce negative charge carriers via a hydrogen transfer reaction, as will be discussed in Section 8. In order to ensure successful charge transfer onto P(NDI2OD-T2), it is of vital importance to store N-DPBI in an inert atmosphere, as compounds with reducing properties are prone to degradation reactions with the oxygen present in ambient atmosphere.

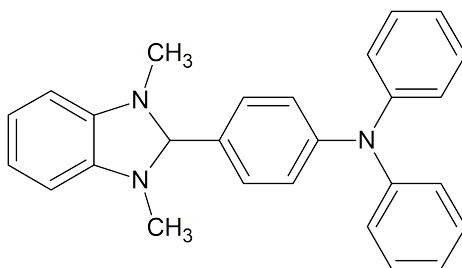


Figure 4.5: Chemical structure of the small molecule N-DPBI, used for doping of P(NDI2OD-T2).

Ionic liquids (ILs)

Figure 4.6 shows the different ILs used for post-treatment of PEDOT:PSS, the results for which are discussed in Chapter 7. 1-ethyl-3-methylimidazolium dicyanamide (EMIM DCA) ($\geq 98.5\%$) and 1-ethyl-3-methylimidazolium tetrafluoroborate (EMIM BF_4) ($\geq 97\%$) were purchased from Sigma-Aldrich GmbH, while 1-ethyl-3-methylimidazolium tetracyanoborate (EMIM TCB) was purchased from Merck KGaA EMD Millipore Corporation, Darmstadt, Germany. All ILs are in liquid state at room temperature. For the investigation in Chapter 7, it was ensured that the cation is the same, while the anion was varied. This allowed for better comparability of the results and helped with the deduction of the improvement mechanism.

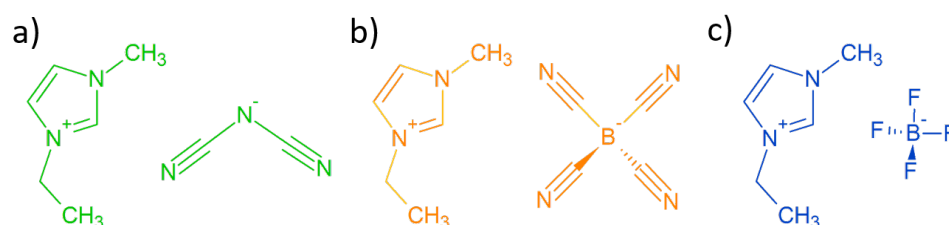


Figure 4.6: Ionic liquids used for the post-treatment of PEDOT:PSS films. a) EMIM DCA (green), b) EMIM TCB (orange) and c) EMIM BF_4 (blue). The color code is also used for the whole Chapter 7, in order to link the measured quantities with the respective ILs.

4.1.3 Substrate materials

For the largest part of this thesis standard microscopy slides made of soda-lime glass (Carl Roth GmbH & Co. KG, Darmstadt, Germany) of 1 mm thickness were used as substrates due to their insulating properties. For neutron scattering experiments, p-doped silicon wafers (SiMat, Kaufering, Germany), with a thickness of 525 μm , were cut into sizes of 7 cm \cdot 7 cm. These were polished on one side, exposing the (100) orientation. Both glass and silicon substrates were subjected to cleaning in an acid bath and plasma treatment prior to film deposition, as described in Section 4.2.1.

FTO-coated glass substrates (FTO TEG 7/2.2) were used for the investigations of P(NDI2OD-T2) in Chapter 8. They were purchased from SOLEMS S.A., Palaiseau, France.

Figure 4.7 shows two types of steel substrates used for IRT, which will be discussed in Section 3.1.5. Free-standing PEDOT:PSS films are suspended on both types of substrates in order to measure IRT using the substrate with small cavities, seen in Figure 4.7a, and to perform UV-Vis spectroscopy with the substrate with the large cavity in Figure 4.7b.

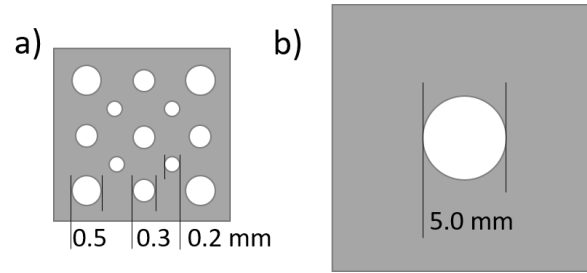


Figure 4.7: Schematic drawing of the steel substrates used for the transfer of free-standing PEDOT:PSS films. Substrate used for a) IRT with small cavities of varying sizes and for b) UV-Vis spectrscopy with larger cavity.

Since homogeneous films cannot be fabricated on these substrates because of the cavities, PEDOT:PSS films are transferred onto them with a procedure detailed in Section 4.2.3.

4.2 Thin film preparation

This section summarizes all the procedures involved in the fabrication of thermoelectric polymer thin films. Thus, it comprises cleaning procedures for the substrates, as well as different subsections detailing the involved procedures for the four projects discussed in the results part of this thesis. Additionally, the fabrication procedure for a thermoelectric generator based on conducting polymers as active materials is described.

4.2.1 Substrate cleaning

Rigorous cleaning of substrates is crucial for the successful fabrication of thin films, since the interactions of substrates with the material to be deposited can largely influence the homogeneity of the final film, as is also the case with impurities. Therefore, when employing glass or silicon substrates, all substrates were subjected to an acid bath, the components for which are listed in Table 4.1. The water, hydrogen peroxide (30 %, Carl Roth GmbH Co. KG) and sulfuric acid (to EMSURE, for analysis, Sigma-Aldrich Chemie GmbH, Steinheim, Germany) are mixed in the order given in the table, with the mixture then being heated to 80 °C. Since the temperature sensor cannot be placed directly into the acid, the temperature of a water bath heating the vessel containing the acid was controlled. After reaching the target temperature, the acid bath was allowed to take on the temperature of the water bath during an equilibration period of 15 min. The substrates were then placed in PTFE holders and submerged into the acid bath, while letting the cleaning take place for another 15 min. By washing the substrates with copious amounts of deionized water, residues of the acid mixture were removed. The

wet substrates were then dried on a spin-coater (Delta 6 RT CC, Süß Microtech AG, Garching, Germany) at 1500 rpm for 30 s.

Table 4.1: Chemicals used for the preparation of an acid bath for substrate cleaning, with the respective amounts. [35]

Chemical	Volume [mL]
Deionized water	45
Hydrogen peroxide (30 %)	70
Concentrated sulfuric acid	165

After acid cleaning, an oxygen plasma treatment was performed using a Plasma System Nano (Diener Electronics). After applying vacuum inside the chamber, a defined partial pressure for oxygen of 0.4 mbar is set, allowing for a continuous oxygen flow while simultaneously applying vacuum in order to remove reaction products. For pure glass and silicon substrates, plasma powers of 250 W were applied for 10 min. For PDMS-coated glass substrates used for the preparation of free-standing PEDOT:PSS films, an increased plasma power of 300 W was necessary. In all cases, the plasma treatment serves the removal of organic residues on the substrate in addition to the hydrophilization of the glass/silicon/PDMS surfaces, respectively. This facilitated the wetting of the water-based PEDOT:PSS solution, and led to more homogeneous films. For the deposition of hydrophobic P(NDI2OD-T2) solutions in DCB on glass substrates, the plasma treatment was omitted.

FTO substrates were cleaned by successively immersing them in four different solvents. These were the detergent *Alconox* (Sigma-Aldrich Chemie GmbH, Steinheim Germany), ethanol, acetone and isopropanol (all Rothipuran, $\geq 99.8\%$, Carl Roth GmbH Co. KG, Karlsruhe, Germany). This sequence allowed for an increasing hydrophobization of the substrate surface. Each step was performed for 10 min in an ultrasonic bath. Between each step, the samples were rinsed with the next solvent in which they were about to be immersed. After the cleaning procedure, the substrates were dried with a nitrogen gun.

4.2.2 PEDOT:PSS thin films

This section lays out a base process for the preparation of PEDOT:PSS solutions. Afterwards, the different subsections refer to the thin film preparation procedures for the different research projects.

Aqueous PEDOT:PSS solutions contain colloidal particles which comprise an excess of PSS, with shorter fragments of PEDOT attached. A sonication step for 15 min breaks these particles down, since larger particles increase the risk of forming inhomogeneous films. Afterwards, the solution was run through a poly(vinylidene difluoride) (PVDF, Puradisc 25, Whatman, GE Healthcare) filter with a pore size of 0.45 μm . Residuals of particles larger than the pores were thus excluded from the filtered solution. For all investigations on PEDOT:PSS, Zonyl was added due to its ability to modify interfaces and improve electrical characteristics of the final film. Also, the addition of Zonyl to the PEDOT:PSS solution allows for film fabrication even on rather hydrophobic substrates such as silicon or PDMS. Since Zonyl is a surfactant, it is not possible to accurately measure precise volumes with the used pipettes, which is why the amount was always determined such that the final weight content in the PEDOT:PSS solution was roughly 1 wt%. Firstly, the required amount of Zonyl was put in a glass vial, on top of which the appropriate amount of PEDOT:PSS solution was added. The mixture was then put on a shaker for two hours, while being covered in aluminum foil. After that, the solution was used further, as indicated in the following sections.

Thin PEDOT:PSS/Si-NP nanocomposite thin films

Figure 4.8 shows a scheme for the preparation of PEDOT:PSS/Si-NPs composite films investigated in Chapter 5. Thin films were fabricated by alternating deposition of PEDOT:PSS and Si-NPs, such that a five-layered system could be achieved. The PEDOT:PSS solution was used as described above, while dilutions of the Si-NPs dispersion in absolute ethanol were prepared in the desired concentrations of 0.3 wt%, 0.5 wt% and 0.7 wt%. For the first layer of PEDOT:PSS, 300 μL of solution were used, while for every subsequent layer 400 μL were used. For each deposition step of Si-NPs dilution, 300 μL were used. An annealing step at 140 $^{\circ}\text{C}$ for 10 min was performed after each deposition of PEDOT:PSS, in order to allow for evaporation of the solvent and simultaneous crystallization of the film. After achieving a five-layered stack with three layers of PEDOT:PSS sandwiching two layers of Si-NPs in an alternating fashion, a post-treatment step with EG was performed. This was done by drop-casting 500 μL EG on the substrate, letting it take effect for one minute, drop-casting another 500 μL EG on top, and immediately starting the spin-coating process. The spin-coating parameters for all steps were chosen to be 1500 rpm for the rotation speed, acceleration level 9 (corresponding to 4.5 s for acceleration and deceleration) and 60 s total rotation time.

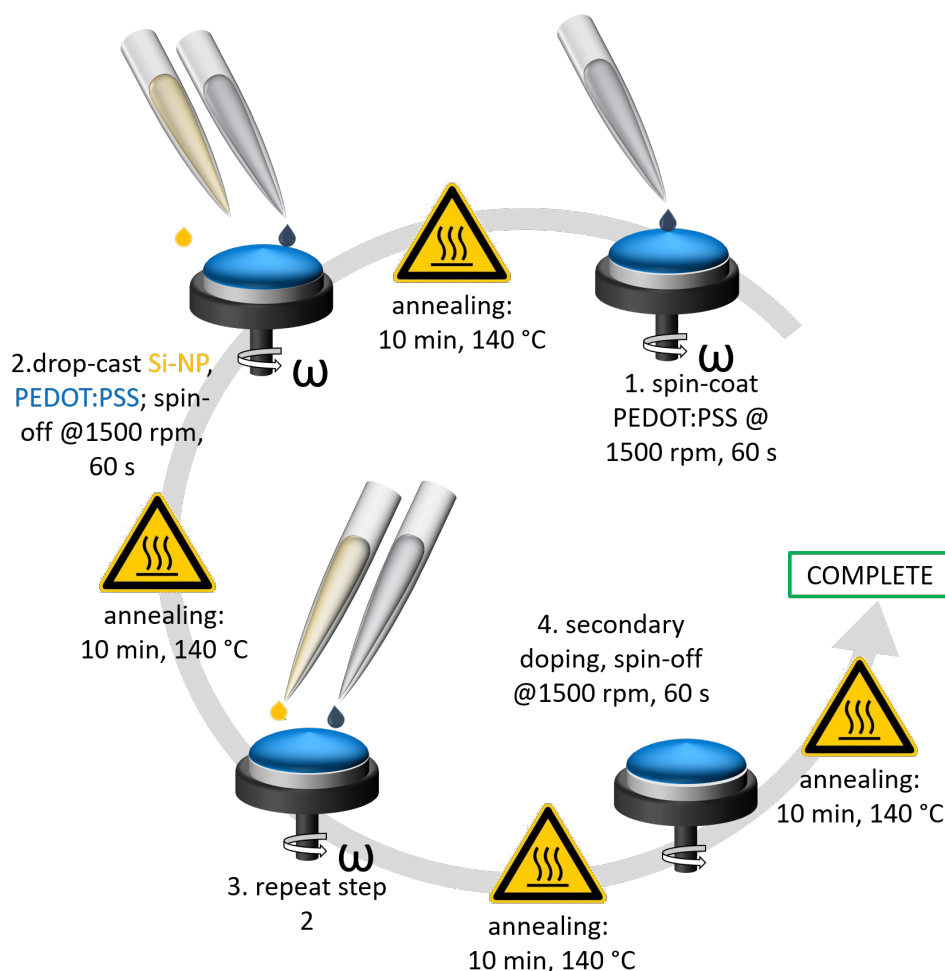


Figure 4.8: Sample preparation scheme for the fabrication of PEDOT:PSS/Si-NPs composite thin films, indicating the alternating fashion of deposition, with annealing steps in between.

Dedoped PEDOT:PSS thin films

The preparation of PEDOT:PSS dedoped with the inorganic salts NaHCO_3 , Na_2SO_3 and NaBH_4 is shown in Figure 4.9. Aqueous solutions of the inorganic salts were prepared with a concentration of 1 M each. Small amounts were added to the PEDOT:PSS solution in order to achieve different concentrations of dedopant, and afterwards subjected to shaking while covered in aluminum foil for 30 min. This ensured a complete reaction between the polymer and the salt. Afterwards, two PEDOT:PSS layers were prepared on top of each other by spin-coating with the parameters given above and annealing steps in between. Finally, EG post-treatment was applied as described previously, in order to study the effects of the dedoping on the electronic structure of the films.

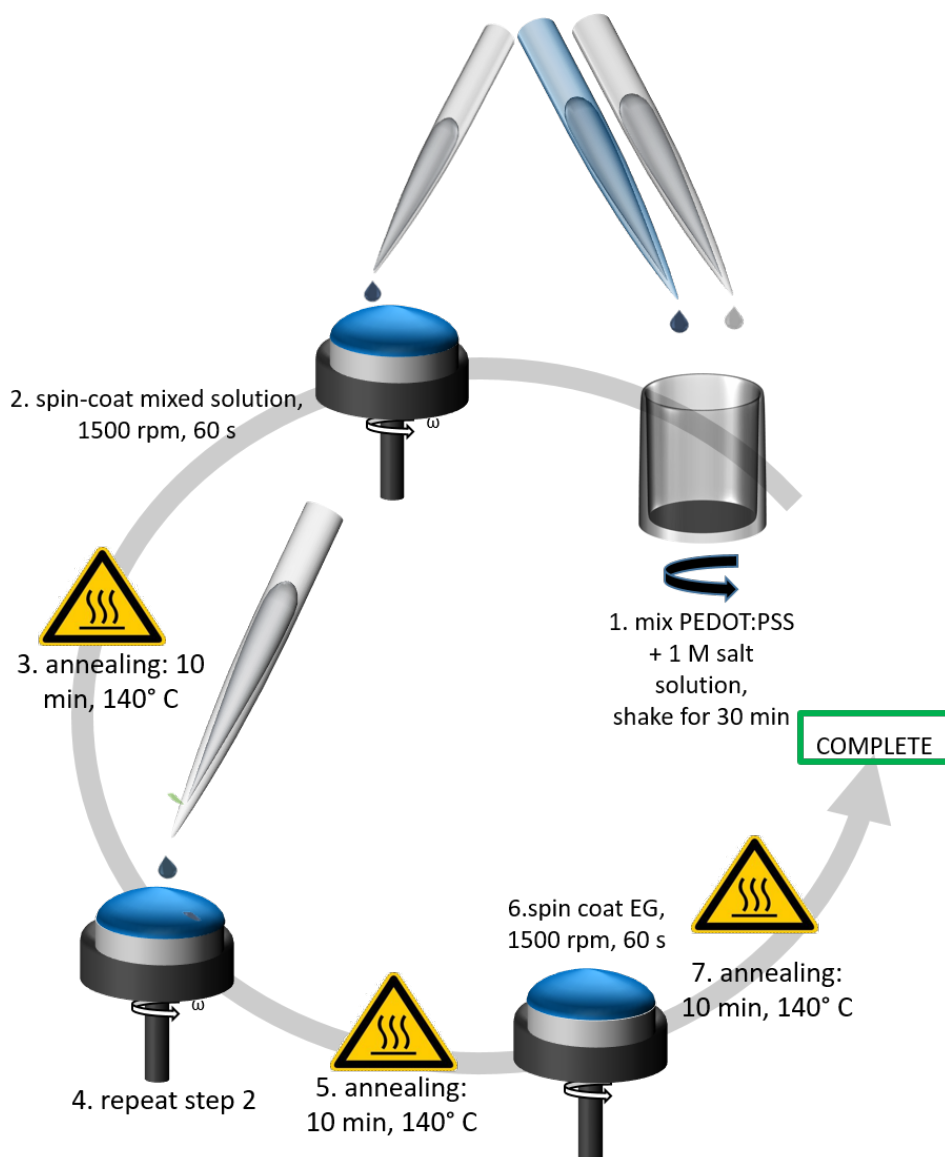


Figure 4.9: Sample preparation scheme for the fabrication of PEDOT:PSS films dedoped with inorganic salts. The mixing of aqueous salt solutions with the polymer solution prior to spin-coating is highlighted.

Post-treatment of PEDOT:PSS thin films with ionic liquids

In Figure 4.10, the fabrication process for IL-post-treated PEDOT:PSS films is shown. Direct mixing of PEDOT:PSS and IL leads to direct gelation of the polymer, which then cannot be processed into thin films with spin-coating anymore. Thus, an alternative approach was chosen, in which first a two-layered PEDOT:PSS film was prepared, with rotation speeds of 1500 rpm, acceleration level 9 for 60 s and two annealing steps in between at 140°C for 10 min. All ILs shown in Figure 4.6 were each dissolved in THF in different

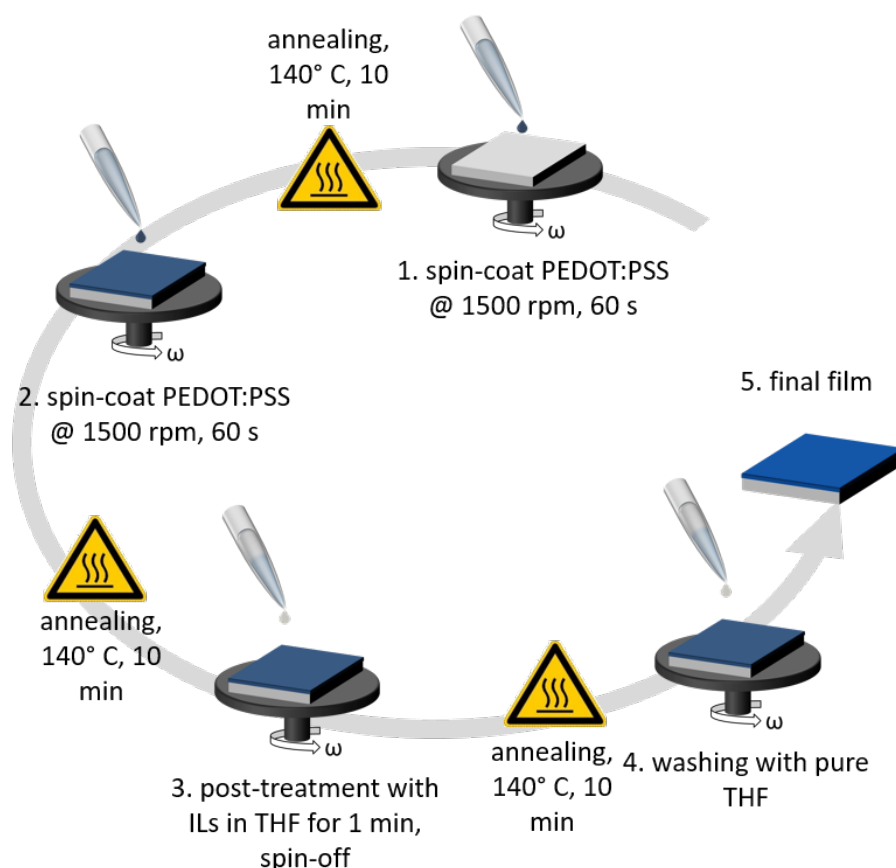


Figure 4.10: Sample preparation scheme for IL-treated PEDOT:PSS films. In addition to the post-treatment step with ILs dissolved in THF, the final washing step with pure THF is also shown.

concentrations and sonicated for 10 s prior to the post-treatment step. This was performed by drop-casting 400 μL of the IL- solution, letting it take effect for one minute, then drop-casting another 400 μL , and immediately starting the spin-coating process. Another annealing step ensured the removal of residual THF. Still, due to their high boiling points, it was expected that the ILs could not be removed from the films through annealing. After characterizing the films regarding their Seebeck coefficients and sheet resistances, the films were therefore subjected to a washing step with pure THF. This was done by drop-casting 200 μL of pure THF, letting it take effect for one minute, spin-coating and annealing with the same parameters as before. After the washing step the samples were subjected to thermoelectric characterization once again, in addition to UV-Vis spectroscopy, height profilometry and GIWAXS.

4.2.3 Free-standing PEDOT:PSS films

The preparation of free-standing films was necessary for the determination of the thermal conductivities of those films. There are methods to determine the thermal conductivity of thin films, such as time-domain thermoreflectance (TDTR). Since it relies heavily on the observation of acoustic waves on the surface of the investigated thin films induced by thermal stress, metal layers are typically evaporated on the surface. There is a high risk for damage in the film, due to e.g. diffusion of metal into the polymer, among others. Thus, we opted for IRT as alternative measurement technique.

The procedure for the preparation of free-standing PEDOT:PSS films is schematically shown in Figure 4.11. It was adopted from the work by Greco *et al.* [36] Firstly, soda-lime glass substrates were cleaned as described in Section 4.2.1 and subjected to oxygen plasma treatment. For the fabrication of a thin PDMS layer, first the mixture of oligomer and cross-linker had to be prepared. A weight ratio of 10 : 1 of oligomer to cross-linker was chosen. However, this mixture exhibits a very high viscosity which impedes the formation of a homogeneous thin film during spin-coating. Thus, 30 wt% of hexane were added to

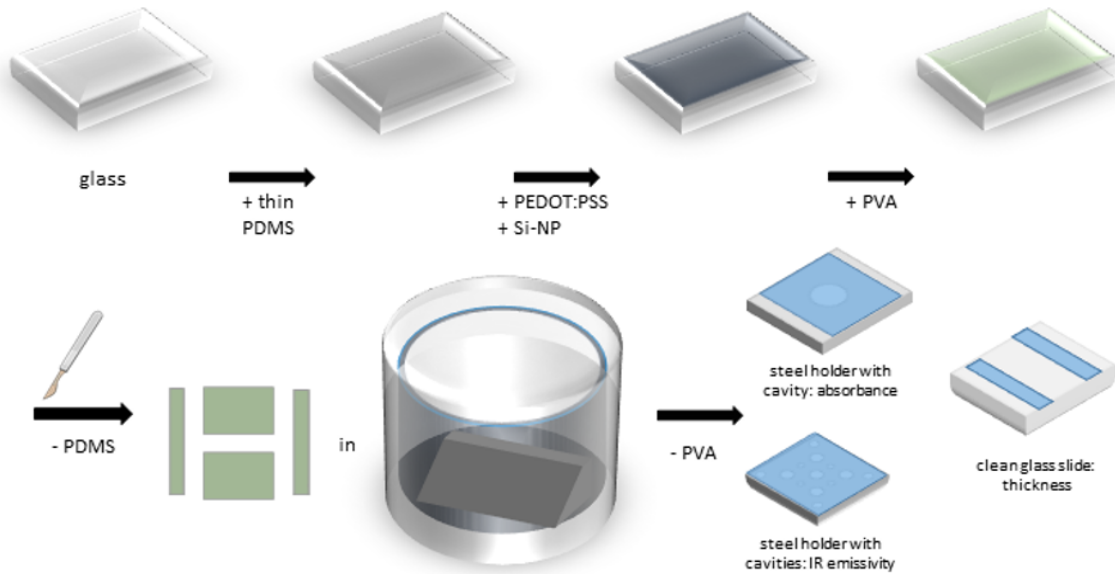


Figure 4.11: Scheme of the procedure for the production of free-standing PEDOT:PSS films, highlighting the individual steps. Thin PDMS were prepared on clean glass substrates. After fabrication of PEDOT:PSS on top of the PDMS, a layer of PVA was drop-cast, in order to support the former upon removal from the PDMS substrate. Immersion of the PVA-supported PEDOT:PSS into the water bath led to the dissolution of PVA, allowing for the transfer of PEDOT:PSS onto the desired substrates for measurement of the thermal conductivity.

the oligomer/cross-linker mixture, followed by thorough mixing with a metal spatula. The mixture was deemed fluid enough when air bubbles in the mixture were visibly diffusing to the top of the vial. Immediately after plasma-treatment, 500 μ L of the PDMS mixture were spin-cast on the clean substrates at 2000 rpm, acceleration level 9 for 90 s, and then subjected to annealing at 95 °C for one hour.

After plasma-treatment at high power, as described in Section 4.2.1, the PDMS is functionalized with hydroxyl groups which allows for better wetting of the aqueous PEDOT:PSS solution. It should be mentioned that addition of Zonyl is still crucial for homogeneous film formation on PDMS. After the preparation of the PEDOT:PSS film, PVA was dissolved in deionized water such that the final concentration was 10 wt%. 500 μ L of the PVA solution were drop-cast on the films and allowed to dry overnight, while covered with a glass lid to avoid the setting of dust in the PVA layer. Letting the film dry overnight was necessary, as the water evaporated only very slowly from the film. PVA served as support for the PEDOT:PSS layer, after removal from the PDMS. PDMS possesses a low interfacial energy, which leads to weak adhesion of other materials. Thus, after cutting the film into desired shapes and sizes using a sharp razor blade, the PEDOT:PSS layer supported on PVA could be simply pulled from the PDMS substrate using tweezers.

For the transfer of the PVA-supported PEDOT:PSS layer on the substrates needed for IRT, the setup shown in Figure 4.12 was used. It consists of a small glass container which holds a bath of deionized water in which a beveled block made of aluminum or PTFE is submerged. A syringe pump is connected to the water bath via PTFE tubes. After submerging the PVA-supported PEDOT:PSS layer in the water bath, the PVA began to dissolve while the PEDOT:PSS layer retained its shape and structural integrity. This allowed for the transfer of the PEDOT:PSS layer onto the metal substrates with the cavities. This was done by carefully agitating the free-standing PEDOT:PSS layer, such that it was located over the metal substrate, and then starting to drain out the water using the syringe pump. It was operated at a draining speed of 8 mL/min, in order to ensure slow enough drainage allowing for sufficient time to re-adjust the film. During the draining process, the film slowly set on top of the cavities. After careful removal of the block from the water bath, the substrate with the suspended film on top was slowly pushed to one edge of the block. After the substrate was removed from the block, the film was allowed to dry slowly in air, in order to avoid wrinkle formation, which could impede subsequent measurements. Afterwards, the obtained samples were subjected to IRT, UV-Vis spectroscopy and height profilometry.

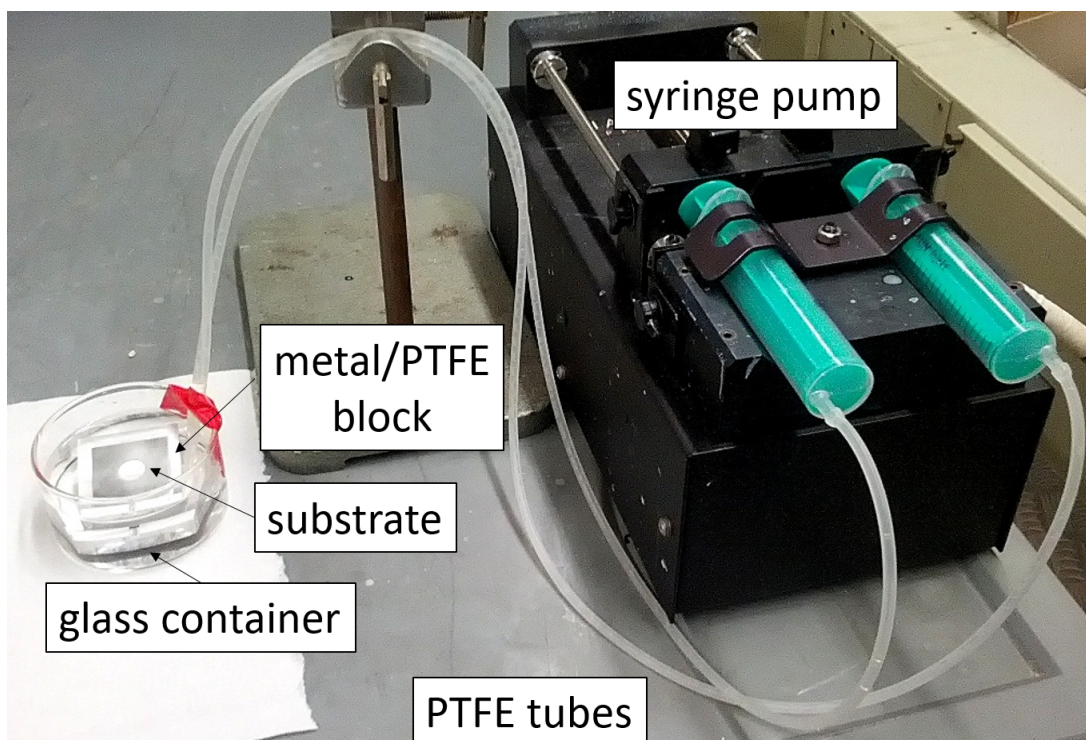


Figure 4.12: Setup for the transfer of the PVA-supported PEDOT:PSS onto the desired substrate for IRT measurements, comprising a glass container for the water bath, a beveled metal/PTFE block, PTFE tubes and a syringe pump.

4.2.4 P(NDI2OD-T2) thin films

This section deals with the fabrication of P(NDI2OD-T2) films, the results for which are discussed in Chapter 8 of this thesis. The preparation included the fabrication of doped P(NDI2OD-T2) films on glass and FTO-coated glass substrates in various geometries, allowing for the investigation of the thermoelectric properties in-plane, cross-plane and pseudo-in-plane, all of which can be seen in Figure 4.13. In order to avoid degradation of the doped P(NDI2OD-T2) in ambient atmosphere, all preparation steps including the preparation of the solutions, spin-coating and annealing steps were performed in a nitrogen-filled glovebox.

For the fabrication of samples in in-plane geometry (seen in Figure 4.13), glass was chosen as substrate. As shown in Figure 4.14, both the P(NDI2OD-T2) and N-DPBI were dissolved separately in DCB at a concentration of 10 mg/mL each. Both solutions were then stirred at 80 °C for 30 min. A hydrophobic PTFE filter (Rotilabo, Carl Roth GmbH Co. KG, Karlsruhe, Germany) with a pore size of 0.45 μm was used for removing larger particles from the polymer solution. The latter was then mixed with the dopant solution in order to obtain the desired dopant concentration. The mixture was again stirred at

80 °C for two hours. This step is crucial, as it induces the doping through activation of the dopant molecule, as will be discussed later. For the spin-coating 200 μL of solution was used, after which the samples were annealed at 140 °C. Aluminum electrodes were then evaporated with areas of 2 mm \cdot 15 mm at a distance of 10 mm. The defined area and distance of the electrodes ensured comparability of the measurements.

The deposition process for cross-plane samples was similar. However, the FTO substrates had to be pre-treated by etching the FTO coating away partially. It was removed through etching by applying zinc powder and hydrochloric acid on the respective areas on the sample using Q-tips, before the cleaning procedure described in Section 4.2.1. The etching, as well as the evaporation of the top aluminum electrode was done in such a way that the electrode areas were 18 mm \cdot 25 mm from opposite sides of the 25 mm \cdot 25 mm substrate. Thus, an overlap area between the top and bottom electrode was achieved. In addition, the outermost 7 mm of the aluminum layer did not have an FTO coating underneath, which prevented short-circuits upon contacting with the copper tips. The opposite is true for the side at which the FTO layed bare, since it was masked with PTFE tape prior to film deposition and electrode evaporation. The effective area in which the film is truly sandwiched between the electrodes amounted to 11 mm \cdot 25 mm, which can also be seen in Figure 4.13. The polymer was applied by preparing solutions with concentrations of 20 mg/mL and 10 mg/mL for the polymer and dopant, respectively, in order to achieve thicker films and decrease the risk of short-circuits. Prior to the spin-coating of the doped P(NDI2OD-T2) layer, the substrate was partially masked with PTFE tape. Annealing was carried out as pointed out above.

Samples in the pseudo-in-plane geometry, also seen in Figure 4.13, were prepared in a similar fashion to the cross-plane samples. The areas for the top and bottom electrodes were each chosen to be 10 mm \cdot 25 mm, while again having been placed at opposite edges of the 25 mm \cdot 25 mm substrate. This yielded an area of 5 mm \cdot 25 mm which was only

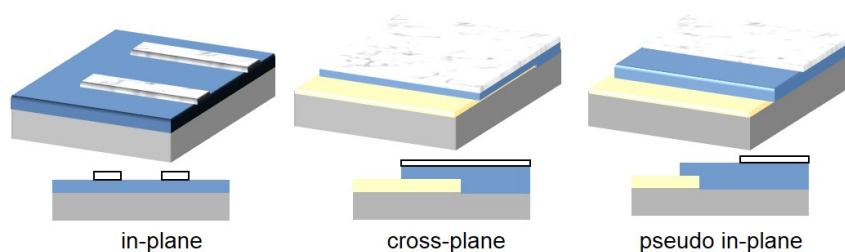


Figure 4.13: Schematics of three different sample geometries for determination of thermo-electric properties of doped P(NDI2OD-T2) thin films in angular and cross-section perspective. The exemplary samples consist of glass substrates (gray boxes), FTO-coatings (yellow boxes), P(NDI2OD-T2) films (blue boxes) and aluminum electrodes (white boxes).

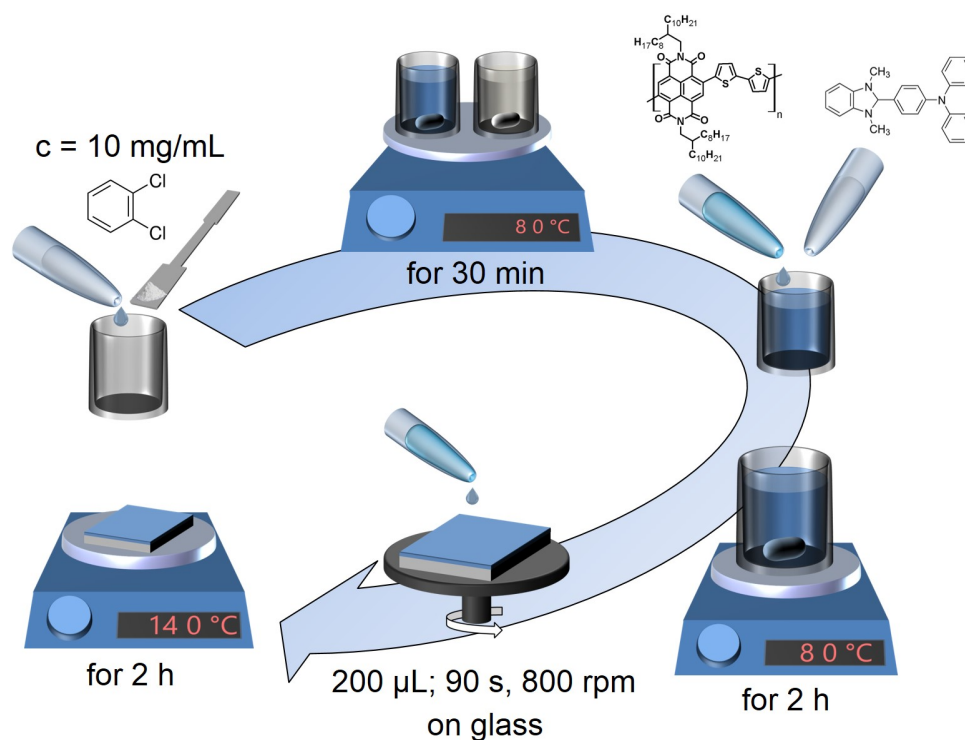


Figure 4.14: Scheme for the fabrication of P(NDI2OD-T2) films doped with N-DPBI. After dissolving polymer and dopant separately at elevated temperatures, they are combined at elevated temperatures in different ratios and spin-cast on substrates. A final annealing step is performed in order to induce crystallization.

covered by the polymer film. The lack of overlap between the top and bottom electrode led to the prevention of short-circuits. Charge transport in this geometry was expected to primarily occur in lateral direction, since macroscopic distances have to be covered as opposed to the film thickness in the range of nanometers. In general, the cleaning and film fabrication were performed as described above.

4.3 Thermoelectric generator based on conducting polymers as active materials

The investigation of P(NDI2OD-T2), led to its choice as potential candidate as n-type leg in a thermoelectric generator based on conducting polymers as active materials. Due to its favorable properties, which are discussed in Chapter 8, the pseudo-in-plane geometry was adopted for both N-DPBI-doped P(NDI2OD-T2) as n-type and EG-treated PEDOT:PSS as p-type leg. A schematic for the fabrication process is shown in Figure 4.15.

Firstly, a large sheet of FTO-coated glass was cut into substrates of $25\text{ mm} \cdot 50\text{ mm}$.

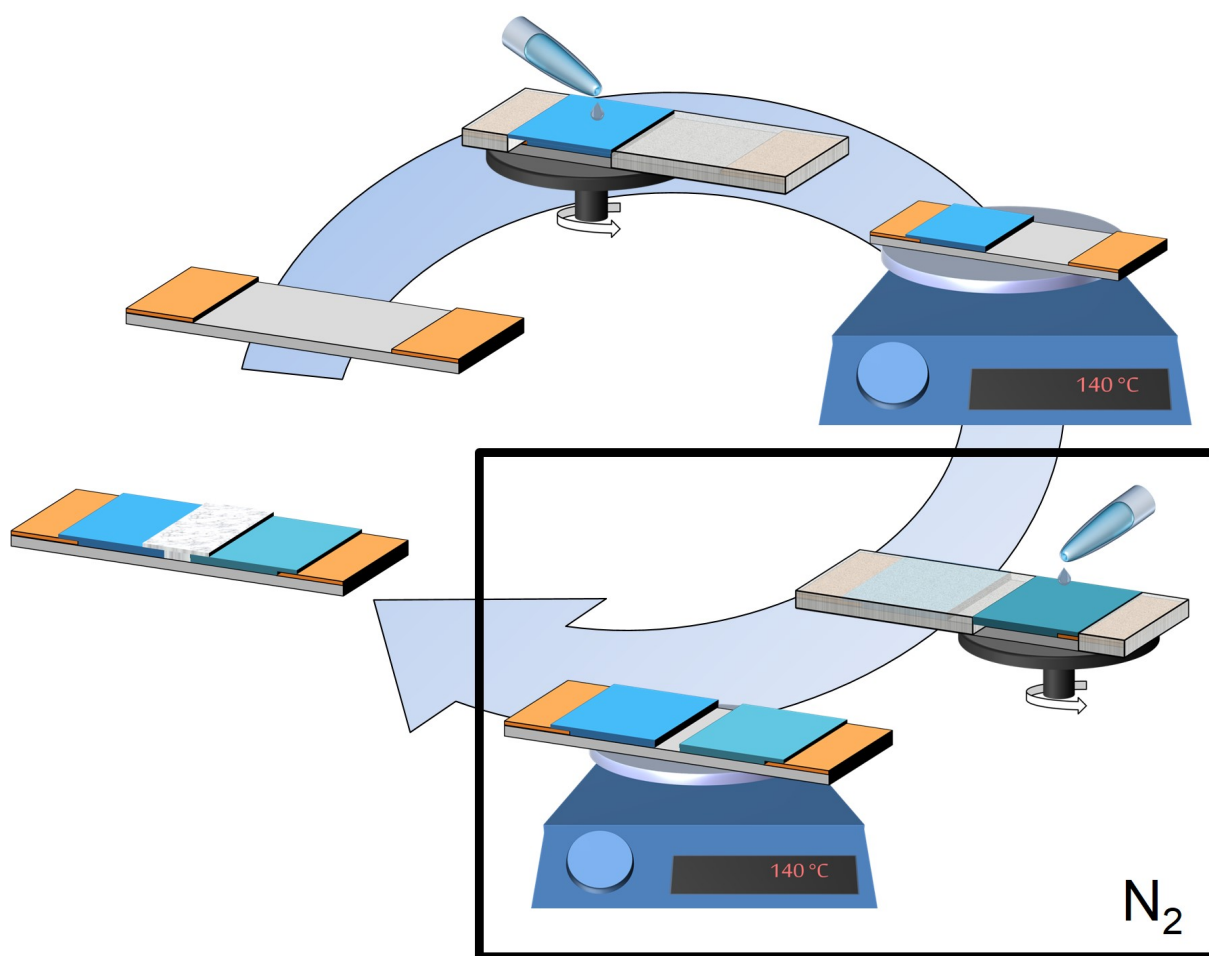


Figure 4.15: Schematic for the fabrication of a thermoelectric generator based on P(NDI2OD-T2) and PEDOT:PSS. Through selective masking with PTFE band, defined areas of the p-type and n-type legs can be achieved. After fabricating the p-type leg in ambient atmosphere, the substrates are transferred into a nitrogen-filled glovebox to fabricate the n-type leg. Both legs are electrically bridged by the aluminum top electrode in the center, while the FTO electrodes at both ends of the substrate are used for contacting during measurement.

Large parts of the FTO-coating were etched away, as described above, such that areas of 10 mm · 25 mm remained covered with FTO on both ends of the substrate. Through masking of the substrate with PTFE band, an area of 13 mm · 25 mm was firstly covered with PEDOT:PSS and subjected to annealing at 140 °C for 10 min. An overlap area of 3 mm · 25 mm with the bottom FTO electrode ensured electrical contactability. Post-treatment with EG was performed by again drop-casting 1 mL in two steps, as described above. After spin-coating at 1200 rpm for 60 s, annealing at 140 °C was again performed for 10 min. This then became the p-type leg of the generator. Before transfer into a nitrogen-filled glovebox, the PEDOT:PSS-covered part of the substrate was again masked with

PTFE band. P(NDI2OD-T2) films were fabricated in the same fashion as the samples in pseudo-in-plane geometry described above, leaving blank space in the center of the substrate. As a last step, the top aluminum electrode, with an area of $16\text{ mm} \cdot 25\text{ mm}$ was evaporated onto the center of the substrate, with an overlap area of $3\text{ mm} \cdot 25\text{ mm}$ with both legs. Thereby, a closed circuit could be obtained by contacting the FTO electrodes on both ends of the substrates.

5 Nanostructuring of PEDOT:PSS thin films with silicon nanoparticles for enhancement of thermoelectric properties

The article 'Morphology-Function Relationship of Thermoelectric Nanocomposite Films from PEDOT:PSS with Silicon Nanoparticles' (N. Saxena et al., Adv. Electron. Mat., 3, 1700181, 2017, DOI: 10.1002/aelm.201700181) is largely based on results shown in this chapter. [2]

The emergence of organic thermoelectrics in recent years is in large part owed to the decades of research which went into the synthesis and characterization of inorganic thermoelectric materials, which usually consist of elements such as bismuth, tellurium, silicon, germanium, selenium, sulfur, etc. [37] Up to the 1990s, it was believed that the highest achievable value for ZT would be close to 1, due to the interdependence of S , σ and κ to the charge carrier concentration, since experiments did not yield higher values. [38] The fact that theory did not pose such strict limits puzzled researchers and led to groundbreaking research by Hicks and Dresselhaus *et al.*, who found drastic changes in thermoelectric properties for lower dimensionalities of nanostructured Bi_2Te_3 . [1] They ascribed the found trends to changes in the density of states (DOS), and increase in the phonon surface scattering, while also highlighting the increase in ZT upon stronger confinement. This incentivized other approaches at optimizing ZT , which for the most part focused on decreasing the thermal conductivity. Due to the electronic contribution to the thermal conductivity being linked to the electrical conductivity via the Wiedemann-Franz law (see Equation 2.13), it is difficult to decouple it from the other thermoelectric quantities. In order to lower the lattice thermal conductivity of a system, it is necessary to introduce grain boundaries from which phonons can be scattered. This can be done in a top-down approach by e.g. ball-milling, or in a bottom-up approach through chemical synthesis of nanoparticles. Also methods like introduction of superstructures or heteroatoms seem

promising regarding increase of phonon scattering for reduction of the phonon contribution to the thermal conductivity. [37]

Drawing an analogy to organic thermoelectrics, preparing inorganic-organic composite thin films appears to be a viable solution. For example, Yee *et al.* synthesized hybrid tellurium nanowires assisted by PEDOT:PSS and prepared composites with PEDOT:PSS doped with EG and dimethyl sulfoxide (DMSO). [39] The combination of the intrinsically high Seebeck coefficient of tellurium, combined with an apparent increase in ordering of PEDOT chains in vicinity of the Te nanowires leading to improved electrical conductivities, ultimately yielded higher power factors of more than $100 \text{ W K}^{-2} \text{ m}^{-1}$. This idea was improved upon by Bae *et al.* through a simple treatment of the Te/PEDOT:PSS hybrid composite films with sulfuric acid. [40] The drastic increase in electrical conductivity up to 5000 S/cm therefore led to power factors of up to approximately $300 \text{ W K}^{-2} \text{ m}^{-1}$. Yan *et al.* took a different route in sandwiching post-treated, highly conductive PEDOT:PSS layers of different thicknesses in between aluminum electrodes. As an explanation for the increased Seebeck coefficients, the authors discussed phonon scattering at the metal/polymer interfaces through acoustic mismatch, even though in this specific case they did not make statements about potential changes in the electrical conductivity.

This part of the work deals first and foremost with the influence of Si-NPs on the thermoelectric properties of nanocomposite thin films with PEDOT:PSS. This hybrid nanostructuring approach is expected to yield a decrease of the phonon contribution to the thermal conductivity due to phonon scattering off of the Si-NPs. Two different fabrication routes for composite films are analyzed and evaluated using TOF-GISANS. In one instance, PEDOT:PSS and Si-NPs are deposited separately on a substrate in a layer-by-layer fashion, whereas in the other instance Si-NPs are mixed with the polymer solution prior to deposition. TOF-GISANS allows for the determination of lateral structures and for analysis of the composition by investigating the SLD profiles of the samples and comparing to theoretical values. After deciding on one fabrication route, PEDOT:PSS/Si-NPs composite films are characterized regarding their thermoelectric properties, including the thermal conductivity measured by IRT, in order to calculate the full figure of merit ZT. Additionally, GIR-TeXs is employed for the elucidation of structural changes upon introduction of different amounts Si-NPs and also for the discovery of a morphology-function relationship.

5.1 Selection of a fabrication route

Figure 5.1 compiles exemplary 2D TOF-GISANS scattering patterns for PEDOT:PSS/Si-NPs composite films prepared in the layer-by-layer and mixing approach, respectively.

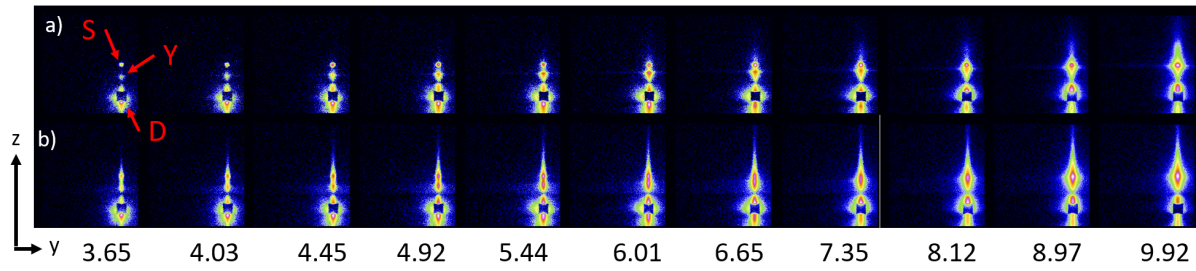


Figure 5.1: Selected 2D TOF-GISANS scattering patterns of PEDOT:PSS/Si-NPs composite films prepared by the a) layer-by-layer and b) mixing approach. Average wavelengths of the respective images are given below the scattering patterns in Angstrom. The specular peak (S), Yoneda peak (Y) and direct beam (D) covered by a beam stop are marked exemplarily.

For both approaches, the concentration of Si-NPs is set to 0.7 wt%. While the obtained scattering patterns clearly differ for both approaches, the Yoneda peak shifts in z -direction towards larger angles as function of wavelength. For the mixing approach, the Yoneda and specular peaks extend in z -direction irrespective of λ , hinting at an increased roughness of the sample.

Horizontal line cuts are extracted for both samples for the different wavelengths, in order to obtain information on the lateral structure. These are shown in Figure 5.2, together with the corresponding model curves. One of the main advantages of TOF-GISANS is the accessible q -range which shifts towards lower values with increasing wavelength. This is accounted for in the modeling of the scattering curves. The model includes three distinct families of spherical structures which are arranged in a one-dimensional paracrystalline lattice. Parameters such as the average sizes of objects and their average center-to-center distances with the respective distributions are chosen in a way that for a single sample all the scattering curves can be modeled with a single set of parameters. Variations in the intensity are to be expected as the neutron flux is different for different wavelengths. Qualitatively, the curves for the two samples differ in their shape, hinting at changes in the morphology due to the different fabrication routes.

As mentioned above, after modeling of the scattering curves, structural parameters of the two samples can be extracted and compared, the results for which can be seen in Figure 5.3. The notion that preparation of the samples by different fabrication routes leads to a different morphology is evident from close investigation of the parameters. For the sample prepared in the layer-by-layer approach, the radii of the spherical structures are 180 nm, 100 nm and 60 nm, representing large, medium and small structures, respectively. The mixing approach yields in general spherical structures with smaller radii, namely 150 nm, 80 nm and 10 nm. Another aspect is the center-to-center distance of the spherical structures, which is represented by the structure factor in Figure 5.3b. In the layer-by-

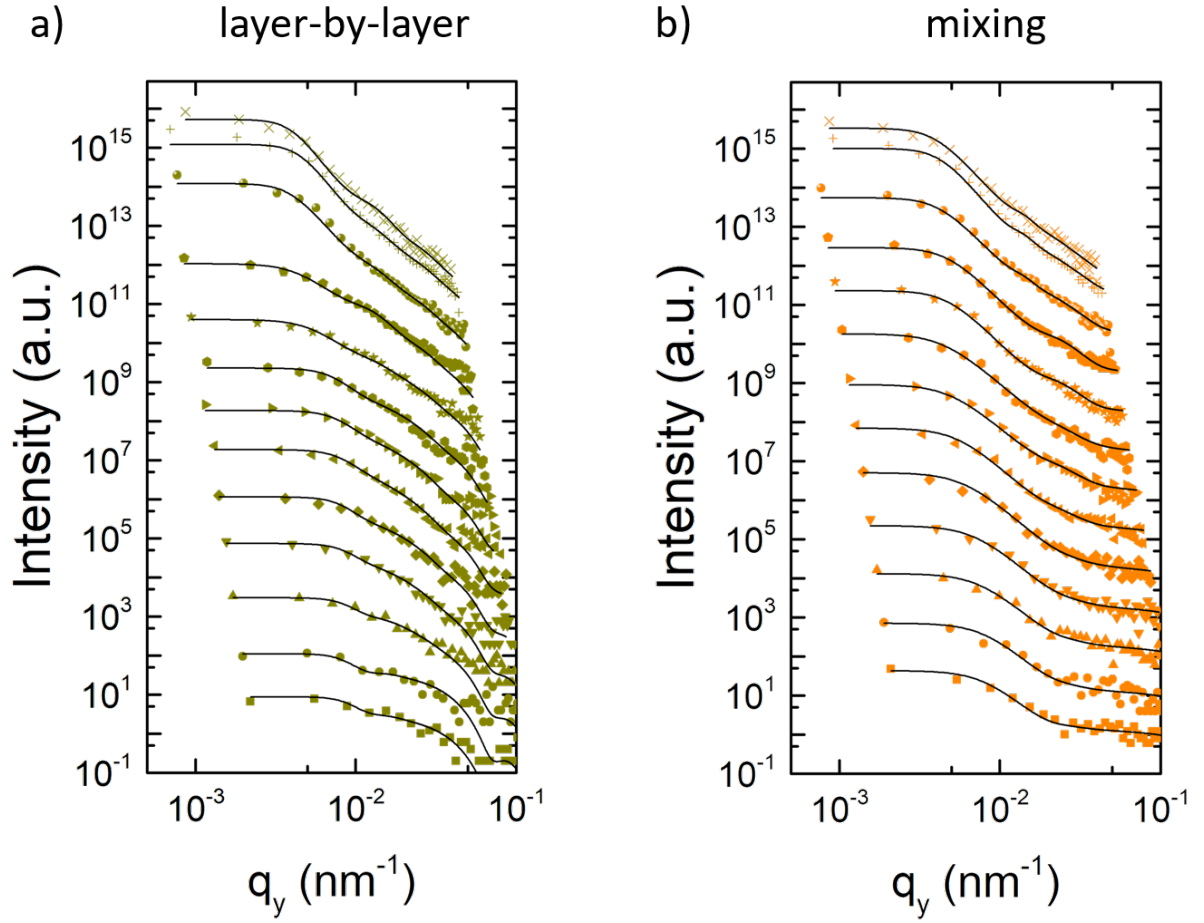


Figure 5.2: Horizontal line cuts for PEDOT:PSS/Si-NPs composite films prepared in a) layer-by-layer (dark yellow) and b) mixing (orange) approach. Modeled curves are shown in black. The curves are stacked vertically for clarity of presentation, with increasing wavelength. For each sample one set of structural parameters was found, with which the scattering curves could be modeled.

layer case, the values are 370 nm, 300 nm and 250 nm, whereas the mixing approach yields values of 400 nm, 200 nm and 150 nm.

The spherical structures can be discussed in terms of radius distributions and the number of domains. The size distributions for both preparation procedures are shown in Figure 5.4. It represents the distribution of domains as function of size, whereas the amplitude for a given domain size represents the corresponding number of domains of that specific size. The relation between the size of a domain, the scattering intensity and the number of domains can be understood when referring to Equations 2.25 and 2.26. Therewith, it can be seen that the scattering intensity is proportional to both the volume of a domain or the number of domains with a given size. Consequently, by extracting the

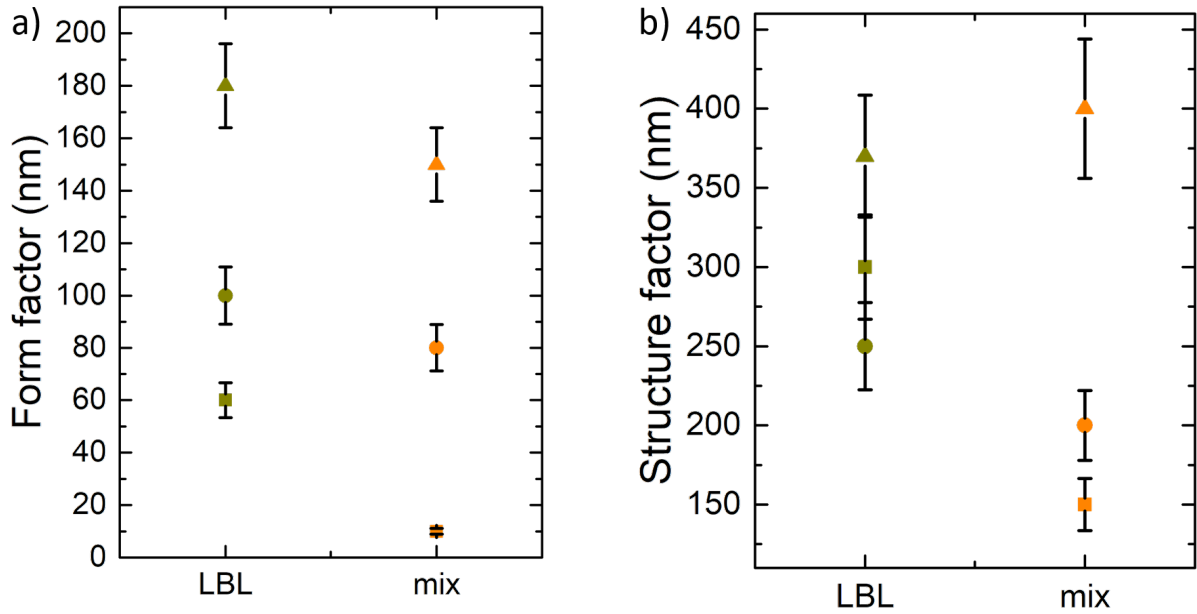


Figure 5.3: a) Structure radii and b) structure distances obtained from horizontal line cuts of TOF-GISANS measurements for PEDOT:PSS/Si-NPs composite films prepared in a layer-by-layer (LBL, dark yellow) and mixing (mix, orange) approach. Three distinct structural families were included in the modeling, referred to as large (triangles), medium (circles) and small (square) structures.

scattering intensity for each contribution from the model and dividing by the volume of the domain, the number of domains can be obtained.

Upon closer investigation of Figure 5.3, one can then immediately understand the large number of small domains obtained with the mixing approach. In order to compensate for the small scattering volume, a large number of small domains is required to achieve a certain scattering intensity. This also explains the decreasing amplitude observed for the medium and large structures, as in those cases the relatively larger scattering volume leads to a larger scattering intensity. In general, the notion that the layer-by-layer approach yields overall larger structures, as is also shown in Figure 5.3a, is also evident here. When regarding the morphology of PEDOT:PSS/Si-NPs composite films in terms of their potential thermoelectric capabilities, the former is deemed more favorable the larger the domains are. PEDOT:PSS is known to phase-separate upon deposition on a substrate, yielding PEDOT-rich domains with thin PSS-rich shells. [41] The PSS-shell presents a barrier for charge-transport, making the reduced surface area through increased domain sizes obtained from the layer-by-layer approach more promising with respect to charge transport within the film.

TOF-GISANS offers two distinct advantages compared to x-ray scattering. Firstly, the

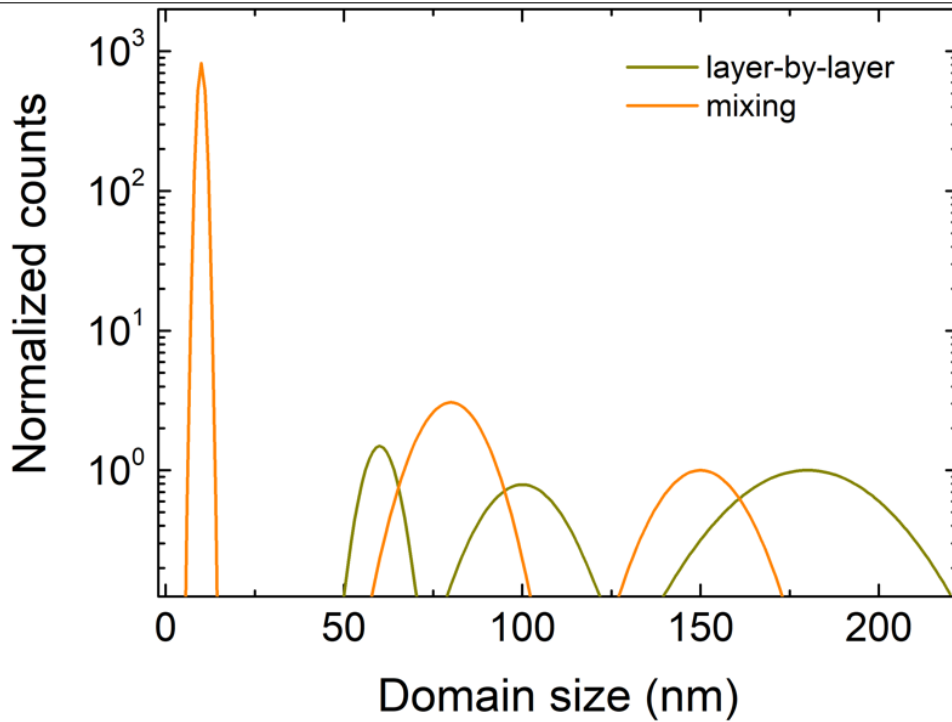


Figure 5.4: Analysis of domain size distribution for PEDOT:PSS/Si-NPs composite films prepared in a layer-by-layer (dark yellow) and mixing (orange) approach. The values are normalized to those of the respective large domain radii, obtained from the analysis of horizontal cuts of the TOF-GISANS measurements.

direct proportionality of the critical angle to the neutron wavelength and, more importantly, secondly, the ability of performing the measurement in the time-of-flight mode. The latter allows for collection of scattering patterns originating from different neutron wavelengths in a single measurement. By monitoring the position of the Yoneda peak in the vertical cuts seen in Figure 5.5a and 5.5b, correcting for the incident angle and plotting it as function of wavelength, a linear fit can be performed, as is done in Figure 5.5c. From the slope the SLD can be extracted according to Equation 3.19, which gives insight into the chemical composition of the probed samples. An increased SLD of $1.80 \cdot 10^{-6} \text{ \AA}^{-2}$ is obtained for the PEDOT:PSS/Si-NPs composite prepared in the layer-by-layer approach, compared to $1.42 \cdot 10^{-6} \text{ \AA}^{-2}$ for the mixing approach. With the knowledge of the SLD for each of the film components, namely PEDOT, PSS and the Si-NPs, the obtained SLD values can be put into perspective.

In comparison to the reference values for each component given in Table 5.1, one can observe that the SLD value obtained for layer-by-layer sample is significantly larger than the one for pure PEDOT. On the other hand, the SLD value for sample prepared in the mixing approach closely resembles that of pure PSS. Two possible conclusions can

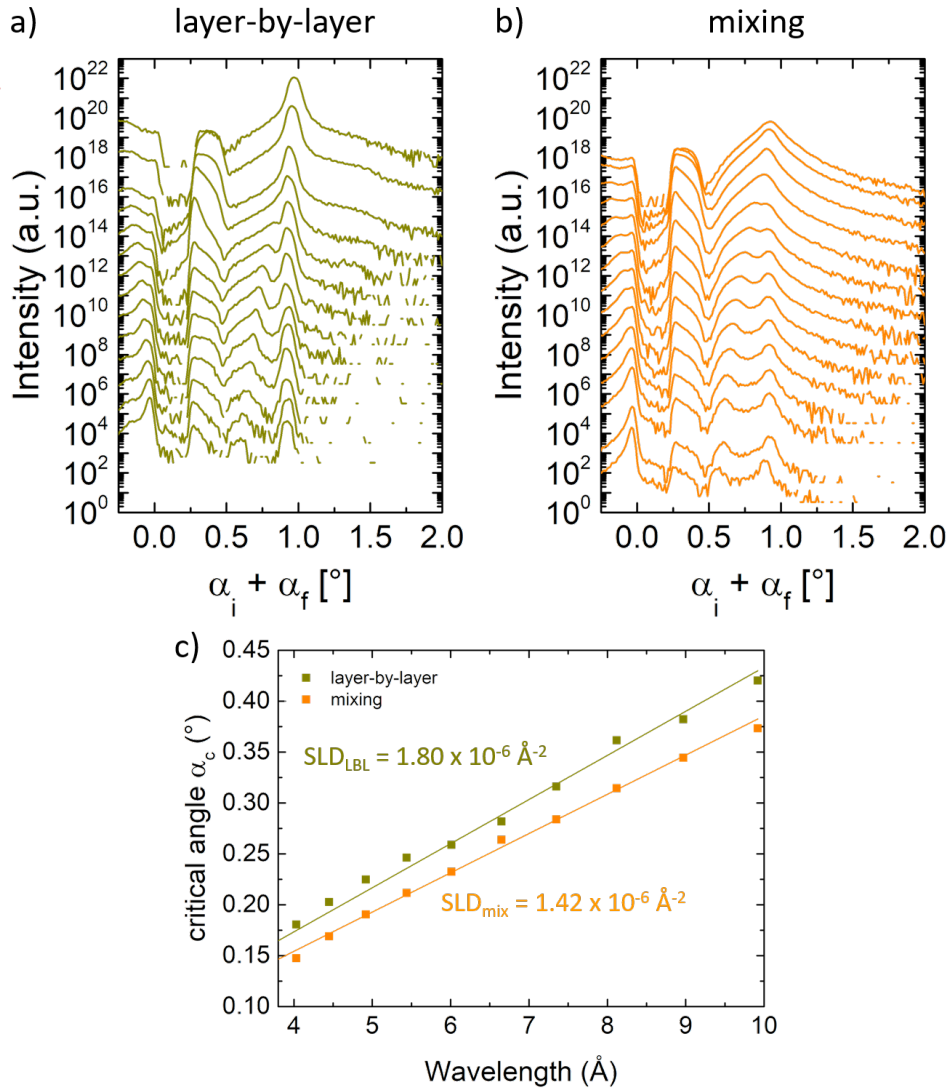


Figure 5.5: Vertical line cuts extracted from 2D TOF-GISANS data of for different wavelengths, shown for PEDOT:PSS/Si-NPs composite films in the a) the layer-by-layer and b) mixing approach. c) Critical angle values α_c as function of neutron wavelength for PEDOT:PSS/Si-NPs prepared in a layer-by-layer (dark yellow) and mixing (orange) approach. The critical angle values are corrected for the incident angles, also taking gravity effects into account. Solid lines in the respective colors are linear fits from which the SLD can be calculated. Extracted values obtained from the slopes of the linear fits are given additionally.

be drawn from this. Firstly, the inclusion of Si-NPs into the composite film appears to be more efficient in the layer-by-layer approach than for the mixing approach, as the SLD of the Si-NPs is larger than for pure PEDOT, thus leading to an increased overall SLD for the composite. Nominally, the same amount of Si-NPs was employed for both fabrication routes, which hints at differences in the film formation. This most

Table 5.1: SLD values for PEDOT, PSS and Si.

material	SLD (\AA^{-2})
PEDOT	$1.71 \cdot 10^{-6}$
PSS	$1.42 \cdot 10^{-6}$
Si	$2.07 \cdot 10^{-6}$
H ₂ O	$-5.61 \cdot 10^{-6}$

likely originates from the nature of the Si-NPs, which are known and expected to carry a silicon oxide shell in ambient atmosphere. [42] The rather hydrophobic nature of the Si-NPs, requires a more organic solvent like ethanol, in order for them to fully disperse and prevent aggregation. Upon introduction into the aqueous PEDOT:PSS solution, it is conceivable that they aggregate and subsequently cannot be processed properly anymore. This was also observed from visual inspection of the solution after introduction of Si-NPs, which showed signs of aggregation. In the layer-by-layer approach, this problem is circumvented, since the Si-NPs do not come in contact with the aqueous solvent, but are instead deposited on annealed PEDOT:PSS.

A possible explanation for the drastically lower SLD obtained for the sample prepared in the mixing approach can be given, considering the ability of the PSS-component of PEDOT:PSS films to absorb water from the atmosphere, leading to subsequent swelling. [43] As both the sample preparation and the TOF-GISANS measurements were performed in ambient atmosphere, a certain degree of swelling and thus presence of water in the composite films is to be expected. The negative SLD of light water (H₂O) of $-5.61 \cdot 10^{-6} \text{\AA}^{-2}$ would thus lead to a decrease of the SLD of both samples, with the case of the mixing approach being more severe due to the less efficient inclusion of Si-NPs.

Thus it can be concluded that, from a structural point of view, the layer-by-layer route for the fabrication of PEDOT:PSS/Si-NPs composite films is superior to the mixing approach. TOF-GISANS revealed a more favorable morphology due to larger domains obtained in the layer-by-layer fabrication, as well as a more efficient inclusion of Si-NPs into the film due to prevention of aggregation. Therefore, the layer-by-layer fabrication will be used in the following for the investigation of changes in thermoelectric properties as function of Si-NPs concentration.

5.2 Thermoelectric properties of composite PEDOT:PSS/Si-NPs thin films

In the following, changes in the Seebeck coefficient, electrical conductivity and power factor as function of Si-NPs concentration will be discussed. In addition, IRT is used to measure the thermal conductivity of free-standing PEDOT:PSS thin films and also to determine changes upon introduction of Si-NPs.

5.2.1 Influence of Si-NPs on power factor

Figure 5.6a shows the evolution of Seebeck coefficient as function of Si-NPs concentration. From the reference value of PEDOT:PSS only post-treated with EG of approximately 15.3 V/K, an increase is observed with increasing amount of Si-NPs in the film, yielding a maximum value of 24.3 V/K for 0.5 wt% Si-NPs, only to slightly drop to 23.4 V/K for the highest concentration. Since the exact mechanism of Seebeck coefficient enhancement is still elusive at this point, two possible explanations will be given in the following.

Introduction of the Si-NPs could lead to a disruption of the intermolecular order of PEDOT chains or the polymer matrix in general and thus impede charge transport between chains. This may result in increased Seebeck coefficients, which is in line with what was observed for nanostructured inorganic thermoelectric (TE) materials. Low-energy carrier scattering at interfaces, grain-boundaries or impurities (generally denoted as energy-filtering) is deemed responsible for the enhancement in those cases. A similar mechanism could be at work in the case of the ternary composite.

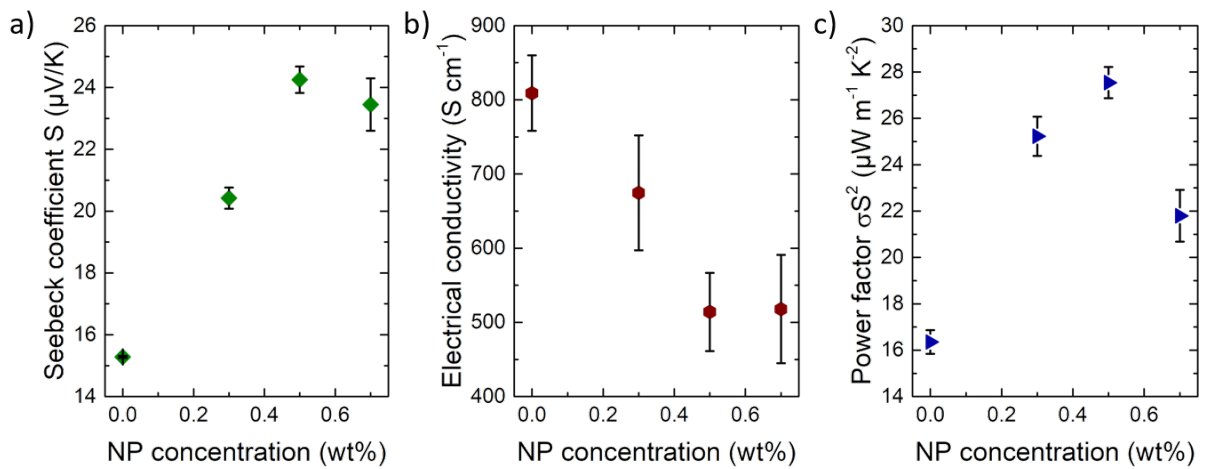


Figure 5.6: a) Seebeck coefficient, b) electrical conductivity and c) power factor of PEDOT:PSS thin films as function of Si-NP concentration. Adapted from [2].

Another feasible explanation for the increase could be given assuming a non-negligible Seebeck coefficient of the Si-NPs themselves. It is conceivable that they are subjected to the temperature gradient themselves and generate an electrical potential accordingly which simply adds to the one of the PEDOT:PSS. This can explain the increase up to concentrations of 0.5 wt% . However, the slight drop in Seebeck coefficient for concentrations of 0.7 wt% would then have to be explained in terms of size changes of nanoparticle clusters. As Chen *et al.* found, the Seebeck coefficient of particles is inversely correlated to their respective size. [44] Drawing an analogy to the present case, this suggests aggregation of Si-NPs which would lead to increased effective sizes and therefore to lower intrinsic Seebeck coefficients.

While both approaches at understanding the effects are reasonable, the discovery of the true enhancement mechanism is subject to further investigation.

Nevertheless, the introduction of Si-NPs the polymer films appears to also have implications on the electrical conductivity, as can be seen in Figure 5.6b. Increasing concentrations of Si-NPs have an adverse effect on the electrical conductivity, since it decreases from 809 S/cm for the reference film without Si-NPs to 517 S/cm for the highest concentration. This is easily understood, considering that the single-crystalline Si-NPs carry an insulating shell of silicon dioxide of few nanometers thickness. [34] The notion that they thusly do not contribute to the conductivity of the composite film, but instead disturb the semicrystalline order of the PEDOT:PSS matrix is also supported by the first explanation given above for the enhancement of the Seebeck coefficient. The incorporation of Si-NPs would hinder charge transport most likely between or within conducting, PEDOT-rich domains, which is macroscopically measured as drop in electrical conductivity.

Combining both the Seebeck coefficient and the electrical conductivity, the power factor σS^2 can be calculated, as shown in Figure 5.6c. The steady increase from values of $16.4 \text{ WK}^{-2} \text{ m}^{-1}$ for the reference up to $27.6 \text{ WK}^{-2} \text{ m}^{-1}$ for 0.5 wt% Si-NPs concentration is for the most part governed by the changes in the Seebeck coefficient. The drop which was seen for the latter at Si-NPs concentrations of 0.7 wt% is even more prominent for the power factor, due to its square dependence on the Seebeck coefficient. For that specific sample a power factor of $21.8 \text{ WK}^{-2} \text{ m}^{-1}$ is obtained.

In summary, Si-NPs can be used to enhance the TE capabilities of PEDOT:PSS beyond either of the constituents, mainly due to the increase in Seebeck coefficient which most likely stems from the semiconducting nature of the Si-NPs themselves. At an optimal concentration of 0.5 wt%, the power factor is roughly improved by a factor of 1.3. As a next step, IRT is used in order to measure the thermal conductivity of PEDOT:PSS as function of Si-NPs concentration.

5.2.2 Measurement of thermal conductivity: Infrared thermography

Many techniques for the measurement of thermal conductivities exist, such as TDTR, the 3ω -method, etc. [45,46] However, they often pose strict constraints on sample geometries or their film properties such as low roughness, etc. Especially for TDTR, a thin metal layer has to be fabricated on top of the film by lithography, potentially altering the latter's structure. [47] Additionally, the films have to be suspended on a substrate, which might affect the measured thermal conductivity due to its large thickness discrepancy to the film to be investigated. IRT is a method which was co-developed in the framework of this thesis, and is thus the technique of choice. It allows for the contact-free measurement of the thermal conductivity on films which are suspended on steel substrates with small spherical cavities. On top of these cavities, the film is actually free-standing, therefore rendering the obtained values more accurate. Exemplary optical and infrared micrographs of a PEDOT:PSS films suspended on a steel substrate with spherical cavities are shown in Figure 5.7.

Exemplary infrared micrographs for the composite PEDOT:PSS/Si-NPs films with different concentrations of the latter are shown in Figure 5.8. For the discussion of the micrographs, it is useful to refer to the principle of IRT which is schematically shown in Figure 3.7. The free-standing sections of the suspended thin films are illuminated via a red light-emitting diode and subsequently thermally excited. Depending on their respective in-plane thermal conductivity, the heat is either dispersed through emission of infrared radiation or through heat conduction to the steel substrate, which acts as heat sink. The fact that qualitative differences between the different images can be discerned, is already

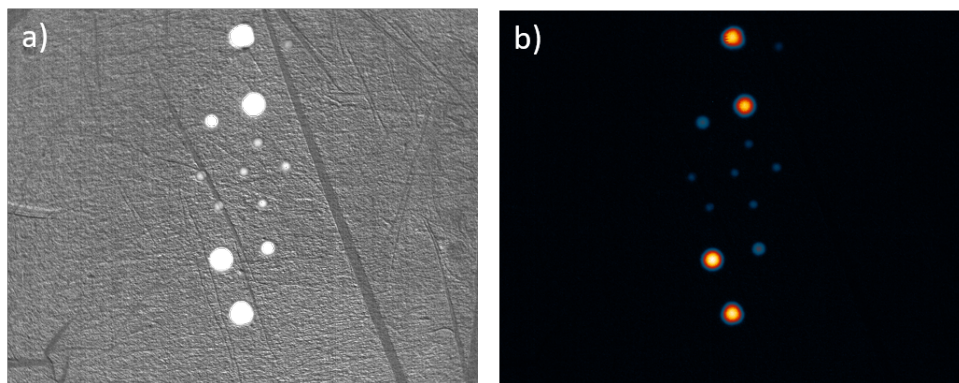


Figure 5.7: a) Optical micrograph of PEDOT:PSS film suspended on steel substrate with spherical cavities of different sizes. b) Infrared micrograph of film upon thermal excitation with visible light. Larger amplitudes of thermal radiation are represented by the transition from black to white.

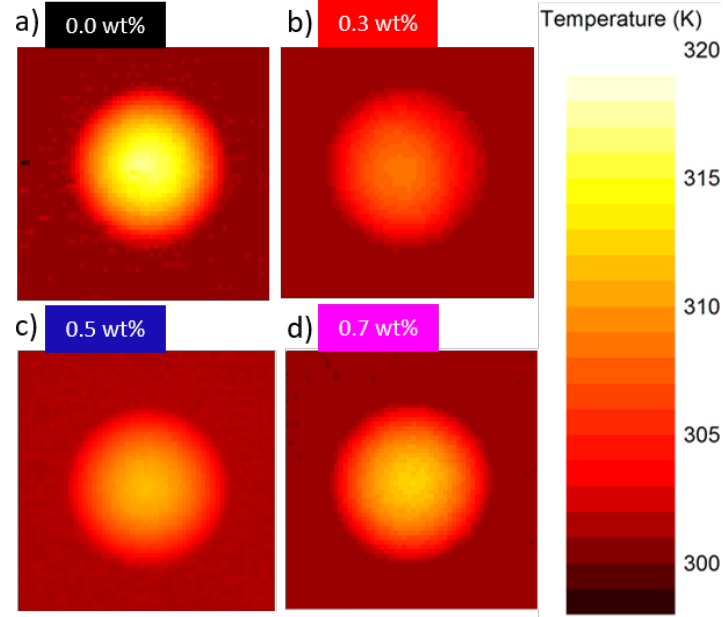


Figure 5.8: Infrared thermographs of PEDOT:PSS films a) without Si-NPs, b) 0.3 wt% Si-NPs, c) 0.5 wt% Si-NPs and d) 0.7 wt% Si-NPs suspended on a cavity of 0.3 mm diameter on a stainless steel holder and the corresponding temperature scale. Taken from [2].

a first indication that the thermal conduction properties are modified by the presence of the Si-NPs.

In decreasing order, the largest temperature increases are found for the reference sample without Si-NPs, followed by 0.7 wt%, 0.5 wt% and 0.3 wt%. This indicates a corresponding increase in the values for κ . With the correction for the film thickness d and the absorbed areal power density p_{abs} according to Equation 3.11, the thermal conductivity as function of Si-NPs can be obtained, the results for which are shown in Figure 5.9.

A thermal conductivity of approximately $1 \text{ Wm}^{-1}\text{K}^{-1}$ for PEDOT:PSS post-treated with EG fits well to the results of Wei *et al.* [48] Surprisingly, non-linear changes are observed with increasing Si-NPs amount. A maximum of $1.37 \text{ Wm}^{-1}\text{K}^{-1}$ is observed at 0.3 wt%, which subsequently drops again to $0.97 \text{ Wm}^{-1}\text{K}^{-1}$ for the highest concentration of 0.7 wt%. This unexpected behavior will be explained below, in the discussion of morphology changes deduced from SEM and GIR-TeXS.

5.2.3 Calculation of full figure of merit ZT

Nevertheless, with the measurement of all relevant thermoelectric quantities, namely Seebeck coefficient, electrical conductivity and thermal conductivity, as function of Si-NPs concentration, the full figure of merit ZT can be calculated. It can be seen in Figure 5.10.

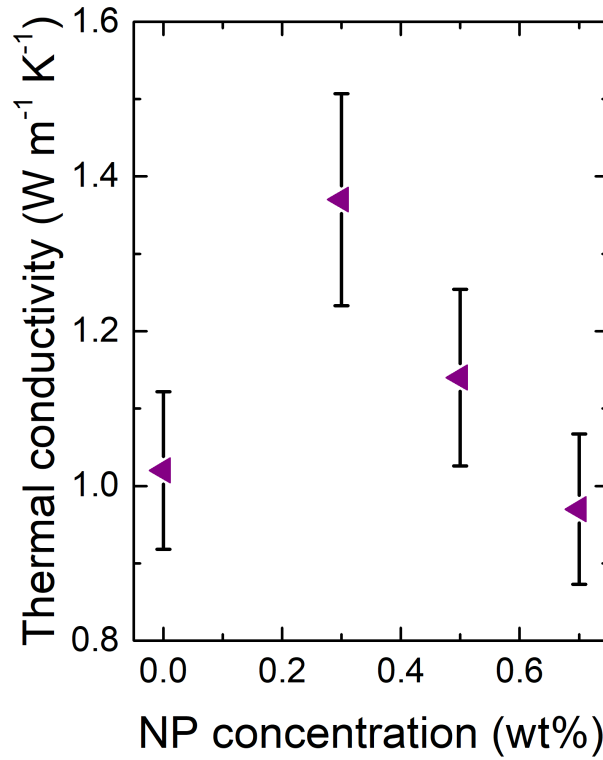


Figure 5.9: Thermal conductivity of PEDOT:PSS films as function of Si-NP concentration, as determined from IRT.

The increasing trend of ZT follows for the most part that of the Seebeck coefficient with increasing Si-NPs concentration. While for the reference film without Si-NPs a ZT value of roughly 0.005 is achieved, the maximum value of 0.008 is found for a Si-NPs concentration of 0.5 wt%. The subsequent slight drop can be explained with the drop in the Seebeck coefficient, which enters into Equation 2.7 squared. It can be concluded that the enhancement of ZT originates from a combination of different factors. Firstly, the Seebeck coefficient is enhanced up to intermediate concentrations. Secondly, while the introduction of Si-NPs with their insulating oxide shell is detrimental to the overall electrical conductivity of the films, it is still sufficiently high. Thirdly, even though the thermal conductivity increases for low amounts of Si-NPs, further addition yields values close to that of the reference film. The improvement of ZT by a factor of roughly 1.5 renders the hybrid nanostructuring approach feasible regarding improvement of thermoelectric properties, especially since IRT is a viable method for measuring and understanding potential implications thereof on the thermal conductivity.

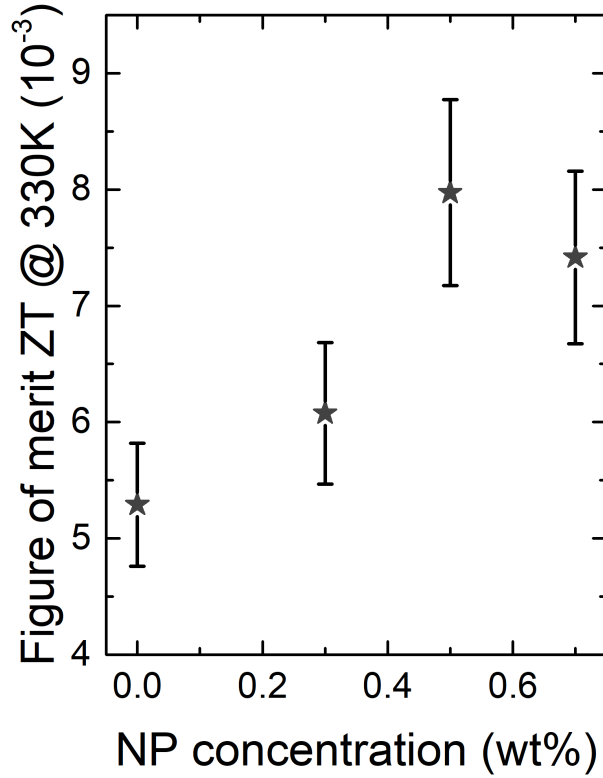


Figure 5.10: Full figure of merit ZT of PEDOT:PSS films with varying concentrations of Si-NPs, calculated for an average temperature of 330 K. Adapted from [2].

5.3 Morphological properties of composite PEDOT:PSS/Si-NPs thin films

After establishing the feasibility of the nanostructuring approach of PEDOT:PSS with Si-NPs, the next step is to understand how the presence of the latter affects the morphology of the composite films and if a link to the observed thermoelectric properties can be found. For this purpose, SEM is used as a real-space technique to investigate the surface structure of the composite films. Additionally, the bulk structure of the ternary composite films is studied with GIR-TeXS. As will be discussed below, GIR-TeXS offers a range of advantages over a classical GISAXS experiment regarding the ability to assign structural features to the different components.

5.3.1 Real-space morphology: scanning electron microscopy

Electron micrographs of the PEDOT:PSS/Si-NPs composite films are shown in Figure 5.11 as function of nanoparticle concentration. For the reference PEDOT:PSS film shown in Figure 5.11a, features with both high and low intensity can be seen in the micrograph.

These correspond to PEDOT and PSS, respectively, as they exhibit different electrical conductivities. Upon increase of the Si-NPs concentration to 0.3 wt%, larger structures emerge. Notably, no individual Si-NPs are visible, even though they should be resolvable with their sizes in the range of 30 nm. This might originate from the preparation of the composite films outlined in Section 4.2.2. Alternating deposition of PEDOT:PSS and Si-NPs may lead to burying of the latter beneath a polymer layer, explaining why they cannot be seen in the top-view electron micrographs. Even for concentrations up to 0.7 wt%, no Si-NPs can be discerned.

This notion is supported when looking at the radial power spectral densities (RPSDs) shown in Figure 5.12. Compared to the PEDOT:PSS film without Si-NPs, all other samples show an increased RPSD intensity at small q -values which indicates morphological rearrangement due to the emergence of larger structures, which is induced by the introduction of Si-NPs. Notably, the intensity at small q -values is largest for concentrations of 0.3 wt% and 0.7 wt%, which also exhibit large structures in the micrographs. It can thus be concluded that SEM by itself is insufficient to understand the structural impact of the Si-NPs. In the following, the analysis of GIR-TeXs data will shed light on changes in the bulk morphology of the PEDOT:PSS/Si-NPs films.

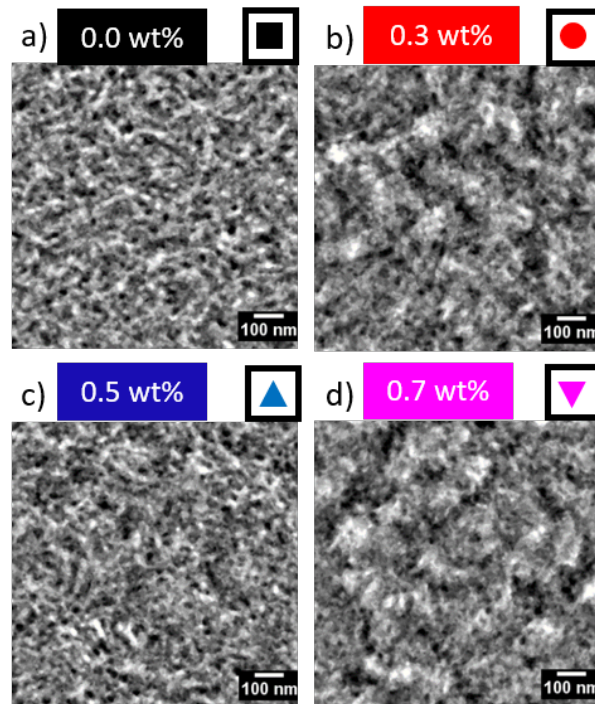


Figure 5.11: Scanning electron micrographs of PEDOT:PSS films a) without Si-NPs, b) 0.3 wt% Si-NPs, c) 0.5 wt% Si-NPs and d) 0.7 wt% Si-NPs. Taken from [2].

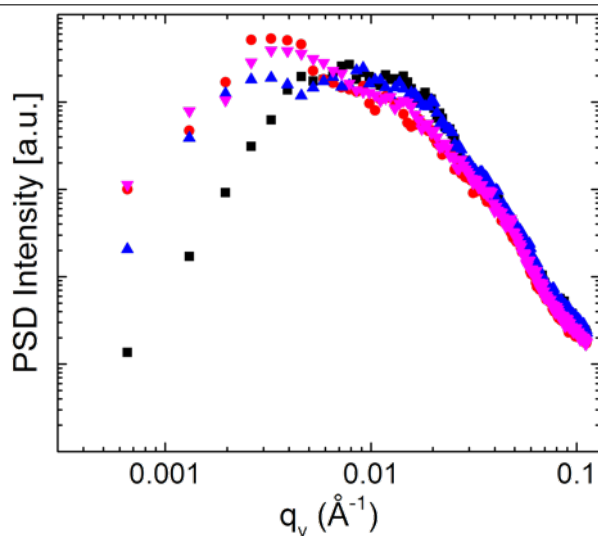


Figure 5.12: Radial power spectral density curves extracted from 2D fast Fourier transform images, obtained from scanning electron micrographs of PEDOT:PSS films without Si-NPs (black), 0.3 wt% Si-NPs (red), 0.5 wt% Si-NPs (blue) and 0.7 wt% Si-NPs (magenta). Taken from [2].

5.3.2 Grazing-incidence resonant tender x-ray scattering

The discussion of the GIR-TeXS data for the elucidation of the structure of PEDOT:PSS/Si-NPs films will follow the workflow layed out in Section 3.3.3. It is therefore divided into discussion of NEXAFS data, the modeling of horizontal line cuts from the 2D scattering patterns, calculation of the energy-dependent scattering contrast and lastly the elucidation of a morphological model and its correlation to thermoelectric properties.

Near-edge x-ray absorption fine structure (NEXAFS): calculation of β and δ

As mentioned above, the strength of GIR-TeXS is its ability to distinguish components of similar electron density by employing incident x-ray energies which match core electron transitions of constituent atomic species. In this case, measurements are performed at the sulfur K-edge, located at approximately 2473 eV. [49] The high sensitivity for chemical shift of a NEXAFS measurement makes it possible to distinguish the main polymeric components PEDOT and PSS. As can be seen in Figure 2.3, both parts of the blend are sulfur-containing. However, in the case of PEDOT the sulfur is bound within the thiophene group, while in PSS it is surrounded by three oxygen atoms. Despite the similar chemical composition, their absorption behavior at the sulfur K-edge is expected to differ according to the atomic configuration. In contrast, the Si-NPs are not expected to show any non-linearities in their optical behavior, as they do not contain sulfur. NEXAFS

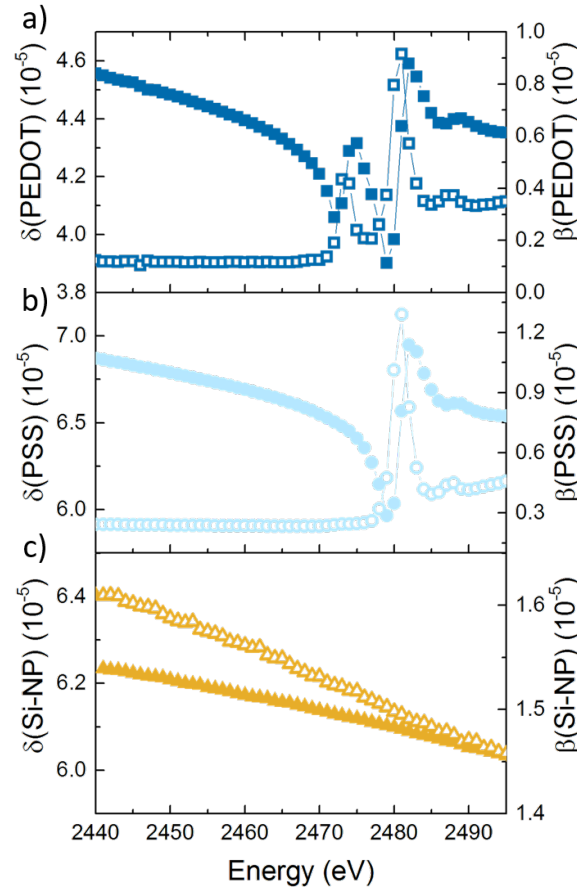


Figure 5.13: Real part δ (solid symbols) and imaginary part β (hollow symbols) of refractive index for a) PEDOT, b) PSS and c) Si-NPs, as determined from NEXAFS measurements at the sulfur K-edge and using the Kramers-Kronig relations. Taken from [2].

measurements are performed on the three individual components as described in Section 3.2.4, in order to extract values for the imaginary part of the refractive index β , as function of energy. In turn, the latter can be used to calculate the corresponding values for the real part of the refractive index δ using the Kramers-Kronig relations shown in Equations 2.29 and 2.30.

In a NEXAFS measurement, the mass absorption coefficient is obtained, which gives insight into the fine structure of a material close to a core electron resonance. The *Henke* database lists atomic scattering form factors f , which then allows for calculation of optical properties according to Equation 2.20. However, the fine structures strongly differ from molecule to molecule, and thus have to be measured separately. Similarly to a UV-Vis measurement, the energy of the x-ray beam incident on the sample is tuned, while simultaneously detecting the absorbed fraction of light. β is then calculated using Equation 3.16. The latter can be transformed into the imaginary part of the refractive

index n β with Equation 2.28. The Kramers-Kronig relations in Equations 2.29 and 2.30 link β to the real part of the refractive index δ , which is not easily measurable. In this case, the freely available software package *KKcalc* is used for the calculation of δ .

The obtained spectra are shown in Figure 5.13. Drastic differences in the spectra for the different components can be seen immediately. Most significantly, PEDOT exhibits a strong absorption peak located very close to the sulfur K-edge in both the curves for δ and β , as seen in Figure 5.13. This signal originates from the resonance of the x-ray beam with the thiophene sulfur found in PEDOT. In contrast, PSS shows no such non-linearities close to the sulfur K-edge. Instead, a strong signal is located at roughly 2480 eV, and thus not covered by the GIR-TeXs measurements. Most likely, this can be assigned to the sulfur found in the sulfonate group, surrounded by three oxygen atoms. As expected, the Si-NPs show no non-linearities in their optical response, due to the absence of sulfur. However, the order of magnitude for the δ - and β -values is still comparable to that found for PEDOT and PSS.

From the obtained values for δ and β as function of energy, the scattering contrast can be inferred according to Equation 2.31.

Grazing-incidence small-angle scattering (GISAXS): lateral structure

As described in Section 2.3.1, 2D GISAXS patterns can be analyzed in two different ways. A vertical line cut contains information on the existing chemical components in the investigated material, which can be differentiated with their respective critical angles, in addition to vertical correlation. A horizontal line cut on the other hand contains information on the presence of mesoscopic structures and their lateral correlation, i.e. their arrangement in the plane of the substrate. The sizes and shapes of structures, as well as their arrangement are extracted from the horizontal cuts through modeling in the framework of the DWBA.

PEDOT:PSS/Si-NPs composite films with different concentrations of Si-NPs are investigated with GIR-TeXs. This is done by recording 2D GISAXS patterns for six different incident beam energies, namely 2465 eV as 'off-resonance' and in the range from 2471 eV to 2475 eV as 'on-resonance' energies. The extracted horizontal line cuts shown in Figure 5.14, have to be treated in a certain way for GIR-TeXs measurements. For a single sample, it should be possible to model all horizontal cuts with the same set of parameters, as changes in the structure cannot be expected due to the minute changes in the beam energies used herein. This was done for all four samples, which were all measured at the six aforementioned energies.

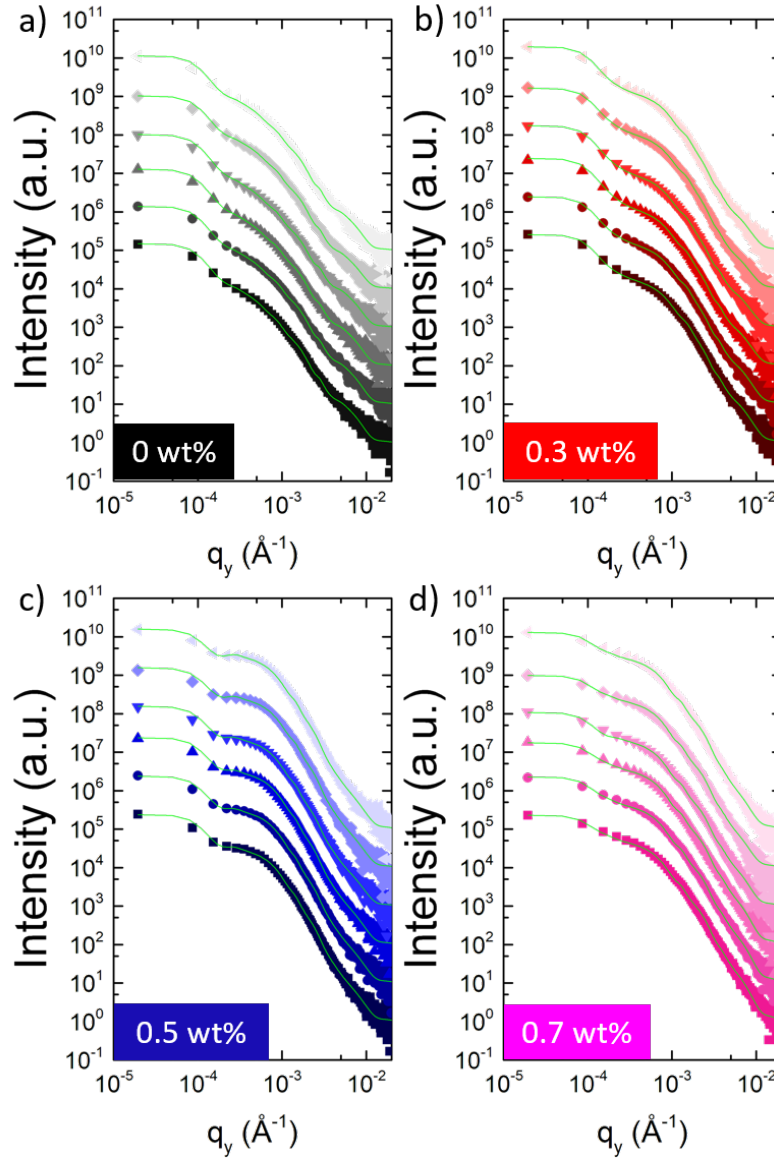


Figure 5.14: Energy series of horizontal line cuts for PEDOT:PSS/Si-NPs composite films. a) 0 wt% Si-NPs, b) 0.3 wt% Si-NPs, c) 0.5 wt% Si-NPs and d) 0.7 wt% Si-NPs. Color gradients from dark to bright indicate increasing energy, starting at the 'off-resonance' energy 2465 eV and increasing to the 'on-resonance' energies from 2471 eV to 2475 eV. Modeled curves are shown in green on top of the corresponding data. The horizontal line cuts and modeled curves are stacked vertically for clarity.

Qualitatively, changes in the line cuts can be discerned as function of Si-NPs concentration, which already hint at the structural impact of the Si-NPs. Especially at q -values close to $5 \cdot 10^{-4} \text{ \AA}^{-1}$, the scattering intensity increases up to Si-NPs concentrations of 0.5 wt%. This is also evident from the structural parameters seen in Figure 5.15 which were used for modeling of the curves. Basically, the composite thin films can be described

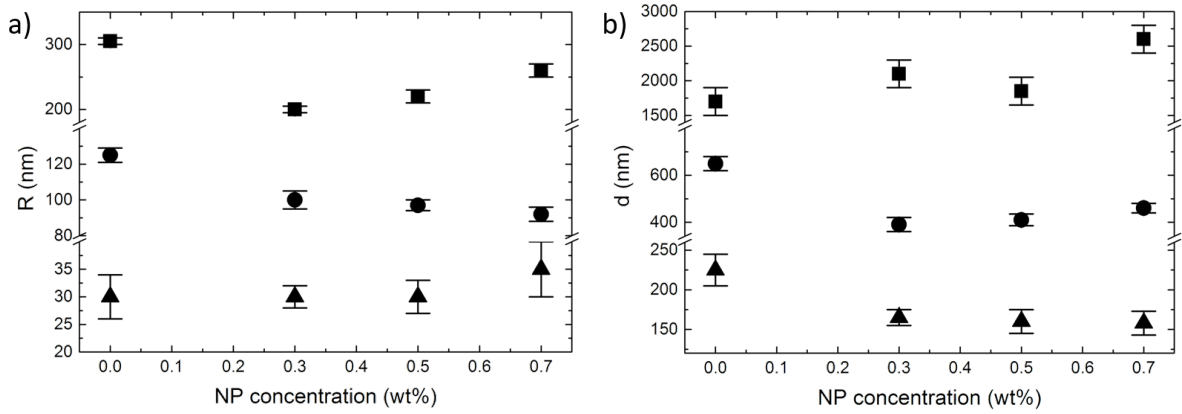


Figure 5.15: Structure radii R and average distances d derived from modeling of horizontal line cuts of PEDOT:PSS/Si-NPs composite films. Three distinct structural families are used for modeling, referred to as large ($R1/d1$, square), medium ($R2/d2$, circle) and small structures ($R3/d3$, triangle). Taken from [2].

by a set of three distinct structural families, which will be referred to as large, medium and small structures for the remainder of this discussion. These are each characterized by the radii R of the spherical structures and their average distances d .

Most notably, changes can be seen for large and medium-sized structures in Figure 5.15a. In the case of a PEDOT:PSS film without Si-NPs, the large structures are approximately 300 nm in size. Upon introduction of Si-NPs, these shrink to approximately 200 nm, only to again grow for further increasing concentrations. For the medium structures a steady decreasing size trend is found. From radii of about 125 nm for the 0 wt% sample the medium structures shrink to about 85 nm at the highest concentration of Si-NPs. Within the error of the modeling, the small structures retain their sizes of about 30 nm.

Also the average distances between the spherical structures are subject to change, as shown in Figure 5.15b. Large structures become less densely packed, as their center-to-center distances increase from roughly 1700 nm to 2500 nm with increasing Si-NPs concentration. On the other hand, medium structures pack slightly more densely as their distances decrease from roughly 600 nm to 450 nm as function of concentration. Again, the results indicate changes of the structure upon introduction of the Si-NPs. Therefore, in the following section, the enhanced chemical sensitivity of GIR-TeXs will be used to determine how the Si-NPs are actually incorporated into the composite films using the energy-dependent scattering contrast.

Scattering contrast: deduction of composition

Through measurement of the 2D GISAXS patterns at energies close to the sulfur K-edge, a strong influence of the non-linearities of the optical properties on the observed scattering intensities can be achieved. Specifically, PEDOT shows such a response in the 'on-resonance' energy range from 2471 eV to 2475 eV, as seen in Figure 5.13.

The scattering contrast can be calculated according to Equation 2.31. Therein, the contrast at the interface between two dissimilar materials is taken into account as an average δ_1/β_1 and δ_2/β_2 , respectively. For the case of the ternary PEDOT:PSS/Si-NPs composite films, this yields two possibilities for a general morphology. In the first case, it is assumed that Si-NPs are quantitatively dispersed within PEDOT-rich domains, whereas the latter are themselves dispersed in a PSS-rich matrix. In the second case, the Si-NPs are fully dispersed in the PSS-rich matrix, which contains PEDOT-rich domains free of nanoparticles. Both cases are schematically shown in Figure 5.16, and referred to as Model 1 and Model 2, respectively.

For the calculation of the scattering contrast $\Delta n_{1,2}^2$ as function of both energy and Si-NPs, the volume fraction v_{Si} of the latter within the PEDOT-rich domains for Model 1 and within the PSS-matrix for Model 2 is taken into account. In turn, this can be calculated with the knowledge of the average size of the Si-NPs of roughly 30 nm. Thus, the scattering contrasts $\Delta n_{1,2}^2$ for both models can be computed according to Equations 5.1 and 5.2, respectively.

$$\Delta n_1^2 = (\delta_{PSS} - ((1 - v_{Si})\delta_{PEDOT} + v_{Si}\delta_{Si}))^2 + (\beta_{PSS} - ((1 - v_{Si})\beta_{PEDOT} + v_{Si}\beta_{Si}))^2 \quad (5.1)$$

$$\Delta n_2^2 = (((1 - v_{Si})\delta_{PSS} + v_{Si}\delta_{Si}) - \delta_{PEDOT})^2 + (((1 - v_{Si})\beta_{PSS} + v_{Si}\beta_{Si}) - \beta_{PEDOT})^2 \quad (5.2)$$

Figure 5.16 summarizes the evolution of the energy-dependent scattering contrast as function of Si-NPs concentration for both models discussed above. It can be seen that the scattering contrast increases strongly with increasing introduction of nanoparticles, which is also independent of the assumed model. Considering Equations 5.1 and 5.2, this simply originates from the increasing volume fraction of Si-NPs in the PEDOT-rich grains and the PSS-rich matrix, respectively. However, a clear distinction can be made between the two models in the 'on-resonance' regime. While for Model 1 a local minimum of the scattering contrast is observed, the opposite is true for Model 2.

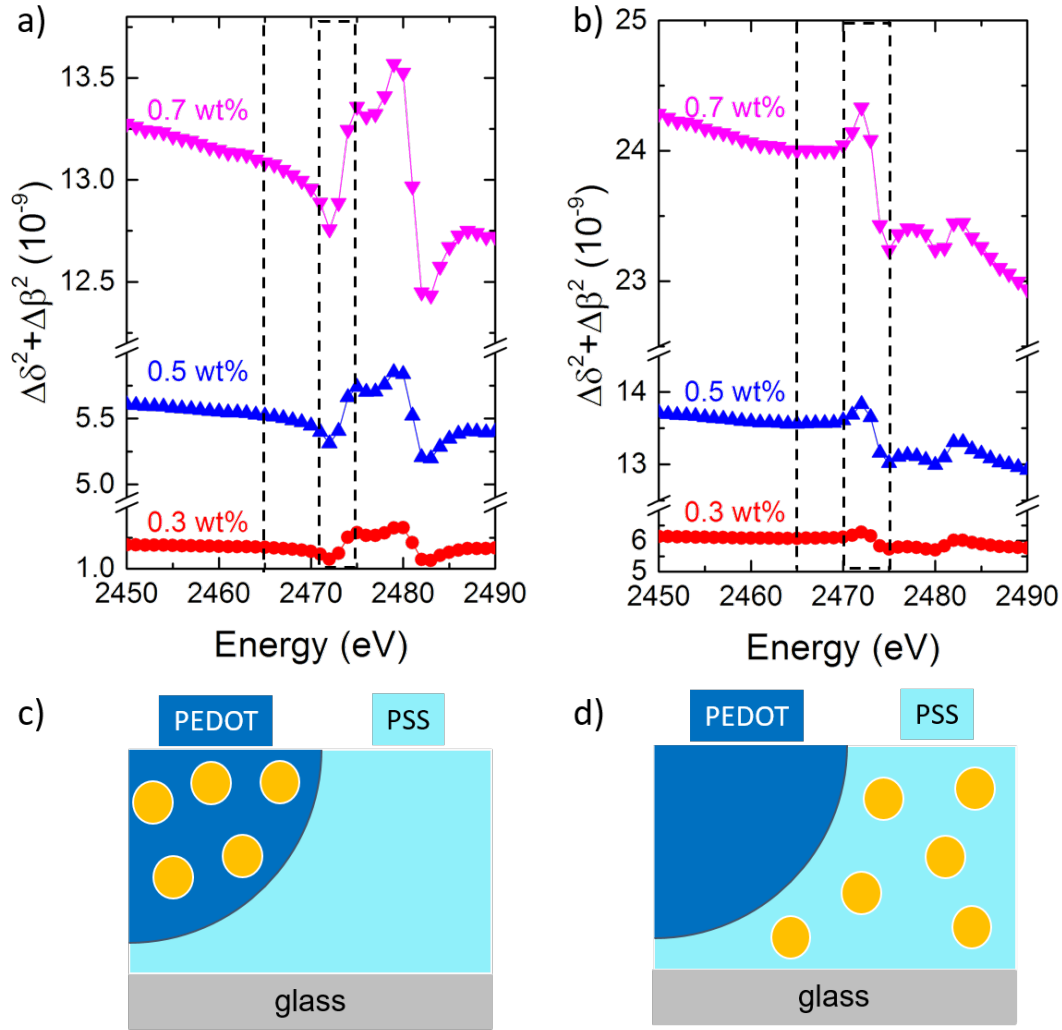


Figure 5.16: Energy-dependent scattering contrast as function of Si-NPs concentration for a) Model 1 and b) Model 2. The 'off-resonance' and 'on-resonance' energies are marked with dashed black lines and boxes, respectively. Schemes of Model 1 and 2 are shown in c) and d), respectively. Model 1: PEDOT-rich grains containing Si-NPs are surrounded by a PSS-rich matrix. Model 2: PEDOT-rich grains are embedded in a PSS-rich matrix, whereby the latter contains the Si-NPs. PEDOT-rich domains are shown in dark blue, while the PSS-matrix is presented in light blue. Si-NPs are shown as brown spheres. Taken from [2].

For a GIR-TeXS measurement, the dependency of the scattering cross-section, shown in Equation 2.25, on changes in the contrast as function of energy is crucial. Therefore, several things have to be kept in mind for an analysis regarding changes in the composition of the investigated films. As the scattering contrast in a classical GISAXS experiment depends on factors such as the illumination volume and the diffuse scatter-

ing factor P_{diff} , the experiment itself and the subsequent analysis of the data has to be performed accordingly.

In order to keep the illumination volume constant, one needs to make sure that the area of the sample over which the beam is scanned possesses a homogeneous thickness, which is the case here. The four-crystal monochromator beamline at BESSY II allows for the variation of the beam energy, while keeping the alignment of the beam with respect to the sample intact. Thus, no changes in the incident angle are observed, keeping the illuminated sample volume constant. All 2D GISAXS patterns are also normalized by the incident beam intensity, in order to exclude variations of the scattering intensity.

The influence of differences in scattering intensity due to scattering objects of certain shapes, sizes and spatial distributions is excluded in the modeling. It should be stressed that for one energy series of a single sample, structural parameters had to be found which can be used for modeling of each curve within the series. The parameters listed in Figure 5.15 fulfill this condition.

A discussion of the observed scattering intensities is therefore enabled. Figure 5.17 compiles the scattering intensities from the modeling sorted by the three structural families which were considered. Therein, the intensities are shown as both function of energy and Si-NPs concentration.

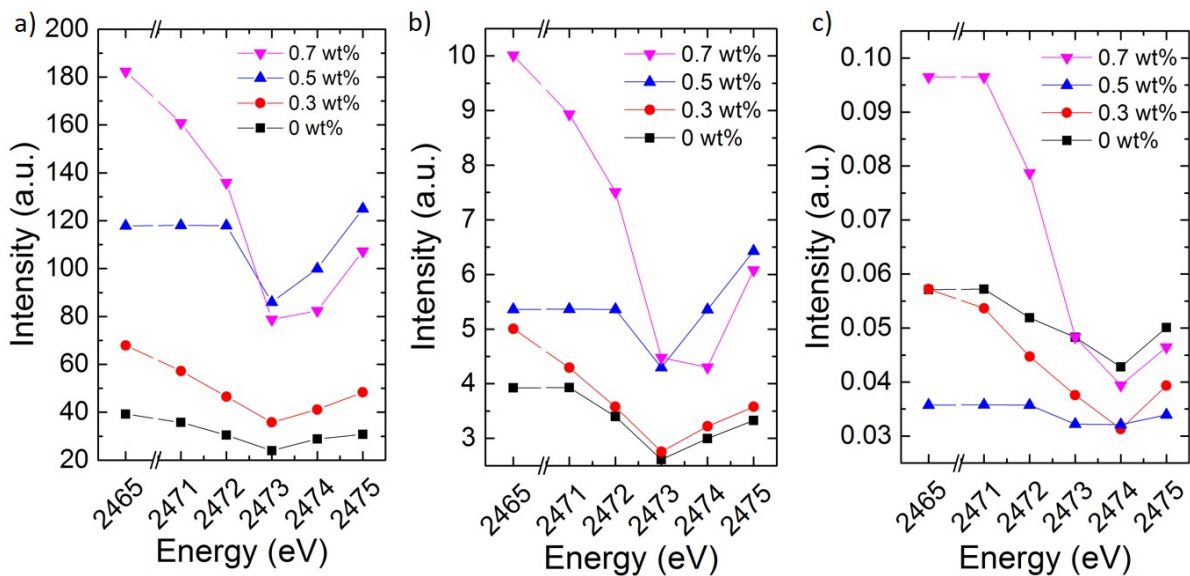


Figure 5.17: Scattering intensities for a) large, b) medium and c) small structures included in the modeling of the horizontal line cuts, as function of energy. Colored data points represent 0 wt% (black), 0.3 wt% (red), 0.5 wt% (blue) and 0.7 wt% (magenta) Si-NPs in the composite films. All intensities are normalized for fluctuations in the incident beam intensity. Taken from [2].

The scattering intensity for large structures, shown in Figure 5.17a, appears to increase with increasing amount of Si-NPs. When referring back to the scattering contrasts in Figure 5.16, this indicates increasing incorporation of Si-NPs into the film. Moreover, the presence of a local minimum of the intensity at 2473 eV fits well to the proposed Model 1, in which the Si-NPs are incorporated in PEDOT-rich grains.

A similar trend is also seen for the medium structures in Figure 5.17b. Also here the scattering intensity increases as more Si-NPs are added to the composite film. The local minimum observed at 2473 eV suggests inclusion of the nanoparticles into the PEDOT-rich grains, rather than the PSS-rich matrix.

Lastly, for the small structures neither a systematic increase in the intensity as function of Si-NPs, nor a consistent local minimum/maximum at 2473 eV can be seen. An absence of Si-NPs both within the PEDOT-rich grains and the PSS-rich matrix is suggested. At least for the former case, this is in line with the constant sizes of the small structures as function of Si-NPs observed in Figure 5.15a.

Morphological model and morphology-function relationship

From the structural and compositional information obtained from the GIR-TeXs measurement, it is possible to draw a morphological scheme seen in Figure 5.18. It contains both the information on the spherical shape of PEDOT-rich domains, their average sizes and additionally their arrangement. More importantly however, the comparison of the scattering intensities in Figure 5.17 with the scattering contrast evolutions for the two possible suggested models in Figure 5.16 reveals changes in the composition. As pointed out above, an overall increase of the scattering intensity for large and medium structures, as well as the local minimum at 'on-resonance' energies is found. This suggests incorporation of Si-NPs in PEDOT-rich grains, which becomes more prominent the more the Si-NPs concentration is increased.

Returning to the initial discussion of the thermoelectric properties of PEDOT:PSS/Si-NPs composite films and how they change as function of nanoparticle concentration, implications of the structure can be expected. These will be discussed in the following. Specifically, a correlation between the changes in the electrical and thermal conductivity and the modifications of the structure is found.

Figure 5.19 attempts at highlighting a correlation between the specific thermal resistance κ^{-1} (the inverse of the thermal conductivity) and the large structures, as well as the electrical conductivity and the medium structures. As discussed in Section 5.2.2, the thermal conductivity changes non-linearly as function of Si-NPs concentration. The specific thermal resistance κ^{-1} in Figure 5.19a amounts to 0.98 KmW⁻¹ for the pure PEDOT:PSS

film. It decreases in an unfavorable way to values of 0.73 KmW^{-1} for 0.3 wt% Si-NPs only to increase again. At the highest concentration of 0.7 wt%, a value of 1.03 KmW^{-1} slightly larger than that of the reference is reached. This implies a two-fold effect of the presence of nanoparticles on the specific thermal resistance of the film. Firstly, as found out in the compositional analysis using GIR-TeXS, an increasing incorporation of Si-NPs into PEDOT-rich domains could be responsible for the increase in the specific thermal resistance. The inner structure of the latter could be disturbed by the Si-NPs, leading to less efficient propagation of phonons and thus to larger values for κ^{-1} . The initial decrease of the latter, is easily understood when considering the single-crystalline nature of the Si-NPs. [34] At low concentrations, the improved phonon transport within the Si-NPs could possibly overcompensate the loss of short-range order within the PEDOT-rich grains, which is why κ^{-1} decreases. Secondly, increasing sizes of the structures seem to favor phonon scattering, as a correlation between the sizes of the large structures and κ^{-1} can be seen.

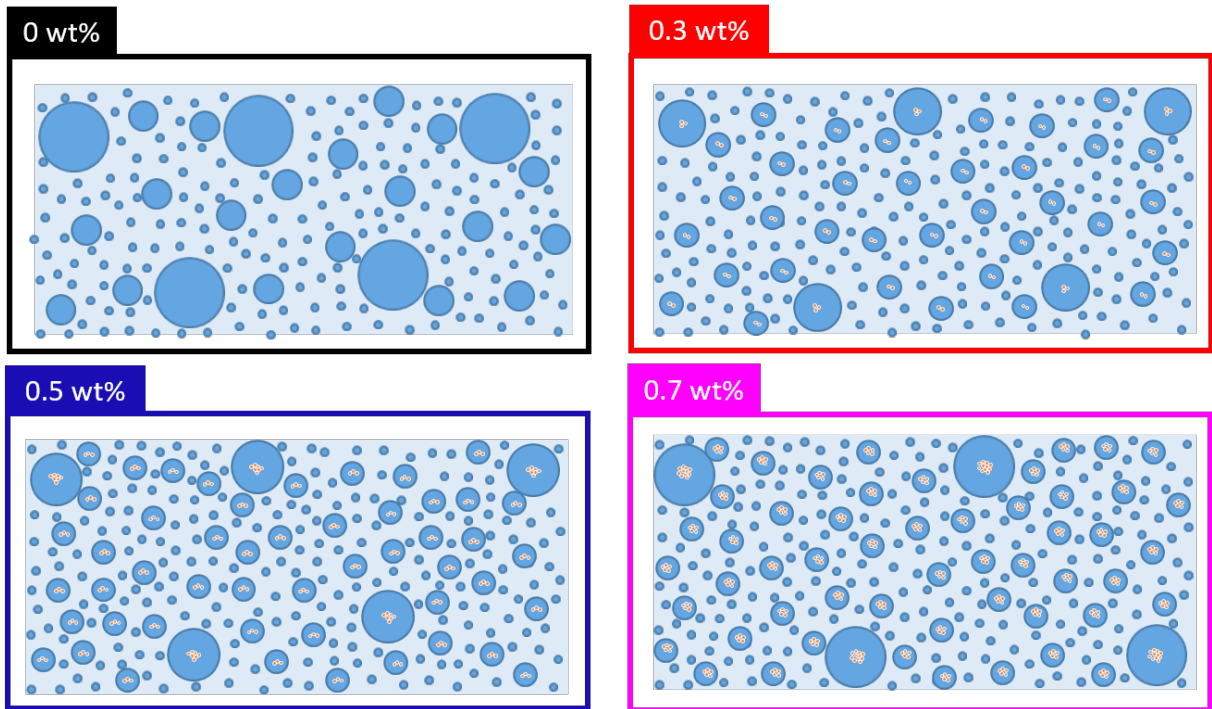


Figure 5.18: Morphological model of PEDOT:PSS/Si-NPs composite films for different nanoparticle concentrations, as deduced from GIR-TeXS measurements and subsequent modeling. The spherical PEDOT-rich grains are shown in blue, which themselves are embedded in a PSS-rich matrix, shown in light blue. Analysis of the scattering intensities and comparison to the scattering contrast reveals validity of Model 1. Si-NPs are incorporated in large and medium structures, while small ones retain their purity. Additionally, Si-NPs are more efficiently included the higher the nominal concentration becomes. Taken from [2].

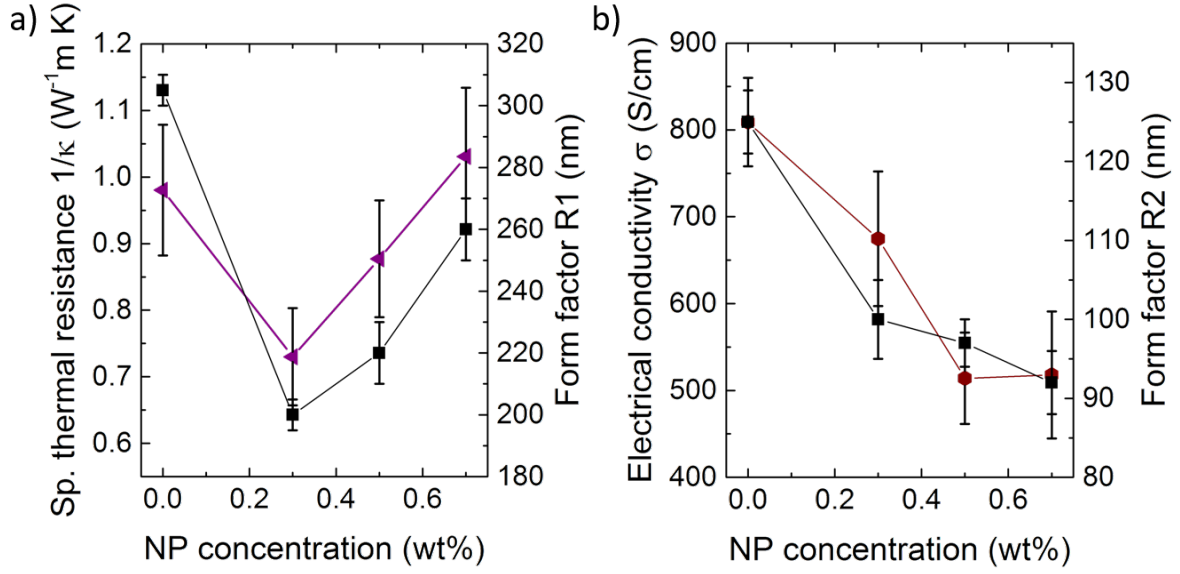


Figure 5.19: a) Correlation of specific thermal resistance κ^{-1} (purple) with sizes of large structures R1 (black) as function of Si-NPs concentration. b) Correlation of electrical conductivity (brown) with sizes of medium structures R2 (black) as function of concentration. Adapted from [2].

In Figure 5.19b the correlation between the electrical conductivity and the sizes of the medium structures R2 are shown. Also here, a two-fold explanation can be given for the observation of correlation. Similarly to κ^{-1} , an increasing amount of Si-NPs is detrimental to the charge transport within a single PEDOT-rich grain. The Si-NPs all carry a shell of insulating SiO_2 , and thus cannot contribute to the charge transport. This effect is expected to become more prominent with increasing Si-NPs content within the PEDOT-rich grains, as suggested by the compositional analysis above. Therefore, the negative impact of the presence of Si-NPs on the inner structure of PEDOT-rich domains expresses itself as loss in electrical conductivity. Additionally, since the decrease in the electrical conductivity coincides with that of R2, loss of percolation pathways for charge carriers could be responsible.

5.4 Summary

In summary, the current chapter deals with a hybrid nanostructuring approach of PEDOT:PSS with Si-NPs. The principle idea is to introduce Si-NPs as phonon scattering centers, in order to lower the phonon contribution to the thermal conductivity.

TOF-GISANS reveals the layer-by-layer fabrication route to yield more favorable prop-

erties of PEDOT:PSS/Si-NPs composite films as compared to the ones prepared in a mixing approach, especially with respect to sizes of domains as well as the degree of Si-NPs inclusion in the film.

Composite films prepared in a layer-by-layer approach with different concentrations of Si-NPs are then investigated regarding their thermoelectric properties. The improvement of the power factor is ascribed to an increase in the Seebeck coefficient for concentrations up to 0.5 wt%. However, the electrical conductivity decreases simultaneously to approximately 500 S/cm. Thus, optimal power factors of $27.6 \mu\text{WK}^{-2}\text{m}^{-1}$ are achieved at a Si-NPs concentration of 0.5 wt%.

IRT is used in order to determine changes in the thermal conductivity as function of Si-NPs concentration. It is a contact-free method, which allows for the measurement of the in-plane thermal conductivity of the composite films, without the influence of a substrate. Free-standing PEDOT:PSS/Si-NPs films are prepared and suspended on steel substrates with small cavities, on top of which the film is actually free-standing. The presence of Si-NPs modifies the thermal conductivity non-linearly. Still, an overall improvement of the figure of merit ZT of a factor of 1.5 is found for the 0.5 wt% sample.

GIR-TeXS at the sulfur K-edge is used to elucidate the structural properties of the composite films as function of Si-NPs. Therein, the fact that both PEDOT and PSS contain sulfur but in different atomic configurations yields a different optical response for each component close to the sulfur K-edge, as seen from the NEXAFS measurements. From the optical properties (namely δ and β), the energy-dependent scattering contrast is calculated. Two structural models are proposed, one in which Si-NPs are completely dispersed in PEDOT-rich grains, and a second one in which the Si-NPs are solely dispersed in the PSS-rich matrix. Horizontal line cuts of the 2D GISAXS patterns are modeled with three distinct structural families, namely large, medium and small spherical structures. Modeling yields structural parameters which can be used to model all horizontal line cuts within a single energy series. Since the scattering contrast changes with the incident beam energy, the same is expected for the scattering intensity off the different structures. Analysis of the intensity as function of energy and Si-NPs concentration, suggests validity of Model 1. Si-NPs are increasingly incorporated in large and medium PEDOT-rich grains, while the small ones retain their purity.

A morphological model is suggested, in addition to a morphology-function relationship. Therein, the thermal conductivity appears to be influenced by changes in the sizes of the large structures, while the electrical conductivity is mostly governed by changes in the sizes of medium structures. Changes in both thermoelectric quantities can additionally be explained by the increasing incorporation of Si-NPs into these domains.

6 Dedoping of PEDOT:PSS with inorganic salts for optimization of thermoelectric power factors

Large parts of this chapter have been published in the article: Facile Optimization of Thermoelectric Properties in PEDOT:PSS Thin Films through Acido-Base and Redox Dedoping Using Readily Available Salts (N. Saxena et al., ACS Appl. Energy Mater., 1, 336-342, 2018, DOI: 10.1021/acsaem.7b00334). [3] Parts of this chapter are based on the bachelor's thesis of Josef Keilhofer, [50] with initial studies having been performed by Anjani Kumar Maurya in the framework of his master's thesis. [51]

Primary doping is a term which describes the introduction of charge carriers into conjugated polymer chains by a doping process, as discussed in Section 2.2.1. In the case of PEDOT as conjugated polythiophene, charges are introduced during the polymerization process and subsequently stabilized in an electrostatically. In the case of e.g. PEDOT:Tos, the stabilization is mediated by negatively charged toluenesulfonate, or tosylate (Tos) ions. The electrical conductivities typically achieved for these types of films are among the highest measured for conducting polymer systems, with record values to date reaching up to 5400 S/cm. Gueye *et al.* used a structural variant of the tosylate anion and added it to the polymerization mixture, in order to achieve these high conductivities. [52]

In the case of PEDOT:PSS, the negatively charged polyanion PSS is responsible for stabilization of charges on the PEDOT chains. This allows for dispersion of the otherwise completely insoluble PEDOT in aqueous solution, and thereby enables solution-processing techniques, such as spin- or spray-coating for thin film fabrication. Through variation of the PEDOT-to-PSS ratio during production, the properties of the dispersion, and thus of the final films can be manipulated. For different applications, specific formulations of PEDOT:PSS are used, which mostly vary in the ratio of PEDOT-to-PSS and therefore in their electrical and/or optical properties when fabricated as thin film, as summarized in the review of Shi *et al.* [53] One of these formulations is commonly referred to as *Clevios* PH1000, with a mass ratio of PEDOT-to-PSS of 1:2.5. In their study, Park *et al.*

demonstrated the impact of PEDOT-to-PSS ratio on the electrical conductivity, with the aforementioned ratio yielding the highest conductivity values. [13] These findings can be combined with the investigation of Massonnet *et al.*, who performed UV-Vis spectroscopy on thin films of the PH1000 formulation, and found strong optical absorption in the far-infrared region of the spectrum. The authors assigned this to the presence of bipolarons, which act as majority charge carriers. The occurrence of bipolarons is synonymous with a high charge carrier density, which is in line with the potentially very high electrical conductivities that can be achieved in thin films of PH1000.

While these properties make PEDOT:PSS a viable choice for application as e.g. transparent electrode in organic solar cells or light-emitting diodes, there are also drawbacks. As discussed in Section 2.1.2, a high charge carrier concentration is typically associated with low Seebeck coefficients. Due to quantities such as the figure of merit ZT or the power factor showing a square dependence on the Seebeck coefficient, this fact impedes the obtainment of high efficiency devices. Thus, researchers have attempted to overcome this problem by modifying the charge carrier concentration of PEDOT:PSS mostly after film fabrication. Bubnova *et al.* used vapors tetrakis(dimethylamino) ethylene (TDAE) vapors, and were able to modify oxidation levels in PEDOT:Tos as they showed using XPS. This way they could achieve power factors of over $300 \mu\text{WK}^{-2}\text{m}^{-1}$, which for the most part stems from the improvement of the Seebeck coefficient. [54] As an alternative approach, Fan *et al.* performed post-treatment steps of PEDOT:PSS films with sulfuric acid and sodium hydroxide. Through analysis of the films with various spectroscopic techniques, the authors deduced that reduction of the charge carrier concentration was caused by the basic properties of sodium hydroxide, and therefore allowed for improvement of the Seebeck coefficient. [55] Massonnet *et al.* used various reducing agents, such as hydrazine, NaBH_4 , Na_2SO_3 or the above-mentioned TDAE. [56] These were chosen on the basis of their different redox potentials, expected to yield increased Seebeck coefficients after post-treatment of PEDOT:PSS films. With UV-Vis spectroscopy, the authors observed changes in the absorption behavior upon dedoping. The large absorption in the far-infrared range of the spectrum assigned to the presence of bipolarons steadily shifts towards lower wavelengths when the reducing agents are applied to the polymer films. Strong reducing agents yielded strong absorption features in the visible region, and were assigned to the presence of neutral states.

Similarly, this study attempts to investigate the influence of dedoping in PEDOT:PSS films more closely in terms of changes in the thermoelectric properties caused by changes in charge carrier concentration. Dedopants are chosen according to their acido-basic or redox properties, and compared regarding their dedoping efficiency. Various spectroscopic

techniques are used to analyze changes in the electronic structure, composition and conformation of the films.

6.1 Thermoelectric characterization of dedoped PEDOT:PSS thin films

In the following section, PEDOT:PSS thin films will be dedoped using inorganic salts, which exhibit either acido-basic or redox properties. NaHCO_3 exhibits acido-basic properties, while Na_2SO_3 and NaBH_4 show redox behavior. Dedoping is done in a facile approach, in which aqueous solutions of the inorganic salts are mixed in different amounts into PEDOT:PSS solutions prior to film fabrication. EG post-treatment is performed on all samples in order to increase the electrical conductivity through secondary doping to levels at which the influence of the charge carrier concentration can be discerned. A detailed description of the experimental procedure is given in Section 4.2.2.

The properties of the samples are discussed in terms of changes in the Seebeck coefficient, electrical conductivity and power factor as function of dedopant concentration. Dedoping with the redox-active salts is also analyzed with respect to the absolute number of reducing equivalents, in an effort to understand if the choice of redox-active salt influences the outcome.

6.1.1 Acido-basic dedoping with sodium hydrogencarbonate

Firstly, NaHCO_3 is employed as inorganic salt with purely acido-basic properties. It decomposes into carbon dioxide, sodium and hydroxyl ions, as seen in Equation 6.1.



In Figure 6.1, the three important thermoelectric quantities, namely Seebeck coefficient (green), electrical conductivity (brown) and power factor (blue) are shown as function of NaHCO_3 concentration. An increase of the Seebeck coefficient from $24.7 \mu\text{V/K}$ for the sample without NaHCO_3 to a maximum value of $54.8 \mu\text{V/K}$ at a concentration of 70 mM is observed, which levels off for higher concentrations. Simultaneously, a strong decrease in the electrical conductivity from 875 S/cm to approximately 115 S/cm is found, after reaching a maximum value close to 1000 S/cm for low concentrations. Since all samples were treated with EG, there is an indication that the negative effect on the

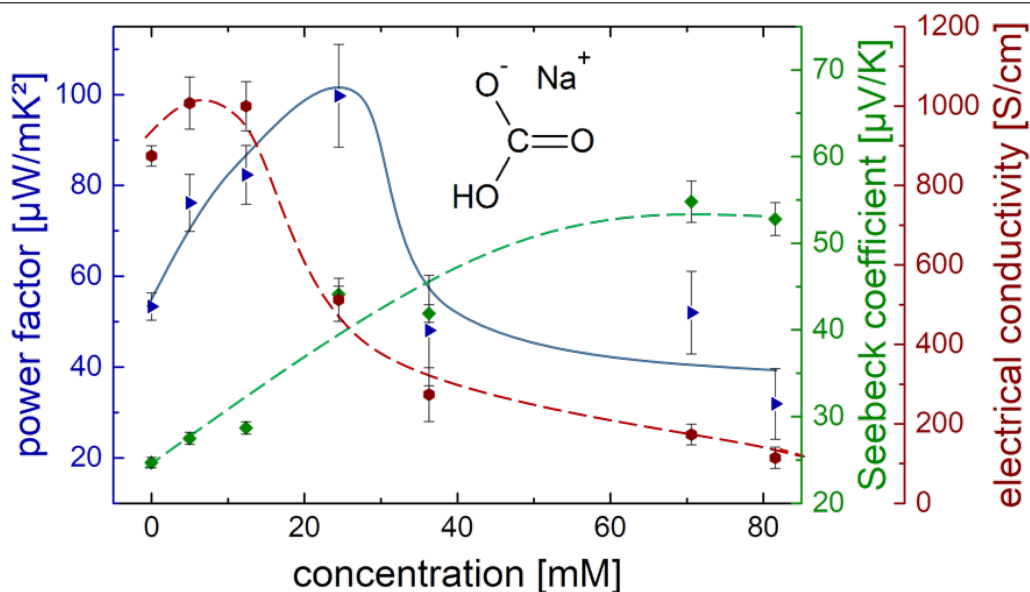


Figure 6.1: Seebeck coefficient (green diamonds), electrical conductivity (brown hexagons) and power factor (blue triangles) of PEDOT:PSS films dedoped with different concentrations of NaHCO₃. Dashed lines in the respective colors serve as guides to the eye. Taken from [3].

electrical conductivity comes from changes in the charge carrier concentration, which is also supported by the increase in the Seebeck coefficient. Nevertheless, the thermoelectric quantities were altered in such a way that the power factor (blue data points) shows a maximum value of approximately $100 \mu\text{W}\text{K}^{-2}\text{m}^{-1}$ at a concentration of 24 mM, with the reference value being $53 \mu\text{W}\text{K}^{-2}\text{m}^{-1}$. Due to the square dependence of the power factor on the Seebeck coefficient, a certain drop in the electrical conductivity can be accepted, since the Seebeck coefficient increases accordingly and is therefore mainly responsible for the improvement. Further increase of the dedopant concentration leads to even higher Seebeck coefficients but to drastically lower electrical conductivities which result in an overall decrease of power factors in this concentration range. Another noteworthy fact is that the maximum NaHCO₃ concentration used in this study is significantly lower than for the other salts. This is owed to the fact that the inorganic salts not only alter the electronic structure of PEDOT, but also modify the electrostatic interaction between PEDOT and PSS. As PEDOT by itself is completely insoluble, a disturbance in the coordination of PSS onto PEDOT chains leads to inhomogeneous film formation, which can be observed in the optical microscopy images in Figure 6.2. While both the pristine, EG-treated PEDOT:PSS film and the one with the optimal concentration of dedopant appear homogeneous, the optical micrograph of the film dedoped with very high NaHCO₃ concentrations of 193 mM appear much darker. A strong increase in the viscosity of the polymer solution is observed, when high concentrations of NaHCO₃ are added, which

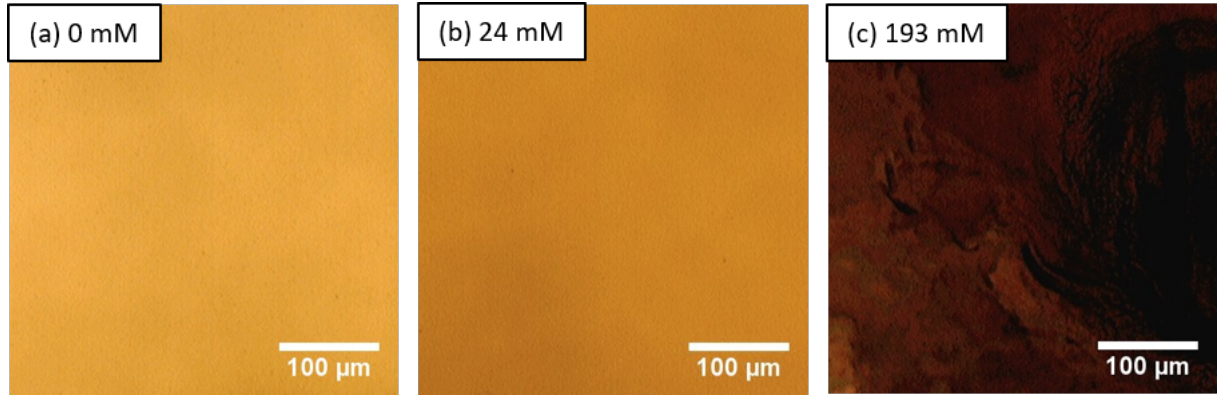
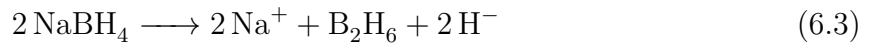
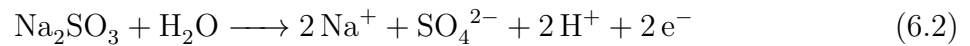


Figure 6.2: Exemplary optical micrographs of PEDOT:PSS films dedoped with NaHCO_3 in different concentrations: a) 0 mM, b) 24 mM and c) 193 mM. Taken from [3].

in turn makes the flinging-off of material less efficient. Also, measuring the Seebeck coefficient becomes exceedingly difficult if no closed film is present on the substrate, which is why the maximum concentration of NaHCO_3 was 82 mM.

6.1.2 Redox dedoping with sodium sulfite and sodium borohydride

In a complementary approach, dedoping of PEDOT:PSS thin films was also attempted with the inorganic salts Na_2SO_3 and NaBH_4 since they possess redox-properties, due to them being able to release electrons and hydride ions (negatively charged hydrogen atoms), respectively. For both salts, the decomposition reactions in aqueous solution are shown in Equations 6.3 and 6.2, respectively.



Redox-dedoping with sodium sulfite (Na_2SO_3)

As shown in Equation 6.2, sodium sulfite decomposes into sulfate anions and protons under release of two equivalents of electrons per equivalent of salt, whereas the former are expected to interact with PEDOT in a charge-neutralizing fashion. Figure 6.3 summarizes the impact of dedoping PEDOT:PSS as function of Na_2SO_3 concentration. As with dedoping using NaHCO_3 , also here an increase of Seebeck coefficient to $69.0\ \mu\text{V/K}$

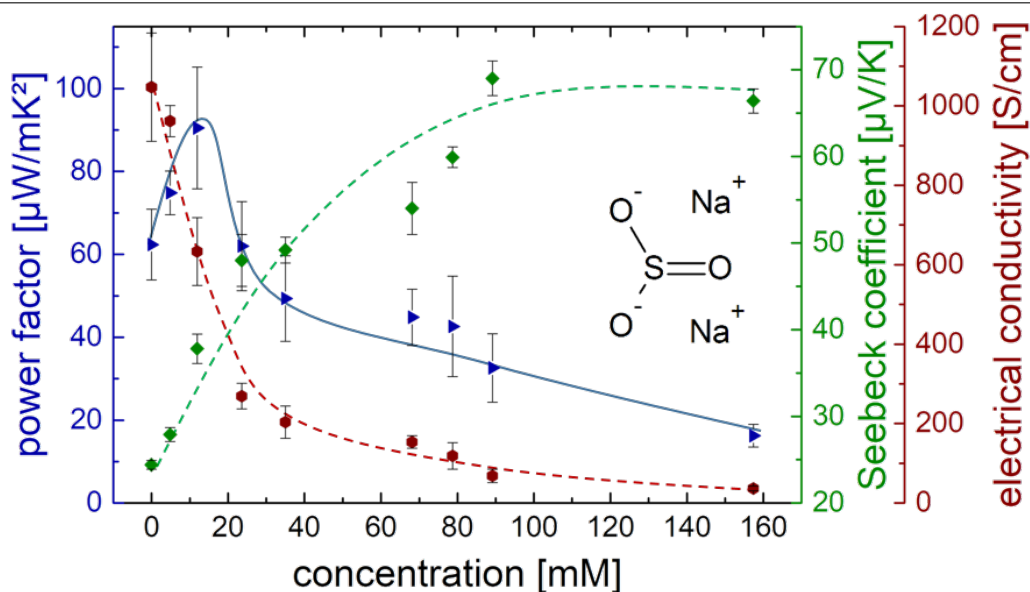


Figure 6.3: Seebeck coefficient (green diamonds), electrical conductivity (brown hexagons) and power factor (blue triangles) of PEDOT:PSS films dedoped with different concentrations of Na_2SO_3 . Dashed lines in the respective colors serve as guides to the eye. Taken from [3].

from $24.4 \mu\text{V}/\text{K}$ is observed, which levels off for high concentrations. Notably, the maximum Seebeck coefficient for dedoping with Na_2SO_3 is higher than in the other cases, which will be discussed below. Again, the rise in Seebeck coefficient is complemented by a drastic decrease in electrical conductivity, with the reference value being 1050 S/cm and falling down to 36 S/cm for high concentrations. As discussed before, due to the square dependence of the power factor on the Seebeck coefficient, again an optimum value of $90 \mu\text{W}\text{K}^{-2}\text{m}^{-1}$ of the former is found at concentrations of 12 mM Na_2SO_3 , compared to the reference value of approximately $60 \mu\text{W}\text{K}^{-2}\text{m}^{-1}$. For high concentrations, the power factor drops to $20 \mu\text{W}\text{K}^{-2}\text{m}^{-1}$, due to the loss in electrical conductivity.

Redox-dedoping with sodium borohydride (NaBH_4)

NaBH_4 decomposes in aqueous solution into the stable diborane (B_2H_6) and sodium ions under the release of negatively charged hydride anions (H^-), which are responsible for the reductive properties of the salt. This is highlighted in Equation 6.3. Figure 6.4 shows the evolution of thermoelectric properties as function of NaBH_4 concentration. As previously seen, the addition of dedopant yields changes in the Seebeck coefficient, which increases from $23.0 \mu\text{V}/\text{K}$ for the reference to $58.0 \mu\text{V}/\text{K}$ for the highest concentration of 160 mM NaBH_4 . Consequently, the electrical conductivity drops from 940 S/cm for the sample without dedopant, to 49 S/cm for the highest concentration of 160 mM . In addition,

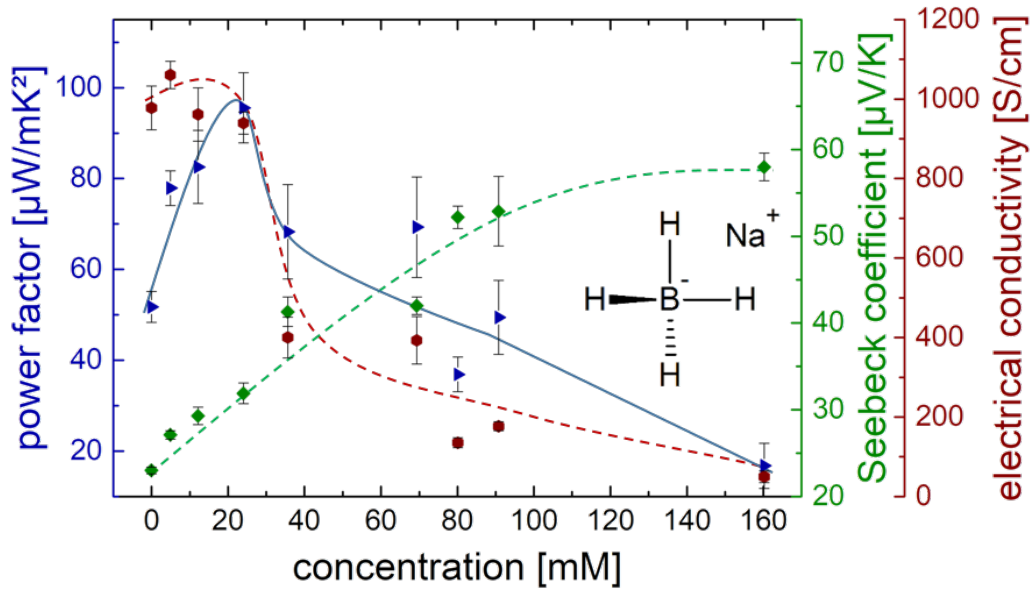


Figure 6.4: Seebeck coefficient (green diamonds), electrical conductivity (brown hexagons) and power factor (blue triangles) of PEDOT:PSS films dedoped with NaBH₄. Dashed lines in the respective colors serve as guides to the eye. Taken from [3].

the latter quantity shows a only a very slight decrease for concentrations up to 24 mM. Interestingly, this is also the concentration at which the maximum value for the power factor of $96 \mu\text{WK}^{-2}\text{m}^{-1}$ is found, giving an improvement of factor two compared to the reference. As before, a large drop down to approximately $20 \mu\text{WK}^{-2}\text{m}^{-1}$ is observed for large concentrations.

Comparison of redox dedopants

In the discussion above, changes among the different redox dedopants regarding the magnitudes of the different thermoelectric properties are apparent. The question whether this stems from differences in redox potential or not, is reasonable. Therefore, in Figure 6.5, the three previously discussed quantities are discussed in terms of the absolute number of reducing equivalents. These were calculated based on the reaction schemes given in Equations 6.2 and 6.3. From these, it can be concluded that per mole of Na₂SO₃ two moles of electrons are released, while per mole of NaBH₄ only one mole of H⁻ is released into the solution. The employed salt concentrations were thusly modified with a factor of two in the case of Na₂SO₃ and with a factor of one in the case of NaBH₄, in order to give show the thermoelectric quantities as function of a 'normalized' concentration.

For both the Seebeck coefficient and electrical conductivity, a very good agreement between the two redox-active salts is found as function of reducing equivalent concentration.

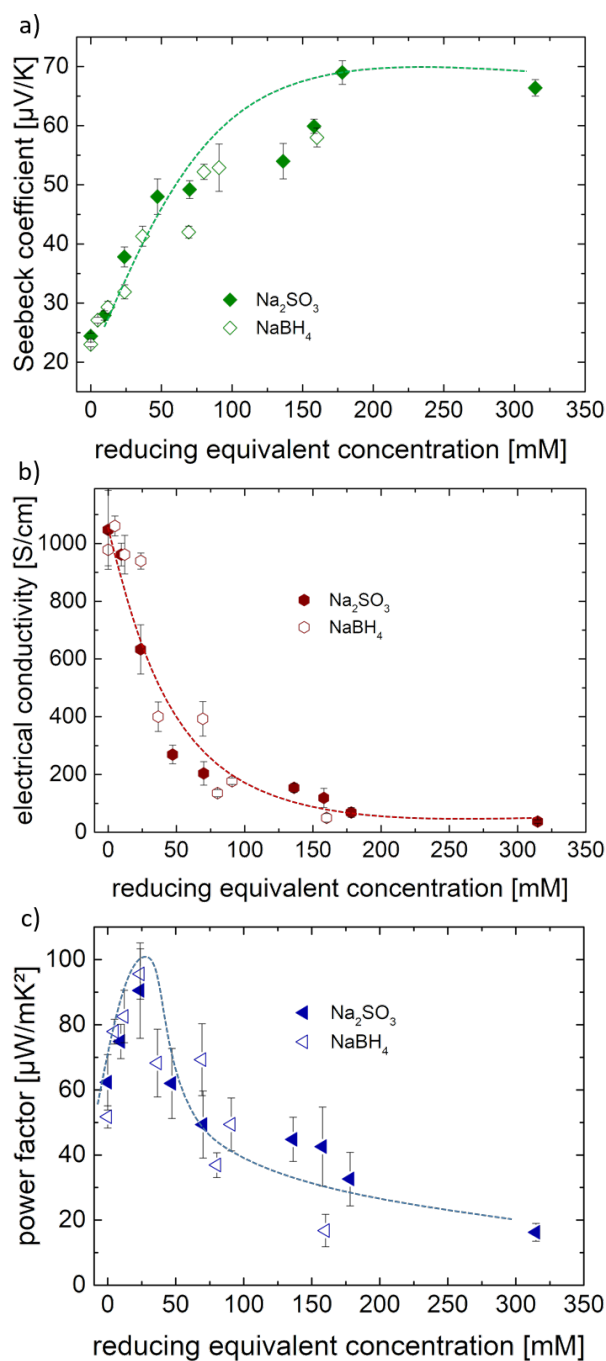


Figure 6.5: a) Seebeck coefficient, b) electrical conductivity and c) power factor for PEDOT:PSS films dedoped with Na_2SO_3 (solid symbols) and NaBH_4 (hollow symbols) as function of absolute number of reducing equivalents. These were calculated based on the decomposition reactions given in Equations 6.2 and 6.3. Dashed, colored lines serve as guides to the eye. Taken from [3].

The Seebeck coefficient increases steadily and reaches saturation for high concentrations at values close to 70 $\mu\text{V/K}$. Consequently, the electrical conductivity decreases drastically,

since already reducing equivalent concentrations of approximately 70 mM reduce the electrical conductivity below 200 S/cm. Naturally, by combining the different trends for the Seebeck coefficient and electrical conductivity, an overall optimum of the power factor is expected, which is also seen in Figure 6.5c. It can be observed that only minor increases of the Seebeck coefficient of up to approximately 40 $\mu\text{V/K}$ are needed to achieve the maximum power factor, since this goes along with reasonably high electrical conductivities of approximately 500 S/cm.

The good agreement of the parameters for the two salts is a clear hint that the individual properties of the redox-active salts have less of an impact than the absolute amount of reducing equivalents in solution which can interact with the positive charge carriers on the PEDOT chains.

In summary, inorganic salts with acido-basic and redox-active properties can be used in order to tune the thermoelectric properties of PEDOT:PSS thin films. In order to understand the source of these effects the dedoped films are analyzed using various spectroscopic techniques in an effort to understand whether the intended modification of charge carrier concentration is solely responsible or not.

6.2 Spectroscopic characterization

6.2.1 Analysis of electronic structure with UV-Vis spectroscopy

UV-Vis spectroscopy is a non-destructive method, with which the electronic structure of PEDOT:PSS can be analyzed. Massonnet *et al.* used this technique in their own dedoping study to not only deduce the electronic structure of pristine PEDOT:PSS, but also to monitor changes upon addition of dedopants. In the former case, absorption primarily takes place in the infrared region of the spectrum, due to the high concentration of bipolarons as charge carriers, which are easily excited by low-energy light. [56] Upon addition of dedopant, they found a steady decrease of absorption in this region, while simultaneously increased absorption in the near-infrared and visible range was found. The authors assigned this to a transition from bipolarons to polarons and neutral species with increasing reducing power of dedoping agent.

In this study, UV-Vis spectroscopy is similarly used to determine changes in the electronic structure of PEDOT:PSS. Specifically, we want to monitor changes in the charge carrier distribution and link them to changes in the thermoelectric properties.

Figure 6.6 shows the evolution of UV-Vis absorption spectra as function of concentration for all three previously discussed dedopants. Normalization of the spectra at

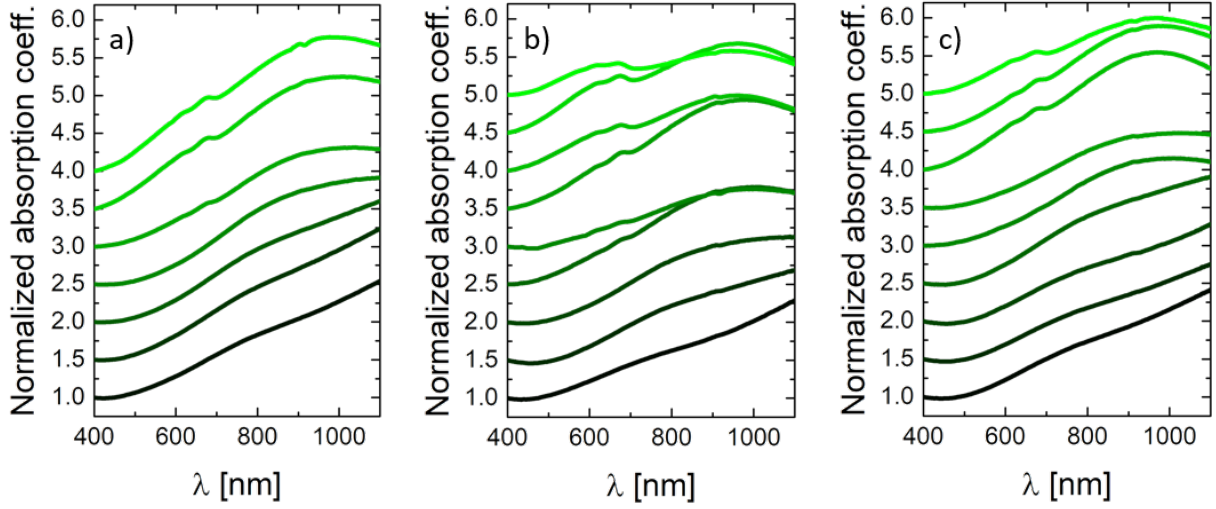


Figure 6.6: Normalized absorption coefficients of PEDOT:PSS films dedoped with a) NaHCO_3 , b) Na_2SO_3 and c) NaBH_4 . The curves are stacked along the y-axis for clarity, with the concentration of the respective dedopant increasing from bottom to top. Normalization to the absorption coefficient at 400 nm was performed for all curves in order to highlight the changes upon dedoping. In each graph, the bottom-most graph (black) represents PEDOT:PSS treated with EG but not with dedopant. Taken from [3].

wavelengths of 400 nm was performed in order to highlight changes with increasing concentration of each dedopant, but also possible differences between each dedopant. Each graph contains the reference curve for PEDOT:PSS only post-treated with EG in black, while the color gradient transitioning to light green is supposed to link the increasing dedopant concentration to the increasing Seebeck coefficient for all cases.

As seen by Massonnet *et al.*, due to bipolarons being the majority charge carrier type, pristine PEDOT:PSS shows increased absorption towards longer wavelengths. Visible wavelengths are absorbed to lesser extent, which is why thin films of PEDOT:PSS typically appear semi-transparent. Upon dedoping with NaHCO_3 , the broad absorption shoulder at high wavelengths gradually transforms into a broad peak. This can be assigned to the gradual transformation of bipolarons into polarons. For concentrations exceeding 24 mM, another feature arises at around 650 nm. This is typically assigned to the presence of neutral states of PEDOT. The increase in absorption corresponding to polaron states on the one hand, and also the increased concentration of neutral states fits well with the rise in Seebeck coefficient, since an inverse relation of Seebeck coefficient and number of charge carriers is expected.

A similar general trend is also seen for dedoping with the redox-active salts Na_2SO_3 and NaBH_4 , which also exhibit increase in polaron concentration with lower amounts of salt, and additional neutral states appearing, which can be deduced from the presence of ab-

sorption features around 650 nm. For Na_2SO_3 , these appear for concentrations exceeding 12 mM, while for NaBH_4 , they appear at concentrations higher than 24 mM. Interestingly, in all cases the concentration of dedopant at which absorption features related to neutral species arise, also mark the point at which the optimum power factor is already exceeded. A possible conclusion which can be drawn from this finding is that the presence of polarons is favorable, while neutral states impede the electrical conductivity too much. Even the maximum Seebeck coefficients that can be achieved with the highest dedoping concentrations cannot compensate this in terms of the power factor. Additionally, despite the inorganic salts presumably reacting with PEDOT chains in different ways due to NaHCO_3 possessing acido-basic and Na_2SO_3 and NaBH_4 having redox-active properties, dedoping appears to have very similar effects on the thermoelectric properties of PEDOT:PSS thin films.

6.2.2 Compositional analysis with x-ray photoelectron spectroscopy

In order to understand the effects of the different dedopants more, in the following section XPS is employed. It not only allows to determine the composition of dedoped films but also if the average oxidation levels of sulfur in PEDOT change, which can in principle be linked to changes in charge carrier concentration. In this specific case, measurements were performed at the S2p-absorption edge of sulfur. Sulfur is present in both PEDOT and PSS, albeit with different chemical environments. Due to the sensitivity of XPS to differences in chemical environments or chemical shift, these two different species of sulfur can be distinguished by the binding energy of electrons in the 2p-orbitals. One is therefore able to make statements about the chemical composition of the films, simply by analyzing peak areas. In addition, since the peak position is sensitive to the binding energy of electrons, it is therefore also subject to change during oxidation/reduction processes. Here, this fact will be used to make statements about the average oxidation levels of PEDOT. For this purpose, PEDOT:PSS films were dedoped with the different inorganic salts in exemplary concentrations.

The reference measurement for PEDOT:PSS only post-treated with EG (black curve in Figure 6.7a), reveals a strong contribution of the PSS signal at higher binding energies, centered at around 168 eV. This can be easily understood when considering the nature of the chemical shift. The sulfur in PSS is bound to three oxygen atoms which strongly decrease the electron density around it. Each individual core electron thus experiences a higher electrostatic binding through the positive charge of the sulfur core, which manifests itself as a shift towards higher binding energies in the XPS spectra. [55] The weak PEDOT signal is found at comparatively lower binding energies of around 165 eV due to the binding

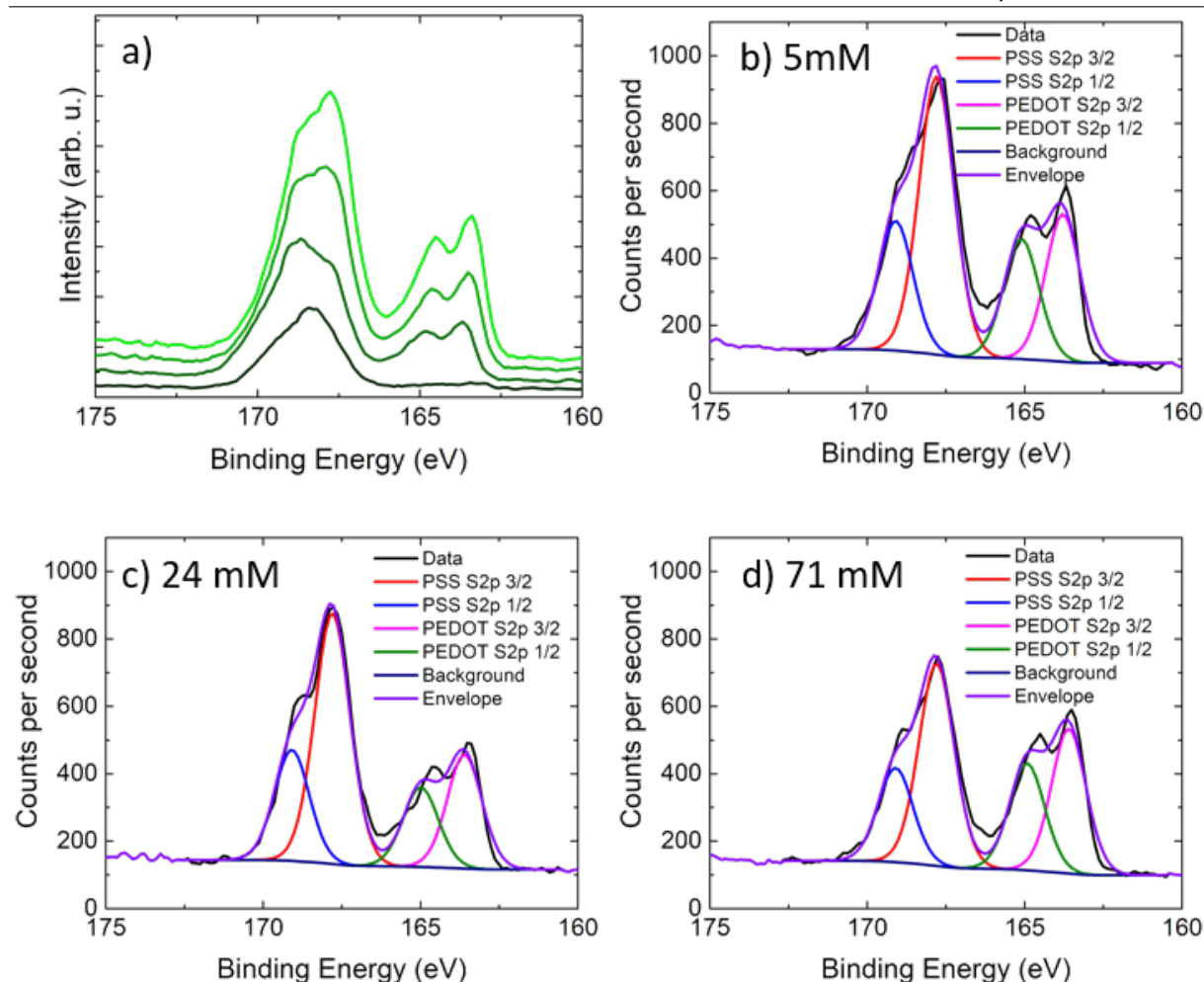


Figure 6.7: a) High resolution XPS S2p spectra of PEDOT:PSS dedoped with NaHCO₃ in concentrations of 5 mM, 24 mM and 71 mM, with PEDOT:PSS only post-treated with EG is shown as reference in black. Curves obtained from samples with increasing concentrations of dedopant are stacked along the y-axis for clarity. b)-d) Deconvolutions of high resolution XPS spectra, for the dedoped samples with concentrations indicated as above. Spin-splitting of the signal is accounted for in the fitting of the peaks with Gaussian-Lorentzian lineshapes. Adapted from [3].

of the sulfur in the thiophene unit of the monomer. From the peak areas, conclusions about an excess of PSS can be made. However, it should be noted that the limited information depth of XPS of approximately 8 nm limits this statement to the uppermost layers of the film. This strong disbalance in peak area therefore corresponds to a thin capping layer of PSS which rests on top of the PEDOT:PSS film after post-treatment with EG.

An aspect that is also of interest for this discussion is tracking peak positions of the PEDOT contribution to the XPS spectra as function of dedopant concentration. This

will give more insight into the reduction mechanism and possibly into differences among the different dedopants.

In Figure 6.7a no significant shift of the PEDOT signal towards lower binding energies, as one would expect from reduced thiophene sulfur, can be detected. This is supported by closer investigation of the deconvolution spectra in Figure 6.7b-d. Mechanistically, this speaks for a decrease in charge carrier concentration solely due to neutralization of protons with the hydroxyl anions that form upon decomposition of NaHCO_3 in aqueous solution (see Equation 6.1). This finding is in good agreement with the work of Fan *et al.*, who used sodium hydroxide (NaOH) for post-treatment of PEDOT:PSS and similarly saw increased optical absorption in the visible region of the spectrum, as well as changes in the PEDOT-to-PSS ratio but no shift of the PEDOT contribution in the XPS spectra. [55]

In the case of Na_2SO_3 dedoping, as seen in Figure 6.8a, a similar relative increase in the PEDOT contribution is seen, which most likely originates from a decrease in the relative amount of PSS on the surface. The additional shoulder appearing at high binding energies is most likely related to sulfur in the form of sulfate ions, which form after decomposition of Na_2SO_3 in aqueous solution (as can be seen in Equation 6.2). Since four oxygen atoms are bound to a single sulfur atom, the decreased electron density should increase the binding energy for each individual electron compared to the sulfonate sulfur present in PSS. Additionally, a shift of the PEDOT contribution towards lower binding energies is observed, as seen from the deconvolutions of the $\text{S}2\text{p}$ signal in Figures 6.8b-d. This indicates a reduction in the average oxidation level of thiophene sulfur, and therefore corresponds to a loss in charge carrier concentration in PEDOT chains. As opposed to dedoping with NaHCO_3 , actual reduction of positive charge carriers within PEDOT chains takes place with the help of electrons which are released from the salt upon decomposition in water.

Lastly, the XPS spectra after dedoping of PEDOT:PSS with NaBH_4 are shown in Figure 6.9. Also here, the removal of PSS is more efficient, which manifests itself as relative increase of the PEDOT-associated peaks. Notably, a strong shift of approximately 0.7 eV those peaks towards lower binding energies are observed for high concentrations of NaBH_4 . The hydride ions (H^-) which are released upon reaction of NaBH_4 in aqueous solution, as seen in Equation 6.3, are responsible for the apparent reduction of thiophene sulfur. The indicated reduction of charge carrier concentration is in line with the observation in UV-Vis spectra of dedoped PEDOT:PSS films and also with the increase in Seebeck coefficient. One thing which should be kept in mind is that NaBH_4 not only possesses purely redox-active properties, but also acido-basic ones since the hydride anion can also act as a strong base. At the highest concentration of 91 mM, PEDOT:PSS solutions show pH values of approximately 12.7, while the pristine solutions exhibit pH values of 1.5.

Still, the acido-basic properties themselves cannot solely be responsible for the observed effects, since the shift of the PEDOT peaks in the XPS spectra indicates actual reduction of the average oxidation level of the thiophene sulfur. This notion is supported by the PEDOT:PSS films dedoped with NaHCO_3 showing no shift of the PEDOT-associated peaks in the XPS spectra.

As described above, XPS also allows for analysis of the composition, by simply calculating ratios of peak areas. Here, an estimate of the PSS-to-PEDOT ratio is obtained by summing the peak areas of the peaks associated to PSS and PEDOT, respectively and

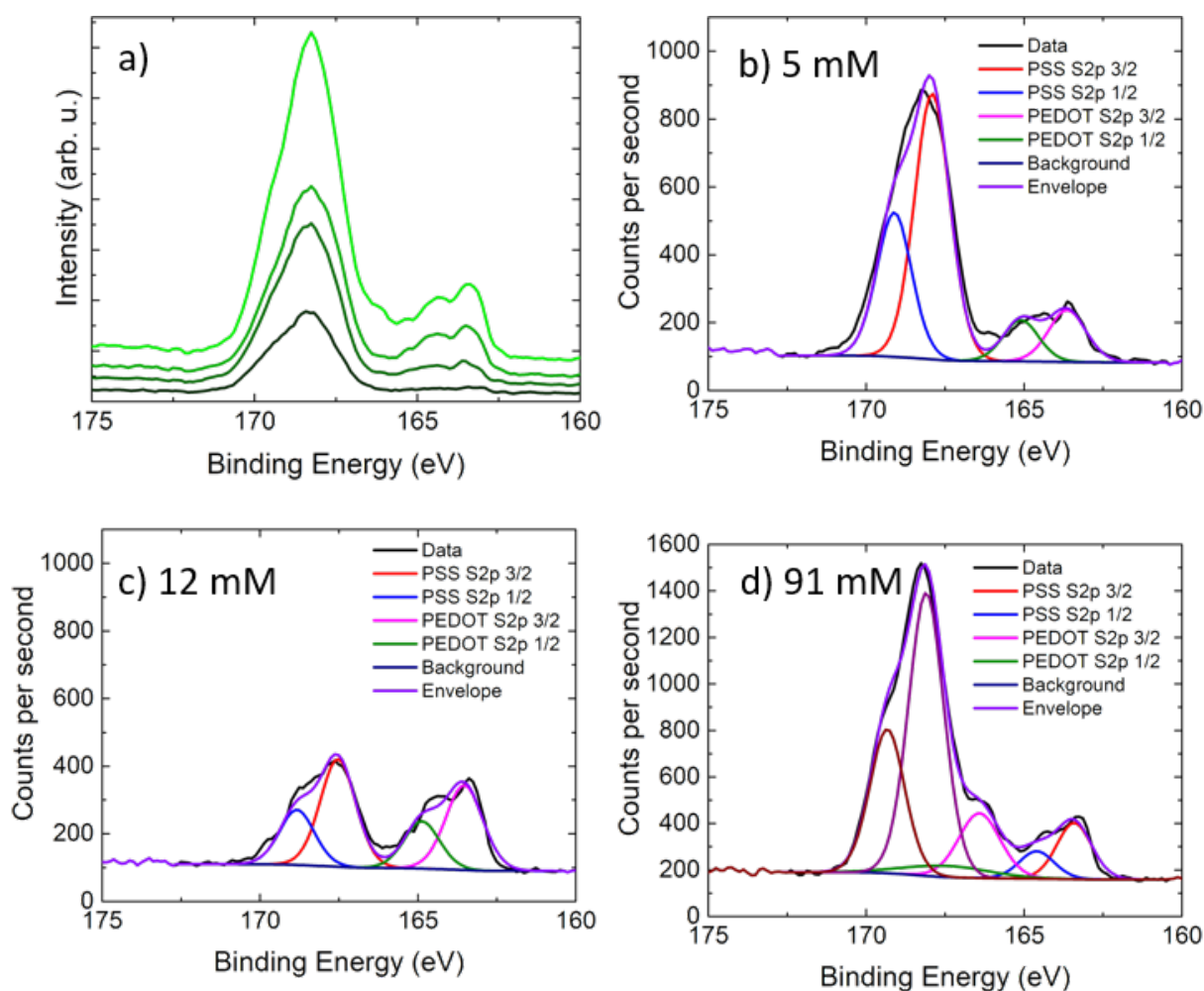


Figure 6.8: a) High resolution XPS S2p spectra of PEDOT:PSS dedoped with Na_2SO_3 in concentrations of 5 mM, 12 mM and 91 mM, with PEDOT:PSS only post-treated with EG is shown as reference in black. Curves obtained from samples with increasing concentrations of dedopant are stacked along the y-axis for clarity. b)-d) Deconvolutions of high resolution XPS spectra, for the dedoped samples with concentrations indicated as above. Spin-splitting of the signal is accounted for in the fitting of the peaks with Gaussian-Lorentzian lineshapes. Adapted from [3].

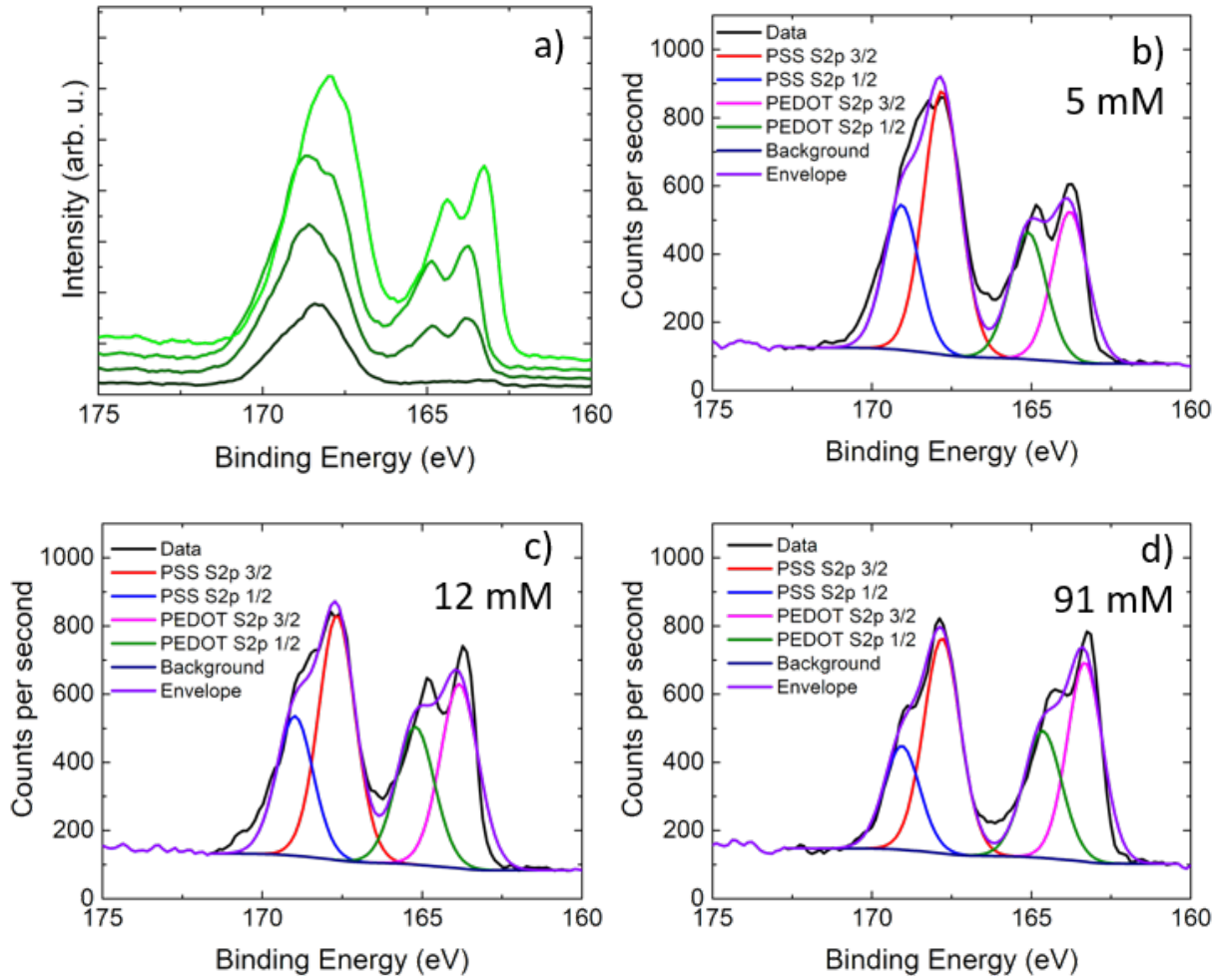


Figure 6.9: a) High resolution XPS S2p spectra of PEDOT:PSS dedoped with NaBH_4 in concentrations of 5 mM, 24 mM and 91 mM, with PEDOT:PSS only post-treated with EG is shown as reference in black. Curves obtained from samples with increasing concentrations of dedopant are stacked along the y-axis for clarity. b)-d) Deconvolutions of high resolution XPS spectra, for the dedoped samples with concentrations indicated as above. Spin-splitting of the signal is accounted for in the fitting of the peaks with Gaussian-Lorentzian lineshapes. Adapted from [3].

calculating the ratio. The result for the different dedopants in exemplary concentrations is shown in Figure 6.10. As can already be seen in the XPS spectra discussed previously, the PEDOT:PSS film without dedopant but after post-treatment with EG possesses a capping layer of PSS, which yields the high apparent PSS-to-PEDOT ratio. In all cases of dedoping, this ratio drastically reduces due to improved removal of PSS due to post-treatment and shows a monotonous decreasing trend. One exception is the PEDOT:PSS film dedoped with high concentrations of Na_2SO_3 , for which the ratios slightly increases again. Remnants of sulfate formed after the decomposition of Na_2SO_3 might make the

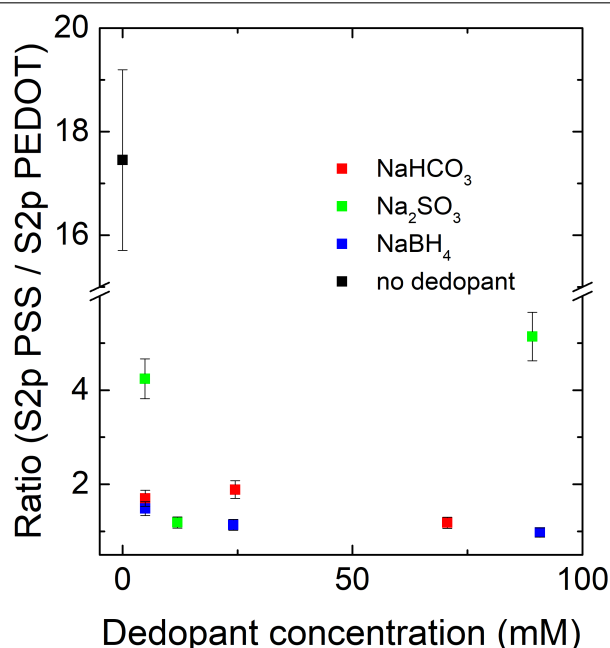


Figure 6.10: Ratio of PSS to PEDOT extracted from peak areas in S2p XPS scans for selected concentrations of NaHCO₃ (red), Na₂SO₃ (green) and NaBH₄ (blue). Taken from [3].

determination of the PSS peak area inaccurate, and are therefore most likely responsible for this observation.

6.2.3 Conformational analysis with Raman spectroscopy

Raman spectroscopy is employed in this study to investigate changes in the conformation of polymer chains upon dedoping. In the case of polythiophenes, or more specifically PEDOT, Raman spectroscopy enables the distinction between the two distinct states in which the monomer exists, namely the benzoid and quinoid forms of PEDOT, as seen in Figure 6.11 on the left and right respectively. The question is whether the dedoping process influences the structure of the EDOT monomers as compared to the reference sample, and if those changes can be linked to the observed drop in electrical conductivity for all dedopants. Implications of the monomer structure on macroscopically measured properties are expected since both forms of the monomer favor different conformations of the chain. While the benzoid form of the monomer bonds to the next repeating unit of the polymer chain via a single bond, in the quinoid form monomers are connected via double bonds. In the former case rotation around the bond axis is energetically more favored than in the latter case. This causes differences in the conformation of the polymer chain, as a more coil-like conformation is taken on by the chain if the benzoid form is prevalent. If the quinoid form dominates, the opposite is the case, since the high energy barrier for

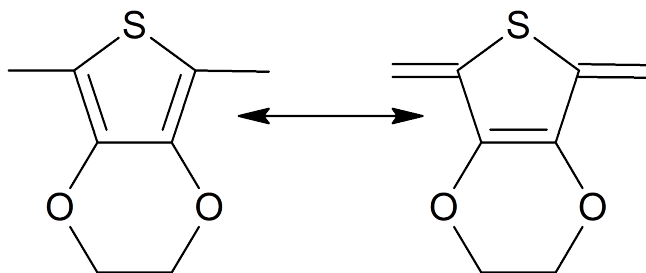


Figure 6.11: Benzoid (left) and quinoid form (right) of EDOT, impacting polymer chain conformation.

rotation causes the chains to adapt an extended-coil or linear conformation. This in turn is expected to be more favorable for charge transport due to better overlap of p-orbitals and therefore greater spatial extent of the conjugated π -system.

For the acquisition of Raman spectra of dedoped PEDOT:PSS films, preliminary tests were performed regarding feasible intensities of the excitation laser, as well as suitable integration times. Figure 6.12 shows spectra obtained at 2 mW laser power on the left and 0.5 mW on the right for different integration times. Irrespective of laser power, additional peaks arise in the spectra after longer integration times, mostly located around 1500 cm^{-1} , in addition to an increased background. Therefore, for all measurements discussed in this study, spectra were acquired by scanning across the sample, in order to decrease the dwell-time of the excitation laser on each individual spot. This allowed for usage of higher laser powers and additionally shorter integration times, without damaging the samples.

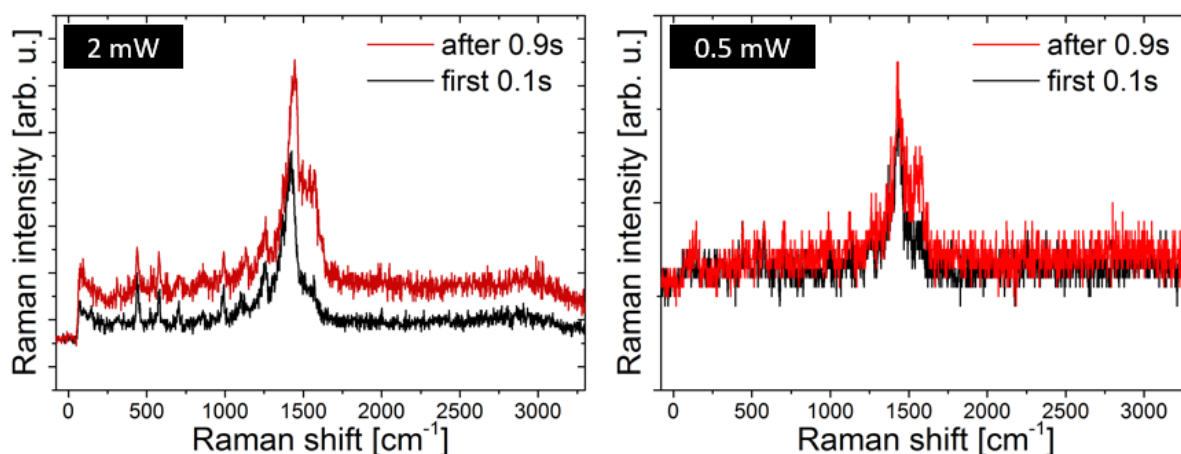


Figure 6.12: Raman spectra of an exemplary PEDOT:PSS film acquired at laser powers of 2 mW (left) and 0.5 mW (left). Integration times of 0.1 s are represented in black spectra, while times of 0.9 s are shown in red spectra. Taken from [3].

Raman spectroscopy was performed on PEDOT:PSS thin films prepared on glass substrates by irradiating macroscopic, representative sections of the films and measuring

Raman spectra at each illuminated spot. Figure 6.13a shows an optical micrograph of an exemplary film overlayed with a Raman intensity map, which was obtained from the measurement of the intensity of a prominent Raman band (located at 1435 cm^{-1}) within

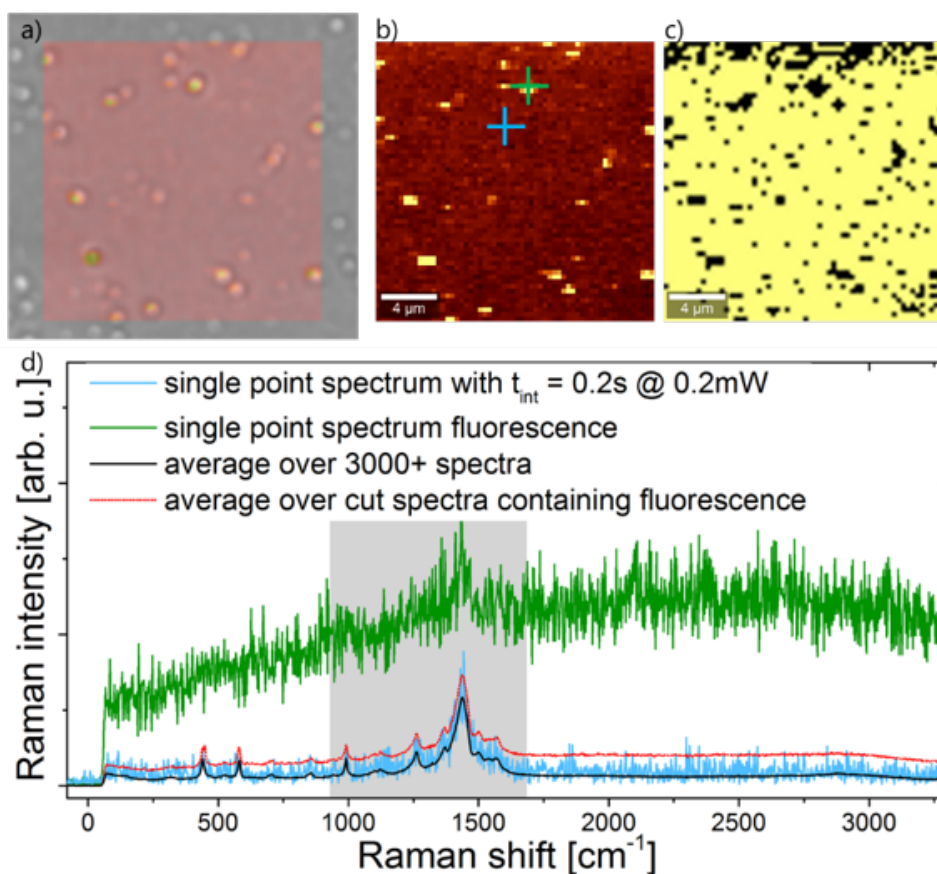


Figure 6.13: a) Overlay of an optical micrograph of an exemplary PEDOT:PSS film, with a corresponding $20\text{ }\mu\text{m} \cdot 20\text{ }\mu\text{m}$ Raman intensity map. A correlation between particles visible in the micrograph and a very high Raman intensity is apparent. The strong signal typically originates from a strongly fluorescent background. b) Raman intensity map corresponding to a), obtained using a band-pass filter around $1435.0(375)\text{ rel cm}^{-1}$. c) Mask used for averaging multiple Raman spectra over the scanned area. Out of the $60 \cdot 60$ pixels, corresponding to 3600 spectra, only the yellow pixels are considered for averaging. Black ones were deemed unsuitable, due to fluorescence contributions to the signal. A Raman map was used for averaging of the spectra, if more than 3000 pixels in the mask were yellow. d) Green and blue spectra taken at the positions indicated with the cross-hairs in b) after an integration time of 0.2 s . Noisy spectra were obtained in both cases, however with a strong fluorescence signal in the green spectrum. The red curve represents the average Raman spectrum after taking into account all pixels, exhibiting a larger background in the entire spectrum, while the signal-to-noise ratio is improved in the black curve after omitting the black pixels. Here, characteristic signals of PEDOT become visible due to averaging of the noise. Taken from [3].

the spectrum across a macroscopic area of $20\text{ }\mu\text{m} \cdot 20\text{ }\mu\text{m}$. Upon closer investigation of the overlay image, the correlation between impurities on the film surface and exceptionally strong signals becomes apparent. The latter signals typically have strong contributions from fluorescence. The Raman intensity maps are thus carefully analyzed regarding fluorescence signals, as highlighted by the blue and green cross-hairs in Figure 6.13b. These correspond to the blue and green spectra in Figure 6.13, which show large contributions from fluorescence in the green spectrum that are absent in the blue spectrum. In order to avoid detriments to the data analysis, a mask is used (shown in Figure 6.13c) which neglects pixels in the Raman intensity map that show strong fluorescence contributions. The neglected pixels are shown in black, while the ones used for averaging the Raman signal over more than 3000 pixels are highlighted in yellow. The improvement due to exclusion of fluorescence can be seen when comparing the red spectrum (averaged with fluorescence signal) to the black spectrum (averaged under exclusion of fluorescence) in Figure 6.13d. Averaging under the exclusion of fluorescent pixels yields a better signal-to-noise ratio, with background levels reduced in general.

For discussion of the Raman spectra of dedoped PEDOT:PSS films, the same concentrations as for the XPS measurements shown above were used. Figure 6.14 shows Raman spectra obtained for the three dedopant salts, with the reference curve for a PEDOT:PSS film only post-treated with EG in black. The band positions for the latter match very well with the ones measured by Stavytska-Barba *et al.* [57] Upon dedoping, the central band located at around 1420 cm^{-1} becomes narrower with increasing concentration of dedopant. More accurately, since the central band is asymmetric, with the lower wavenumber contribution decreasing in intensity, the dedoping makes the former appear narrower. Taking

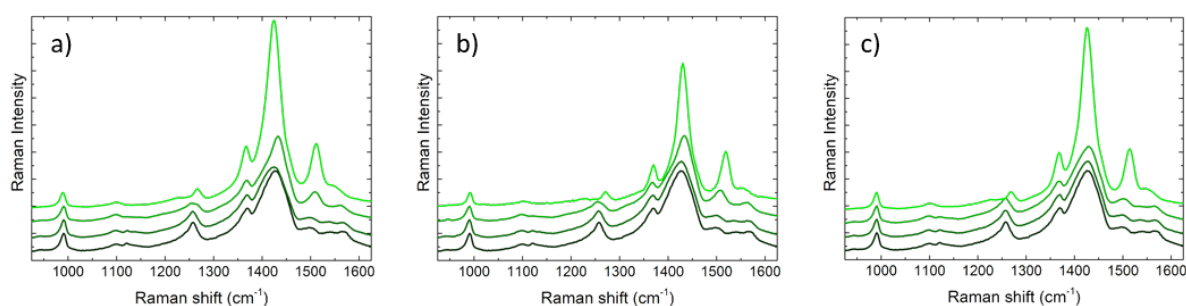


Figure 6.14: Raman spectra of PEDOT:PSS dedoped with a) NaHCO_3 in concentrations of 5 mM, 24 mM and 71 mM, b) Na_2SO_3 in concentrations of 5 mM, 12 mM and 91 mM and c) NaBH_4 in concentrations of 5 mM, 12 mM and 91 mM. Spectra are stacked on top of each other for clarity. While the black spectra in each image represent PEDOT:PSS without dedopant, the color gradient from dark to light green indicates increasing concentration of the respective dedopant. Taken from [3].

the analysis of Raman spectra performed by Nevrela *et al.* into consideration, this lower wavenumber contribution can be assigned to the quinoid form of PEDOT. A decrease of this contribution therefore indicates a decrease in relative amount of that form. Additionally, the shoulder located at 1499 cm^{-1} in the reference spectrum, becomes more pronounced and shifts to larger wavenumbers upon dedoping in all cases. This is again indicative of an increase in the relative amount of the benzoid form of PEDOT as function of dedopant concentration. Both the decrease of the amount of quinoidal PEDOT, and the increase in benzoidal PEDOT are in line with the observed loss in electrical conductivity which was observed for increasing concentrations of dedopant, irrespective of the type of employed dedopant. As discussed above, this most likely correlates with a transition from a more extended-coil or linear conformation of PEDOT chains when the quinodal form is present, into a more coil-like conformation after dedoping, due to a strong increase in the amount of the benzoidal form. In conclusion, the macroscopic loss in electrical conductivity can be assigned to the combination of the transition from a linear or extended-coil conformation to a more coil-like conformation, and a decrease in the number of charge carriers.

6.3 Summary

In summary, dedoping of PEDOT:PSS thin films with readily available inorganic salts presents a facile and feasible way of optimizing thermoelectric properties. The improvement relies largely on the increase of Seebeck coefficients, while a simultaneous decrease in electrical conductivity is observed. This can be tolerated, since the Seebeck coefficient of highly conducting PEDOT:PSS in the PH1000 formulation is typically very low and thus the limiting factor. Notably, the Seebeck coefficients and power factors improve for all dedopants, irrespective of the latter's chemical properties. NaHCO_3 which decomposes in acido- basic reactions increases the Seebeck coefficient just as well as Na_2SO_3 and NaBH_4 which exhibit redox-activity. When comparing the latter two salts, it was also found that the improvement depends less on the employed reducing agent and its properties (e.g. redox potential) and more on the absolute number of reducing equivalents which are present in solution and able to interact with PEDOT. The maximum power factors achieved in this study were $100\text{ }\mu\text{WK}^{-2}\text{m}^{-1}$ upon dedoping with NaHCO_3 , $90\text{ }\mu\text{WK}^{-2}\text{m}^{-1}$ with Na_2SO_3 and $95\text{ }\mu\text{WK}^{-2}\text{m}^{-1}$ with NaBH_4 at optimal concentrations.

UV-Vis spectroscopy is a non-destructive way of determining changes in the charge carrier concentration, and allows to monitor a steady transition of bipolarons as majority charge carriers into polarons for low and intermediate concentrations of dedopant, which can be detected in the infrared region of the spectrum. With further increase, absorption

features in the visible region of the spectrum appear, which correspond to neutral states of PEDOT. A correlation between dedopant concentrations at which the optimum power factors are exceeded, and the onset of appearance of absorption features related to neutral states was also found.

XPS aids in understanding the ramifications of the dedoping process both in terms of changes in the average oxidation state of PEDOT (thus the charge carrier concentration) and the PSS-to-PEDOT ratio. Dedoping with all three salts yielded more efficient removal of PSS as function of dedopant concentration, as compared to the reference. Notably, treatment with NaHCO_3 does not cause a shift of the PEDOT-associated peaks, supporting the purely acido-basic nature of the reaction in that case. As opposed to this, for both Na_2SO_3 and NaBH_4 these peaks shift towards lower binding energies, indicating a decrease of the average oxidation level. This is in line with the observed transition of bipolarons as primary charge carriers to polarons, and finally to neutral states for high dedopant concentrations. The peak shift thus indicates dedoping through redox reactions.

Finally, Raman spectroscopy revealed conformational changes in PEDOT chains upon dedoping with all three of the salts. The relative amount of the quinoidal form of PEDOT diminishes with increasing concentration of dedopant, steadily increasing the fraction of the benzoidal form. The former favors extended-coil or linear conformations, which are more suitable for charge transport, while the latter favors more coil-like conformations of PEDOT chains. This observed transition fits well with the decrease in the electrical conductivity, irrespective of the type of dedopant.

In conclusion, dedoping of PEDOT:PSS films using readily available inorganic salts, is a viable method for the improvement of thermoelectric properties. The comprehensive picture drawn in this study, should provide a stimulus for further research using more complex types of agents with acido-basic and redox-active properties.

7 Simultaneous enhancement of Seebeck coefficient and electrical conductivity in PEDOT:PSS through post-treatment with ionic liquids

Results of this chapter have been published in the article: Ionic Liquids as Post-Treatment Agents for Simultaneous Improvement of Seebeck Coefficient and Electrical Conductivity in PEDOT:PSS Films (N. Saxena et al., ACS Appl. Mater. Interfaces, 11, 8060-8071, DOI: 10.1021/acsaem.7b00334). [3] Parts of this chapter are based on the bachelor's theses of Benjamin Pretzl [50] and Xaver Lamprecht. [24]

In Chapters 5 and 6, the thermoelectric properties of PEDOT:PSS thin films were improved through the targeted modification of the thermal conductivity and Seebeck coefficient, respectively.

PEDOT:PSS is regarded as one of the most promising materials for usage in thermoelectric devices and applications. This can be seen in the vast amount of publications which came out in recent years. For instance, it was found that the electrical conductivity of PEDOT:PSS could be greatly improved through treatment of the thin films with different chemicals. Among these are e.g. high boiling point solvents such as EG [58], DMSO [59, 60] or organic solutions of inorganic salts. [61]

In a similar fashion inorganic and organic acids and bases can be used, often to even stronger effect. Yeon *et al.* achieved electrical conductivities up to 4000 S/cm by treating PEDOT:PSS films with concentrated nitric acid. [62] Other acids such as hydrochloric or sulfuric acid are also promising regarding the achievable electrical conductivities of up to approximately 2000 S/cm. [63, 64] Ouyang *et al.* used organic acids such as oxalic acid, malonic acid or methanesulfonic acid and obtained PEDOT:PSS films with electrical conductivities of up to 3300 S/cm. [65] PEDOT:PSS is known to phase-separate upon film deposition, with conducting, PEDOT-rich grains being surrounded by a PSS-shell and

embedded in a matrix thereof. However, since PSS itself does not allow for charge transport, its presence is detrimental to the overall conductivity of the film. In all the cases, the often drastic improvement of the electrical conductivity is assigned to a multitude of factors. Firstly, the employed agents are often polar in nature and/or possess high dielectric constants. This facilitates electrostatic interactions with the negative polyanion PSS, and aids in the removal of the latter from the film, leading to improved charge transport between the grains. Due to its conjugated nature, PEDOT forms super-molecular aggregates via π - π -interactions. Charge transfer between different chains is more favored, the smaller the distance between them becomes. Lastly, the predominant orientation has implications on the preferred direction of charge transport. One typically distinguishes a face-on orientation, which favors charge transport perpendicular to the substrate surface and an edge-on orientation, which favors charge transport parallel to the substrate surface. [66, 67]

The PH1000 formulation of PEDOT:PSS possesses a PEDOT-to-PSS ratio of 1 : 2.5, and is such that the PEDOT chains are heavily doped with positive charge carriers. While thin films prepared with this formulation allow for the high electrical conductivities discussed above, the high charge carrier concentration typically leads to low Seebeck coefficients of approximately 20 $\mu\text{V/K}$. As seen in Chapter 6, the Seebeck coefficient has a larger impact on the obtainable electrical power in a thermoelectric device, due to its square dependence on the Seebeck coefficient. Thus, much emphasis has also been put on the improvement of the latter through dedoping, as discussed before. [68]

Both approaches for the enhancement of thermoelectric properties in PEDOT:PSS thin films are legitimate. However, the employed agents and methods typically only address the improvement of one thermoelectric quantity at a time. To this end, the material class of ILs came into focus. ILs are ionic compounds which typically consist of a large organic cation, often based on imidazole, pyridine, etc., and an anion. Due to weak interactions between the ions, melting points of ILs typically lie below 100 $^{\circ}\text{C}$, or often even around room temperature, in addition to a large boiling point giving them a large temperature window in which the liquid phase is stable. A feature that makes them suitable for usage in the enhancement of properties of PEDOT:PSS films, is the binary nature of both the ILs and PEDOT:PSS. The electrostatic bond between PEDOT and PSS can be broken due to electrostatic screening and selective interactions of PEDOT with the anions of the ILs, while PSS interacts with the corresponding cations.

Badre *et al.* made use of these features, by adding the IL EMIM TCB to a PEDOT:PSS solution, prior to film deposition. Apart from high electrical conductivities of around 2000 S/cm, they also observed exceptional transparency properties of the thin films, making them suitable for application as transparent electrodes. [69] They could show using

infrared spectroscopy and atomic force microscopy that EMIM TCB is incorporated into the film.

In a follow-up study by Murphy *et al.*, x-ray and neutron scattering experiments revealed the interactions of EMIM TCB with PEDOT:PSS in more detail. It was found that EMIM TCB disturbs the mesh-like structure of PSS, to which shorter fragments of PEDOT are attached. As discussed above, this originates from a modification in the electrostatic interactions due to the addition of EMIM TCB, which leads to interactions of PEDOT with the TCB-anion and of PSS with the EMIM cation. This was an additional hint at the modification of the structure upon IL-treatment. [70]

Following this, Izarra *et al.* performed density functional theory calculations, in order to predict interactions between different ILs with EMIM cations and PEDOT:PSS. Notably, their study confirmed the results obtained by Kee *et al.*, who investigated the impact of five EMIM-based ILs on the electrical properties of PEDOT:PSS thin films, while attempting to link them to the results of their spectroscopic and morphological analysis. [71, 72]

Since most of the discussed studies mainly focus on the changes in the electrical conductivity upon IL-treatment, this chapter additionally investigates potential modifications of the electronic structure of PEDOT:PSS. Therefore, PEDOT:PSS films subjected to a post-treatment with three different ILs are characterized regarding Seebeck coefficients and electrical conductivities, allowing for the calculation of power factors. Due to the high boiling points of ILs, an additional washing step with THF is introduced, in order to deduce whether potential changes in the thermoelectric properties are correlated with the presence of ILs in the films. UV-Vis spectroscopy reveals modifications of the charge carrier concentration and allows for a link to the Seebeck coefficients. On the other hand, GIWAXS gives insight into the influence of ILs on the structure of PEDOT:PSS, and thus allows for a link to the electrical conductivity and the deduction of a morphological model. The three ILs were chosen on a rational basis, such that they possess the same EMIM cation, while the anion changes. Specifically, EMIM DCA, EMIM TCB and EMIM BF₄ were chosen for the post-treatment. An additional PEDOT:PSS film was treated with pure THF in order to prove that the properties of the film were not influenced by the solvent for the ILs itself, and thus serves as reference. The washing step is also performed on this sample, to further strengthen the viability of THF as carrier for the ILs.

7.1 Thermoelectric characterization

IL-treated films are investigated regarding changes in their thermoelectric properties. Figure 7.1a shows the Seebeck coefficients of PEDOT:PSS films treated with EMIM DCA (green), EMIM TCB (orange) and EMIM BF₄ (blue) before the washing step with pure

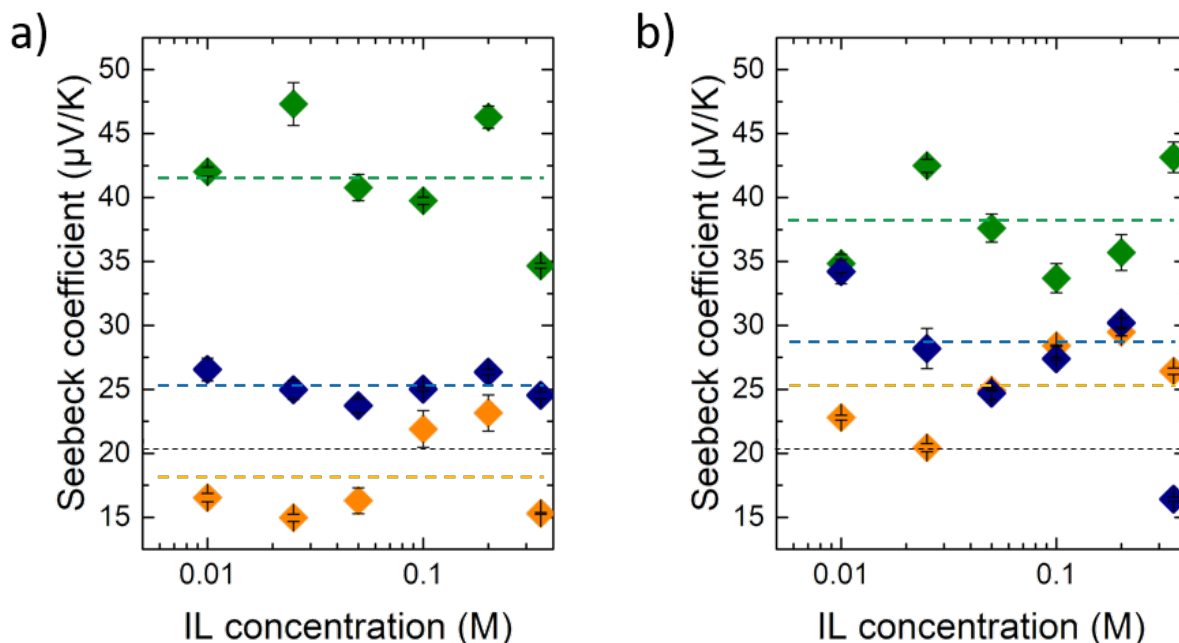


Figure 7.1: Seebeck coefficients for PEDOT:PSS films post-treated with EMIM DCA (green), EMIM TCB (orange) and EMIM BF₄ (blue) a) before and b) after the washing step with pure THF. Reference values for PEDOT:PSS post-treated with pure THF are indicated by dashed black lines, while colored dashed lines represent guides to the eye. Y-axis scales were chosen to be the same, in order to highlight the changes upon washing with pure THF. Adapted from [4].

THF, with the reference value for PEDOT:PSS only treated with pure THF indicated by the dashed black line. One immediately finds drastic changes in the Seebeck coefficients upon treatment with EMIM DCA and EMIM BF₄, while treatment with EMIM TCB yields values varying around the reference value. While there appears to be a weak concentration dependence of the Seebeck coefficients, different distinct levels are discernible for the employed ILs. The average Seebeck coefficients are roughly 42 μV/K, 26 μV/K and 18 μV/K, for treatment with EMIM DCA, EMIM TCB and EMIM BF₄, respectively. This is already a first indication of the influence of the chosen anion on the electronic interaction with PEDOT chains, since the latter are for the most part responsible for the thermoelectric properties. The results after the washing step with pure THF, which was performed in order to ensure complete removal of the ILs, are shown in Figure 7.1b. The weak concentration dependence remains, while the average values of the Seebeck coefficients change slightly. While for EMIM DCA-treated samples the average value lies at around 37 μV/K, for both EMIM BF₄- and EMIM TCB-treated samples a slight increase to 28 μV/K and 25 μV/K is seen, respectively.

These results can be put into perspective with the ones obtained by other researchers. Fan *et al.* performed a post-treatment of PEDOT:PSS films with sulfuric acid and/or

sodium hydroxide prior to treatment with different ILs dissolved in methanol. [73] The Seebeck coefficients of their EMIM DCA-treated samples closely match the ones shown in Figure 7.1, albeit at much larger electrical conductivities, which will be discussed below. Sulfuric acid is known to strongly alter the morphology of PEDOT:PSS thin films, by efficiently removing PSS and improving the structural order of the PEDOT-component within the film. This is the reason for the high electrical conductivities which were observed in the study. Additionally, methanol was used as solvent for the ILs, which itself also has the ability to modify PEDOT:PSS films, even though to a lesser degree. As is proven in our case for the 0 M samples, THF itself does not change the Seebeck coefficient of the treated PEDOT:PSS films, leading to values around $20 \mu\text{V/K}$. The former thus qualifies as solvent, since it allows for closer study of the direct impact of the ILs on the electronic properties of PEDOT:PSS.

When discussing the mechanism behind the improvement of the Seebeck coefficient, ion migration and accumulation on the surface of the PEDOT:PSS films due to the temperature gradient could be listed as possibility. An ionic contribution to the Seebeck coefficient would then lead to the observed improvement. In this case, it is however believed not to be the case. As was studied in great detail and observed by Wang *et al.*, no time-dependence of the Seebeck coefficient is observed during the measurement. [74] Each measurement was performed for more than 20 min, in order to be able to neglect possible contributions from ion migration/accumulation. It should also be mentioned that values for the ionic Seebeck coefficient are typically found in the mV/K range, which are significantly larger than the obtained values from this study. Fan *et al.* came to a similar conclusion, and also deemed ionic Seebeck coefficient contributions as non-significant.

Apart from that, the values for the Seebeck coefficient obtained after treatment with both EMIM DCA and EMIM BF_4 match very well with their findings.

In Figure 7.2, the electrical conductivities of PEDOT:PSS films post-treated with the employed ILs in different concentrations are summarized. In its pristine state, PEDOT:PSS is only weakly conducting, showing values for the electrical conductivity on the order of 1 S/cm , as indicated by the dashed black line. The post-treatment with all three ILs appears to positively affect the electrical conductivity, as in all three cases an increase compared to the reference can be observed. The maximum conductivities found for the highest concentrations of EMIM DCA, EMIM TCB and EMIM BF_4 are roughly 900 S/cm , 600 S/cm and 470 S/cm , respectively. In all cases, the conductivity increases with IL concentration, until a saturation level is reached, which is different depending on the employed IL. Notably, for the lowest concentration of EMIM BF_4 , already an electrical conductivity exceeding 120 S/cm is reached, while the obtained values for the other two ILs are much closer to the reference value. As seen in Figure 7.2b, a drastic decrease in the

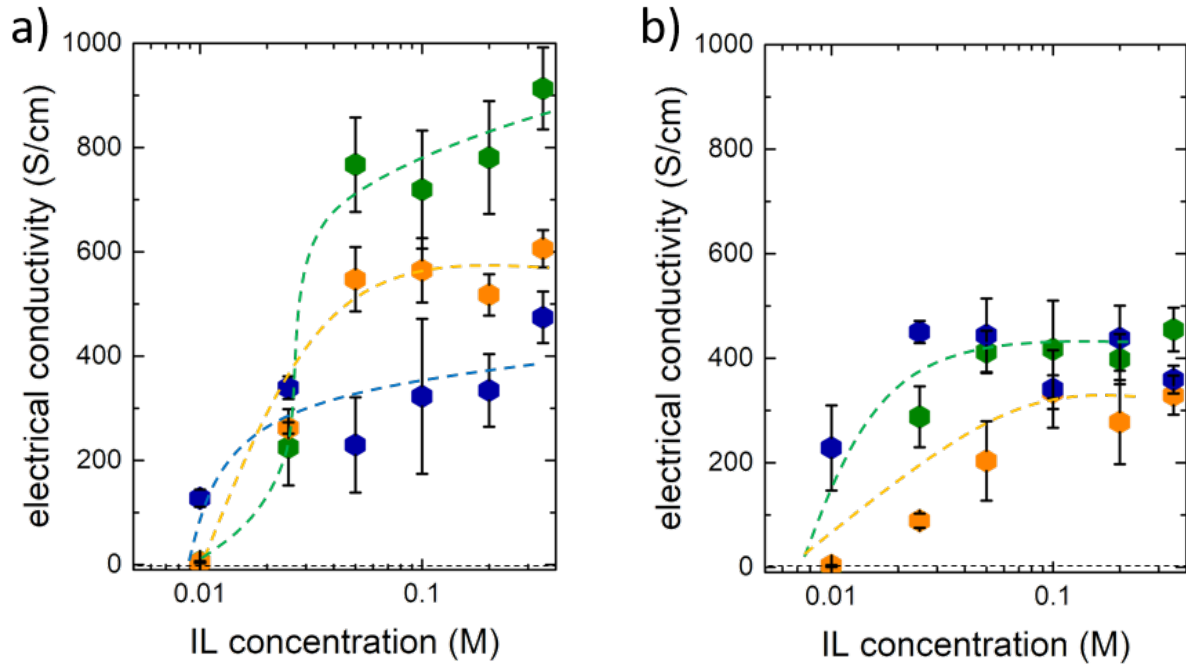


Figure 7.2: Electrical conductivities for PEDOT:PSS films post-treated with EMIM DCA (green), EMIM TCB (orange) and EMIM BF₄ (blue) a) before and b) after the washing step with pure THF. Reference values for PEDOT:PSS post-treated with pure THF are indicated by dashed black lines, while colored dashed lines represent guides to the eye. Y-axis scales were chosen to be the same, in order to highlight the changes upon washing with pure THF. Adapted from [4].

saturation conductivities, especially for EMIM DCA- and EMIM TCB-treated samples, is observed. The respective maximum conductivities are around 450 S/cm and 330 S/cm, while the saturation conductivity of EMIM BF₄-treated samples is mostly unaffected. While EMIM DCA- and EMIM BF₄-treated samples show similar saturation conductivities, EMIM TCB-treated ones exhibit the lowest values after the washing step with pure THF.

The simultaneous increase of both Seebeck coefficient and electrical conductivity due to the post-treatment with ILs is counter-intuitive at first, since an inverse relationship between these two quantities is expected from theory. However, the electrical conductivity in polymer thin films is not only governed by the number of charge carriers, but also by their mobility or the charge-transport properties in general. These are for the most part governed by the inner structure of the polymer film, which is most probably affected due to electrostatic interactions of the negatively charged PSS and the positively charged EMIM cation. The post-treatment with ILs can therefore capitalize on the binary nature of both PEDOT:PSS and the three chosen ILs, and thus allows for simultaneous en-

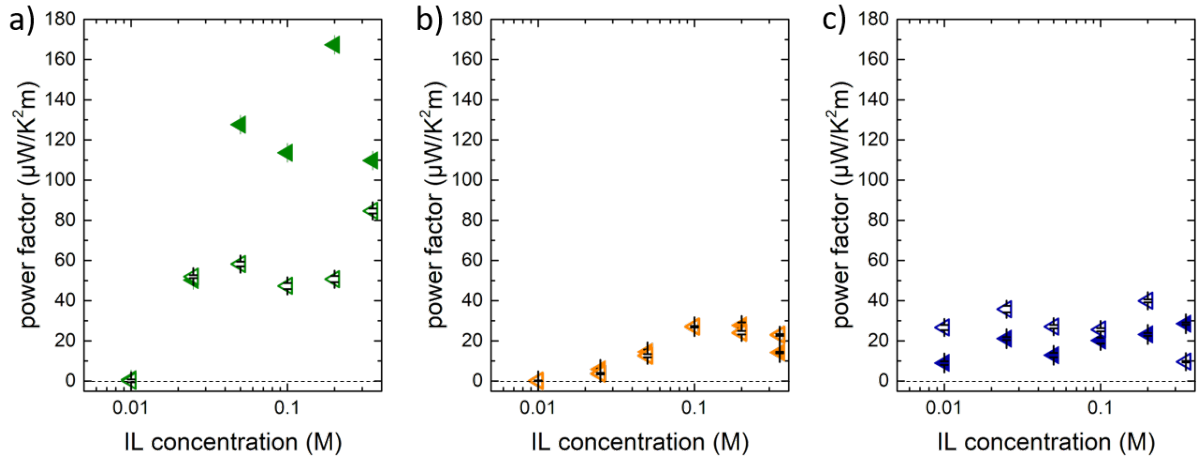


Figure 7.3: Power factors for PEDOT:PSS films post-treated with a) EMIM DCA (green), b) EMIM TCB (orange) and c) EMIM BF_4 (blue) before (solid symbols) and after (hollow symbols) the washing step with pure THF. Reference values for PEDOT:PSS post-treated with pure THF are indicated by dashed black lines. Y-axis scales were chosen to be the same, in order to highlight the differences between the employed ILs. Adapted from [4].

hancement of both the Seebeck coefficient and electrical conductivity through Coulombic screening of the coordinative bond between PEDOT and PSS. Therefore, it is expected that the anions of the ILs primarily interact with PEDOT chains carrying positive charge carriers and thus influence the primary doping levels, which ultimately affects the Seebeck coefficient. In line with this, the positively charged EMIM cations are expected to interact with the negative polyelectrolyte PSS, and influence the secondary doping through morphological re-arrangement. Both notions will be investigated further in the sections on the spectroscopic and morphological characterization below.

Nevertheless, the thermoelectric power factors can be calculated for the different ILs before and after washing step with pure THF, as shown in Figure 7.3. The power factor of the reference PEDOT:PSS film only treated by THF is most strongly limited by the low electrical conductivity, which is in the order of 1 S/cm. Obtained power factors for the reference PEDOT:PSS film are therefore approximately $0.02 \mu\text{WK}^{-2}\text{m}^{-1}$.

The power factors obtained for EMIM DCA-treated films are among the highest values obtained in this work. The trend is largely governed by the increasing electrical conductivity as function of EMIM DCA concentration, since the Seebeck coefficient is mostly independent of the latter. Thus, a maximum power factor of $170 \mu\text{WK}^{-2}\text{m}^{-1}$ is found at a concentration of 0.2 M, which is approximately three orders of magnitude larger than for the reference sample only treated with pure THF. The washing step drastically reduces the power factor roughly by a factor of 0.5. The maximum value of $82 \mu\text{WK}^{-2}\text{m}^{-1}$ is now found at the highest concentration of 0.35 M, with the trend of increasing values as

function of IL concentration still remaining. Decreasing levels of the Seebeck coefficient and the electrical conductivity upon washing with pure THF are mostly responsible for this observation.

In the case of EMIM TCB-treatment, the maximum achieved power factor both before and after the washing step is $27 \mu\text{WK}^{-2}\text{m}^{-1}$. The generally lower values can be explained by the Seebeck coefficients after the EMIM TCB-treatment lying very close to the reference value. The increase of the electrical conductivity in comparison to the reference, is mostly responsible for the observed jump in the power factor. Washing does not influence the values greatly, since the decrease of the maximum conductivity from roughly 600 S/cm to 330 S/cm is compensated by a slight increase of the average Seebeck coefficient from roughly $18 \mu\text{V/K}$ to $25 \mu\text{V/K}$. Nevertheless, a trend towards increasing power factors with increasing IL concentration is discernible.

Lastly, EMIM BF_4 -treated samples show the weakest concentration dependence with the values varying around $20 \mu\text{WK}^{-2}\text{m}^{-1}$ before washing and even slightly increasing to $28 \mu\text{WK}^{-2}\text{m}^{-1}$ after the washing step with pure THF. The increase in power factor is easily understood, when considering the slightly rising saturation levels of the electrical conductivity in combination with higher average Seebeck coefficients obtained after the washing step.

In conclusion, the post-treatment of PEDOT:PSS films with ILs is a promising approach for improving thermoelectric properties, due to the simultaneous enhancement of the Seebeck coefficient and the electrical conductivity. Therein, post-treatment with EMIM DCA yields the highest power factors through the combination of an almost doubled Seebeck coefficient, along with a high electrical conductivity. It is followed by the treatment with EMIM BF_4 , which also gives increased Seebeck coefficients alongside decent electrical conductivities. Even though higher than the reference values, the power factors after EMIM TCB-treatment are low in comparison to the other investigated ILs. This originates from a lack of notable increase in the Seebeck coefficient compared to the reference, while still yielding improved electrical conductivities.

It can therefore be concluded that the initial hypothesis, of the anion only influencing the Seebeck coefficient due to electrostatic interactions between the former and the positively charged PEDOT, is too simple. It fails to take the effect of the anion on the intra-molecular binding forces within the ion pairs of the ILs into account. Men *et al.* found in their systematic study of pyridinium-based ILs that an increasing basicity of the anions increases the magnitude of charge transfer from the anions to the positively charged nitrogen atoms in the EMIM cations. Thus, a difference in the inter-molecular binding forces might lead to a change in the properties which affect PEDOT:PSS both on

an electronic and morphological level. Both aspects will be studied further in the sections on the spectroscopic and morphological characterization, respectively.

7.2 Spectroscopic characterization

As already discussed in Chapter 6, UV-Vis spectroscopy is a facile method for determining the electronic structure of conjugated polymer thin films. In the case of IL-post-treatment, it allows for the elucidation of differences in the charge carrier concentration, which will for the most part affect the Seebeck coefficient of the treated films.

In Chapter 6, it was seen that PEDOT:PSS in its pristine state is heavily doped, due to the PEDOT-to-PSS ratio of 1 : 2.5. This leads to the predominant presence of bipolarons as majority charge carriers in pristine PEDOT:PSS. The black curves in all three graphs of Figure 7.4 represent PEDOT:PSS films in their pristine state. The lack of notable absorption features in the visible range is in line with the observations made by e.g. Massonnet *et al.*, who measured UV-Vis spectra up to wavelengths of 2500 nm. [56] Due to bipolarons being the primary type of charge carriers, optical absorption mostly takes place at very high wavelengths, or low energies, as the charge carriers are easily

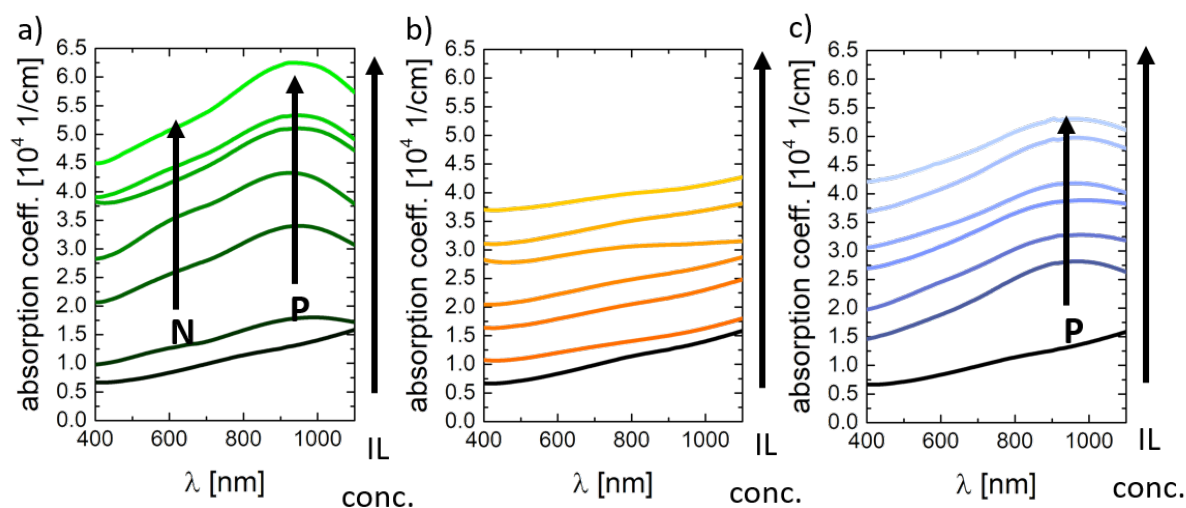


Figure 7.4: Absorption coefficients of PEDOT:PSS films treated with a) EMIM DCA, b) EMIM TCB and c) EMIM BF₄. Increasing concentrations of the respective ILs are represented by the gradient from darker to brighter colors, while in all graphs the spectrum for the reference PEDOT:PSS film only treated with pure THF is added in black for comparison. The curves are stacked vertically for clarity. Absorption features assigned to the presence of polaronic states (P) and neutral states (N) are marked with black arrows. Adapted from [4].

excited. The emergence of absorption features at smaller wavelengths indicates a loss in charge carrier concentration. [3, 56]

UV-Vis spectra of EMIM DCA-treated PEDOT:PSS films can be seen in Figure 7.4a. Immediate changes are observable upon IL-treatment. The broad shoulder assigned to bipolarons which normally extends from the infrared wavelength range into the visible one, transforms into an absorption peak centered around 900 nm. This feature is assigned to polaronic states, as discussed in Section 6.2.1. Additionally, the presence of neutral species is observed, which is concluded from the absorption peaks centered around 600 nm. It can be concluded that the treatment of PEDOT:PSS with EMIM DCA leads to a strong reduction of bipolarons into polarons and neutral species, which is in agreement with the strong increase in the Seebeck coefficient. Also the fact that the features do not significantly change as function of EMIM DCA concentration corresponds to the lack of concentration dependence of the Seebeck coefficient.

In contrast, EMIM TCB-treated films behave very differently, as can be seen in Figure 7.4b. For all concentrations the shape of the curve is mostly retained. No additional peaks arise, suggesting no loss of charge carriers. The fact that this treatment does not significantly alter the Seebeck coefficient fits very well with this notion.

Lastly, EMIM BF₄-treated films in Figure 7.4c are again subject to changes. An absorption feature similar to the one observed in EMIM DCA-treated films at around 900 nm is again found here, although the peak around 600 nm is almost not discernible. This suggests that EMIM BF₄-treatment leads to the transformation of bipolarons into polarons, but almost no neutral species can be found.

When comparing the treatment of PEDOT:PSS films with the three ILs, a correlation between the average Seebeck coefficients and the charge carrier concentration is found. EMIM TCB-treatment does not induce polaronic or neutral states, and thus leads to no significant improvement of the Seebeck coefficient. EMIM BF₄-treatment mostly leads to the formation of polaronic states and thus shows slightly improved Seebeck coefficients. In this regard, EMIM DCA-treatment is the most promising, as both polaronic and neutral states are induced, and therefore also the largest Seebeck coefficients are achieved.

A question which arises upon closer investigation of the results, is if there is a structural motive through which one can predict the effect of the anion on the electronic properties of PEDOT:PSS and therefore the possible increase in the Seebeck coefficient. When looking at the structure of the anions, seen in Section 4.1.2, there are two different aspects in which the structures of the anions differ. The DCA-anion is angulate, while both the TCB- and BF₄-anion possess spherical symmetry. Also the sizes of the anions vary, especially when comparing the TCB- and BF₄-anion. In the latter case, the central boron atom is surrounded by four fluorine ligands, whereas in the TCB-ion the boron is surrounded by

four biatomic cyano-ligands. Both the symmetry and the size of the anion influence how the nominal single negative charge is distributed over the atoms. For both the spherical TCB- and BF_4 -anion, the charge is homogeneously distributed over the spatial extent of both ions. It should be mentioned that since the TCB-anion is larger in size, the effective 'density' of negative charge is expected to be smaller than in the case of the BF_4 -anion. In the DCA-anion, the charge is expected to be concentrated for the most part on the central nitrogen atom. Regarding the interaction between the anions and the conjugated PEDOT chains, it seems to be more favorable to have the negative charge strongly localized on the anion.

With this notion, it is easy to find a correlation between the structures of the anions used in this study and the resulting Seebeck coefficients after post-treatment. The TCB-anion shows no significant improvement, due its large size and spherical symmetry. The BF_4 -anion is more favorable, being able to concentrate the negative charge better due to its smaller size. In the DCA-anion, the negative charge is strongly localized on the central nitrogen atom, and therefore leads to the highest observed Seebeck coefficients in this study.

This hypothesis is further supported by the systematic study performed by Spange *et al.* [75] In their work, they listed so-called Kamlet-Taft solvent parameters for 102 different ILs, which also describe their hydrogen-bond-donating and -accepting ability. Therein, the hydrogen-bond basicity, i.e. the ability of an anion to use its negative charge for interactions with cations, is largest for the DCA-anion, followed by the BF_4 - and the TCB-anion. In the given order, these anions interact less strongly with PEDOT chains through increase of the latters' electron density. An increase in the electron density could be linked to a decrease in the average oxidation level and thus to the observed increase in the Seebeck coefficient.

In conclusion, anions with a larger hydrogen-bond basicity appear to more efficiently increase the electron density of PEDOT chains, thus leading to more strongly increased Seebeck coefficients.

7.3 Structural characterization

In the previous sections, it was seen that the treatment of PEDOT:PSS films with ILs affects the thermoelectric properties in a multi-faceted way. This originates from the binary nature of both PEDOT:PSS and the ILs. While the anions primarily interact with the conducting PEDOT and thus mostly affect the Seebeck coefficients, an interaction between the negatively charged PSS and the cations can be expected. In this respect, it

would be interesting to find out, whether the rational choice of the anion also influences the way that this interaction takes place.

In literature, it was seen many times that the morphology of PEDOT:PSS films can be influenced by treatment with high-boiling point solvents [66], acids [55,65] and organic solutions of inorganic salts [61]. This effect mostly relies on the removal of excess PSS,

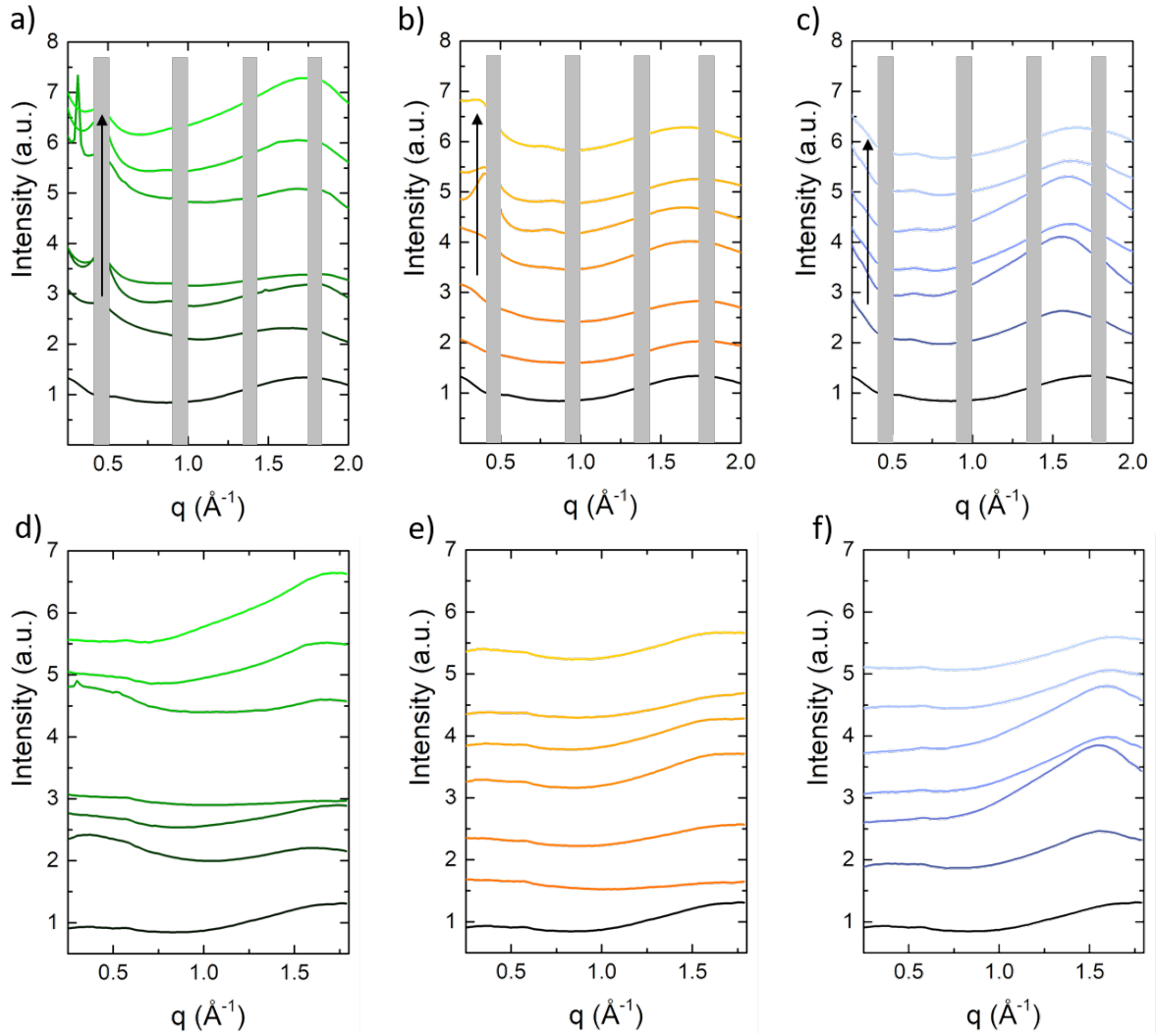


Figure 7.5: Sector integrals obtained from GIWAXS for PEDOT:PSS films post-treated with EMIM DCA (green), EMIM TCB (orange) and EMIM BF₄ (blue). a)-c) Vertical sector integrals calculated for azimuthal angles χ of -15° to 15° , d)-f) horizontal sector integrals calculated for azimuthal angles χ of 70° to 80° . Gray bars in a)-c) represent inter-module gaps of the detector, while black arrows indicate long-range stacking of PEDOT chains. The curves for the reference PEDOT:PSS film are shown in black, while the gradients from dark to bright colors indicate increasing IL concentrations. For clarity of presentation, the curves are shifted along the y-axis. Adapted from [4].

which inhibits charge transport between conducting PEDOT domains, in addition to preferable re-arrangement of PEDOT crystallites in terms of intermolecular stacking of chains and their orientation with respect to the substrate. All these properties can be measured using GIWAXS, and therefore will be discussed in the following section.

Since the morphology of PEDOT is expected to have ramifications on the electrical conductivity, the establishment of a link between these properties will be attempted. Figure 7.5 shows the sector integrals of PEDOT:PSS films post-treated with the employed ILs. These integrals can be calculated in two primary directions of interest: in vertical direction (along q_z), indicating prevalent orientation in face-on direction, or in horizontal direction (along q_r), being susceptible towards an edge-on orientation of polymer chains.

The sector integrals in q_z direction are shown in Figure 7.5a-c for the three ILs. Changes in comparison to the reference sample (represented by the black curves) are easily observed. Looking at scattering curves obtained from EMIM DCA-treated films in Figure 7.5a, with increasing concentration of EMIM DCA features arise at q -values of around 0.50 \AA^{-1} , which corresponds to a characteristic stacking distance of approximately 14 \AA . This type of signal in thin PEDOT:PSS films is assigned to the so-called vertical layering. [76] A similar feature is found for EMIM TCB-treated samples, seen in Figure 7.5b, although at a different position. Herein, a peak is found at 0.41 \AA^{-1} (corresponding to 15 \AA), which is interestingly most pronounced for intermediate concentrations. For high EMIM TCB concentrations, it also shifts towards lower q -values, which translate to a characteristic vertical layering distance of 18 \AA . Another feature that appears to be a higher-order peak, is also found at q -values slightly below 0.8 \AA^{-1} . Lastly, for EMIM BF_4 -treated samples shown in Figure 7.5, the first-order peak is found at small q -values of approximately 0.31 \AA^{-1} , corresponding to a real-space distance of roughly 20 \AA . For all concentrations of EMIM BF_4 an apparent second order peak centered at around 0.63 \AA^{-1} , thus the doubled value of the first-order peak, is found. This suggests a higher order of the vertical layering for all concentrations of EMIM BF_4 , compared to the other ILs.

In the horizontal sector integrals shown in Figure 7.5d-f, changes are less obvious. For the most part, changes at large q -values can be seen upon treatment of the PEDOT:PSS films with the different ILs. The absence of features at low q -values suggests that no layering, as it is observed in the vertical sector integrals, is present in horizontal direction.

Nevertheless, both vertical and horizontal sector integrals can be analyzed regarding three main types of structural information, which will aid in the understanding of the conductivity enhancement: average π - π -stacking distances of PEDOT, the ratio of PEDOT to PSS, and the ratio of PEDOT stacks oriented in edge-on direction to the ones oriented in face-on direction.

7.3.1 Analysis of π - π -stacking distances

The first structural parameter which is investigated in this study is the π - π -stacking distance. Due to their conjugated nature, PEDOT chains are prone to forming supermolecular aggregates via interactions of extended π -orbitals. While it is possible for charges to be transported within a single π -orbital, the interaction between numerous chains in the form of π - π -stacking additionally allows for charge transport between neighboring chains through orbital overlap. It can be understood that charge transport along this channel is facilitated the closer the chains move together. Therefore, the π - π -stacking distances are a characteristic parameter of the structure, which directly correlate to the macroscopically measurable electrical conductivity.

In Figure 7.6a, characteristic π - π -stacking distances of IL-treated PEDOT:PSS films are shown in face-on direction. Changes as function of type of IL as well as the respective concentrations can be seen. For low concentrations of EMIM BF₄, large π - π -stacking distances around 4.00 Å are observed, compared to the reference value of roughly 3.70 Å⁻¹. With increasing concentration, a decreasing trend is observed ultimately resulting in π -

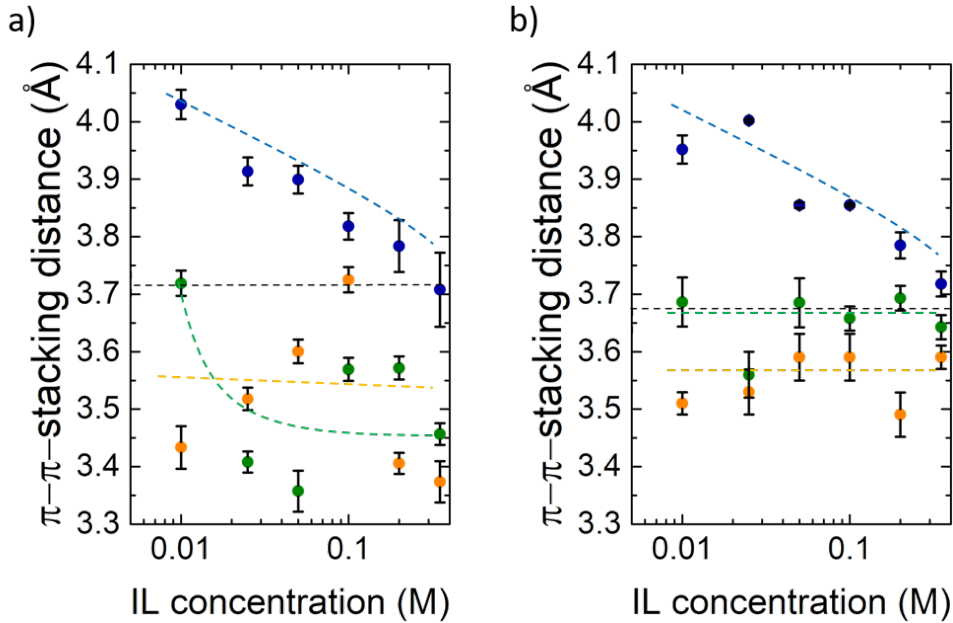


Figure 7.6: Average PEDOT π - π -stacking distances in a) face-on and b) edge-on direction, extracted from the respective sector integrals of 2D GIWAXS images (Figure 7.5) of PEDOT:PSS films treated with EMIM DCA (green), EMIM TCB (orange) and EMIM BF₄ (blue). The values extracted for the reference PEDOT:PSS film post-treated with pure THF are represented by the dashed black lines. Dashed colored lines serve as guides to the eye for the ILs in corresponding colors. Adapted from [4].

π -stacking distances corresponding to the reference value. EMIM DCA-treated films show a different behavior. Except for the sample treated with the lowest concentration, all π - π -stacking distances are significantly smaller than the reference value, at values of around 3.50 Å. In general, a decrease in the π - π -stacking distances is observed, which suggests improved charge transport capabilities perpendicular to the substrate. π - π -stacking distances obtained for EMIM TCB-treated films are also mostly smaller than the reference values indicated by the dashed black line. Also in this case, the decreased π - π -stacking distances are favorable for charge transport in vertical direction.

Since all thermoelectric measurements were carried out in an in-plane geometry, the sector integrals in horizontal direction shown in Figure 7.6b are expected to have a greater impact on the macroscopically measurable electrical conductivity as function of type and concentration of the used ILs.

The π - π -stacking distances of EMIM BF₄-treated films show a similar trend in edge-on direction as in face-on direction. While the characteristic distances are again comparatively larger at low concentrations, a value close to that of the reference is again obtained at higher concentrations. However, in contrast to the reference PEDOT:PSS film treated with pure THF, EMIM BF₄-treated ones show vastly improved electrical conductivities in in-plane direction, which does not match well with the similar values obtained for the π - π -stacking distances. It is thus concluded that the latter cannot explain the observed differences in the electrical conductivities on their own.

In contrast to the discussion of the face-on sector integrals for EMIM DCA-treated films, here no significant changes in the π - π -stacking distances are observed. The obtained values are very close to that of the reference, being centered at around 3.67 Å⁻¹. Also in the case of the EMIM DCA-treatment a concentration-dependent change in the electrical conductivity is observed which does not align well with the observation of constant π - π -stacking distances. Therefore, also here it is suggested that the π - π -stacking cannot fully explain the trends of the rising electrical conductivity.

Lastly, π - π -stacking distances of EMIM TCB-treated films also show no significant dependence on the concentration, but are rather found at a constant value of approximately 3.55 Å⁻¹. Even though these values indicate increased orbital overlap of PEDOT chains, and therefore suggest improved charge transport in in-plane direction, the observed increase of the electrical conductivity as function of EMIM TCB concentration can also not be fully explained at this point.

Throughout this discussion it was seen that the post-treatment of PEDOT:PSS films with ILs seems to affect the way in which PEDOT chains stack both perpendicular and parallel to the substrate. An explanation for this observation could be possible intercalation of anions within the PEDOT crystallites. The rational choice of ILs involves the

study of differently sized anions. Therefore, also the difference in obtained π - π -stacking distances for the three ILs appears reasonable. This assumption of intercalated anions in the PEDOT stacks is further strengthened by the observed changes in the Seebeck coefficients, which imply interactions between PEDOT and the anionic components of the ILs.

Still, in most cases, the observed trends for the π - π -stacking distances for different ILs do not fully match the evolution of the corresponding electrical conductivities. For this reason, possible changes in the PEDOT-to-PSS ratio will be discussed in the following.

7.3.2 Analysis of changes in the PEDOT-to-PSS ratio

Over the many years in which researchers have performed structural studies on PEDOT:PSS, a commonly accepted morphological model was elucidated. Therein, upon film formation a phase separation process leads to the formation of conducting, PEDOT-rich domains, which are typically surrounded by a shell of excess PSS and embedded in a matrix of the latter. The PEDOT-rich domains possess a semi-crystalline structure in

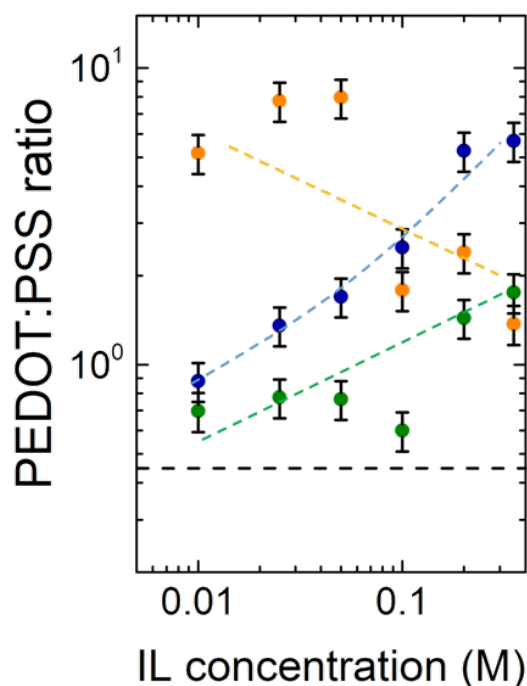


Figure 7.7: PEDOT-to-PSS ratios extracted from powder-like sector integrals of 2D GIWAXS images of PEDOT:PSS films treated with EMIM DCA (green), EMIM TCB (orange) and EMIM BF₄ (blue). The value extracted for the reference PEDOT:PSS film post-treated with pure THF is represented by the dashed black lines. Dashed colored lines serve as guides to the eye for the ILs in corresponding colors. Adapted from [4].

which the π - π -stacking of PEDOT chains is prevalent, and thus allow for charge-transport within the domains. Barriers for the transport of charge carriers arise at the interfaces between the conducting, PEDOT-rich domains and the PSS matrix, since PSS itself is electrically insulating. Therefore, it is generally believed that, while PSS aids in the dispersion of PEDOT in aqueous solution, it is detrimental to the macroscopically measurable electrical conductivity of the film. Most treatments, which have been devised for the improvement of electrical properties in PEDOT:PSS films, thus aim at selective interactions with PSS for its removal from the film. ILs are expected to have a similar effect, in that the positively charged EMIM-cations can interact with the polyanion PSS electrostatically, and thus aide in the removal of the latter from the films. To this end, the sector integrals shown in Figure 7.5 are analyzed regarding changes in the relative amounts of PEDOT and PSS through analysis of the characteristic scattering signals of both components. For our purposes a larger PEDOT-to-PSS ratio is more favorable for charge transport, since charges can then be transported more easily between different conducting, PEDOT-rich domains and should therefore result in improved electrical conductivities.

The results of this analysis are shown in Figure 7.7. For all ILs an improvement compared to the reference value of 0.42 can be seen. This reference value is fairly close to the nominal specification of the manufacturer, regarding the PEDOT-to-PSS ratio in the PH1000 formulation. Especially in the cases of EMIM DCA and EMIM BF₄ the PEDOT-to-PSS ratio increases as function of IL concentration. This implies a favorable effect on the electrical conductivity, as PSS is usually considered detrimental to charge transport within the polymer thin film. Notably, the achieved PEDOT-to-PSS ratio is for the highest concentration of 0.35 M, is highest for EMIM BF₄. On the other hand, EMIM TCB seems to be able to efficiently remove PSS at low concentrations. However, with increasing amount of EMIM TCB a slightly adverse effect on the PEDOT-to-PSS ratio is observed.

Still, it can be concluded that the notion of selective electrostatic interactions between the cations of the ILs and the polyanion PSS holds for all ILs. As a consequence, PSS is removed from the film during the spin-coating process and leads to a morphological re-organization. The loss of insulating PSS is advantageous in terms of the electrical conductivity, as charge carriers can be transported more easily through the film. For all three ILs the increase in the PEDOT-to-PSS ratio is deemed a contributing factor in the enhancement of the electrical conductivity.

7.3.3 Analysis of preferred orientation

Figure 7.8 shows the ratio of PEDOT crystallites oriented in edge-on to face-on direction. A higher ratio is preferable, since a larger degree of edge-on orientation also implies improved charge transport capabilities in in-plane direction. The ratio was calculated from the division of peak areas of scattering signals which are typically assigned to π - π -stacking of PEDOT chains in both edge-on and face-on orientation.

The reference PEDOT:PSS film exhibits a ratio close to one, suggesting a balance between PEDOT π - π -stacks oriented in edge-on and face-on direction. Upon post-treatment of the PEDOT:PSS films, differences between the employed ILs can be discerned. EMIM DCA- and EMIM TCB-treated films show a very low ratio, indicating an unfavorable predominant orientation of PEDOT stacks in face-on direction. In comparison to this, low concentrations of EMIM BF_4 show much larger values for the ratio which could be an explanation for the comparatively higher electrical conductivities obtained for these samples. While for EMIM BF_4 -treated samples a maximum edge-on to face-on ratio is

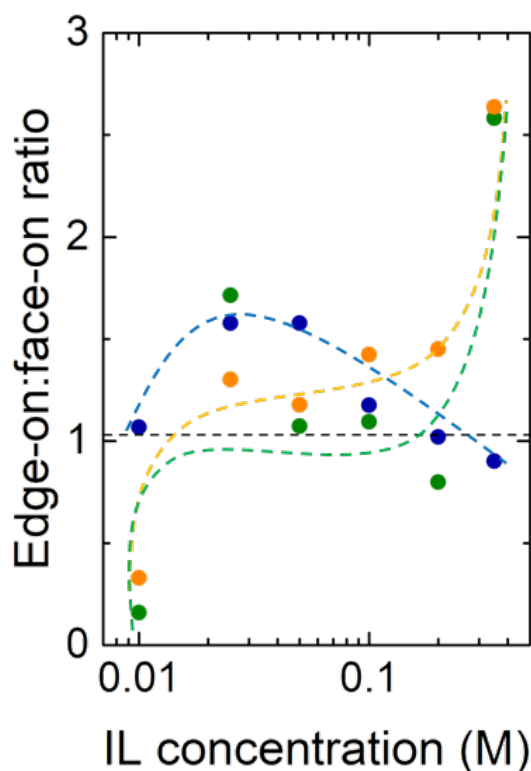


Figure 7.8: Edge-on to face-on ratio extracted from the respective sector integrals of 2D GI-WAXS images of PEDOT:PSS films treated with EMIM DCA (green), EMIM TCB (orange) and EMIM BF_4 (blue). The ratio extracted for the reference PEDOT:PSS film post-treated with pure THF is represented by the dashed black lines. Dashed colored lines serve as guides to the eye for the ILs in corresponding colors. Adapted from [4].

obtained at intermediate concentrations, this drops again to a value close to that of the reference for high concentrations. In the case of EMIM TCB and EMIM DCA a steady increase as function of concentration is observed. This is in line with the increasing electrical conductivity as function of IL concentration. It can be concluded that especially for EMIM TCB- and EMIM DCA-treated films the orientation is most favorable at high concentrations, while in the case of EMIM BF_4 -treatment the fraction of edge-on orientation is sufficiently high for all concentrations.

7.4 Structure-conductivity correlation

Figure 7.9 is a visual representation of the results from the morphological characterization using GIWAXS, discussed above. It summarizes the changes in the obtained π - π -

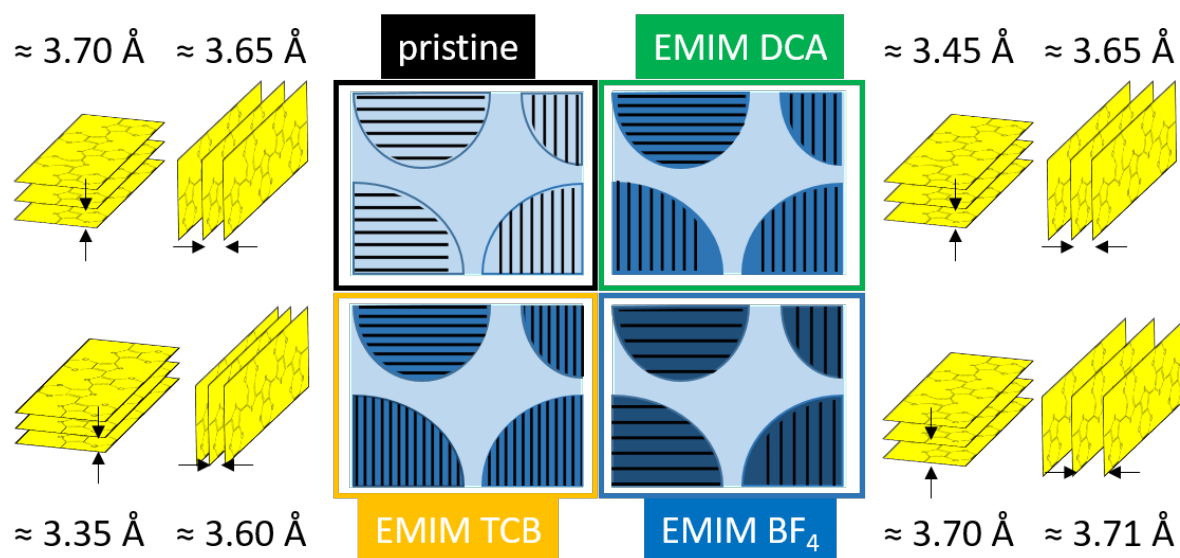


Figure 7.9: Morphological model of PEDOT:PSS treated with pure THF as reference (top left), treated with EMIM DCA (top right), EMIM TCB (bottom left) and with EMIM BF_4 (bottom right). Values for the average π - π -stacking distances in both face-on (left) and edge-on (right) are given, respectively. The schematics in the center of the figure represent differences in the three main structural quantities discussed, with PEDOT-rich crystallites (dark blue) embedded in a PSS-rich matrix (light blue). Average π - π -stacking distances are schematically shown as black lines inside the PEDOT-rich crystallites in different densities, depending on the magnitude of the respective π - π -stacking distances. The PEDOT-to-PSS ratio is represented by the color gradient from dark blue (PEDOT-rich) to light blue (PSS-rich) inside the PEDOT-rich crystallites. The predominant orientation of the PEDOT π -stacks is represented by the stacking direction of the black bars inside the PEDOT crystallites. Taken from [4].

stacking distances, PEDOT-to-PSS ratios and edge-on to face-on ratios for the reference PEDOT:PSS film, as well as for the IL-treated ones.

For pristine PEDOT:PSS, average π - π -stacking distances in face-on and edge-on direction are 3.70 Å and 3.65 Å, respectively. The determined PEDOT-to-PSS ratio is very close to the nominal one provided by the manufacturer, and amounts to roughly 0.37. Regarding the orientation of PEDOT π -stacks, there is a balance between face-on and edge-on orientation as shown by the equal distribution of stacks among the PEDOT crystallites.

EMIM DCA-treated films show π - π -stacking distances of 3.45 Å and 3.65 Å in face-on and edge-on, and therefore a much denser stacking in face-on direction than the reference. While initially low, the PEDOT-to-PSS ratio strongly increases in edge-on direction as function of concentration. In face-on direction it appears to be concentration-independent. Treatment of PEDOT:PSS with high concentrations of EMIM DCA also favorably alters the predominant orientation of PEDOT π -stacks towards a larger degree of edge-on orientation. The strong improvement in the electrical conductivity of these samples can be assigned to the combination of an improved PEDOT-to-PSS ratio and re-orientation into an edge-on configuration.

π - π -stacking distances in EMIM TCB-treated films are 3.35 Å and 3.60 Å in face-on and edge-on direction, respectively. In edge-on direction this is a slight improvement compared to the reference, as smaller π - π -stacking distances correlate with improved inter-chain charge transport. In face-on direction the difference is much more drastic, as the smallest distances are achieved here. For both the face-on and edge-on direction a decrease of the PEDOT-to-PSS ratio as function of concentration is observed. This is more pronounced for the face-on direction, but is in general unfavorable for inter-grain charge transport between different PEDOT-rich domains, as more insulating PSS is present. Also for the EMIM TCB-treatment a favorable re-orientation of PEDOT π -stacks into a more predominant edge-on configuration is observed, especially for high concentrations. Both the advantageous orientation and enhanced inter-chain charge transport are in line with the increasing electrical conductivity, while the comparatively lower PEDOT-to-PSS ratios are detrimental due to impeded inter-grain charge transport.

For low concentrations, the π - π -stacking distances in EMIM BF₄-treated samples are much larger in both face-on and edge-on direction. At high concentrations they decrease to 3.70 Å and 3.71 Å, and are therefore close to the reference value of pristine PEDOT:PSS. The PEDOT-to-PSS ratios in both face-on and edge-on direction change favorably as function of concentration, while the increase in face-on direction is more pronounced than in the edge-on case. Regarding the ratio of edge-on to face-on orientation, a maximum is seen at intermediate concentrations, with the remaining samples exhibiting values close

to that of the reference. Both π - π -stacking distances and edge-on to face-on ratios are close to the values seen in the reference sample, wherefore the high PEDOT-to-PSS ratios are suggested as main driving force behind the improvement in electrical conductivities.

In conclusion, GIWAXS allowed to determine the great impact ILs have on the structure of PEDOT:PSS. The manifold effects include changes in the π - π -stacking distances, the PEDOT-to-PSS ratio and the edge-on to face-on ratio. Different ILs influence these properties differently, even though the cations which chosen to be the same. As discussed above, this might originate from changes in the intrinsic properties of the ILs due to the charge localization on the anions. It can be expected that this changes the way in which the EMIM cations can interact with the negatively charged PSS. Also changes in the π - π -stacking distances could be assigned to possible inclusion of the anions into the structure, which would explain how they evolve differently as function of IL type.

7.5 Summary

This chapter deals with the simultaneous improvement of Seebeck coefficients and electrical conductivities through post-treatment of PEDOT:PSS films with ILs. The binary nature of PEDOT:PSS is complemented by the ionic nature of the ILs in that the latter's anions selectively interact with PEDOT, while the cations selectively interact with PSS. Ramifications on both the Seebeck coefficient and the electrical conductivity are expected.

In order to study changes in the electronic structure, which strongly influences the obtainable Seebeck coefficients, UV-Vis spectroscopy is performed. It reveals different interactions of the anions with PEDOT, which conforms to the observation of changes in the Seebeck coefficients for the three employed ILs. Treatment with EMIM DCA leads to the highest Seebeck coefficients around 40 $\mu\text{V/K}$, which can be explained by the emergence of absorption features that can be assigned to both polaronic and neutral states in PEDOT chains. EMIM BF_4 -treatment leads to slightly improved Seebeck coefficients of approximately 30 $\mu\text{V/K}$, and is explained by the sole emergence of polaronic bands. A lack of new absorption features for EMIM TCB-treated samples is in line with the Seebeck coefficients being around the reference value of approximately 20 $\mu\text{V/K}$. The trends are explained through the charge distribution on the respective anions, with the DCA-anion showing the highest degree of charge localization due to its angulated structure. The spherically symmetrical BF_4 - and TCB-anion differ in their overall size, with the latter being larger because of its biatomic ligands. Therefore, the higher charge density of the BF_4 -anion leads to improved interactions with PEDOT and thus to higher Seebeck coefficients. Additionally, the hydrogen-bond basicity is identified as possible parameter with which changes in the Seebeck coefficients can be predicted.

GIWAXS is used to study the structure of PEDOT:PSS and potential changes upon treatment with the different ILs. The investigation was carried out focusing on average π - π -stacking distances, the PEDOT-to-PSS ratio and the edge-on to face-on ratio. Changes in the π - π -stacking distances strongly depend on the employed ILs as vastly different trends and average values are found as function of both type and concentration of IL used for post-treatment. Especially for treatment with EMIM DCA and EMIM TCB lower π - π -stacking distances are observed, which contribute to improved inter-chain charge transport. Intercalation of anions into the PEDOT π -stacks is proposed as possible mechanism. Also regarding the PEDOT-to-PSS, changes between the ILs are discernible. In most cases, PSS is removed from the film due to its electrostatic interactions with the EMIM cations, leading to larger PEDOT-to-PSS ratios. EMIM TCB shows adverse trends for both the face-on and edge-on orientation, while still being improved compared to the reference value. Thus, especially for treatment with EMIM DCA and EMIM BF₄ the inter-grain charge transport is improved. The edge-on to face-on ratio gives insight into preferred directions of charge transport, with a higher fraction of PEDOT π - π -stacks oriented edge-on being favorable for high electrical conductivities. Treatment with EMIM BF₄ leads to a maximum at intermediate concentrations, while EMIM DCA- and EMIM TCB-treatments lead to greatly increased ratios especially at high concentrations. All findings are compiled in the morphological model shown in Figure 7.9.

In summary, post-treatment of PEDOT:PSS with IL is a promising approach at improving the thermoelectric properties of thin films of the former. This is achieved by the simultaneous enhancement of the Seebeck coefficient and the electrical conductivity. Through the rational choice of ILs used in this study, in which the cations are the same and only the anions differ, many interesting features of the treatment are found. Firstly, the structure of the anion has serious ramifications on the resulting Seebeck coefficients, as the former are expected to primarily interact with the conjugated PEDOT. Therein, a stronger localization of the negative charge on the anion appears to be more favorable for the achievement of high Seebeck coefficients. The notion of the variation of the anion not influencing the electrical conductivity is proven to be incorrect. The properties of the anion greatly influence the intrinsic properties of the ILs, and therefore affect the interaction with PSS. This is seen in the differing dependencies of the investigated structural parameters on the type of IL. This study provides a starting point for further investigations in which the impact of other anions with different structural motives can be studied. The vast catalogue of possible combinations of cations and anions in ILs opens a large window of tunability of thermoelectric properties in PEDOT:PSS.

8 P(NDI2OD-T2) as n-type polymer for thermoelectric applications

This chapter is largely based on the results obtained with Regina Kluge in the framework of her master's thesis. [25]

Since their inception, conducting polymers have experienced a growth in popularity amongst researchers. This led to a strong emphasis on the synthesis of new materials, which were expected to possess interesting properties especially for application in optoelectronics, e.g. in transistors, organic solar cells, etc. As a result, a plethora of different polymers were fabricated with a large window of tunability regarding energy levels of the HOMO and LUMO of those materials.

While polymers with the ability to transport positive charges are comparatively easy to synthesize, due to their structural simplicity, the opposite is the case for polymers with the ability to transport negative charge carriers. Restrictions regarding the inclusion of groups with the ability to transport negative charges and stability, among others, make these polymers usually very complex on atomic scales. This caused a certain neglect of these polymers, regarding both, their basic characterization and potential application in organic electronics. This work attempts to understand the mechanisms determining the properties of n-type polymers by studying a commonly used representative, namely P(NDI2OD-T2).

In this study, the well-known alternating copolymer P(NDI2OD-T2) is studied regarding the influence of doping with a benzimidazoline derivative on optical, morphological and thermoelectric properties. For this purpose, UV-Vis spectroscopy is performed on doped films in order to investigate changes in the electronic structure, and link those to thermoelectric measurements of the doped films. GIWAXS is used to study the structure of the pristine polymer thin film and changes thereof upon doping. Regarding the thermoelectric characterization, different sample geometries are employed, and examined regarding the feasibility of their usage in thermoelectric generators. Thermoelectric quantities are measured along and perpendicular to the sample-substrate interface in these different geometries. Based on these results, a comprehensive model is given which sums up the

findings of the spectroscopic and morphological analysis and links those to the observed thermoelectric properties.

P(NDI2OD-T2) is combined with PEDOT:PSS in order to fabricate a thermoelectric generator based on polymers as active materials.

8.1 Spectroscopic characterization using UV-Vis spectroscopy

Intrinsically, P(NDI2OD-T2) is an electrical insulator. Therefore, doping of the conducting polymer is required in order to introduce charge carriers and thereby enable charge transport. In this case, P(NDI2OD-T2) is doped with a benzimidazoline derivative called N-DPBI in different concentrations. The effect of doping is studied using UV-Vis spectroscopy, similarly to how it was used on PEDOT:PSS films in order to investigate changes in the charge carrier concentration. More specifically, UV-Vis spectra are analyzed regarding the appearance and disappearance of features as function of dopant concentration, but also as function of temperature in order to understand the stability of doped films.

8.1.1 Influence of dopant concentration

The employed dopant N-DPBI is expected to transfer negative charges in form of electrons or hydride ions onto the polymer P(NDI2OD-T2) in order to increase the charge carrier density. To find out how this reaction proceeds, solutions of the dopant in dichlorobenzene

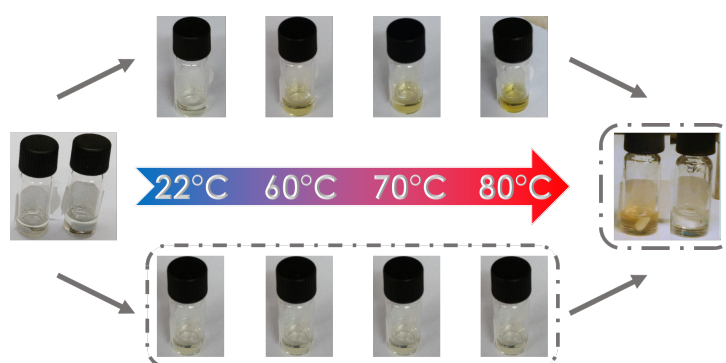


Figure 8.1: Photographic comparison of N-DPBI solutions in chlorobenzene stored either in ambient atmosphere (top row) or a nitrogen-filled glovebox (bottom row, indicated by the dashed boxes) when subjected to different temperatures. Temperatures are increasing from left to right, as indicated by the arrow. For the final photo on the right, both solutions were transferred into the glovebox.

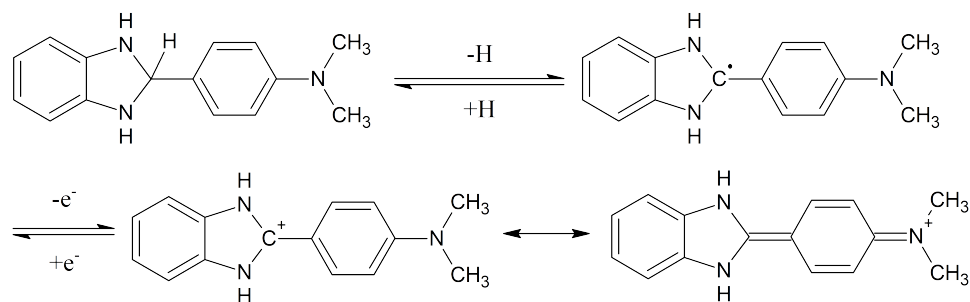


Figure 8.2: Presumed redox reaction of dopant N-DPBI in solution, under hydrogen transfer following Wei *et al.* [77]

are subjected to different temperatures, with one vial being stored in a nitrogen-filled glovebox, and the other one being stored in ambient atmosphere. Figure 8.1 shows the results for both solutions. Notably, there is a distinct difference in color between the two solutions, as the one stored in air exhibits a yellow color for temperatures exceeding 60 °C, while the solution stored in nitrogen atmosphere remains colorless. There are two things that can be learned from this experiment. Firstly, a reaction of the dopant only takes place with an appropriate reaction partner, which in this case was most likely oxygen from the atmosphere. Secondly, a certain temperature has to be exceeded for the dopant to react.

The presumed reaction is shown in Figure 8.2, as proposed by Wei *et al.* [77] The splitting off of a hydrogen atom, which must be activated by an energy transfer to the dopant, e.g. by increasing temperature, is followed by the loss of an electron, leaving the oxidized form of the dopant. Under re-organization of bonds, an extended conjugated π -system is formed, which could be a viable explanation for the occurrence of a yellow color. Thus, it is concluded that in order for the reduction reaction to occur, P(NDI2OD-T2) and N-DPBI have to be combined at elevated temperature in nitrogen atmosphere to ensure successful transfer of the negative charge to the polymer.

Doped thin films of P(NDI2OD-T2) are prepared as outlined in Section 4.2.4, making use of the findings of the preliminary experiment discussed above. UV-Vis spectroscopy, as seen in previous chapters, can be used to deduce the electronic structure of a conducting polymer, as charge carriers can be typically excited electronically using light and therefore yield characteristic features in the spectra. The UV-Vis spectra for films doped with up to 40 wt% N-DPBI are shown in Figure 8.3. In the pristine state, P(NDI2OD-T2) already shows two interesting features, one at lower and one at higher wavelengths, which originates from its donor-acceptor copolymer structure. As discussed by Steyrleuthner *et al.*, the former peak can be associated to the presence of π - π -stacks of P(NDI2OD-T2) chains in solution, which can be also found after deposition on a substrate. [78] Through

stacking, an extended π -system is formed, which can be excited electronically by UV-light. The second feature originates from the donor-acceptor nature of the polymer. While the naphthalene-diimide possesses electron-accepting properties, the bithiophene-unit shows electron-donating properties. The redistribution of electrons from the donor to the acceptor moiety can be stimulated with visible light, which is also why reason that the pristine film shows a vibrant turquoise color, as seen in Figure 8.3. Changes in these intrinsically occurring features not only give information on the electronic structure, but also on changes in the morphology due to interaction with the dopant molecules. Upon doping with N-DPBI, a general decrease of intensity of the aforementioned features is observed in addition to a blue-shift of the low-wavelength peak. In the case of the low-wavelength band, the blue-shift is an indication of less efficient π - π -stacking, possibly due to incorporation of the dopant molecules within the intrinsically present π - π -stacks, which will be discussed in greater detail in the morphological analysis below. The decrease of the charge-transfer band at high wavelengths may be indicative of changes in the conformation of the chains, respectively the orbital overlap between the donor- and acceptor-moieties within the chains. Nevertheless, additional absorption features appear at around 500 nm and 800 nm, which are indicators for the presence of negative polaronic species, as found by Caironi and co-workers. [79] All these findings support the notion of charge transfer from the dopant N-DPBI to P(NDI2OD-T2), with an indication of incorporation of the dopant into the π - π -stacks of the polymer, which will be discussed in more detail below.

8.1.2 Influence of temperature

A general problem one encounters with n-type conducting polymers is their instability towards oxidation in an ambient atmosphere. The reaction with oxygen in general creates additional states which trap negative charge carriers, and thereby inhibit their transport. It can be expected that this process is facilitated and accelerated by increasing the temperature of the films. Therefore, temperature-dependent UV-Vis measurements are performed for films doped with different concentrations of N-DPBI, which are compiled in Figure 8.4.

While temperature-dependent UV-Vis measurements are performed, reference measurements at room temperature are carried out at the same time with films of the same dopant concentration. Since the oxidation and therefore degradation of the films is also expected to happen in ambient conditions, these measurements are performed while the samples at room temperature in order to pinpoint the influence of temperature on the appearance or disappearance of certain features. Similarly to Figure 8.3, doped P(NDI2OD-T2) films show gradual decrease in the π - π -stacking and charge-transfer contribution to the spectra

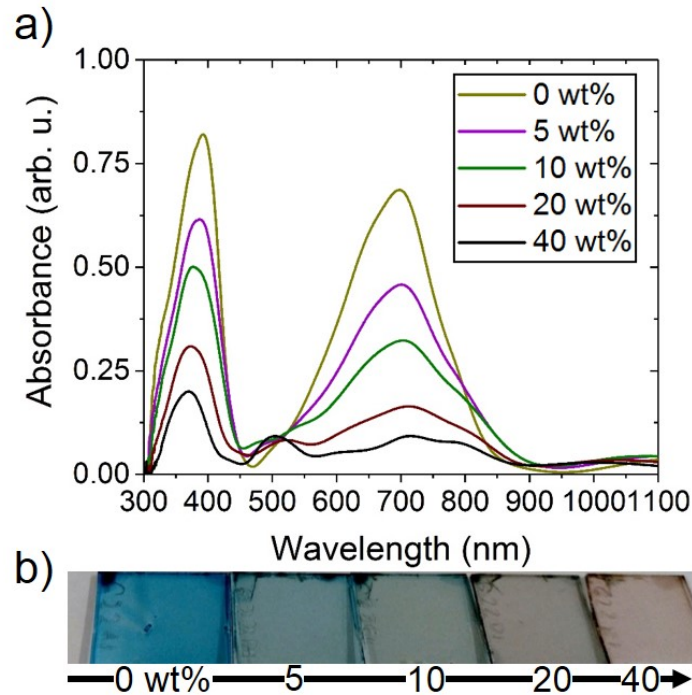


Figure 8.3: a) UV-Vis spectra of P(NDI2OD-T2) thin films on glass doped with different concentrations of N-DPBI, as indicated in the legend. b) Photographs of P(NDI2OD-T2) thin films doped with the corresponding concentrations of N-DPBI.

found close to 370 nm and 700 nm. In addition, bands assigned to the presence of negative polarons appear at 500 nm and 800 nm, indicating successful doping. The changes in the reference spectra hint at re-oxidation of the doped polymer films. Interestingly, also for the pristine film in Figure 8.4 minute changes are detected, since the absorbance of both the π - π -stacking and charge-transfer peaks increases slightly over time. In the case of doping in concentrations of 40 wt%, significant changes in the spectra are most apparent after approximately 50 min, since the absorbance of the polaron peaks found at 500 nm and 800 nm decrease, and the charge-transfer peak slightly increases again. Regarding the influence of temperature, similar trends are found, although to a larger extent. As discussed before, oxidation of the doped polymer leads to the formation of trap states which manifest themselves as decrease of the polaronic contributions to the spectra. Temperatures above 70 °C seem to vastly accelerate the oxidation process, which can be most clearly seen from the sample with the highest concentration of N-DPBI in the bottom right corner of Figure 8.4, but is expected to be similar for the other investigated concentrations. There is a steep decrease in the absorbance of the high-wavelength polaronic band for temperatures of 80 °C and higher, which coincides with the simultaneous drastic increase in absorbance of the charge-transfer peak. For all investigations

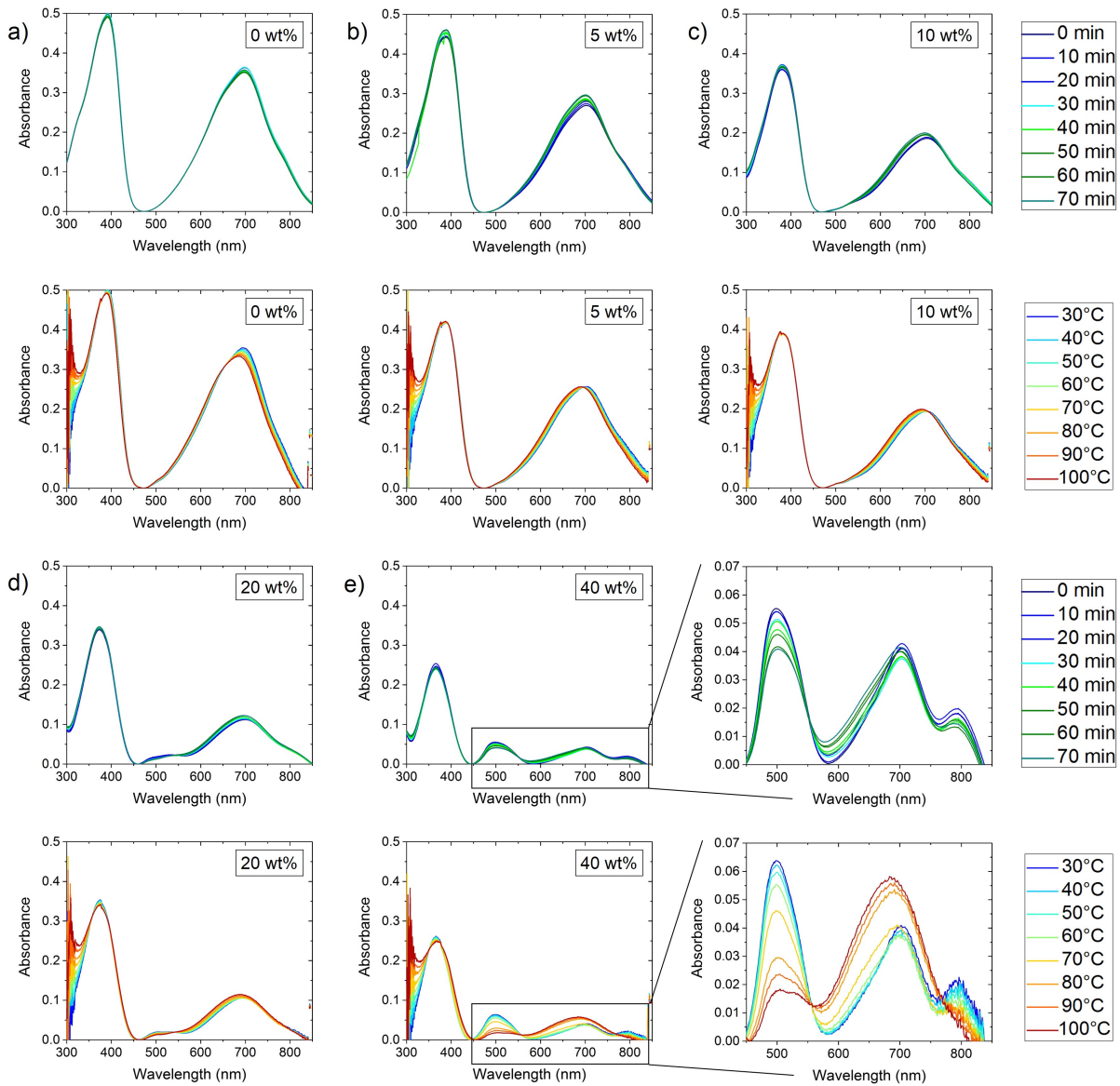


Figure 8.4: Temperature-dependent UV-Vis measurements of doped P(NDI2OD-T2) films in concentrations of a) 0 wt%, b) 5 wt%, c) 10 wt%, d) 20 wt% and e) 40 wt%. In addition, a zoom-in of the 40 wt% sample spectrum in the high wavelength region is shown in the bottom right of the figure, in order to highlight the effect of degradation due to temperature. Since the measurements were carried out in ambient atmosphere, reference measurements at room temperature were carried out simultaneously to the temperature-dependent ones and are shown as the top graph for each dopant concentration. Both measurements were carried out simultaneously in intervals of 10 min. In the temperature dependent measurement, the temperature was ramped from room temperature to 100 °C in steps of 10 °C while the reference measurement was conducted at room temperature.

of the thermoelectric properties, this critical temperature of 80 °C will be taken avoided when performing the measurement of the Seebeck coefficient and temperature-dependent resistances of the doped P(NDI2OD-T2) films.

In summary, UV-Vis spectroscopy represents a facile and non-destructive method of confirming successful doping of P(NDI2OD-T2) thin films with different concentrations of N-DPBI. Additionally, performing temperature-dependent UV-Vis measurements allows for understanding the role of oxygen and elevated temperatures on the degradation process of the doped polymer films. It becomes thus possible to take degradation of the films during characterization into account and to adjust the measurement protocol accordingly, as will be discussed further on.

8.2 Structure characterization using grazing-incidence wide-angle x-ray scattering

As previously discussed, doping of P(NDI2OD-T2) films with N-DPBI as small molecular dopant has implications on the electronic structure of the conducting polymer. However, since as opposed to inorganic semiconductors the concentrations are not in the parts per million (ppm) or parts per billion range, but instead amount to a significant fraction of material in solution, ramifications on the final structure in the thin film are expected. Therefore, after a short literature review of previous studies on the structure, GIWAXS will be performed on P(NDI2OD-T2) films fabricated on glass and FTO substrates. As will be seen in Section 8.3, different substrates are used for the different measurement geometries for the thermoelectric characterization of the films. This study will thus help in understanding potential differences and if the final film structure is influenced by the substrate or not.

Due to P(NDI2OD-T2) being an alternating copolymer, it shows several interesting structural features, which will be discussed in the following. [80–87] On a molecular level, each monomer unit can be divided into the naphthalene-diimide acceptor-subunit and the bithiophene donor-subunit. As per several studies, these subunits are believed to be tilted against each other, which can be seen in more detail in Figure 8.5a. Going to supermolecular lengthscales, the polymer chains are expected to form aggregates due to π - π -stacking. In the specific case of P(NDI2OD-T2) this can potentially happen in two ways: either by segregated stacking (e.g. donor-donor and acceptor-acceptor stacking) or by a mixed stacking. Both versions are depicted in 8.5b. Due to the separation of the naphthalene-diimide subunits by thiophene units, whereas the latter ones do not contribute to negative charge transport, a segregated π - π -stacking would be preferred,

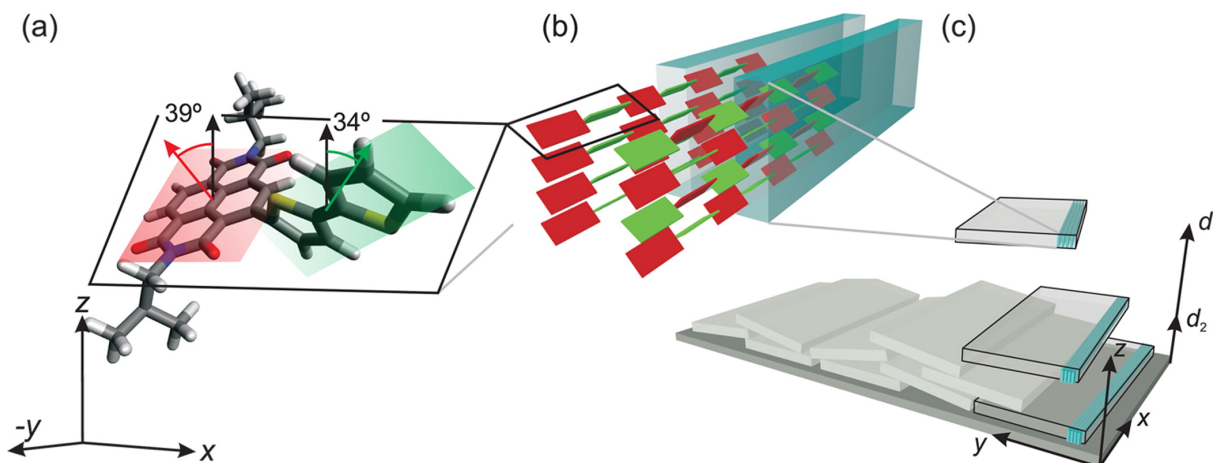


Figure 8.5: Proposed morphological model for P(NDI2OD-T2), combining different findings from literature. [89] a) Structure of a single P(NDI2OD-T2) monomer, highlighting the tilt between the acceptor- (red) and donor-subunit (green). b) Polymer chains interact with each other via segregated or mixed π -stacking and thereby build up lamellae, as indicated by the turquoise boxes. c) Crystallites consisting of lamellar stacks of P(NDI2OD-T2), with the former arranging in a face-on manner with respect to a substrate when fabricated as thin film. Small degrees of tilt represent deviations from a perfect horizontal alignment of the crystallites on the substrate.

since this would allow charge transport between different chains. [88] The π -stacks are connected through the bithiophene units along the direction of the polymer chains and arrange on another length scale in a lamellar fashion. The lamellae formed by the extended polymer chains are highlighted by the turquoise boxes containing the π -stacks in Figure 8.5b. Steyrleuthner *et al.* measured the vertical electron mobility in unipolar diodes. They revealed that crystallinity along the π - π -stacking direction is highly important for achieving high charge carrier mobilities. However, the alkyl side chains create barriers for charge carrier transfer in lamellae, whose ordering plays little role in charge transport. [87] Still, the lamellar stacking in horizontal direction leads to the formation of flat crystallites, which are depicted in Figure 8.5c. In a thin film these crystallites are arranged in a face-on manner, and stack upon each other, with slight deviations to a perfect horizontal alignment thereof.

In summary, a preferential orientation of the π -stacks perpendicular to the plane of the crystallites is found, while inside the crystallites themselves are built-up by in-plane interaction of regions where polymer chains are regularly ordered via π -stacking, also called lamellae. The crystallites preferably rest on top of the substrate being aligned, i.e. in a face-on manner. Since charge transport is assumed to take place along the π -stacks, [87] it can be concluded that for the pristine P(NDI2OD-T2) film charge transport is assumed

to be most efficient perpendicular to the substrate. The question that then arises is, if doping of the polymer with N-DPBI in different concentrations influences the structure of the polymer. This question will be discussed in terms of ordering perpendicular and along the substrate, and in the preferential orientation which is adopted by the π -stacks, which in turn will influence the orientation of the crystallites. For the investigated in-plane and cross-plane measurement geometries discussed below in Section 8.3, P(NDI2OD-T2) films were prepared on glass substrates. This way, in in-plane measurements, charge transport is probed parallel to the substrate. FTO-coated glass substrates are used for cross-plane and pseudo-in-plane measurements, with the charge transport having being primarily probed in the respective directions. Therefore, GIWAXS measurements are carried out with samples in the corresponding sample geometries.

8.2.1 P(NDI2OD-T2) films on glass substrates for in-plane measurements

Firstly, doped P(NDI2OD-T2) films are prepared on insulating glass substrates. Glass is a well-suited substrate material for the measurement of thermoelectric properties along the substrate, since it itself is insulating and therefore does not influence the measurements. Dopant concentrations are chosen in conformity with the spectroscopic characterization discussed above, in order to link electronic and morphological properties of the doped P(NDI2OD-T2) films in order to find a link.

Figure 8.6 shows the 2D GIWAXS patterns as function of N-DPBI concentration. Several distinct scattering features are present for the pristine P(NDI2OD-T2) film, which are highlighted by the white circles in Figure 8.6a. In q_z -direction, the signal at large q -values is typically assigned to the segregated π - π -stacking discussed above. The fact that the signal is oriented in the z -direction also indicates the predominant direction of the stacking in the same direction. As discussed above, the lamellar stacking in the pristine polymer film is in in-plane direction. Therefore, the corresponding peaks in the 2D GIWAXS pattern can be found in q_{xy} -direction. The first order of the lamellar stacking peak is located at around 0.25 \AA^{-1} . With increasing dopant concentration a corresponding peak emerges at the same value but in q_z -direction. It is represented by the first-order scattering peak in q_z -direction found at values of approximately 0.25 \AA^{-1} . These findings are consistent with the morphological picture previously drawn by other researchers. Upon doping, the scattering patterns change, as indicated by loss of signals and rearrangement of scattering peaks.

Sector integration within 2D GIWAXS patterns allows analysis of the crystallinity in the polymer film perpendicular to the plane of the substrate. Figure 8.7a shows the evolution

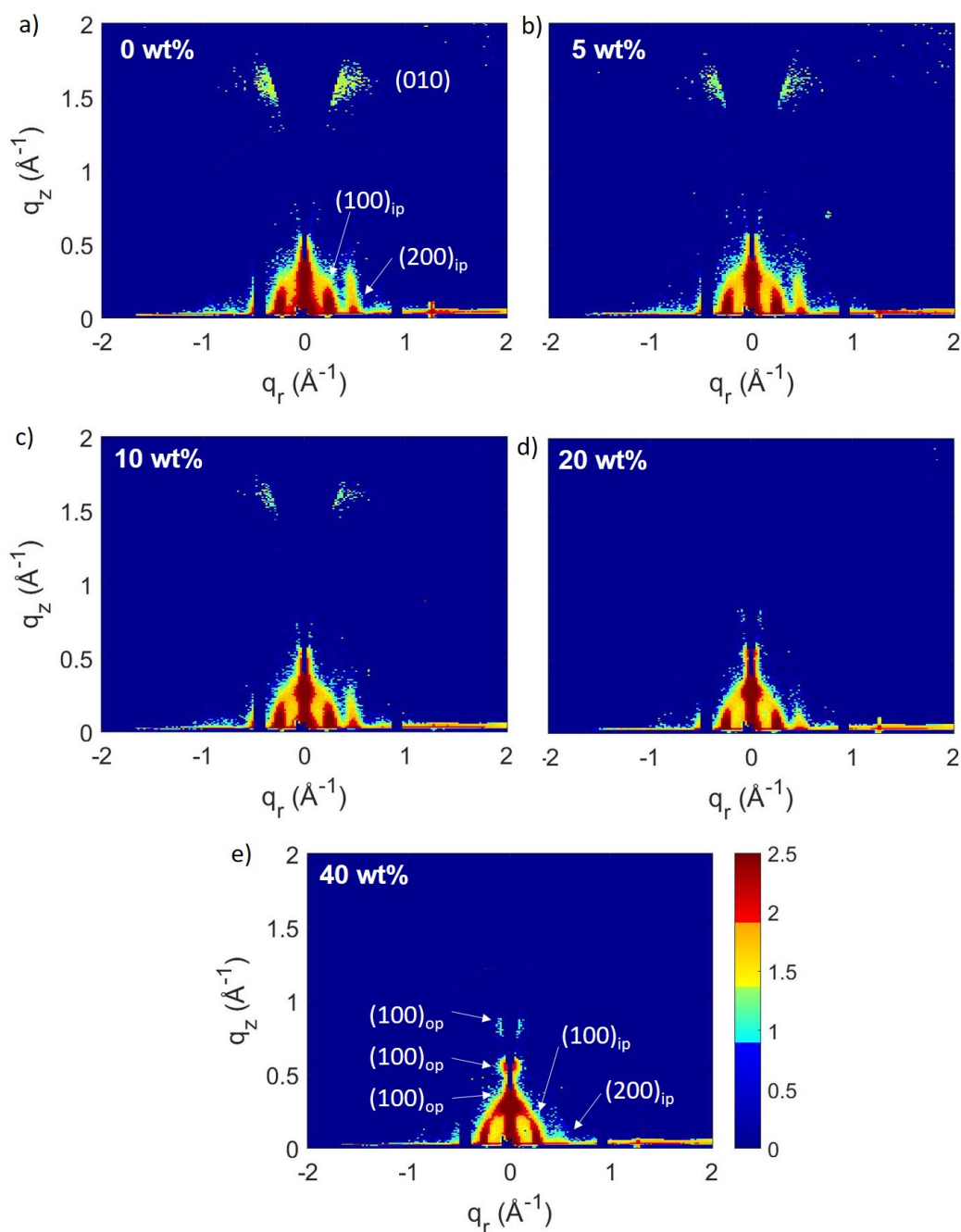


Figure 8.6: 2D GIWAXS data of P(NDI2OD-T2) films on glass substrates doped with a) 0 wt%, b) 5 wt%, c) 10 wt%, d) 20 wt% and e) 40 wt% N-DPBI. For the 0 wt% sample, the π - π -stacking peak is denoted with (010), while the signals ascribed to in-plane (ip) lamellar stacking are denoted with $(100)_{ip}$ and $(200)_{ip}$. Due to re-orientation upon dedoping, lamellar stacking is found in out-of-plane (op) direction, with the corresponding signals being denoted by $(100)_{op}$, $(200)_{op}$ and $(300)_{op}$.

of vertical sector integrals as function of doping concentration. With increasing values of q , the above-mentioned structural features in the following order: first-order lamellar stacking, second-order crystallite stacking, third-order lamellar stacking and finally π - π -stacking. While the former two appear to shift towards larger q -values, and even a third-order peak arises at q -values of around 0.8 \AA^{-1} , which can also be seen in Figure 8.7b, the intensity of the π - π -stacking peak at q -values of approximately 1.6 \AA^{-1} seems to decrease as function of dopant concentration. While the latter is indicative of loss in order on very small length-scales in vertical direction, the combination of peak shifts, new peaks arising and the practically unchanged peak widths will be discussed below, after the discussion of the horizontal sector integrals.

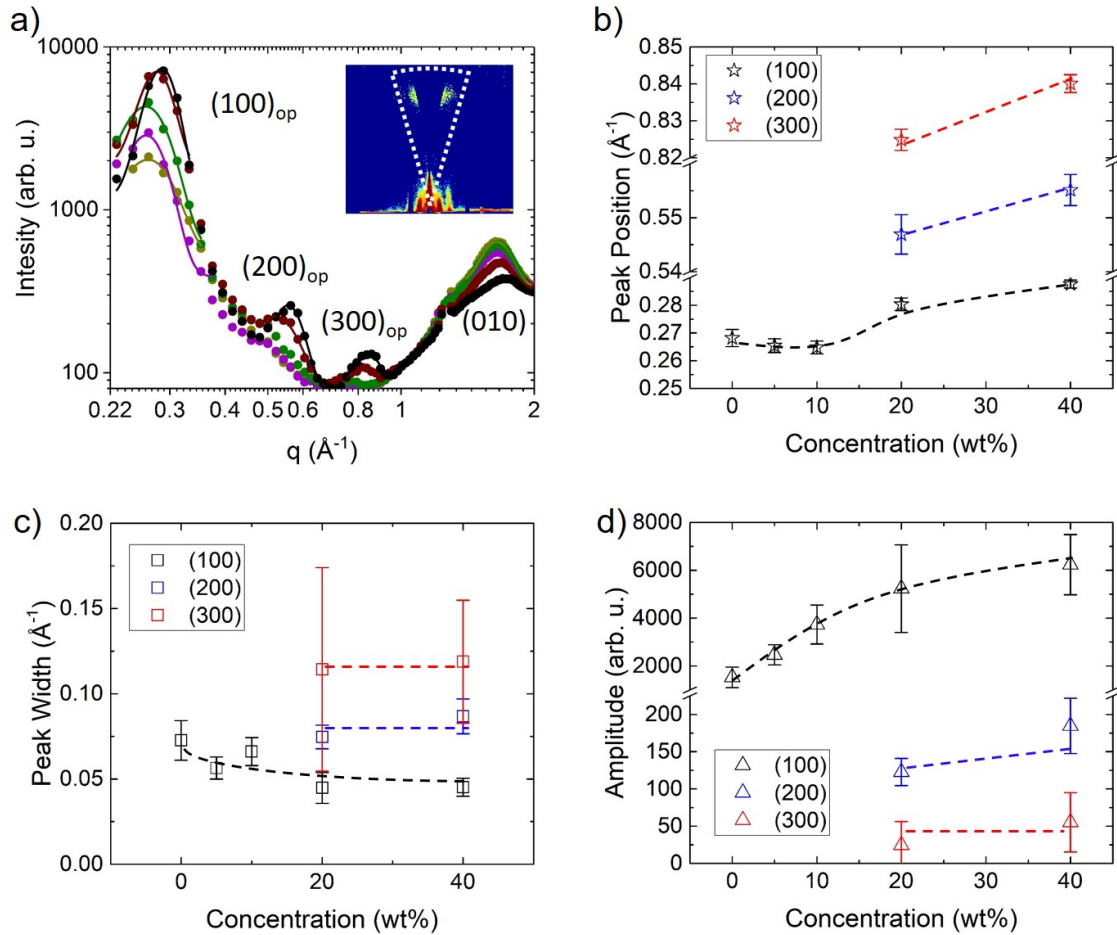


Figure 8.7: a) Vertical sector integrals obtained from 2D GIWAXS data of P(NDI2OD-T2) films prepared on glass with varying doping concentrations: 0 wt% (yellow), 5 wt% (magenta), 10 wt% (green), 20 wt% (brown) and 40 wt% (black). Inset: exemplary 2D GIWAXS pattern, with the integrated area marked by dashed gray lines. b) q -positions of peaks, c) peak widths and d) peak amplitudes as function of doping concentration.

Sector integration in horizontal direction reveals crystalline structures parallel to the substrates, and therefore are of great importance for charge transport in in-plane direction, which is measured for the *P(NDI2OD-T2)* films prepared on glass. Figure 8.8a shows the horizontal sector integrals as function of dopant concentration. Two prominent scattering features can be discerned which are assigned to the first and second order of lamellar stacking of *P(NDI2OD-T2)* chains, with increasing *q*-values. For low concentrations up to 10 wt% also a third order peak is visible. As explained above, the π - π -stacks of *P(NDI2OD-T2)* chains extend perpendicular to the polymer backbone. As explained above, extended polymer chains of *P(NDI2OD-T2)* interact with each other via π - π -stacking and thereby build up sheet-like regions of regular chain arrangement which

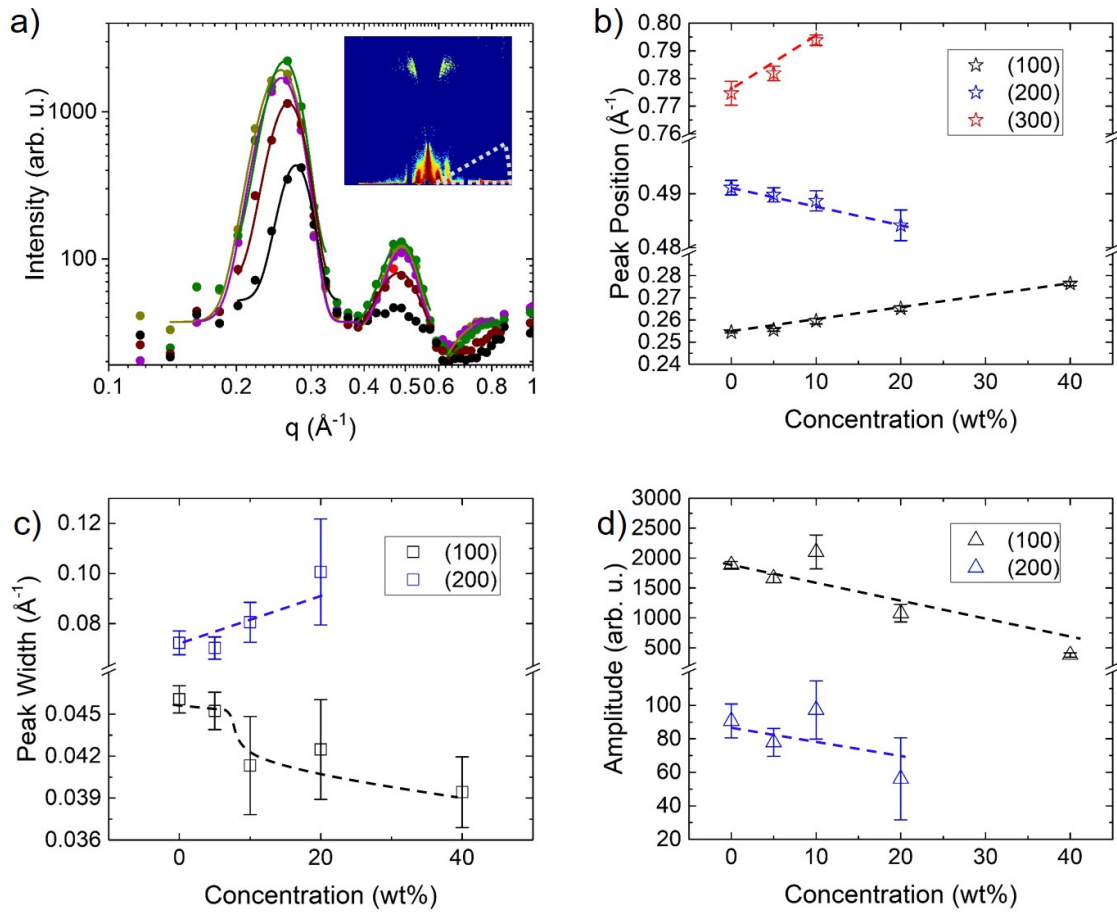


Figure 8.8: a) Horizontal sector integrals obtained from 2D GIWAXS patterns of *P(NDI2OD-T2)* films prepared on glass with varying doping concentrations: 0 wt% (yellow), 5 wt% (magenta), 10 wt% (green), 20 wt% (brown) and 40 wt% (black). Inset: exemplary 2D GIWAXS pattern, with the integrated area marked by dashed gray lines. b) *q*-positions of peaks, c) peak widths and d) peak amplitudes as function of doping concentration.

are called lamellae. These lamellae in turn stack with each other and thereby create flat plate-like crystallites. In the pristine polymer, this lamellar stacking is believed to take place in in-plane direction, which can be confirmed in the GIWAXS measurements presented here, since the corresponding peaks appear in q_{xy} -direction. With increasing concentration of N-DPBI, a shift of the first order towards higher q -values is observed, which indicates denser lamellar stacking, as seen in Figure 8.8b. Meanwhile, the second order peak position is almost constant, whereas the third order peak also moves towards larger q -values. Figure 8.8c shows that the peak widths of the first and second order stay mostly constant, while their respective intensities decrease as function of dopant concentration. The second order is no longer detectable for a dopant concentration of 40 wt%, which hints at a loss of order in lamellar stacking as compared to the pristine P(NDI2OD-T2) film.

GIWAXS also allows for the analysis of predominant orientation of crystallites (which can only be measured indirectly through the orientation of the lamellar stacking) and/or stackings. In this case, the orientation of both the first lamellar stacking and the π - π -stacking is analyzed by performing azimuthal integration of intensities for q -values between 0.2 \AA^{-1} and 0.3 \AA^{-1} . The corresponding results are shown in Figure 8.9 as function of concentration. The azimuthal integrals for the first lamellar stacking peak are shown in Figure 8.9a as function of N-DPBI concentration. This peak increases and shows the maximum intensity at χ -values close to 0° for a concentration of 20 wt%, only to decrease again for higher dopant amounts. In addition, at large χ -values of approximately 80° , a decrease in intensity is observed for increasing dopant concentration. While large intensities at χ -values close to 0° indicate predominant stacking perpendicular to the substrate, the opposite is true for large intensities at high χ -values close to 80° , being indicative of lamellar stacking parallel to the substrate. In Figure 8.9b the face-on-to-edge-on ratio is shown for the differently doped P(NDI2OD-T2) films, which is obtained through simple division of the respective peak amplitudes. The ratio decreases with increasing concentration of N-DPBI, which can be interpreted as transition from predominant face-on stacking towards edge-on stacking of lamellae. Since the lamellar stacking leads to the build-up of crystallites (see Figure 8.5), a change in stacking direction directly influences the orientation of the latter. In this case, a change of lamellar stacking from in- to out-of-plane leads to a re-orientation of the crystallites from face- to edge-on as is schematically shown in the inset of Figure 8.9a. as schematically shown in Figure 8.9a.

The results of the analysis of ordering, which is performed by azimuthal integration for q -values from 1.58 \AA^{-1} to 1.61 \AA^{-1} for the π - π -stacking peak can be seen in Figure 8.9c. The peak, which shows a high amplitude for the pristine film, steadily loses intensity with increasing dopant concentration and ultimately vanishes, which is also reflected in the

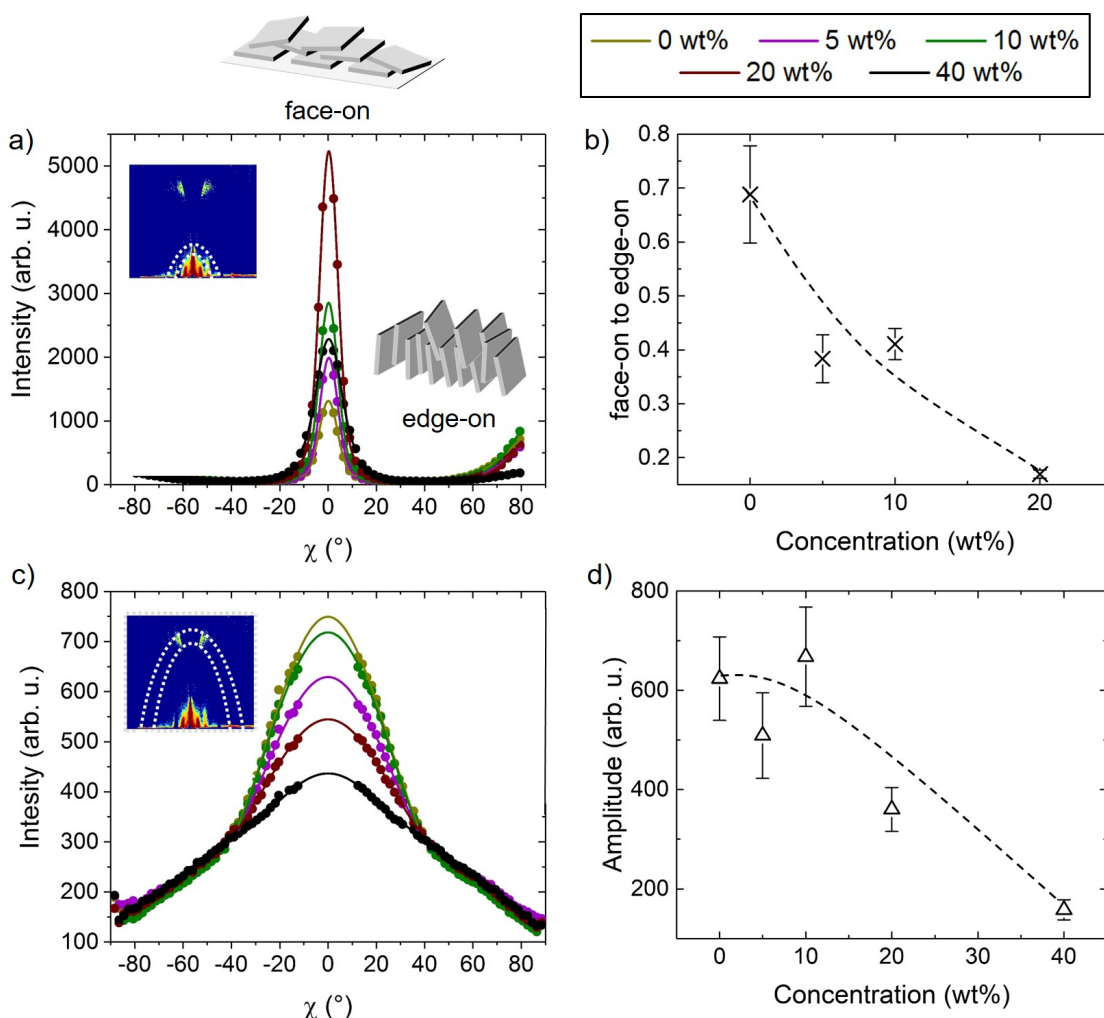


Figure 8.9: a) Azimuthal integrals of the first-order lamellar stacking peak, with the corresponding b) face-on-to-edge-on ratio and c) azimuthal integrals of the π - π -stacking peak, with d) the corresponding peak amplitudes.

peak intensity in Figure 8.9d. This suggests that π - π -stacking becomes less ordered upon doping. A loss in order could be achieved through incorporation of dopant molecules into the π -stacks in between chains of P(NDI2OD-T2), allowing for charge transfer from dopant to polymer, but simultaneously disrupting the inter-molecular ordering. Taking the re-orientation of lamellar stacking into account, one could argue that the ordering of the π -stacks also re-orientates towards a dominant edge-on orientation. However, the absence of such a signal at large values of χ indicates that this is not the case, and thus leads to the conclusion that dopant molecules are increasingly incorporated into the π -stacks and disrupt their inter-molecular order.

Structural analysis of P(NDI2OD-T2) films with even higher concentrations of N-DPBI is also performed and is shown in Figure 8.10. Most structural features disappear for

concentrations above 60 wt%, which suggests a complete loss of order. This strengthens the above-mentioned theory that dopant molecules are increasingly incorporated within the supermolecular structure of P(NDI2OD-T2) films. Thus, concentrations of 60 wt% and 80 wt% will not be considered further.

8.2.2 P(NDI2OD-T2) films on FTO substrates for cross- and pseudo-in-plane measurements

This section discusses the evolution of the P(NDI2OD-T2) thin film structure upon doping. As opposed to the previous section, here the films are prepared on FTO substrates for measurement of thermoelectric properties in a cross-plane and pseudo-in-plane geometry. Charge transport is examined perpendicular to the substrate, which requires a bottom electrode realized by using FTO-coated glass substrates. GIWAXS measurements were performed at the beamline P03 of the DESY in Hamburg, Germany. As previously discussed in Section 8.1, doped P(NDI2OD-T2) are subject to degradation in an oxidative environment, i.e. the effect of doping diminishes when storing doped samples in air. Thusly, there is an urgent need for elucidating a proper way of transporting the doped samples to the measurement site.

Figure 8.11 shows exemplary UV-Vis spectra of P(NDI2OD-T2) doped with 40 wt% N-DPBI stored in two different ways. One sample was stored in a sealed aluminum-foil-composite bag, while the other one was stored in a sealed Duran-glass bottle. Spectra of the initial state and after five hours are shown and reveal drastic differences. While both samples show similar features in the initial state, namely the strongly reduced charge-transfer band around 700 nm and the increased polaron band around 500 nm, the samples stored in the aluminum bag show signs of degradation. As opposed to the sample stored in the Duran bottle, here the polaron band strongly reduces in intensity, while the absorbance of the charge-transfer band again increases. This suggests lower doping levels, which in this case can be attributed to the reaction of the doped P(NDI2OD-T2) films with oxygen. Whether this comes from a leakage in the bag, or residual oxygen trapped inside the bag (although very unlikely, since the samples were packaged inside a nitrogen-filled glove box), remains elusive. Still, storing in a sealed Duran glass bottle appears to be a viable choice for transportation of the samples to the measurement site at DESY. Indeed, when the doped samples were mounted at the instrument, they still exhibited a different color compared to the pristine film (see Figure 8.3b for comparison).

Successful transport of the samples allowed for GIWAXS measurements of the doped P(NDI2OD-T2) films prepared on FTO substrates, the 2D patterns for which can be seen in Figure 8.12. FTO is typically made by a vapor deposition process on top of glass

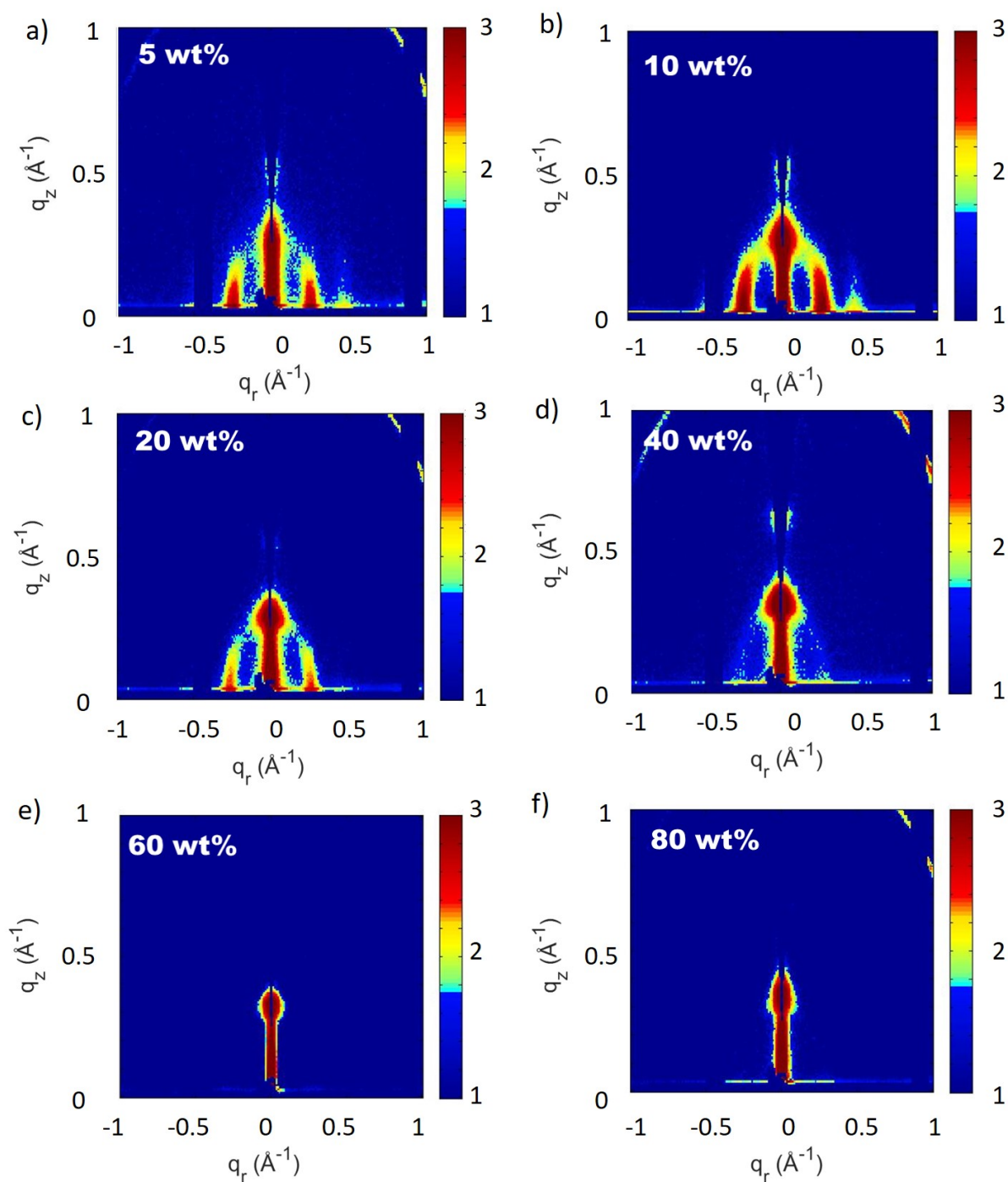


Figure 8.10: 2D GIWAXS data of P(NDI2OD-T2) films doped with increasing concentration of N-DPBI, ranging from 5 wt% to 80 wt%.

substrates. In order to avoid confusion and allow for correct assignment of scattering features to the components, exemplary 2D GIWAXS data of pristine FTO is shown as reference, along with those of the doped P(NDI2OD-T2) films. The pristine P(NDI2OD-

T2) film seen in Figure 8.12b appears to possess very similar structural features compared to the polymer film deposited on glass, as described above. A strong signal at large q_z -values again indicates π - π -stacking of P(NDI2OD-T2) chains in vertical direction. The features found at small q -values can again be assigned to the lamellar stacking, which is oriented parallel to the substrate interface. Qualitatively, the patterns change upon doping which again indicates changes in the film structure. Beside the π - π -stacking decreasing in intensity, again the peaks at small q -values appear to re-arrange.

For a more in-depth analysis, sector integrals in both vertical and horizontal direction are performed of which the former are shown in Figure 8.13 as function of dopant concentration. The overlaid scattering curves obtained from sector integration in vertical direction in Figure 8.13a already indicate strong changes in the morphology. The most obvious change is the decrease in the intensity of the π - π -stacking peak found at q -values of approximately 1.5 \AA^{-1} , which almost disappears at a dopant concentration

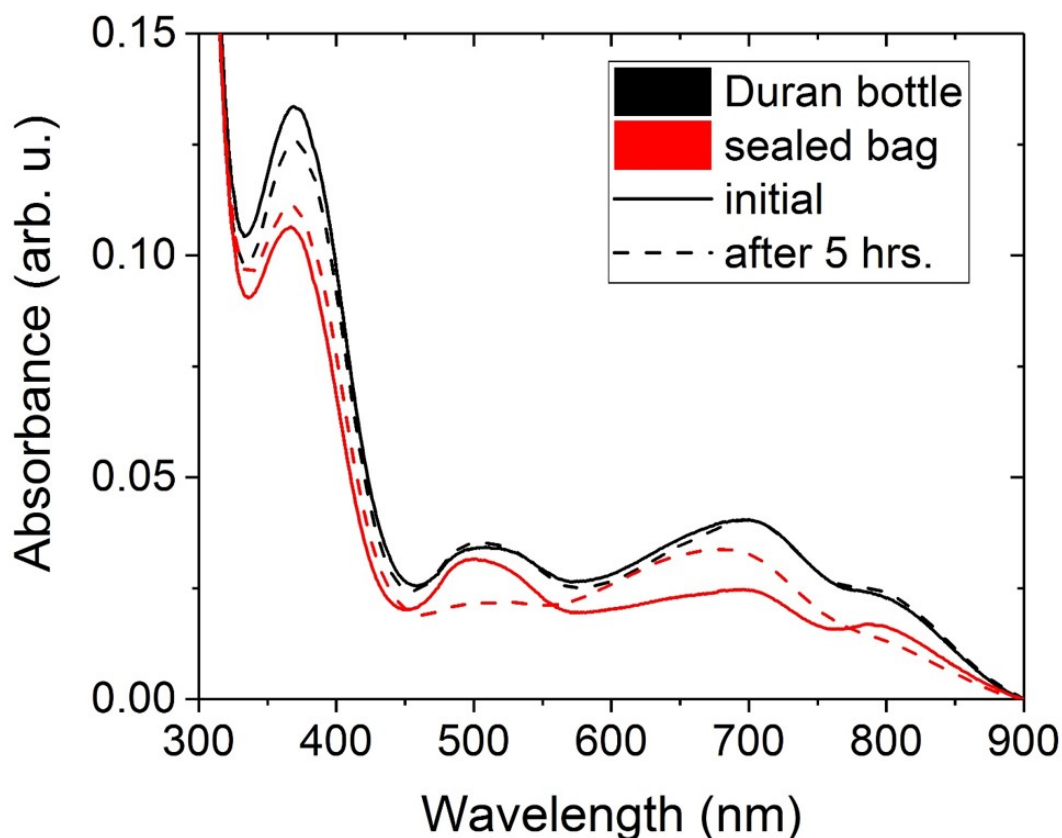


Figure 8.11: UV-Vis absorbance spectra of P(NDI2OD-T2) films doped with 40 wt% N-DPBI stored in a sealed Duran-glass bottle (black) and a sealed aluminum-foil-composite bag (red). Spectra were recorded in the initial state (solid lines) and after five hours (dashed lines).

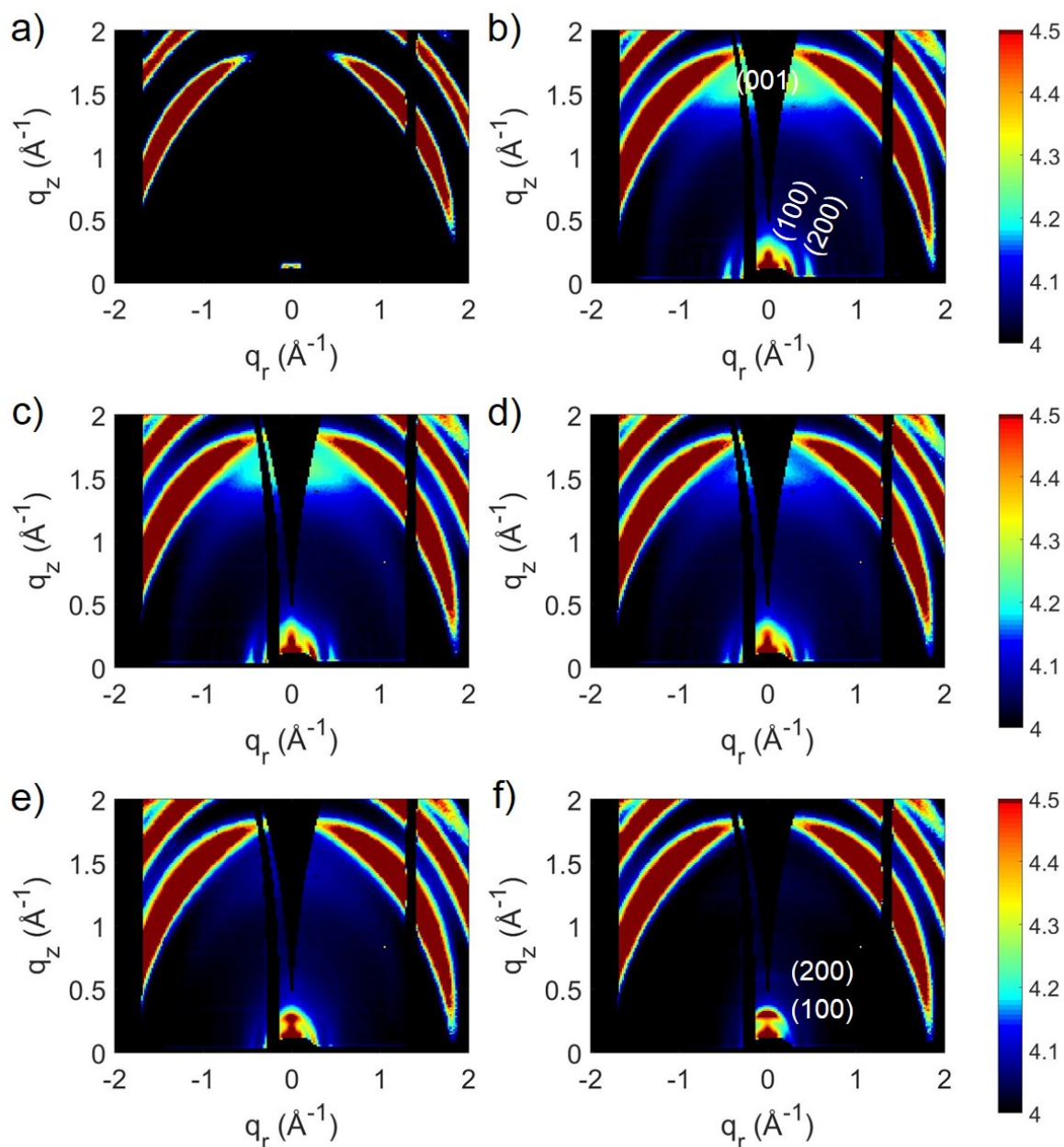


Figure 8.12: 2D GIWAXS data of P(NDI2OD-T2) films prepared on FTO substrates (with pristine FTO shown in a)) with dopant concentrations of b) 0 wt%, c) 5 wt%, d) 10 wt%, e) 20 wt%, and f) 40 wt%.

of 40 wt%. Additionally, a feature emerges at a q -value around 0.3 \AA^{-1} with increasing N-DPBI concentration. A presumed second-order peak is also found close to 0.6 \AA^{-1} for concentrations above 20 wt%, as seen in Figure 8.13b. These signals can be assigned to increasing lamellar stacking perpendicular to the substrate, as function of dopant concentration. Both peaks shift towards larger q -values while also increasing in intensity, as

is shown in Figure 8.13d. The ramification of the peak shifts will be discussed after the analysis of the horizontal sector integrals.

The horizontal sector integrals are shown in Figure 8.14. In the corresponding scattering curves in Figure 8.14a, two distinct features can be discerned. As it was the case for P(NDI2OD-T2) films on glass, these features can again be assigned to the lamellar stacking of P(NDI2OD-T2) parallel to the interface of the substrate. Again, a first-order and second-order peak can be discerned, which shift in opposite directions upon doping with N-DPBI. Their contribution to the scattering signal diminishes with increasing dopant concentration, which indicates loss of structural order at least in in-plane direction.

Together with the information obtained from azimuthal integration, which is shown in Figure 8.15, it becomes possible to fully elucidate the changes in the film structure upon

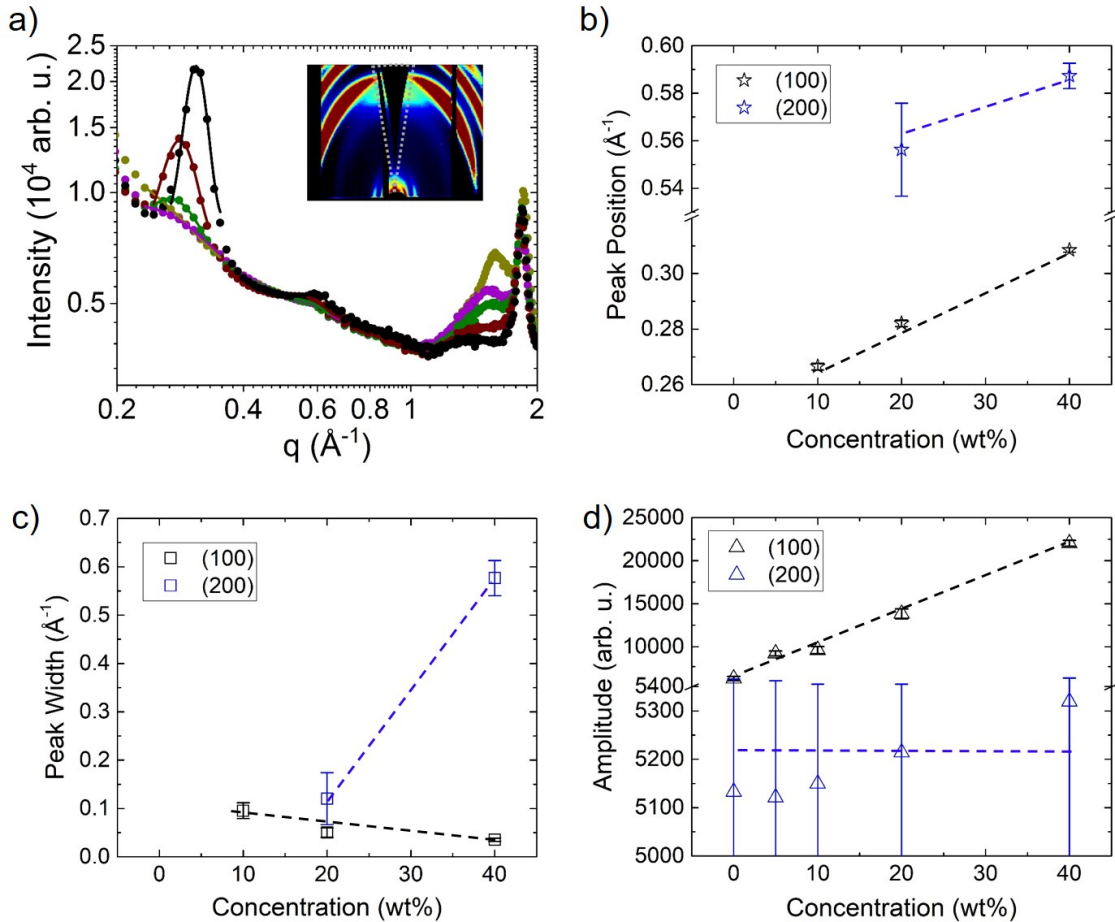


Figure 8.13: a) Vertical sector integrals from 2D GIWAXS data of P(NDI2OD-T2) films doped with 0 wt% (yellow), 5 wt% (magenta), 10 wt% (green), 20 wt% (brown) and 40 wt% (black). b) Peak positions, c) peak widths and d) peak amplitudes of the (100) (black) and (200) (blue) peak.

doping of P(NDI2OD-T2) with N-DPBI. Figure 8.15a shows the azimuthal line cuts as function of concentration for the first-order peak assigned to the lamellar stacking, performed for q -values between 0.2 \AA^{-1} and 0.3 \AA^{-1} . While for the pristine film, intensities both at χ -values around 0° and 70° are similar, the ratio changes strongly upon doping. The scattering contribution at large χ -values is strongly decreased for concentrations of 40 wt%, while the intensity around 0° remains constant. This indicates a change in stacking direction, which can be analyzed in more detail, by calculating the ratio of the respective amplitudes, as is shown in Figure 8.15b. The face-on-to-edge-on ratio is gradually decreasing with increasing amount of dopant, which indicates a re-orientation of the lamellar stacking from being favored parallel to the substrate in the pristine film, to being favored perpendicular to the substrate for high concentration. This finding qualitatively

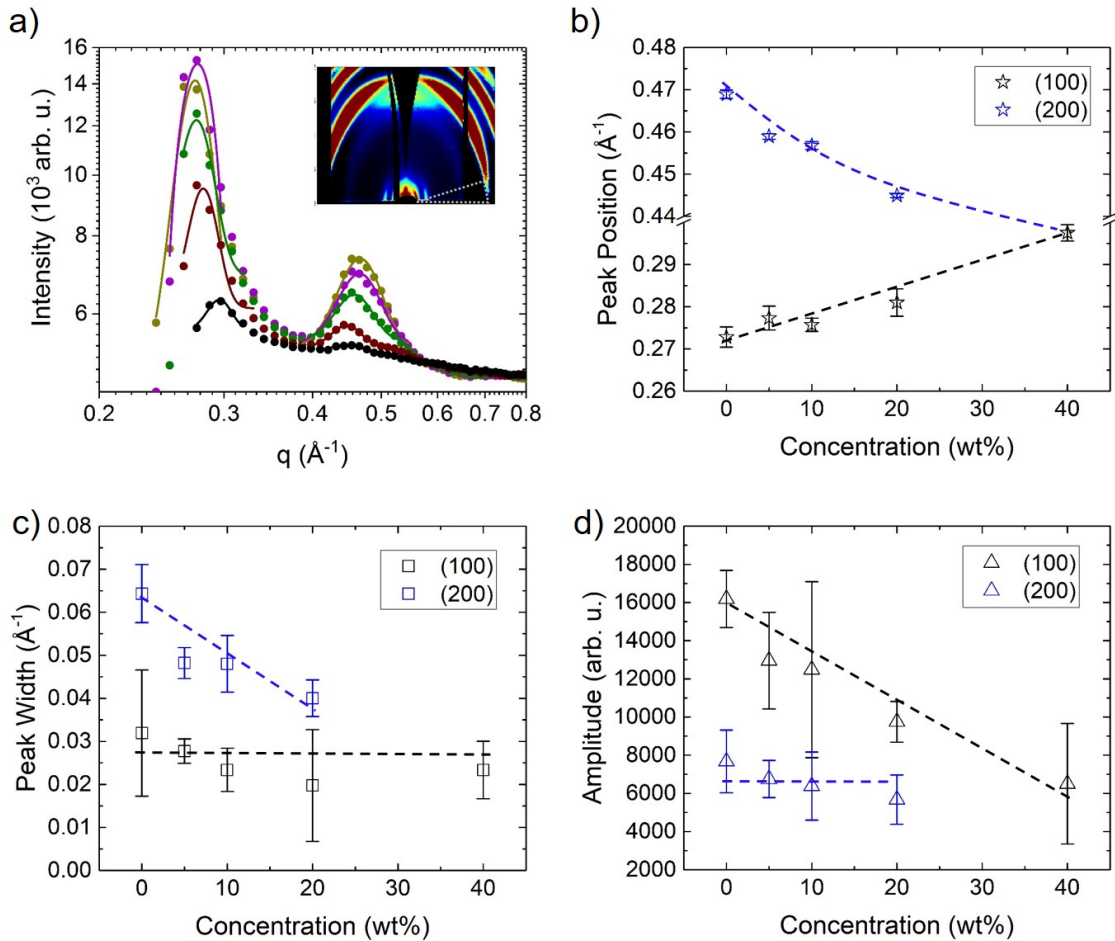


Figure 8.14: a) Horizontal sector integrals from 2D GIWAXS data of P(NDI2OD-T2) films doped with 0 wt% (yellow), 5 wt% (magenta), 10 wt% (green), 20 wt% (brown) and 40 wt% (black). b) Peak positions, c) peak widths and d) peak amplitudes of the (100) (black) and (200) (blue) peak.

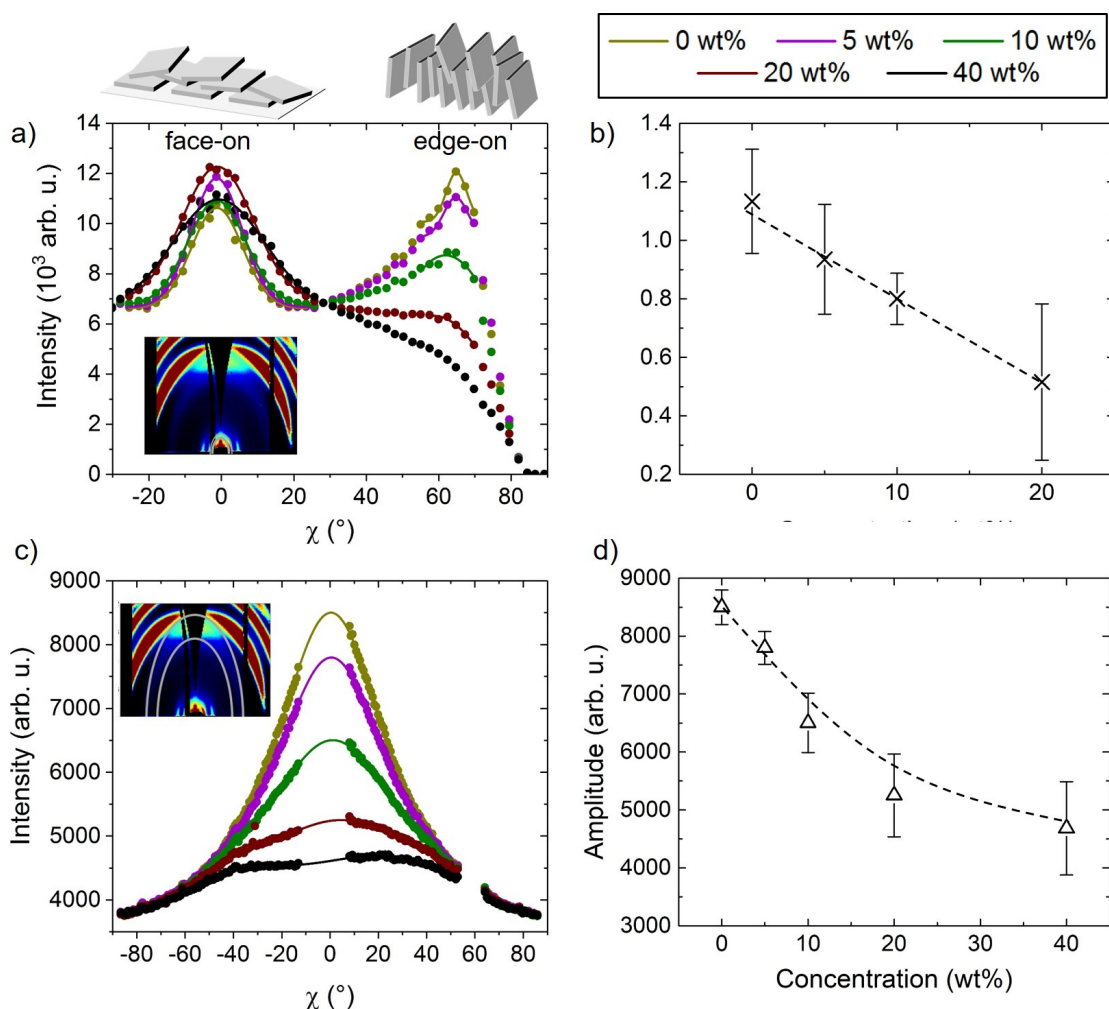


Figure 8.15: a) Azimuthal integrals of the first-order lamellar stacking peak, with the corresponding b) face-on-to-edge-on ratio and c) azimuthal integrals of the π - π -stacking peak, with d) the corresponding peak amplitudes.

resembles that for doped P(NDI2OD-T2) films prepared on glass substrates discussed above. Azimuthal integration of the π - π -stacking peak (between q -values of 1.58 \AA^{-1} and 1.61 \AA^{-1}), again reveals the decreasing order of the π - π -stacking with increasing degree of doping, as seen from the azimuthal line cuts in Figure 8.15c and the respective peak amplitudes in Figure 8.15d. As discussed before, this can most likely be assigned to incorporation of dopant molecules into the π -stacks, allowing for charge transfer from the dopant molecules to the polymer, while simultaneously destroying the order of the π -stacks, especially at high dopant concentrations.

8.2.3 Structural model

Stringing together the results of GIWAXS measurements of doped *P(NDI2OD-T2)* films prepared on both glass and FTO substrates, allows for the proposition of a structural model, which is presented in Figure 8.16. The effects of doping on the thin film structure of the polymer are manifold. Addition of the dopant to the polymer solution prior to film fabrication alters the film formation, which can be seen from qualitative differences in the 2D GIWAXS patterns. Chains of *P(NDI2OD-T2)* preferably form π - π -stacks, which exhibit a characteristic signal at large q -values in out-of-plane direction. Dopant molecules appear to be incorporated in these stacks, as the peak amplitudes decrease with increasing amount of N-DPBI. The latter is indicative of a loss in order. As a consequence of the π -stacking, extended polymer chains are able to form sheet-like regions of crystalline order being referred to as lamellae. These lamellae in turn build up flat plate-like crystallites. Dependent on the direction of the lamellar stacking also the crystallites' orientation changes. In pristine films, in-plane lamellar stacking leads to the formation of face-on oriented crystallites. Azimuthal integration reveals that the preferred in-plane stacking of the lamellae changes with increasing amount of N-DPBI towards a stacking

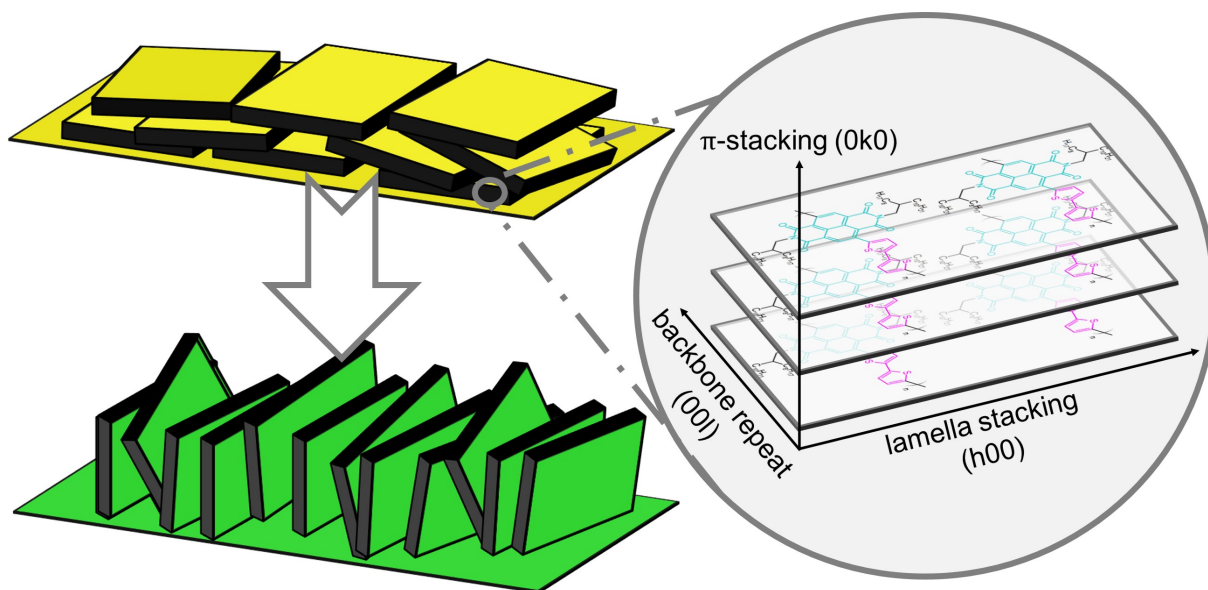


Figure 8.16: Structural model of pristine *P(NDI2OD-T2)* (yellow) and upon doping with N-DPBI (green), with schematic of π - π -stacking of polymer chains. Doping leads to a re-orientation of the lamellar stacking being parallel to being perpendicular to the substrate. As a consequence, the crystallites built up by the lamellar stacking change their orientation from face- to edge-on. However, it should be noted that an overall decrease in order is observed due to incorporation of dopant molecules into the π -stacks, leading to an overall decrease of the π -stacking signal. This is not included in the schematic.

direction perpendicular to the substrate. Besides, also the shift of scattering intensity observed in the azimuthal line cuts of the first-order crystalline stacking peak from small χ -values towards large χ -values is proof for this notion. The herein observed change in lamellar stacking eventually has an influence on the orientation of the crystal which is built up by said lamellar stacking. With increasing dopant concentration, the lamellar stacking becomes perpendicular to the substrate which in turn leads to the formation of a flat crystallite oriented in a face-on manner. The π - and lamellar stacking within a single crystallite as well as the orientation of the crystallites in a thin film are sketched in Figure 8.16. It was also found that the general trends for the morphological evolution are the same, irrespective of the choice of substrate.

In summary, irrespective of the type of substrate, inclusion of dopant molecules in the thin film structure of P(NDI2OD-T2) has drastic ramifications on the latter. Most significantly, structural order is lost in the π -stacks, in addition to changes in the predominant orientation of lamellae and crystallites. These changes are expected to strongly influence the thermoelectric properties, which will be discussed in Section 8.3. Since the doping of P(NDI2OD-T2) with N-DPBI not only changes the electronic properties through introduction of charge carriers, but also changes the morphology through re-orientation of crystallites and decreasing structural order, effects on both the Seebeck coefficient and the electrical conductivity are expected.

8.3 Thermoelectric characterization

Apart from few studies on the matter, [90] due to the lack of extensive investigations of P(NDI2OD-T2) as thermoelectric material, there is only a weak basis for determining an advantageous geometry for fabricating a thermoelectric generator. This led us to investigate three distinct measurement geometries, which are schematically shown in Figure 4.13. The in-plane geometry was used to probe charge transport in a direction parallel to the substrate and is very similar to that of previous studies with PEDOT:PSS, as two electrodes are deposited parallel to each other on top of the film which itself is spin-cast on an insulating glass substrate. In contrast, in the cross-plane geometry, charge transport perpendicular to the sample was examined. The film was fabricated on a conducting FTO-substrate. The conducting part is partially etched away, leaving only the insulating glass underneath in contact with the polymer, in order to prevent short-circuits when pressing an electrode on the top aluminum electrode. This yields a defined geometry which allows charge transport from the bottom electrode (which is the FTO), through the polymer film to the top electrode, which is prepared through vapor deposition of aluminum. The third geometry which is investigated in this study, is the so-called pseudo-in-plane ge-

ometry which is prepared in a similar fashion as the cross-plane version. However, the key difference is the absence of overlap between the bottom and top electrode, as can be seen on the right side of Figure 4.13. This results to charge transport over macroscopic distances in the in-plane direction, while also transport of charges in cross-plane direction, since the distance corresponding to the thickness of the film needs to be traversed by the charges, thus inspiring the name. The study of thermoelectric properties of the in-plane and cross-plane versions allows for comparison with the morphological model presented in the previous section, while the pseudo-in-plane geometry allows for fabrication of a thermoelectric generator purely based on conducting polymers as active materials.

8.3.1 In-plane geometry

Firstly, doped P(NDI2OD-T2) films are prepared in the in-plane geometry, in order to investigate changes in their thermoelectric characteristics. In Figure 8.17 the shown quantities include temperature-dependent resistances, electrical conductivities extracted from these resistances at different temperatures, Seebeck coefficients and power factors as function of dopant concentration. A problem that occurs during the study is the low intrinsic electrical conductivity of undoped P(NDI2OD-T2). As can be seen in Figure 8.17a, the pristine sample does not appear to be measurable at room temperature, since the resistance exceeds the measurable detection limit. Only for temperatures above 60 °C, resistances on the order of $10 \cdot 10^{10} \Omega$ can be detected, which then drop for higher temperatures. For increasing amount of N-DPBI, the resistance curves shift towards lower overall values, with the minimal value being reached for a dopant concentration of 10 wt%. Interestingly, for this sample again an increase in resistance for temperatures higher than 80 °C is observed, which is also present for dopant concentrations of 20 wt% and 40 wt%. Taking into account the findings from the spectroscopic investigation in Section 8.1 and the temperature-dependent UV-Vis investigations, temperature-induced degradation of the doped films is mostly likely responsible for this observation. Upon doping, the films become sensitive to the oxygen contained in the atmosphere, with higher temperatures only increasing the degradation reaction rate. Thus, for all subsequent measurements a maximum temperature of 70 °C was not exceeded, in order not to compromise the measurements due to degradation of the films.

Nevertheless, values for the electrical conductivities are extracted at low and high temperatures, and presented in Figure 8.17b. Dopant concentrations of 10 wt% lead to a maximum conductivity of $1.1 \cdot 10^{-2} \text{ S/cm}$. The initial increase in the electrical conductivity can be attributed to a higher number of charge carriers being introduced by the dopant, as was seen in the UV-Vis spectra. For higher concentrations, the electrical con-

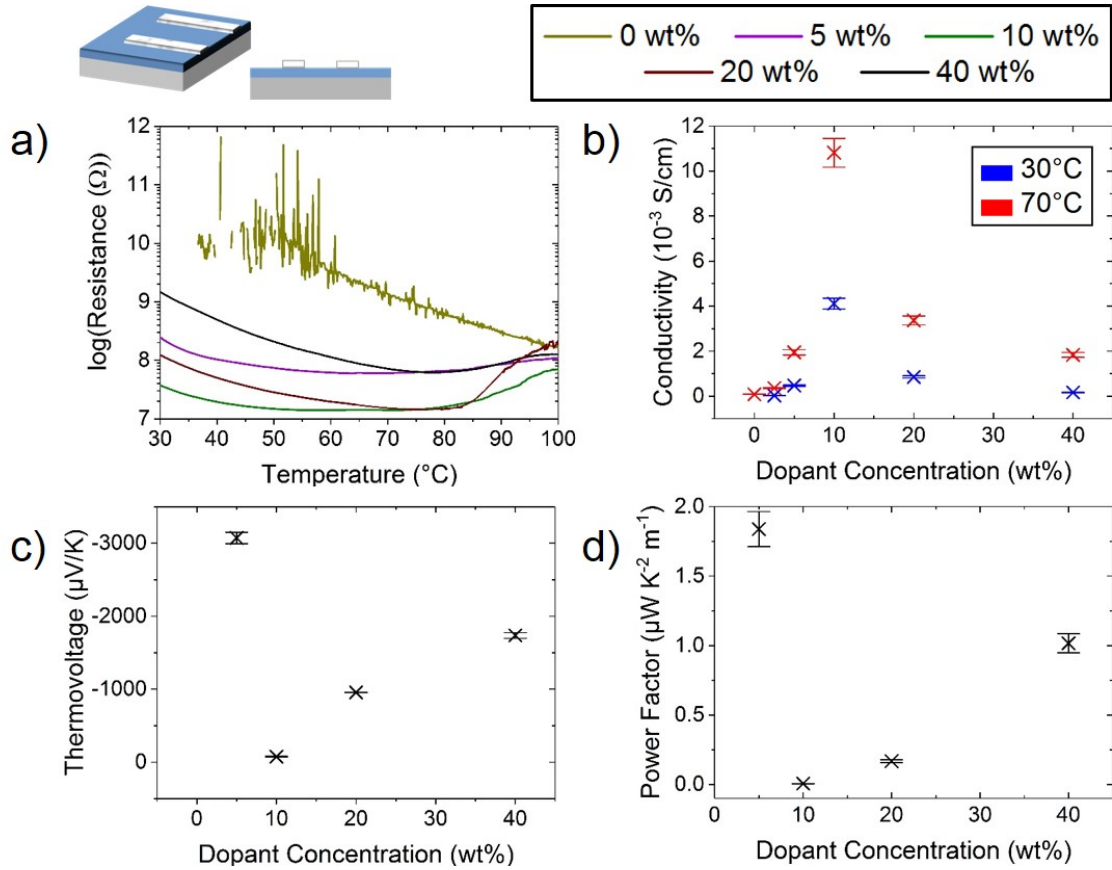


Figure 8.17: Thermoelectric characteristics of doped P(NDI2OD-T2) films prepared in an in-plane geometry on glass substrates. a) Temperature-dependent resistance of P(NDI2OD-T2) doped with 0 wt% (yellow), 5 wt% (magenta), 10 wt% (green), 20 wt% (brown) and 40 wt% (black) N-DPBI. b) Electrical conductivities as function of dopant concentration, extracted at 30 $^{\circ}\text{C}$ (blue) and 70 $^{\circ}\text{C}$ (red) from the resistance curves. c) Seebeck coefficients and d) power factors as function of dopant concentration. It should be noted that the latter two quantities could not be measured for the pristine P(NDI2OD-T2) film, due to insufficient conductivity leading to compromised measurement of the Seebeck coefficient.

ductivity decreases again, although still being improved compared to the pristine film. The electrical conductivities are in general higher for higher temperatures, which stems from the decreasing resistances as function of temperature, as is also the case for typical semiconductors. Also the decrease of electrical conductivities for the high dopant concentrations can be understood, when considering the morphological model presented in Section 8.2. It is found that increased levels of doping lead to re-orientation of the π -stacks from being primarily oriented perpendicular to the substrate, to being primarily oriented parallel to the substrate. Since charge carriers are believed to be transported along the π -stacks, this could explain the drastic increase of the electrical conductivity up to concentrations of 10 wt%. However, the introduction of more dopant into the film

comes at the cost of order within both the π -stacks, which then leads to the observed drop in in-plane electrical conductivity for higher concentrations.

The Seebeck coefficient is also measured for the doped P(NDI2OD-T2) films and is shown in Figure 8.17c. As theory suggests, a completely opposite behavior compared to that of the electrical conductivity is observed, which correlates to the number of charge carriers in the system. [7] The lowest value for the Seebeck coefficient is present at a dopant concentration of 10 wt%, for which also the highest electrical conductivity is found. In comparison to typical PEDOT:PSS films prepared in this thesis, the Seebeck coefficients have an opposite sign in addition to generally strongly increased levels. The first observation is a result of negative polarons being the majority charge carriers, while the generally lower degree of doping in P(NDI2OD-T2) films and the resulting lower electrical conductivity is most likely responsible for the high values. It should be noted that the Seebeck coefficient could not be measured for the pristine P(NDI2OD-T2) sample, due to the high resistance and therefore impeded electrical contactability.

When looking at the power factors in Figure 8.17d, a behavior mostly governed by the Seebeck coefficient as function of concentration is found, with the maximum value being $1.8 \mu\text{WK}^{-2}\text{m}^{-1}$ at a concentration of 5 wt%. For higher concentrations lower values are obtained, for which the decreased Seebeck coefficients are responsible. Notably, despite the low values of electrical conductivity even after doping, the obtained power factors are on the same order of magnitude compared to those of e.g. PEDOT:PSS films post-treated with EG, which again highlights the feasibility of doped P(NDI2OD-T2) films for thermoelectric applications.

8.3.2 Cross-plane geometry

As second measurement geometry, the cross-plane setup is proposed which drew its inspiration from the way thermoelectric generators composed of inorganic materials are constructed. Here, there is an overlap between the FTO electrode on the bottom and the aluminum electrode on the top of the film. This allows for direct charge transport from bottom to top through the polymer film. The results of the thermoelectric characterization are compiled in Figure 8.18. In contrast to the findings for the in-plane geometry, the temperature-dependent resistances all show similar orders of magnitudes around $1 \cdot 10^5 \Omega$, independent of dopant concentration. While the resistances slightly decrease with increasing amount of N-DPBI, the curve at a concentration of 40 wt% appears to be very noisy. This might stem from contacting problems due to a very high overall resistance.

When extracting the electrical conductivities, one comes to the realization that, after taking into account the measurement geometry and the resulting dimensions for charge

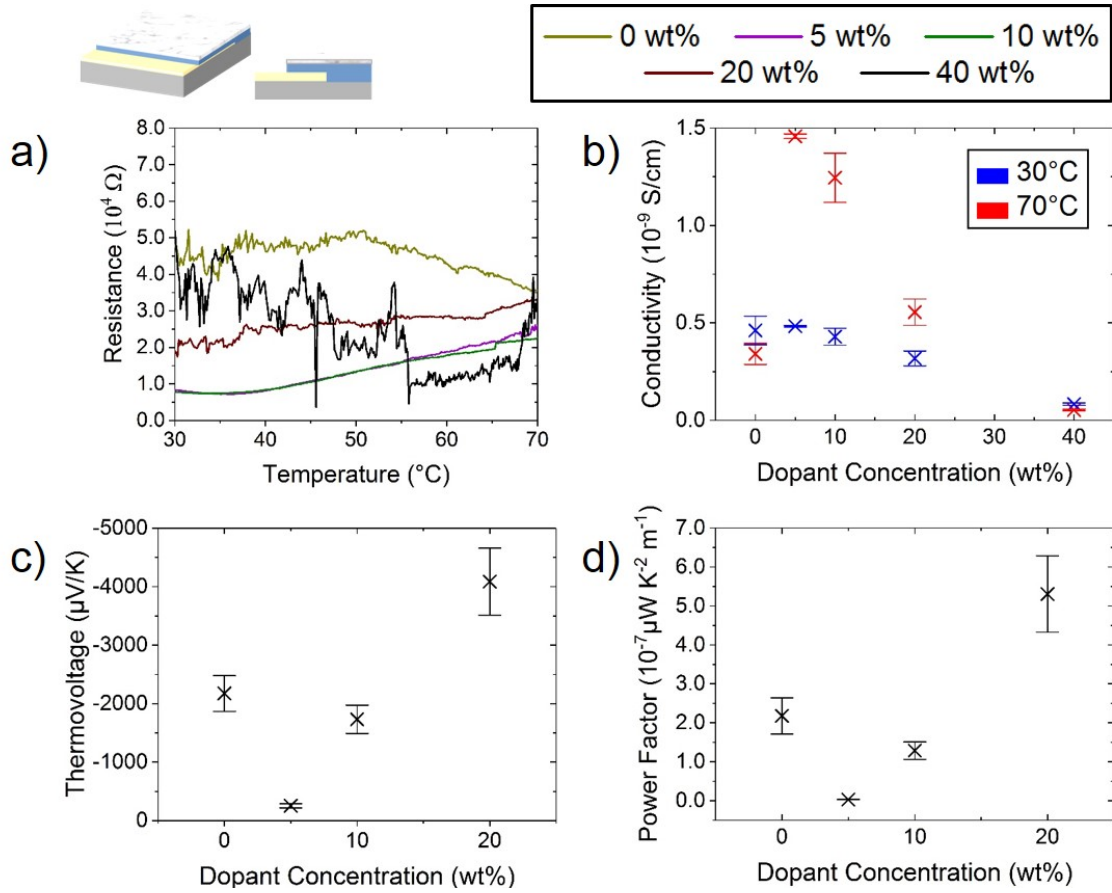


Figure 8.18: Thermoelectric characteristics of doped P(NDI2OD-T2) films prepared in a cross-plane geometry on FTO substrates. a) Temperature-dependent resistance of P(NDI2OD-T2) doped with 0 wt% (yellow), 5 wt% (magenta), 10 wt% (green), 20 wt% (brown) and 40 wt% (black) N-DPBI. b) Electrical conductivities as function of dopant concentration, extracted at 30 $^{\circ}\text{C}$ (blue) and 70 $^{\circ}\text{C}$ (red) from the resistance curves. c) Seebeck coefficients and d) power factors as function of dopant concentration. It should be noted that the latter two quantities could not be measured for the film with a dopant concentration of 40 wt%, due to insufficient conductivity leading to compromised measurement of the Seebeck coefficient.

transport, the obtained values are orders of magnitudes smaller than those for the in-plane measurements. This originates from the combination of a large cross-section (being equivalent to the area of overlap between the bottom and top electrode) and the small distance (being equivalent to the film thickness of few tens of nm) the charges have to travel between the contacts. The maximum value of roughly $1.5 \cdot 10^{-9} \text{ S/cm}$ is thus found at a small dopant concentration of 5 wt%, as seen in Figure 8.18b. Also in this case, the electrical conductivity first increases due to the introduction of charge carriers, but decreases for higher dopant concentrations due to an unfavorable morphology. Doping leads to a re-orientation of the π -stacks from being oriented perpendicular to being

oriented parallel to the substrate, which does not match with the measured direction for charge transport, in addition to an overall loss of order.

The Seebeck coefficients of the cross-plane samples can be found in Figure 8.18c. They again show the inverse trend to the electrical conductivity, with the minimal value being found at 5 wt% dopant concentration. For higher concentrations the Seebeck coefficient increases again, although it cannot be determined for concentrations of 40 wt%. This most likely correlates to the effect of poor contacting seen for the temperature-dependent resistance curve for 40 wt% dopant. Too large resistances lead to poor contactability and thus impede the correct determination of the Seebeck coefficient and should be taken into account when investigating novel systems.

As seen in Figure 8.18d, the power factor is again most strongly influenced by the evolution of the Seebeck coefficient. However, if compared to the values obtained for the in-plane samples, the power factors found are seven orders of magnitudes smaller, with the maximum being $5 \cdot 10^{-7} \mu\text{WK}^{-2}\text{m}^{-1}$ at dopant concentrations of 20 wt%. Thus, it is concluded that the cross-plane geometry is not as favorable as the in-plane one, which can be explained by taking into account the morphology model. The unfavorable re-orientation of π -stacks from perpendicular to parallel, is less suitable for cross-plane charge transport.

A challenge that also arose during film fabrication, is the occurrence of short-circuits between the top and the bottom electrode. Due to the low film thickness of few tens of nanometers, it is possible for the aluminum to come directly in contact with the bottom electrode through defects in the film, while still forming a closed layer on top. Therefore, when contacting both electrodes, short-circuits are obtained which make the measurement of resistances impossible. In order to avoid this issue, a third geometry is presented.

8.3.3 Pseudo-in-plane geometry

Finally, the third geometry investigated in this study is the newly-proposed, so-called pseudo-in-plane geometry. This is an amalgamation of the two previously discussed geometries, in that the doped P(NDI2OD-T2) film is deposited on FTO substrates. The active material on the FTO substrate is etched away in such a fashion that no overlap with the thermally evaporated top aluminum electrode is obtained in the end. This leads to macroscopic lateral distances in addition to the film thickness, which the charge carriers have to traverse, since the electrodes do not sandwich the polymer film. The film geometry is also shown as inset in Figure 8.19.

The thermoelectric properties of doped P(NDI2OD-T2) films are shown in Figure 8.19. Temperature-dependent resistances are, similarly to the cross-plane investigations, on a

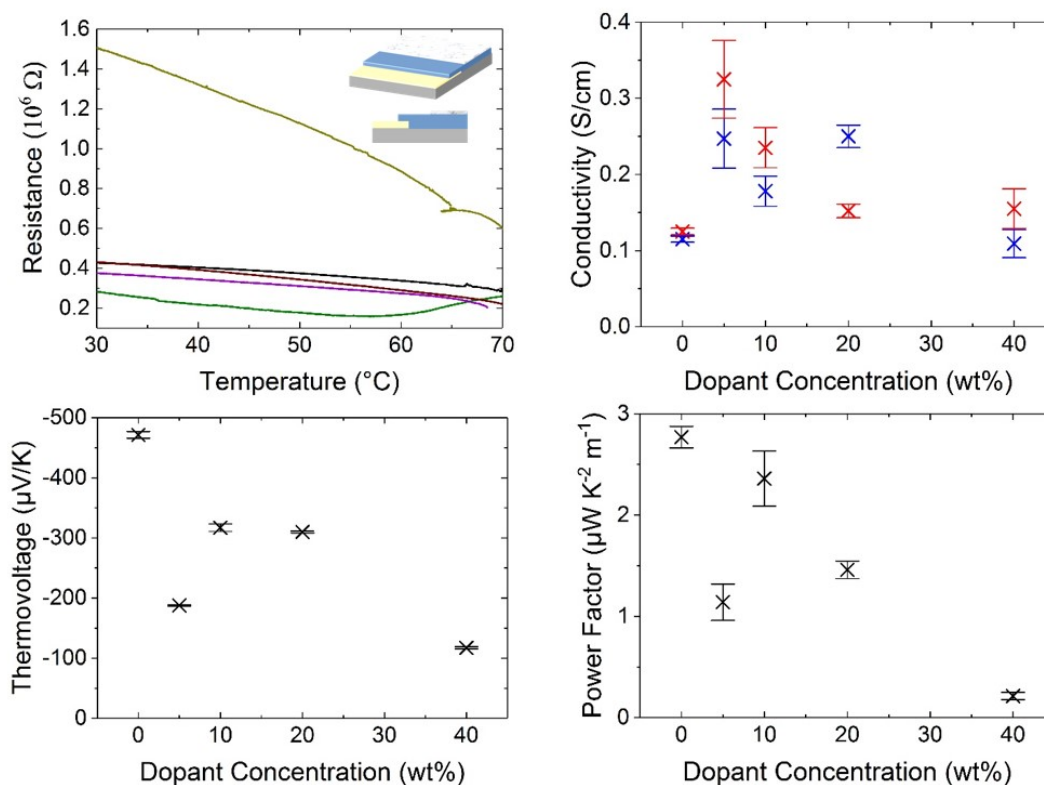


Figure 8.19: Thermoelectric characteristics of doped P(NDI2OD-T2) films prepared in a pseudo-in-plane geometry on FTO substrates. a) Temperature-dependent resistance of P(NDI2OD-T2) doped with 0 wt% (yellow), 5 wt% (magenta), 10 wt% (green), 20 wt% (brown) and 40 wt% (black) N-DPBI. b) Electrical conductivities as function of dopant concentration, extracted at 30 $^{\circ}\text{C}$ (blue) and 70 $^{\circ}\text{C}$ (red) from the resistance curves. c) Seebeck coefficients and d) power factors as function of dopant concentration.

similar order of magnitude. Up to concentrations of 10 wt%, a steady downward shift of the curves can be observed, which is then reversed for higher concentrations, as seen in Figure 8.19a.

The extracted conductivity values in Figure 8.19b again show a maximum of 0.32 S/cm at a N-DPBI concentration of 5 wt%, which is three orders of magnitude higher than the typical values found in the in-plane geometry. The fact that for higher dopant concentrations the electrical conductivity again drops can again be explained by the morphological change induced by the doping process. The re-organization of the π -stacks and the lamellar stacking parallel to the substrate would be favorable for the pseudo-in-plane geometry, since the lateral distance is much larger than the vertical one. This re-orientation, however, comes at the cost of structural order within both types of stacks,

due to the incorporation of dopant molecules into the film. Still, the vastly improved electrical conductivities strengthen the feasibility of this geometry.

The Seebeck coefficients shown in Figure 8.19c show much smaller variations as function of dopant concentration, and in general lower levels with the maximum value of roughly $-470 \mu\text{V}/\text{K}$ being found for the pristine sample. It should be noted at this point that for the in-plane geometry no Seebeck coefficient could be measured, due to the insulating nature of pristine P(NDI2OD-T2) films. The mostly monotonous drop in Seebeck coefficient with increasing amounts of N-DPBI is in agreement with UV-Vis data discussed in Section 8.1, in that higher nominal concentrations of dopant lead to larger charge carrier concentrations.

Finally, the power factors of the pseudo-in-plane samples, seen in Figure 8.19d, show a similar trend to that of the Seebeck coefficient. Pristine P(NDI2OD-T2) yields the maximum value close to $2.7 \mu\text{WK}^{-2}\text{m}^{-1}$, which subsequently drops for higher concentrations of dopant. These values are easily comparable to those of the in-plane samples, discussed above, again strengthening the feasibility of this geometry. However, the pseudo-in-plane geometry has several advantages over the in-plane one, especially regarding fabrication of a thermoelectric generator. As discussed in the following section, when thinking of a way of connecting p-type and n-type legs in a thermoelectric generator while trying to employ an in-plane geometry, alternating deposition of the two different materials becomes difficult. The next section will therefore deal with the conceptualization of a thermoelectric generator based on conducting polymers as active materials, while making use of the advantages the pseudo-in-plane geometry provides for both the p-type PEDOT:PSS and n-type P(NDI2OD-T2) leg.

8.4 Performance of a thermoelectric generator

The main purpose of the whole investigation regarding the thermoelectric properties of doped P(NDI2OD-T2) is to conceptualize and fabricate a thermoelectric generator which is solely based on conducting polymers as active materials, thus the semiconducting legs. As n-type leg the aforementioned P(NDI2OD-T2) is used, while EG-post-treated PEDOT:PSS serves as the p-type leg in the generator. These two halves are fabricated on top of a FTO-coated elongated glass slide, of which the central part is etched away. A full electrical circuit is realized by the top aluminum electrode, which connects the n-type and p-type part. It should be mentioned that for both legs, the pseudo-in-plane geometry is employed as it combines the feasible thermoelectric properties obtained in an in-plane geometry, combined with the relative ease with which the cross-plane geometry can be realized. In addition, due to the absence of overlap area between the top and bottom

electrode, the risk of device failure originating from short-circuits is greatly reduced. A sketch of the thermoelectric generator is shown in Figure 8.20, while a detailed description of the fabrication process is given in Section 4.3.

Electrical contacting is ensured via the FTO electrodes located at each side of the device, while the temperatures of the 'hot' and 'cold' side (i.e. bottom and top) are simultaneously monitored through placement of temperature sensors on one FTO electrode and the aluminum. A temperature gradient is measured between the electrodes. This setup leads to temperature gradients in the range of 5 °C to 7 °C and allows for the comparison of obtainable thermovoltages and I-V-characteristics of two thermoelectric generators, one of which is built using pristine P(NDI2OD-T2) and the other with P(NDI2OD-T2) doped with 40 wt% N-DPBI as n-type leg. Measurements of the output voltage and the device resistance are shown in Figure 8.21, with the former normalized to a temperature difference of 1 K. As seen in Figure 8.21a, the generator with 0 wt% P(NDI2OD-T2) shows a stable output voltage of roughly 0.3 mV/K over time. Upon doping with 40 wt% N-DPBI, the output voltage is nearly tripled, leading to values around 1.1 mV/K. In both cases, the temperature gradients do not show drastic changes, as indicated by the dashed lines in Figure 8.21a.

In order to calculate the full power output P of both devices, a quantity related to the conductivity within both generators is necessary. Therefore, the device resistances are measured by applying different bias voltages between the two FTO electrodes and monitoring the induced currents over time. The mean currents are then plotted against

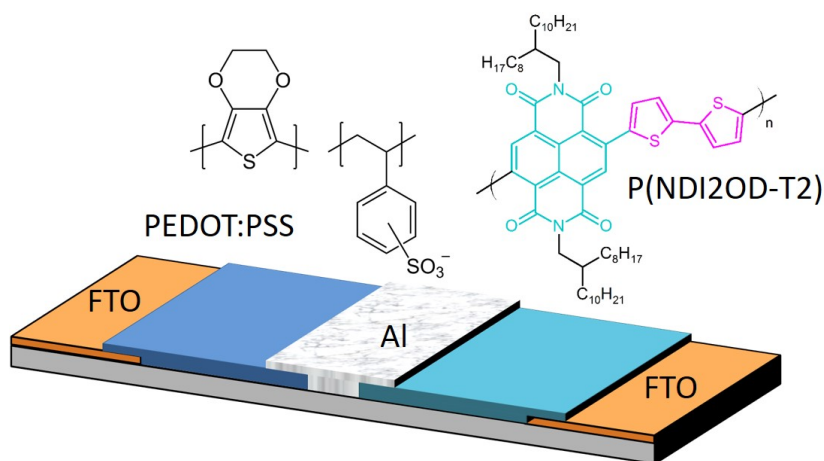


Figure 8.20: Schematic drawing of a thermoelectric generator, employing conducting polymers as active materials. PEDOT:PSS (blue) and P(NDI2OD-T2) (turquoise) are used as p-type and n-type leg in a pseudo-in-plane geometry, respectively. Both legs are electrically connected with aluminum (gray) as top electrode, while a partially etched FTO-coated (yellow) glass slide (gray) serves as bottom electrode.

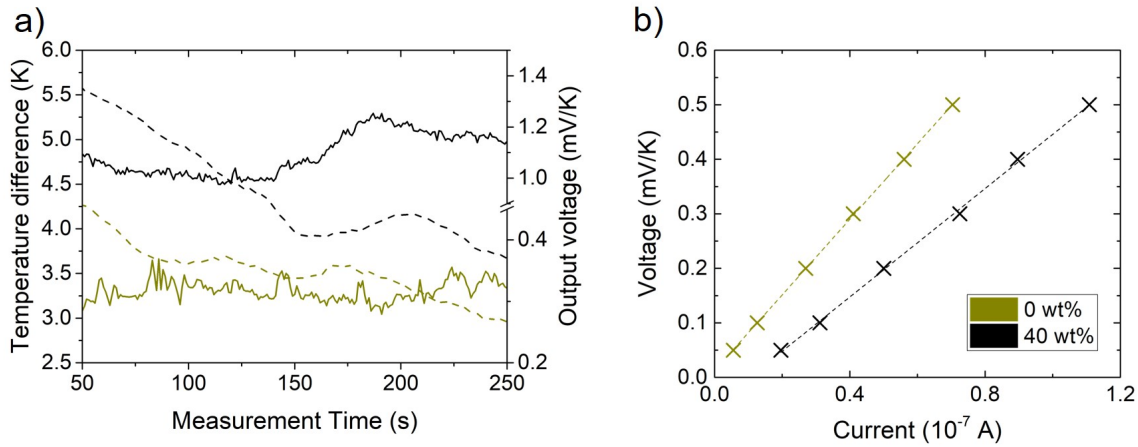


Figure 8.21: a) Output voltages (solid lines) and temperature differences (dashed lines), and b) I-V curves with linear fits of thermoelectric generators based on PEDOT:PSS and P(NDI2OD-T2). Two generators were studied, with dopant concentrations of 0 wt% (dark yellow) and 40 wt% (black).

the respective bias voltages and yield Figure 8.21b. Since a linear relation between the voltage and current is observed for both samples, the existence of internal resistances in the devices can be excluded. From the slopes of the linear fits through the data points for both samples, resistance (R) values can be obtained using Ohm's law in Equation 8.1, in which U represents the bias voltage and I the induced current.

$$R = \frac{U}{I} \quad (8.1)$$

The results of the characterization of both thermoelectric generators are summarized in Figure 8.22. As discussed above, the thermovoltage is nearly tripled upon doping with 40 wt% from roughly 0.3 mV/K to 1.1 mV/K. In addition, the device resistance R is reduced from $7 \cdot 10^6 \Omega$ to roughly $5 \cdot 10^6 \Omega$. Taking both quantities into account, the power output P can be calculated by using Equation 8.2, where U is the Voltage output and R the device resistance.

$$P = \frac{U^2}{R} \quad (8.2)$$

The power output, as seen in Figure 8.22c, strongly changes upon doping. While for the generator without dopant the power output amounts to roughly 0.2 W/K it increases by factor 12 to average values around 2.4 W/K, resulting in largely improved power conversion capabilities.

It should be noted that one was faced with several challenges during the measurement of the full generators. One issue was the slight lateral temperature gradient, which was

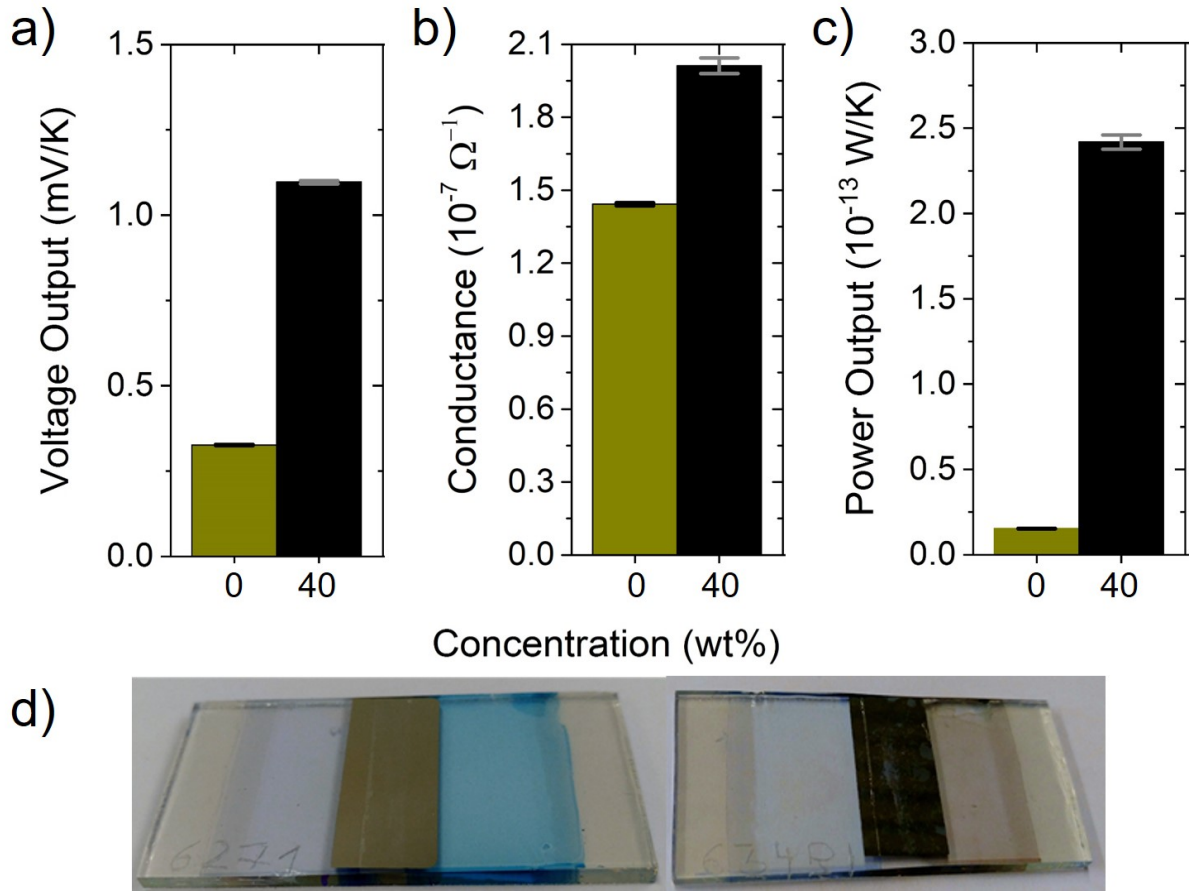


Figure 8.22: a) Voltage output, b) conductance and c) power output for two thermoelectric generators, with dopant concentrations of 0 wt% (dark yellow) and 40 wt% (black). d) Photographs of the investigated generators, with the n-type leg always being on the right side.

induced due to the asymmetric setup in XAVER. Specifically, the hot copper block was placed centered underneath the Al-bridge on the generator. This inevitably led to slightly different temperatures between both FTO electrodes. Additionally, this lateral temperature gradient was enhanced by the presence of water in the cold copper block, which was situated underneath one of the FTO electrodes. As it turns out, the effect of the cold copper block on the lateral gradient is diminished, once the former is emptied of water. It can be argued that the water in the cold copper block acts as heat sink, and thus causes the asymmetry in the temperature distribution along the device. In presence of water, the lateral temperature gradient amounts to roughly 3 °C to 7 °C, while in the former's absence a gradient of barely 1 °C is measured. These issues can potentially be solved through further improvement of XAVER. Still, the discussion of the fabrication and implementation of polymer-based thermoelectric generators up to this point serves as proof-of-concept of the design.

In summary, the implementation of the pseudo-in-plane geometry allowed for the facile fabrication of thermoelectric generators based on the conducting polymers PEDOT:PSS and P(NDI2OD-T2) as active materials. Doping of the n-type component with N-DPBI greatly improves the voltage output, while also reducing the internal device resistance. The combination of both factors leads to a twelve-fold improvement in power output, rendering the design, choice of components and doping promising approaches for thermal energy conversion using thermoelectric generators.

8.5 Summary

In this chapter, the n-type polymer P(NDI2OD-T2) is investigated regarding its thermoelectric capabilities. N-DPBI is used as dopant molecule, in order to introduce charges into the system, allowing for the investigation of changes upon addition of the former.

UV-Vis spectroscopy was used to study the changes on an electronic level. Addition of dopant into the polymer solution prior to film fabrication lead to the decrease of the characteristic absorption bands from the polymer, while bands assigned to the presence of polaronic states appear. This makes UV-Vis spectroscopy a viable tool for the confirmation of successful doping. Degradation as function of temperature and exposure time in air is also studied, indicating that temperatures above 80 °C accelerate the degradation process through reaction of the doped films with atmospheric oxygen.

The morphological changes upon doping of P(NDI2OD-T2) were studied using GI-WAXS. In the pristine state, the polymer forms π -stacks in vertical direction, which extend along the polymer backbone and lead to the formation of lamellae. Macroscopically, these lamellar stacks form crystallites which preferably orient in a face-on manner. Upon doping, N-DPBI molecules are increasingly incorporated into the π -stacks, destroying the order within. The addition of dopant also leads to re-orientation the lamellar stacking, from being oriented primarily parallel to the substrate, to being primarily oriented perpendicular to the substrate. As a consequence, the crystallites built up by lamellar stacking change their orientation from face- to edge-on.

Lastly, the findings of the spectroscopic and morphological investigations are linked with the thermoelectric properties of doped P(NDI2OD-T2) films. Different possible geometries for the implementation of P(NDI2OD-T2) in thermoelectric generators are proposed and investigated regarding temperature-dependent resistances, electrical conductivities, Seebeck coefficients and power factors as function of concentration. The in-plane geometry combines high Seebeck coefficients with moderate electrical conductivities, yielding maximum power factors of $2.7 \mu\text{WK}^{-2}\text{m}^{-1}$, which is on the same order of magnitude as for highly conducting PEDOT:PSS films. The cross-plane geometry suffers from very

low electrical conductivities, therefore strongly limiting the power conversion capabilities. In addition, the risk of short-circuiting due to defects in the film is greatly increased due to the overlap between the bottom FTO and top aluminum electrode. Thus, the pseudo-in-plane geometry is offered as alternative, in which there is no overlap between the aforementioned electrodes. This geometry is also advantageous due to moderately high Seebeck coefficients in the range of hundreds of microvolts per Kelvin, while improving the electrical conductivities even beyond those obtained for the in-plane geometry. It is thus deemed most viable for the fabrication of thermoelectric generators, into which EG-treated PEDOT:PSS as p-type component is added.

The thermoelectric generators are studied with respect to their output voltage, overall device resistance and power output, comparing a generator with pristine P(NDI2OD-T2) to one in which P(NDI2OD-T2) is doped with 40 wt% N-DPBI. Doping leads to a threefold improved output voltage, decreased device resistance and thus twelvefold increased power output of the generator. It should be highlighted that all measurements were performed on a single generator with one p-n-pair. In principle, the adopted sample geometry allows for facile connection of several generators together, in order to increase the absolute power output.

9 Conclusion and outlook

The main focus of the present thesis is the investigation of conducting polymers with respect to their potential thermoelectric capabilities and the elucidation of links between the structure and the performance. As the field of organic thermoelectrics is still quite young, this work aims at the understanding of the underlying concepts and if knowledge gained with inorganic thermoelectrics can be extended to these systems. Therefore, each chapter of this thesis focuses on the directed modification of a thermoelectric parameter, in order to link the thermoelectric properties of a polymer thin film to its structure.

Nanostructuring of PEDOT:PSS thin films is successfully achieved through the inclusion of Si-NPs. TOF-GISANS is used for the elucidation of a suitable fabrication protocol, resulting in the layer-by-layer fabrication for the composite films for further investigations. In order to understand the impact of the latters' inclusion on thermoelectric properties, and specifically on the thermal conductivity, IRT is employed. It is revealed that, apart from the other relevant thermoelectric parameters, the thermal conductivity is indeed modified. Due to the single-crystalline nature of the Si-NPs, the thermal conductivity increases for small concentrations and subsequently drops. An explanation for this behavior is found with the aid of GIR-TeXS, which allows for clear distinction of the individual components in the ternary PEDOT:PSS/Si-NPs hybrid composite films, due to their molecular structure. In this specific case, the nanostructuring approach proved to be successful, since GIR-TeXS revealed the selective incorporation of Si-NPs into PEDOT-rich domains, instead of the PSS-rich matrix, with the former being mostly responsible for the measurable thermoelectric properties. The presence of Si-NPs disturbs the internal order of the domains and subsequently leads to less efficient heat transport within the film, similarly to nanostructuring in inorganic thermoelectric materials.

A high intrinsic charge carrier concentration in the PEDOT:PSS PH1000 formulation is responsible for the observation of potentially high electrical conductivities in thin films, but comes at the cost of low Seebeck coefficients. It is seen that through appropriate choice of treatment agents in the form of inorganic salts with either acido-basic or redox properties, the doping level can be modified. This dedoping yields increased Seebeck coefficients and simultaneously decreased electrical conductivities, supporting a loss of charge carriers during the process. Both UV-Vis spectroscopy and XPS additionally

reveal changes in the electronic structure. With Raman spectroscopy it becomes possible to link the loss in electrical conductivity with changes in the conformation of PEDOT through the transition from the quinoid form of PEDOT to the benzoid form. Most importantly, this transition occurs irrespective of the mechanism by which PEDOT:PSS is dedoped. Regarding redox dedoping, the choice of agent is not critical, as only the absolute number of reducing equivalents interacting with PEDOT determine the final thermoelectric properties of the thin film.

PEDOT:PSS is a binary polymer blend, in which positively charged PEDOT chains interact electrostatically with negatively charged PSS chains. Not only does PSS stabilize the positive charges on PEDOT chains, but it also influences the final morphology of thin films prepared from the polymer blend. One possible way to simultaneously enhance both the Seebeck coefficient and electrical conductivity is to employ ILs, which complement the binary nature of PEDOT:PSS. Through post-treatment of PEDOT:PSS thin films not only the degree of doping is changed, but also the structure of the thin film. The rational choice of ILs in this study serves a dual purpose. Variation of the anion, while keeping the same cation allows for a closer study of the impact of the anions' properties on the final thermoelectric properties. EMIM DCA yielded the highest Seebeck coefficients, followed by EMIM BF₄ and EMIM TCB. These observations are mostly assigned to the ability of the negative charge on the anions to interact with the positively charged PEDOT. Additionally, the interaction between the positively charged EMIM cations and the negatively charged PSS anions is also altered through variation of the ILs' anions, resulting in different structures through secondary doping and improved electrical conductivities. Thus, post-treatment of PEDOT:PSS with ILs enables the simultaneous enhancement of both Seebeck coefficient and electrical conductivity through a combination of primary and secondary doping. The large library of anion-cation combinations in ILs additionally opens a large window for the tunability of thermoelectric properties in PEDOT:PSS.

Lastly, in order to complement PEDOT:PSS as a p-type organic thermoelectric material, P(NDI2OD-T2) is investigated regarding its suitability upon doping with N-DPBI. Successful transfer of negative charge carriers onto the polymer is confirmed through UV-Vis spectroscopy through the emergence of polaronic bands. This also sheds light on an inherent challenge regarding doped n-type polymers, which is their susceptibility towards degradation in ambient atmosphere. The impact of doping on the structure is also evident from GIWAXS measurements indicating re-orientation and a loss of order within in the polymer with increasing amount of dopant. Finally, different geometries of thermoelectric thin films from doped P(NDI2OD-T2) are investigated regarding their suitability in a thermoelectric generator, with the in-plane and pseudo-in-plane showing the most promise. A link between the observations from the spectroscopic and structural investi-

gations to the thermoelectric properties is found in the trends for the Seebeck coefficient and electrical conductivity as function of dopant concentration. Doped P(NDI2OD-T2) is then used in conjunction with PEDOT:PSS in order to build a thermoelectric generator based on conducting polymers as active materials, proving the feasibility of the employed approach.

For future research, it will be interesting to have a closer look at other material systems and their potential thermoelectric capabilities. While PEDOT:PSS is a very good reference system, it has some intrinsic disadvantages like its two-component nature, which proves detrimental in some aspects. P(NDI2OD-T2) on the other hand suffers from comparatively low electrical conductivity, motivating the search for a material system which combines the advantages of the investigated polymers. Also the aspect of implementation into devices and large-scale applications is worth pursuing further, as the potential in energy recovery is significant.

Bibliography

- [1] L. D. Hicks and M. S. Dresselhaus, “Thermoelectric Figure of Merit of a One-Dimensional Conductor,” *Physical Review B*, vol. 47, no. 24, 1993.
- [2] N. Saxena, M. Čorić, A. Greppmair, J. Wernecke, M. Pflüger, M. Krumrey, M. S. Brandt, E. M. Herzig, and P. Müller-Buschbaum, “Morphology-Function Relationship of Thermoelectric Nanocomposite Films from PEDOT:PSS with Silicon Nanoparticles,” *Advanced Electronic Materials*, vol. 3, no. 8, p. 1700181, 2017.
- [3] N. Saxena, J. Keilhofer, A. K. Maurya, G. Fortunato, J. Overbeck, and P. Müller-Buschbaum, “Facile Optimization of Thermoelectric Properties in PEDOT:PSS Thin Films through Acido-Base and Redox Dedoping Using Readily Available Salts,” *ACS Applied Energy Materials*, vol. 1, no. 2, pp. 336–342, 2018.
- [4] N. Saxena, B. Pretzl, X. Lamprecht, L. Bießmann, D. Yang, N. Li, C. Bilko, S. Bernstorff, and P. Müller-Buschbaum, “Ionic liquids as Post-Treatment Agents for Simultaneous Improvement of Seebeck Coefficient and Electrical Conductivity in PEDOT:PSS Films,” *ACS Applied Materials & Interfaces*, vol. 11, pp. 8060–8071, 2019.
- [5] L. Onsager, “Reciprocal Relations in Irreversible Processes. I,” *Physical Review*, vol. 37, no. 4, pp. 405–426, 1931.
- [6] H. J. Goldsmid, *Introduction to Thermoelectricity*, vol. 121. Springer, 2 ed., 2011.
- [7] G. J. Snyder and E. S. Toberer, “Complex Thermoelectric Materials,” *Nature Materials*, vol. 7, no. 2, pp. 105–114, 2008.
- [8] R. Kroon, D. A. Mengistie, D. Kiefer, J. Hynynen, J. D. Ryan, L. Yu, and C. Müller, “Thermoelectric Plastics: From Design to Synthesis, Processing and Structure-Property Relationships,” *Chemical Society Reviews*, vol. 45, no. 22, pp. 6147–6164, 2016.
- [9] W. P. Su, J. R. Schrieffer, and A. J. Heeger, “Solitons in Polyacetylene,” *Physical Review Letters*, vol. 42, no. 25, 1979.
- [10] W. P. Su, J. R. Schrieffer, and A. J. Heeger, “Soliton Excitations in Polyacetylene,” *Physical Review B*, vol. 22, no. 4, 1980.
- [11] J. T. Devreese, “Polarons,” vol. 14 of *Encyclopedia of Applied Physics*, pp. 383–409, Wiley-VCH Publishers, Inc., 1996.

- [12] A. Elschner, S. Kirchmeyer, W. Lövenich, U. Merker, and K. Reuter, *PEDOT: Principles and Applications of an Intrinsically Conductive Polymer*. Boca Raton: CRC Press, Taylor & Francis Group, 2011.
- [13] H. Park, S. H. Lee, F. S. Kim, H. H. Choi, I. W. Cheong, and J. H. Kim, “Enhanced thermoelectric properties of PEDOT: PSS nanofilms by a chemical dedoping process,” *Journal of Materials Chemistry A*, vol. 2, no. 18, pp. 6532–6539, 2014.
- [14] T. Takano, H. Masunaga, A. Fujiwara, H. Okuzaki, and T. Sasaki, “PEDOT Nanocrystal in Highly Conductive PEDOT: PSS Polymer Films,” *Macromolecules*, vol. 45, no. 9, pp. 3859–3865, 2012.
- [15] A. M. Nardes, M. Kemerink, M. M. de Kok, E. Vinken, K. Maturova, and R. Janssen, “Conductivity, Work Function, and Environmental Stability of PEDOT:PSS Thin Films Treated with Sorbitol,” *Organic Electronics*, vol. 9, no. 5, pp. 727–734, 2008.
- [16] Y. Yoneda, “Anomalous Surface Reflection of X Rays,” *Physical Review*, vol. 131, no. 5, 1963.
- [17] B. L. Henke, E. M. Gullikson, and J. C. Davis, “X-ray interactions: photoabsorption, scattering, transmission and reflection at $E = 50\text{--}30000$ eV, $Z = 1\text{--}92$,” *Atomic Data and Nuclear Data Tables*, no. 54, 1993.
- [18] G. Renaud, R. Lazzari, and F. Leroy, “Probing Surface and Interface Morphology with Grazing Incidence Small Angle X-Ray Scattering,” *Surface Science Reports*, vol. 64, no. 8, pp. 255–380, 2009.
- [19] A. Hexemer and P. Müller-Buschbaum, “Advanced Grazing-Incidence Techniques for Modern Soft-Matter Materials Analysis,” *International Union of Crystallography Journal*, vol. 2, no. Pt 1, pp. 106–125, 2015.
- [20] P. Müller-Buschbaum, “Grazing incidence small-angle X-ray scattering: an advanced scattering technique for the investigation of nanostructured polymer films,” *Analytical and Bioanalytical Chemistry*, vol. 376, no. 1, pp. 3–10, 2003.
- [21] R. Lazzari, “IsGISAXS: A Program for Grazing-Incidence Small-Angle X-ray Scattering Analysis of Supported Islands,” *Journal of Applied Crystallography*, vol. 35, 2002.
- [22] R. L. Kronig, “On the Theory of Dispersion of X-Rays,” *Journal of the Optical Society America*, vol. 12, no. 6, pp. 547–558, 1926.
- [23] J. L. Baker, L. H. Jimison, S. Mannsfeld, S. Volkman, S. Yin, V. Subramanian, A. Salleo, A. P. Alivisatos, and M. F. Toney, “Quantification of Thin Film Crystallographic Orientation Using X-Ray Diffraction with an Area Detector,” *Langmuir*, vol. 26, no. 11, pp. 9146–9151, 2010.

- [24] X. Lamprecht, *Influence of Ionic Liquids on Thermoelectric Properties of Polymer Thin Films and Design of a New Seebeck Coefficient Measurement Setup*. Bachelor's thesis, Technical University Munich, 2016.
- [25] R. Kluge, *Investigation of an n-Type Polymer for Thermoelectric Applications*. Master's thesis, Technical University Munich, 2017.
- [26] A. Greppmair, B. Stoib, N. Saxena, C. Gerstberger, P. Müller-Buschbaum, M. Stutzmann, and M. S. Brandt, "Measurement of the In-Plane Thermal Conductivity by Steady-State Infrared Thermography," *Review of Scientific Instruments*, vol. 88, no. 4, p. 044903, 2017.
- [27] M. Krumrey and G. Ulm, "High-Accuracy Detector Calibration at the PTB Four-Crystal Monochromator Beamline," *Nuclear Instruments and Methods in Physics Research Section A: Accelerators, Spectrometers, Detectors and Associated Equipment*, vol. 467-468, pp. 1175–1178, 2001.
- [28] C. A. Schneider, W. S. Rasband, and K. W. Eliceiri, "NIH Image to ImageJ: 25 Years of Image Analysis," *Nature Methods*, vol. 9, no. 7, pp. 671–675, 2012.
- [29] Z. Jiang, "GIXSGUI: A MATLAB Toolbox for Grazing-Incidence X-Ray Scattering Data Visualization and Reduction, and Indexing of Buried Three-Dimensional Periodic Nanostructured Films," *Journal of Applied Crystallography*, vol. 48, no. 3, pp. 917–926, 2015.
- [30] J. Fink, E. Schierle, E. Weschke, and J. Geck, "Resonant Elastic Soft X-Ray Scattering," *Reports on Progress in Physics*, vol. 76, no. 5, p. 056502, 2013.
- [31] J. Wernecke, C. Gollwitzer, P. Müller, and M. Krumrey, "Characterization of an In-Vacuum PILATUS 1M Detector," *Journal of Synchrotron Radiation*, vol. 21, no. Pt 3, pp. 529–536, 2014.
- [32] R. Kampmann, M. Haese-Seiller, V. Kudryashov, V. Deriglazov, M. Trisl, C. Daniel, B. Toperverg, A. Schreyer, and E. Sackmann, "The Potential of the Horizontal Reflectometer REFSANS/FRM-II for Measuring Low Reflectivity and Diffuse Surface Scattering," *Physica B: Condensed Matter*, vol. 350, no. 1-3, pp. E763–E766, 2004.
- [33] P. Müller-Buschbaum, "Grazing Incidence Small-Angle Neutron Scattering: Challenges and possibilities," *Polymer Journal*, vol. 45, no. 1, pp. 34–42, 2013.
- [34] G. Schierning, J. Stoetzel, R. Chavez, V. Kessler, J. Hall, R. Schmechel, T. Schneider, N. Petermann, H. Wiggers, S. Angst, D. E. Wolf, B. Stoib, A. Greppmair, M. Stutzmann, and M. S. Brandt, "Silicon-Based Nanocomposites for Thermoelectric Application," *physica status solidi (a)*, vol. 213, no. 3, pp. 497–514, 2016.

- [35] P. Müller-Buschbaum, “Influence of Surface Cleaning on Dewetting of Thin Polystyrene Films,” *The European Physical Journal. E, Soft Matter*, vol. 12, no. 3, pp. 443–448, 2003.
- [36] F. Greco, A. Zucca, S. Taccola, A. Menciassi, T. Fujie, H. Haniuda, S. Takeoka, P. Dario, and V. Mattoli, “Ultra-Thin Conductive Free-Standing PEDOT:PSS Nanofilms,” *Soft Matter*, vol. 7, no. 22, p. 10642, 2011.
- [37] G. J. Snyder and E. S. Toberer, “Complex Thermoelectric Materials,” *Nature Materials*, vol. 7, no. 2, pp. 105–114, 2008.
- [38] C. B. Vining, “The Thermoelectric Limit $ZT \sim 1$: Fact or Artifact,” *Proceedings of the 10th International Conference on Thermoelectrics*, vol. 10, 1992.
- [39] S. K. Yee, N. E. Coates, A. Majumdar, J. J. Urban, and R. A. Segalman, “Thermoelectric Power Factor Optimization in PEDOT:PSS Tellurium Nanowire Hybrid Composites,” *Physical Chemistry Chemical Physics : PCCP*, vol. 15, no. 11, pp. 4024–4032, 2013.
- [40] E. J. Bae, Y. H. Kang, K.-S. Jang, and S. Y. Cho, “Enhancement of Thermoelectric Properties of PEDOT:PSS and Tellurium-PEDOT:PSS Hybrid Composites by Simple Chemical Treatment,” *Scientific Reports*, vol. 6, p. 18805, 2016.
- [41] C. M. Palumbiny, J. Schlipf, A. Hexemer, C. Wang, and P. Müller-Buschbaum, “The Morphological Power of Soap: How Surfactants Lower the Sheet Resistance of PEDOT:PSS by Strong Impact on Inner Film Structure and Molecular Interface Orientation,” *Advanced Electronic Materials*, vol. 2, no. 4, p. 1500377, 2016.
- [42] S. Niesar, R. N. Pereira, A. R. Stegner, N. Erhard, M. Hoeb, A. Baumer, H. Wiggers, M. S. Brandt, and M. Stutzmann, “Low-Cost Post-Growth Treatments of Crystalline Silicon Nanoparticles Improving Surface and Electronic Properties,” *Advanced Functional Materials*, vol. 22, no. 6, pp. 1190–1198, 2012.
- [43] L. Bießmann, L. P. Kreuzer, T. Widmann, N. Hohn, J.-F. Moulin, and P. Müller-Buschbaum, “Monitoring the Swelling Behavior of PEDOT:PSS Electrodes under High Humidity Conditions,” *ACS Applied Materials & Interfaces*, vol. 10, no. 11, pp. 9865–9872, 2018.
- [44] J. Chen, T. Sun, D. Sim, H. Peng, H. Wang, S. Fan, H. H. Hng, J. Ma, F. Y. C. Boey, S. Li, M. K. Samani, G. C. K. Chen, X. Chen, T. Wu, and Q. Yan, “Sb₂Te₃ Nanoparticles with Enhanced Seebeck Coefficient and Low Thermal Conductivity,” *Chemistry of Materials*, vol. 22, no. 10, pp. 3086–3092, 2010.
- [45] J. Liu, X. Wang, D. Li, N. E. Coates, R. A. Segalman, and D. G. Cahill, “Thermal Conductivity and Elastic Constants of PEDOT: PSS with High Electrical Conductivity,” *Macromolecules*, vol. 48, no. 3, pp. 585–591, 2015.

- [46] D. G. Cahill, "Thermal Conductivity Measurement from 30 to 750 K: The 3w Method," *Review of Scientific Instruments*, vol. 61, no. 2, pp. 802–808, 1990.
- [47] G. Kaune, M. A. Ruderer, E. Metwalli, W. Wang, S. Couet, K. Schlage, R. Röhlsberger, S. V. Roth, and P. Müller-Buschbaum, "In Situ GISAXS Study of Gold Film Growth on Conducting Polymer Films," *ACS Applied Materials & Interfaces*, vol. 1, no. 2, pp. 353–360, 2009.
- [48] Q. Wei, C. Uehara, M. Mukaida, K. Kirihara, and T. Ishida, "Measurement of In-Plane Thermal Conductivity in Polymer Films," *AIP Advances*, vol. 6, no. 4, p. 045315, 2016.
- [49] M. A. Vairavamurthy, D. Maletic, S. Wang, B. Manowitz, T. Eglinton, and T. Lyons, "Characterization of Sulfur-Containing Functional Groups in Sedimentary Humic Substances by X-ray Absorption Near-Edge Structure Spectroscopy," *Energy & Fuels*, vol. 11, no. 3, pp. 546–553, 1997.
- [50] J. Keilhofer, *Enhancement of thermoelectric properties of PEDOT:PSS by redox doping and acid-base doping*. Bachelor's thesis, Technical University Munich, 2017.
- [51] A. K. Maurya, *Optimization of the thermoelectric properties of conducting polymer thin films by dedoping and hybrid approaches*. PhD thesis, Technical University Munich, 2016.
- [52] M. N. Gueye, A. Carella, N. Massonnet, E. Yvenou, S. Brenet, J. Faure-Vincent, S. Pouget, F. Rieutord, H. Okuno, A. Benayad, R. Demadrille, and J.-P. Simonato, "Structure and Dopant Engineering in PEDOT Thin Films: Practical Tools for a Dramatic Conductivity Enhancement," *Chemistry of Materials*, vol. 28, no. 10, pp. 3462–3468, 2016.
- [53] H. Shi, C. Liu, Q. Jiang, and J. Xu, "Effective Approaches to Improve the Electrical Conductivity of PEDOT: PSS: A Review," *Advanced Electronic Materials*, vol. 1, no. 4, p. 1500017, 2015.
- [54] O. Bubnova, Z. U. Khan, H. Wang, S. Braun, D. R. Evans, M. Fabretto, P. Hojati-Talemi, D. Dagnelund, J.-B. Arlin, Y. H. Geerts, S. Desbief, D. W. Breiby, J. W. Andreasen, R. Lazzaroni, W. M. Chen, I. Zozoulenko, M. Fahlman, P. J. Murphy, M. Berggren, and X. Crispin, "Semi-Metallic Polymers," *Nature Materials*, vol. 13, no. 2, pp. 190–194, 2014.
- [55] Z. Fan, P. Li, D. Du, and J. Ouyang, "Significantly Enhanced Thermoelectric Properties of PEDOT: PSS Films through Sequential Post-Treatments with Common Acids and Bases," *Advanced Energy Materials*, vol. 7, no. 8, p. 1602116, 2017.
- [56] N. Massonnet, A. Carella, O. Jaudouin, P. Rannou, G. Laval, C. Celle, and J.-P. Simonato, "Improvement of the Seebeck Coefficient of PEDOT:PSS by Chemical

- Reduction Combined with a Novel Method for its Transfer Using Free-Standing Thin Films,” *Journal of Materials Chemistry C*, vol. 2, no. 7, pp. 1278–1283, 2014.
- [57] M. Stavytska-Barba and A. M. Kelley, “Surface-Enhanced Raman Study of the Interaction of PEDOT: PSS with Plasmonically Active Nanoparticles,” *The Journal of Physical Chemistry C*, vol. 114, no. 14, pp. 6822–6830, 2010.
- [58] Q. Wei, M. Mukaida, Y. Naitoh, and T. Ishida, “Morphological Change and Mobility Enhancement in PEDOT:PSS by Adding Co-Solvents,” *Advanced Materials (Deerfield Beach, Fla.)*, vol. 25, no. 20, pp. 2831–2836, 2013.
- [59] C. Yi, A. Wilhite, L. Zhang, R. Hu, S. S. C. Chuang, J. Zheng, and X. Gong, “Enhanced Thermoelectric Properties of Poly(3,4-ethylenedioxythiophene):poly(styrenesulfonate) by Binary Secondary Dopants,” *ACS Applied Materials & Interfaces*, vol. 7, no. 17, pp. 8984–8989, 2015.
- [60] Z. Zhu, C. Liu, Q. Jiang, H. Shi, F. Jiang, J. Xu, J. Xiong, and E. Liu, “Optimizing the Thermoelectric Properties of PEDOT:PSS Films by Combining Organic Co-Solvents with Inorganic Base,” *Journal of Materials Science: Materials in Electronics*, vol. 26, no. 11, pp. 8515–8521, 2015.
- [61] Z. Fan, D. Du, Z. Yu, P. Li, Y. Xia, and J. Ouyang, “Significant Enhancement in the Thermoelectric Properties of PEDOT:PSS Films through a Treatment with Organic Solutions of Inorganic Salts,” *ACS Applied Materials & Interfaces*, vol. 8, no. 35, pp. 23204–23211, 2016.
- [62] C. Yeon, S. J. Yun, J. Kim, and J. W. Lim, “PEDOT: PSS Films with Greatly Enhanced Conductivity via Nitric Acid Treatment at Room Temperature and Their Application as Pt/TCO-Free Counter Electrodes in Dye-Sensitized Solar Cells,” *Advanced Electronic Materials*, vol. 1, no. 10, p. 1500121, 2015.
- [63] Z. U. Khan, O. Bubnova, M. J. Jafari, R. Brooke, X. Liu, R. Gabrielsson, T. Ederth, D. R. Evans, J. W. Andreasen, M. Fahlman, and X. Crispin, “Acido-Basic Control of the Thermoelectric Properties of Poly(3,4-ethylenedioxythiophene)tosylate (PEDOT-Tos) Thin Films,” *Journal of materials chemistry. C, Materials for optical and electronic devices*, vol. 3, no. 40, pp. 10616–10623, 2015.
- [64] S. R. S. Kumar, N. Kurra, and H. N. Alshareef, “Enhanced High Temperature Thermoelectric Response of Sulphuric Acid Treated Conducting Polymer Thin Films,” *Journal of Materials Chemistry C*, vol. 4, no. 1, pp. 215–221, 2016.
- [65] J. Ouyang, “Solution-Processed PEDOT:PSS Films with Conductivities as Indium Tin Oxide through a Treatment with Mild and Weak Organic Acids,” *ACS Applied Materials & Interfaces*, vol. 5, no. 24, pp. 13082–13088, 2013.

- [66] C. M. Palumbiny, C. Heller, C. J. Schaffer, V. Körstgens, G. Santoro, S. V. Roth, and P. Müller-Buschbaum, "Molecular Reorientation and Structural Changes in Cosolvent-Treated Highly Conductive PEDOT: PSS Electrodes for Flexible Indium Tin Oxide-Free Organic Electronics," *The Journal of Physical Chemistry C*, vol. 118, no. 25, pp. 13598–13606, 2014.
- [67] K. van de Ruit, I. Katsouras, D. Bollen, T. van Mol, R. A. J. Janssen, D. M. de Leeuw, and M. Kemerink, "The Curious Out-of-Plane Conductivity of PEDOT: PSS," *Advanced Functional Materials*, vol. 23, no. 46, pp. 5787–5793, 2013.
- [68] O. Bubnova, Z. U. Khan, A. Malti, S. Braun, M. Fahlman, M. Berggren, and X. Crispin, "Optimization of the thermoelectric figure of merit in the conducting polymer poly(3,4-ethylenedioxythiophene)," *Nature Materials*, vol. 10, no. 6, pp. 429–433, 2011.
- [69] C. Badre, L. Marquant, A. M. Alsayed, and L. A. Hough, "Highly Conductive Poly(3,4-ethylenedioxythiophene): Poly (styrenesulfonate) Films Using 1-Ethyl-3-methylimidazolium Tetracyanoborate Ionic Liquid," *Advanced Functional Materials*, vol. 22, no. 13, pp. 2723–2727, 2012.
- [70] R. J. Murphy, K. M. Weigandt, D. Uhrig, A. Alsayed, C. Badre, L. Hough, and M. Muthukumar, "Scattering Studies on Poly(3,4-ethylenedioxythiophene)–Polystyrenesulfonate in the Presence of Ionic Liquids," *Macromolecules*, vol. 48, no. 24, pp. 8989–8997, 2015.
- [71] A. d. Izarra, S. Park, J. Lee, Y. Lansac, and Y. H. Jang, "Ionic Liquid Designed for PEDOT:PSS Conductivity Enhancement," *Journal of the American Chemical Society*, vol. 140, no. 16, pp. 5375–5384, 2018.
- [72] S. Kee, N. Kim, B. S. Kim, S. Park, Y. H. Jang, S. H. Lee, J. Kim, J. Kim, S. Kwon, and K. Lee, "Controlling Molecular Ordering in Aqueous Conducting Polymers Using Ionic Liquids," *Advanced Materials (Deerfield Beach, Fla.)*, vol. 28, no. 39, pp. 8625–8631, 2016.
- [73] Z. Fan, D. Du, X. Guan, and J. Ouyang, "Polymer films with ultrahigh thermoelectric properties arising from significant seebeck coefficient enhancement by ion accumulation on surface," *Nano Energy*, vol. 51, pp. 481–488, 2018.
- [74] H. Wang, D. Zhao, Z. U. Khan, S. Puzinas, M. P. Jonsson, M. Berggren, and X. Crispin, "Ionic Thermoelectric Figure of Merit for Charging of Supercapacitors," *Advanced Electronic Materials*, vol. 3, no. 4, p. 1700013, 2017.
- [75] S. Spange, R. Lungwitz, and A. Schade, "Correlation of molecular structure and polarity of ionic liquids," *Journal of Molecular Liquids*, vol. 192, pp. 137–143, 2014.

- [76] A. M. Nardes, M. Kemerink, R. A. J. Janssen, J. A. M. Bastiaansen, N. M. M. Kiggen, B. M. W. Langeveld, van Breemen, A. J. J. M., and M. M. de Kok, "Microscopic Understanding of the Anisotropic Conductivity of PEDOT: PSS Thin Films," *Advanced Materials (Deerfield Beach, Fla.)*, vol. 19, no. 9, pp. 1196–1200, 2007.
- [77] P. Wei, J. H. Oh, G. Dong, and Z. Bao, "Use of a 1H-Benzoimidazole Derivative as an n-Type Dopant and to Enable Air-Stable Solution-Processed n-Channel Organic Thin-Film Transistors," *Journal of the American Chemical Society*, vol. 132, no. 26, pp. 8852–8853, 2010.
- [78] R. Steyrleuthner, M. Schubert, I. Howard, B. Klaumünzer, K. Schilling, Z. Chen, P. Saalfrank, F. Laquai, A. Facchetti, and D. Neher, "Aggregation in a High-Mobility n-Type Low-Bandgap Copolymer with Implications on Semicrystalline Morphology," *Journal of the American Chemical Society*, vol. 134, no. 44, pp. 18303–18317, 2012.
- [79] M. Caironi, M. Bird, D. Fazzi, Z. Chen, R. Di Pietro, C. Newman, A. Facchetti, and H. Sirringhaus, "Very Low Degree of Energetic Disorder as the Origin of High Mobility in an n-channel Polymer Semiconductor," *Advanced Functional Materials*, vol. 21, no. 17, pp. 3371–3381, 2011.
- [80] J. Rivnay, R. Steyrleuthner, L. H. Jimison, A. Casadei, Z. Chen, M. F. Toney, A. Facchetti, D. Neher, and A. Salleo, "Drastic Control of Texture in a High Performance n-Type Polymeric Semiconductor and Implications for Charge Transport," *Macromolecules*, vol. 44, no. 13, pp. 5246–5255, 2011.
- [81] E. Giussani, D. Fazzi, L. Brambilla, M. Caironi, and C. Castiglioni, "Molecular Level Investigation of the Film Structure of a High Electron Mobility Copolymer via Vibrational Spectroscopy," *Macromolecules*, vol. 46, no. 7, pp. 2658–2670, 2013.
- [82] E. Giussani, L. Brambilla, D. Fazzi, M. Sommer, N. Kayunkid, M. Brinkmann, and C. Castiglioni, "Structural Characterization of Highly Oriented Naphthalene-Diimide-Bithiophene Copolymer Films via Vibrational Spectroscopy," *Journal of Physical Chemistry B*, vol. 119, no. 5, pp. 2062–2073, 2015.
- [83] A. M. Anton, R. Steyrleuthner, W. Kossack, D. Neher, and F. Kremer, "Infrared Transition Moment Orientational Analysis on the Structural Organization of the Distinct Molecular Subunits in Thin Layers of a High Mobility n-Type Copolymer," *Journal of the American Chemical Society*, vol. 137, no. 18, pp. 6034–6043, 2015.
- [84] T. Schuettfort, S. Huettnner, S. Lilliu, J. E. Macdonald, L. Thomsen, and C. R. McNeill, "Surface and Bulk Structural Characterization of a High-Mobility Electron-Transporting Polymer," *Macromolecules*, vol. 44, no. 6, pp. 1530–1539, 2011.
- [85] T. Schuettfort, L. Thomsen, and C. R. McNeill, "Observation of a Distinct Surface

- Molecular Orientation in Films of a High Mobility Conjugated Polymer,” *Journal of the American Chemical Society*, vol. 135, no. 3, pp. 1092–1101, 2013.
- [86] A. M. Anton, R. Steyrlleuthner, W. Kossack, D. Neher, and F. Kremer, “Spatial Orientation and Order of Structure-Defining Subunits in Thin Films of a High Mobility n-Type Copolymer,” *Macromolecules*, vol. 49, no. 5, pp. 1798–1806, 2016.
- [87] R. Steyrlleuthner, R. Di Pietro, B. A. Collins, F. Polzer, S. Himmelberger, M. Schubert, Z. Chen, S. Zhang, A. Salleo, H. Ade, A. Facchetti, and D. Neher, “The Role of Regioregularity, Crystallinity, and Chain Orientation on Electron Transport in a High-Mobility n-Type Copolymer,” *Journal of the American Chemical Society*, vol. 136, no. 11, pp. 4245–4256, 2014.
- [88] M. Brinkmann, E. Gonthier, S. Bogen, K. Tremel, S. Ludwigs, M. Hufnagel, and M. Sommer, “Segregated versus mixed interchain stacking in highly oriented films of naphthalene diimide bithiophene copolymers,” *ACS Nano*, vol. 6, no. 11, pp. 10319–10326, 2012.
- [89] A. M. Anton, R. Steyrlleuthner, W. Kossack, D. Neher, and F. Kremer, “Spatial Orientation and Order of Structure-Defining Subunits in Thin Films of a High Mobility n-Type Copolymer,” *Macromolecules*, vol. 49, no. 5, pp. 1798–1806, 2016.
- [90] R. A. Schlitz, F. G. Brunetti, A. M. Glaudell, P. L. Miller, M. A. Brady, C. J. Takacs, C. J. Hawker, and M. L. Chabinyc, “Solubility-Limited Extrinsic n-Type Doping of a High Electron Mobility Polymer for Thermoelectric Applications,” *Advanced Materials (Deerfield Beach, Fla.)*, vol. 26, no. 18, pp. 2825–2830, 2014.

List of publications

Publications related to the dissertation

- N. Saxena, M. Coric, A. Greppmair, M. Pflüger, M. Krumrey, M. S. Brandt, E. M. Herzig, P. Müller-Buschbaum, "Morphology-Function Relationship of Thermoelectric Nanocomposite Films from PEDOT:PSS with Silicon Nanoparticles", *Adv. Electron. Mater.*, vol. 3, pp. 1700181 – 1700195, 2017.
- N. Saxena, J. Keilhofer, A. K. Maurya, G. Fortunato, J. Overbeck, P. Müller-Buschbaum, "Facile Optimization of Thermoelectric Properties in PEDOT:PSS Thin Films through Acido-Base and Redox Dedoping Using Readily Available Salts", *ACS Appl. Energy Mater.*, vol. 1, pp. 336-342, 2018.
- N. Saxena, B. Pretzl, X. Lamprecht, L. Bießmann, D. Yang, N. Li, C. Bilko, S. Bernstorff, P. Müller-Buschbaum, "Ionic Liquids as Post-Treatment Agents for Simultaneous Improvement of Seebeck Coefficient and Electrical Conductivity in PEDOT:PSS Films", *ACS Appl. Mater. Interfaces*, just accepted.
- A. Greppmair, B. Stoib, N. Saxena, C. Gerstberger, P. Müller-Buschbaum, M. Stutzmann, M.S. Brandt, "Measurement of the In-Plane Thermal Conductivity by Steady-State Infrared Thermography", *Rev. Sci. Instr.*, vol. 88, pp. 044903, 2017.

Further publications

- M. Coric, N. Saxena, M. Pflüger, P. Müller-Buschbaum, M. Krumrey, E. M. Herzig, "Resonant Grazing-Incidence Small-Angle X-Ray Scattering at the Sulfur K-Edge for Material-Specific Investigation of Thin Film Nanostructures", *J. Phys. Chem. Lett.*, vol. 9, pp. 3081-3086, 2018.
- B. Su, H. A. Caller-Guzman, V. Körstgens, Y. Rui, Y. Yao, N. Saxena, G. Santoro, S.V. Roth, P. Müller-Buschbaum, "Macro-Scale and Nano-Scale Morphology Evolution during In-Situ Spray Coating of Titania Films for Perovskite Solar Cells", *ACS Appl. Mater. Interfaces*, vol. 9, pp. 43724-43732, 2017.

- L. Song, T. Wang, V. Körstgens, W. Wang, N. Saxena, C. J. Schaffer, T. Fröschl, N. Hüsing, S. Bernstorff, P. Müller-Buschbaum, "Wet-Imprinting of Channel-Type Superstructures in Nanostructured Titania Thin Films at Low Temperatures for Hybrid Solar Cells", *ChemSusChem*, vol. 11, pp. 1179-1186, 2018.
- L. Bießmann, N. Saxena, N. Hohn, M. A. Hossain, J. G. C. Veinot, P. Müller-Buschbaum, "Highly Conducting, Transparent PEDOT:PSS Polymer Electrodes from Post-Treatment with Weak and Strong Acids", *Adv. Electron. Mater.*, vol. 5, pp. 1800654 – 180664, 2019.
- N. Hohn, A. E. Hetzenecker, M. A. Giebel, S. Geier, L. Bießmann, V. Körstgens, N. Saxena, J. Schlipf, W. Ohm, P. S. Deimel, F. Allegretti, J. V. Barth, S. V. Roth, T. F. Fässler, P. Müller-Buschbaum, "Amphiphilic Diblock Copolymer-Mediated Structure Control in Nanoporous Germanium-Based Thin Films", *Nanoscale*, vol. 11, pp. 2048-2055, 2019.

Scientific reports

- N. Saxena, A. Greppmair, M. Coric, J. Wernecke, S. Marggraf, E. M. Herzig, M. S. Brandt, P. Müller-Buschbaum, "Hybrid Thermoelectrics Based on a Polymer-Nanoparticle Composite", *Lehrstuhl für Funktionelle Materialien, Annual Report*, 2014.
- N. Saxena, A. Greppmair, M. S. Brandt, P. Müller-Buschbaum, "Full Thermoelectric Characterization of Highly Conducting PEDOT:PSS Thin Films", *Lehrstuhl für Funktionelle Materialien, Annual Report*, 2015.
- A. K. Maurya, N. Saxena, P. Müller-Buschbaum, "Optimization of Thermoelectric Properties of PEDOT:PSS Thin Films through a Dedoping Approach", *Lehrstuhl für Funktionelle Materialien, Annual Report*, 2016.
- N. Saxena, M. Coric, A. Greppmair, J. Wernecke, M. Pflüger, M. Krumrey, M. S. Brandt, E. M. Herzig, P. Müller-Buschbaum, "Morphology-Function Relationship in Thermoelectric Nanocomposites from PEDOT:PSS with Inorganic Silicon Nanoparticles", *Lehrstuhl für Funktionelle Materialien, Annual Report*, 2017.
- P. Müller-Buschbaum, "Full Thermoelectric Characterization of Highly Conducting PEDOT:PSS Thin Films", *CeNS Annual Report*, 2016.
- N. Saxena, J. Schlipf, L. Bießmann, D. Moseguí Gonzalez, S. Bernstorff, P. Müller-Buschbaum, "In-Operando GISAXS and GIWAXS on Novel Thermoelectric Composite Films", *Elettra Annual Report*, 2015.

Conference talks

- N. Saxena, A. Greppmair, F. Baumer, T. Nilges, M. S. Brandt, P. Müller-Buschbaum, "Hybrid thermoelectrics based on conducting polymers", *MSE Colloquium, Garching, Germany*, 2015.
- N. Saxena, M. Coric, A. Greppmair, J. Wernecke, S. Langner, M. Krumrey, M. S. Brandt, E. M. Herzig, P. Müller-Buschbaum, "Thermoelectric thin films based on a polymer/nanoparticle nanocomposite", *DPG Frühjahrstagung, Regensburg*, 2016.
- N. Saxena, M. Coric, A. Greppmair, J. Wernecke, M. Plüger, M. Krumrey, M. S. Brandt, E. M. Herzig, P. Müller-Buschbaum, "Thermoelectric thin films based on a polymer/nanoparticle nanocomposite", *DPG-Frühjahrstagung, Dresden*, 2017.
- N. Saxena, M. Coric, A. Greppmair, J. Wernecke, M. Plüger, M. Krumrey, M. S. Brandt, E. M. Herzig, P. Müller-Buschbaum, "Thermoelectric thin films based on a polymer/nanoparticle nanocomposite", *3rd Internal Biennial Science Meeting of the MLZ, Grainau*, 2017.
- N. Saxena, M. Coric, A. Greppmair, J. Wernecke, M. Plüger, M. Krumrey, M. S. Brandt, E. M. Herzig, P. Müller-Buschbaum, "Thermoelectric thin films based on a polymer/nanoparticle nanocomposite", *European Polymer Federation Congress, Lyon*, 2017.
- N. Saxena, M. Coric, A. Greppmair, J. Wernecke, M. Plüger, M. Krumrey, M. S. Brandt, E. M. Herzig, P. Müller-Buschbaum, "Thermoelectric thin films based on a polymer/nanoparticle nanocomposite", *textitZhejiang Sci-Tech University, Hangzhou, China*, 2017,
- N. Saxena, B. Pretzl, X. Lamprecht, D. Yang, N. Li, C. Bilko, S. Bernstorff, P. Müller-Buschbaum, "Ionic Liquid Post-Treatment of PEDOT:PSS Thin Films for Improvement of Thermoelectric Properties", *DPG-Frühjahrstagung, Berlin*, 2018.

Conference poster presentations

- N. Saxena, A. Greppmair, M. S. Brandt, P. Müller-Buschbaum, "Novel nanostructured thermoelectric hybrid materials", *MSE Colloquium 2014, Garching*, 2014.
- N. Saxena, A. Greppmair, M. Coric, J. Wernecke, S. Marggraf, E. M. Herzig, M. S. Brandt, P. Müller-Buschbaum, "Novel thermoelectric films based on a polymer-nanoparticle composite", *CeNS Workshop "Walk and talk on the nanoscale"*, 2014.
- N. Saxena, A. Greppmair, M. S. Brandt, P. Müller-Buschbaum, "Thermoelektrika: Strom aus Wärme", *NIM Nanoday, Munich*, 2014.

- N. Saxena, A. Greppmair, M. S. Brandt, P. Müller-Buschbaum, "Novel thermoelectric films based on a polymer-nanoparticle composite", *DPG Spring meeting 2014, Berlin*, 2015.
- N. Saxena, A. Greppmair, M. S. Brandt, P. Müller-Buschbaum, "Novel thermoelectric films based on a polymer-nanoparticle composite", *Summer School, Grainau*, 2015.
- N. Saxena, A. Greppmair, M. S. Brandt, P. Müller-Buschbaum, "Novel thermoelectric films based on a polymer-nanoparticle composite", *Congress of European Polymer Federation, Dresden*, 2015.
- N. Saxena, M. Coric, J. Wernecke, S. Langner, M. Krumrey, E. M. Herzig, P. Müller-Buschbaum, "Hybrid thermoelectrics based on a polymer/nanoparticle composite", *SAS 2015, Berlin*, 2015.
- N. Saxena, M. Philipp, L. Song, C. M. Palumbiny, M. Haese-Seiller, J.-F. Moulin, P. Müller-Buschbaum, "Hybrid thermoelectrics based on a polymer/nanoparticle composite", *Jülich Center for Neutron Science Workshop, Tutzing*, 2015.
- N. Saxena, M. Coric, A. Greppmair, J. Wernecke, S. Langner, M. Krumrey, M. S. Brandt, E. M. Herzig, P. Müller-Buschbaum, "Hybrid thermoelectrics based on a polymer/nanoparticle composite", *5th SolarTech International Conference in Munich*, 2016.
- N. Saxena, M. Coric, A. Greppmair, J. Wernecke, S. Langner, M. Krumrey, M. S. Brandt, E. M. Herzig, P. Müller-Buschbaum, "Hybrid thermoelectrics based on a polymer/nanoparticle composite", *MSE Colloquium 2016, Munich*, 2016.
- N. Saxena, M. Coric, A. Greppmair, J. Wernecke, S. Langner, M. Krumrey, M. S. Brandt, E. M. Herzig, P. Müller-Buschbaum, "Hybrid thermoelectrics based on a polymer/nanoparticle composite", *Summer School CEA-TUM 'Future of common european energy strategy', Frauenchiemsee*, 2016.
- N. Saxena, M. Coric, A. Greppmair, J. Wernecke, M. Pflüger, S. Langner, M. Krumrey, M. S. Brandt, E. M. Herzig, P. Müller-Buschbaum, "Tender resonant x-ray scattering (T-ReXS) on polymer/nanoparticle hybrid thermoelectrics", *GISAXS Workshop 2016, Hamburg*, 2016.
- N. Saxena, M. Coric, A. Greppmair, J. Wernecke, M. Plüger, M. Krumrey, M. S. Brandt, E. M. Herzig, P. Müller-Buschbaum, "Thermoelectric thin films based on a polymer/nanoparticle nanocomposite", *NIM Young Ideas in Nanoscience, Munich*, 2017.
- N. Saxena, M. Coric, A. Greppmair, J. Wernecke, M. Plüger, M. Krumrey, M. S. Brandt, E. M. Herzig, P. Müller-Buschbaum, "Thermoelectric thin films based on

- a polymer/nanoparticle nanocomposite”, *Munich School of Engineering Colloquium 2017*, 2017.
- N. Saxena, M. Coric, A. Greppmair, J. Wernecke, M. Plüger, M. Krumrey, M. S. Brandt, E. M. Herzig, P. Müller-Buschbaum, ”Thermoelectric thin films based on a polymer/nanoparticle nanocomposite”, *NIM Nanostructured Functional Materials for Sustainable Energy Provision, Munich*, 2017.
 - N. Saxena, M. Coric, A. Greppmair, J. Wernecke, M. Plüger, M. Krumrey, M. S. Brandt, E. M. Herzig, P. Müller-Buschbaum, ”Thermoelectric thin films based on a polymer/nanoparticle nanocomposite”, *NIM 'The Future of Nanoscience', Tutzing*, 2018.
 - N. Saxena, M. Coric, A. Greppmair, J. Wernecke, M. Plüger, M. Krumrey, M. S. Brandt, E. M. Herzig, P. Müller-Buschbaum, ”Thermoelectric thin films based on a polymer/nanoparticle nanocomposite”, *German Conference for Research with Synchrotron Radiation, Neutrons and Ion Beams at Large-Scale Facilities, Garching*, 2018.

Acknowledgments

In my time as PhD student at the TUM, I made many valuable experiences. For that I owe many people, who I would like to acknowledge at the end of my thesis.

First and foremost, I would like to thank my supervisor Prof. Dr. Peter Müller-Buschbaum for allowing me to join the Chair of Functional Materials, his guidance whenever it was needed, and also for challenging me with the interesting topic of organic thermoelectrics. His drive to send us out to conferences, workshops and meetings, and in general becoming part of the scientific community has enriched my PhD experience, for which I am grateful. His belief in my abilities, as well as his letting me come up with my own ideas and see them come to fruition has strongly shaped my experience.

This work is the product of many fruitful collaborations, which were also largely supported by the MSE seed funding project 'Novel Nanostructured Thermoelectric Hybrid Materials'. Our cooperation with Prof. Martin S. Brandt and Dr. Anton Greppmair on the measurement of thermal conductivity of polymer thin films, and deep discussions on the physics of organic thermoelectrics were some of the highlights of my work. Additionally, I want to thank Prof. Dr. Eva M. Herzig and especially Mihael Coric for the infinite tenacity while tackling the resonant scattering beast, from which I have also benefited. Dr. Krumrey, Dr. Jan Wernecke and Mika Pflüger also receive my thanks for their support with the resonant scattering measurements and challenging evaluation of the data. Dr. Giuseppino Fortunato and Jan Overbeck are also gratefully acknowledged for their great help with X-ray photoelectron spectroscopy and Raman spectroscopy, in my time of need.

My work at the Chair for Functional Materials has allowed me to dive into the world of research at large-scale facilities for the first time in my career. Therefore, I want to acknowledge the team from the MiNaXS-beamline at the DESY, Hamburg, led by Prof. Dr. Stephan Roth, along with Dr. Matthias Schwartzkopf, Calvin Brett, Marc Gensch, Dr. Wiebke Ohm, Sven-Jannik Wöhnert, Jan Rubeck and Dr. Pallavi Pandit. I had great times at the MiNaXS-beamlines, but also at several workshops and conferences. Dr. Sigrid Bernstorff is acknowledged for her support during beamtimes at the Austrian SAXS beamline at the Elettra Sincrotrone Trieste. I would also like to thank Dr. Jean-

Francois Moulin and Martin Haese-Seiller for the TOF-GISANS measurements at the REFSANS-beamline at the FRM II, Garching.

Both the Nanosystems Initiative Munich (NIM) and the Center for Nanoscience (CeNS) receive my thanks for creating such great environments in their graduate programs. Especially, I would like to thank Dr. Peter Sonntag, Dr. Birgit Ziller, Silke Mayerl-Kink, Dr. Isabella Almstätter for organizing many great events, and also Criss Hohmann for design of cover pictures. I thank Prof. Dr. Christine Papadakis for taking over my mentorship.

You guys went under many different names, 'Thermoelectric Workforce', my 'slaves', my 'kiddies': Regina Kluge, Anjani Kumar Maurya, Xaver Lamprecht, Mike J. Jost, Mubashar Rafiq, Benjamin Pretzl, Josef 'Seppi' Keilhofer, Benedikt Fuchs, Paul Steinacker, as well as my NIM summer research students Robin Tyburski and Haider Haseeb. As my students you had such a positive impact on my work at the Chair that I can barely put it into words. Having been your advisor on your individual paths on becoming scientists has really enriched me. Not only did I learn about teaching and understanding others, but I have also learned a lot about myself. Large parts of this thesis only exist because of your hard work, accuracy and motivation. I hope that you learned as much from me, as I did from you. I am really grateful that all of you were part of this journey, and wish you guys all the best for your future!

The Chair for Functional Materials will always hold a special place in my heart. Through tough times, through relaxed times, through fun times, it was always the members of the Chair who kept me coming into the office with a smile on my face every single day. This is why I want to thank Johannes Schlipf, Lorenz Bießmann, Nuri Hohn, Franziska Löhner, Daniel Mosegui Gonzalez, Mihael Coric, Jenny Lebert, Stephan Pröller, Oliver Filonik, Volker Körstgens, Lucas Kreuzer, Tobias Widmann, Sebastian Grott, Simon Schaper, Shambhavi Pratap as well as our 'new' generation, Kerstin Wienhold, Julian Heger, Christina Geiger, Lennart Reb, Roy Schaffrinna, Dominik Schwaiger and Anna-Lena Oechsle from the bottom of my heart. I will always fondly remember our 'escalations/ just one beer's' at Schwasi, Rennbahn, Hopfendolde, etc., Karaoke nights at Kennedy's, exciting and exhausting DPG spring meetings, occasional late shifts at university, beamtimes aided by refrigerating animals, hair straighteners and Celine Dion, workshops, BBQ's, etc.

Our colleagues from China, especially Lin Song, Bo Su, Senlin Xia, Ray Wang, Kun Wang, Dan Yang, Qi Zhong, Wei Chen, Wei Cao, Xiaohan Zhang, Xinyu Jiang, Nian Li, Shanshan Yin, are gratefully acknowledged for giving me interesting insights into chinese culture.

Thank you also to Bart-Jan Niebuur, Chia-Hsin Ko, Florian Jung and Jia-Jhen Kang for always enduring seminar talks on photovoltaics.

In the beginning, our 'alumni' took me in and helped to make my first months at the chair very pleasant. For that I want to thank Kuhu Sarkar, Markus Schindler, Shuai Guo, David Magerl, Claudia Palumbiny, Yuan Yao, Weijia Wang, Margarita Dyakonova, Christoph J. Schaffer, Natalya Vishnevetskaya, Martine Philipp, Konstantinos Raftopoulos, Anatoly Berezkin, Ezzeldin Metwalli, as well as our master students, Sebastian Günther, Christoph Mayr, Michael Bahr, Rosa Torrademe-Torrademe, Lukas Oesinghaus, Edoardo Barabino, Richard Stockhausen, May Kaepfel, Kiran Mathew John, Christoph Senfter, Thomas Kaps, Bernhard Springer, Bernhard Kalis, Gilles Möhl, Fabien Guelle, Andreas Hetzenecker, Steffen Schlosser, Christoph Bilko, Raphael Märkl and Christian Weindl.

Big thank you also to Susanna Fink, Marion Waletzki, Carola Kappauf and Dieter Müller for keeping things running silently in the background, and for their help against the bureaucracy monster. Another big thank you to Reinhold Funer, Nick Schröder, Sebastian Fink, as well as Manfred Pfaller and his team from the central workshop, who all helped with the building of XAVER. Michael Böhmler, Terry Weinmann and Egon Lenker are gratefully acknowledged for their support regarding everything electronics-related.

Another great thing about my time as a PhD student was the formation of the Polymer Music Band, in several line-ups over the years. Here, I want to specifically acknowledge Johannes Schlipf, Claudia Palumbiny, Christoph Schaffer, Eva M. Herzig, Susanna Fink, Jenny Lebert, Michael Bahr, Simon Schaper, Lucas Kreuzer, Wei Chen, Regina Kluge, Gilles Möhl, Fabien Guelle, Shambhavi Pratap, Chia-Hsin Ko, Julian Heger and Christina Geiger. We had lots of amazing gigs, and I am very proud to call myself the drummer of the Polymer Music Band!

Lastly, I want to thank my family and friends for their unconditional support, both mental and emotional. My friends from old times, school times and university times have always helped me getting even through tough times. Especially my parents, my sister, my brother-in-law and my little nephews have been a source of energy and motivation especially in this challenging last period of my work. I am also very grateful for their occasional pushes and motivational speeches when I was not living up to my own expectations. Without you, none of this would have been possible. Therefore, I want to dedicate this work to you!

